2020

Reduction of New Zealand Titanomagnetite Ironsand pellets in H_2 Gas at High Temperatures

Ao Zhang
University of Wollongong

Reduction of New Zealand Titanomagnetite Ironsand pellets in H_2 Gas at High Temperatures

by

Ao Zhang

Supervisors:

Professor Brian Monaghan

Dr Raymond Longbottom

Dr Chris Bumby (Victoria University of Wellington)

This thesis is presented as part of the requirement for the conferral of the degree:

Doctor of Philosophy

under a joint PhD Programme between the University of Wollongong and the Victoria University of Wellington

University of Wollongong

School Mechanical, Materials and Mechatronics Engineering

2020

ABSTRACT

To reduce the emission of the carbon dioxide (CO_2) in New Zealand (NZ), it is proposed to perform direct reduction (DR) of NZ titanomagnetite ironsand pellets using H_2 gas. However, there is limited pre-existing knowledge on the DR behaviour of NZ titanomagnetite ironsand pellets in hydrogen. This thesis addresses this through an experimental investigation of the H_2 gas-based reduction of Ar-sintered and pre-oxidised pellets, and an analytical kinetic model is developed to describe the reduction rate.

The reduction rate of both types of pellets is found to increase with increasing temperature, H_2 gas flow rate, and H_2 gas concentration. For both pellets reduced at 1443 K above the critical flow rate, the maximum reduction degree reaches ~97% with a similar reduction rate. However, in the lower temperature range (< 1143 K), pre-oxidised pellets are reduced much faster than Ar-sintered ones.

During reduction of both types of pellets, any TTH present is rapidly reduced first. After this step, TTM is then reduced to FeO, with Ti becoming enriched in the remaining unreduced TTM. FeO is further reduced to metallic Fe, which makes up to ~90% reduction degree. Eventually Ti-enrichment of the TTM leads to a change in the reduction pathway and it instead directly converts to metallic Fe and $FeTiO_3$. Above ~90% reduction degree, reduction of the remaining Fe-Ti-O phases occurs (leading to the formation of TiO_2 or (pseudobrookite) PSB/ferro-PSB).

At the pellet-scale, both types of pellets present a single interface shrinking core phenomenon at higher temperatures. Metallic Fe is generated from pellet surface with a reaction interface moving inwards. However, at lower temperatures this pellet-scale interface becomes less defined in the pellets. Instead, grain-scale reaction fronts are observed.

A single interface shrinking core model (SCM) is shown to successfully describe the reduction of pellets for reduction degrees < ~90%, at all temperatures studied. The single interface SCM indicates that the reduction rate of the Ar-sintered pellets is controlled by the interfacial chemical reaction rate. However, two different temperature regimes are identified. Above 1193 K, the activation energy is calculated to be 41 ± 1 kJ/mol, but below 1193 K the calculated activation energy increases to 89 ± 5 kJ/mol. This change in activation energy is likely to be associated with the change of the rate-limiting reaction from FeO → metallic Fe to TTM →

FeO. By contrast, the pre-oxidised pellets exhibit mixed control at 1043 K (interfacial chemical reaction rate and the diffusion rate through the product layer). However, at temperatures of 1143 K and above, the pre-oxidised pellets also exhibit interfacial chemical reaction control, with a single activation energy of 31 ± 1 kJ/mol, which seems to be consistent with the rate-limiting reaction being FeO → metallic Fe.

In summary, the findings in this thesis contribute to understanding of the reduction of NZ ironsand pellets in H_2 gas, and establish a kinetic model to describe this process. In the future, this information will be applied to develop a prototype H_2-DRI shaft reactor for NZ ironsand pellets.

ACKNOWLEDGEMENT

During the course of my PhD works, I have received many assistances both in experiment conductions and academic writing. I would like to show my most grateful thanks to those who have assisted and supported me to finish my thesis.

I would like to express my sincere appreciation to my supervisors: Dr Chris Bumby, Professor Brian Monaghan, and Dr Raymond Longbottom. They are knowledgeable, supportive, and patient, even during the time I got lost writing my thesis academically. They had always guide me through my studies, by providing me invaluable inputs for my experimental work and analysis. Besides the assistance for my studies, they are always there to care about my physical and emotional conditions. I am also very grateful for the financial support that Chris offered me during my time of writing the thesis.

I would like to thank Martin Ryan for his time, expertise, and help in TGA experiments, XRD analysis, and ND analysis. He is always willing to help with all sorts of problems that I have encountered during experiments. I am also very grateful that he always drives me home in the raining days.

I would also like to thank Sarah Spencer for her guidance, help, and advice in light microscopy, metallography and SEM-EDS analysis. The assistance she provided with the microscopies are invaluable, and she is always patient and tolerant with my questions. I also want to thank her help with my English language in my thesis.

I would like to thank the Advanced Material Group at Callaghan Innovation. They provide me with a spacious office with all the facilities that I needed and a safety experimental environment. They also helped me with the induction of all the experimental facilities that I needed. Special gratitude to Dr Matthias Vest for assisting in the procedure of the safety assessment for my experimental works; to Diego del Puerto for helping in the engineering works; Dr. Bridget Ingham for her assistance in the ND experiments and analysis and Alison Speakman for assist me finding and accessing all the literature that I required.

I also want to thank the team at Robinson Research Institute. Special thanks to Jeannie Redman and Ursula Muavae for all the administrative works. Special thanks to Jeannie Redman for picking me up from the airport the first time that I arrived in New Zealand; and also to Joseph Bailey (and his partner Jessie Gibbs) for providing a cosy room to stay.

I would also want to thank the Pyrometallurgy Research Group at Faculty of Engineering and information Science at University of Wollongong. They provide me with a comfortable and secure studying environment. Special gratitude to Matthew Franklin for his help in the metallography. Furthermore, I am also grateful for the guidance and assistance in the SEM-EDS analysis from Dr Mitchell Nancarrow and Tony Romeo at Electron Microscopy Centre from the innovation campus.

I would also like to thank Dr Deborah Laurs from the student learning at Victoria University of Wellington to help me through my academic writing.

I am also very grateful for my master's degree supervisors: Dr Erik Skiera and Dr Simone Herzog, for their recommendation letters and support to start the PhD programme.

I would also like to thank all my friends: Oscar Bjareborn, Sigit Prabowo, Dr Apsara Jayasekara, Ai Nguyen, Dr Daniel Jang, Dr Huibin Li, Dr Xuefeng Dong, Dr Sinan Gai and Helena Ding for their friendship, understanding and tolerance.

Finally, I would like to thank my family, especially my mum and dad, for the love, care and support through the years.

Thank you, to all these people for all of your help.

CERTIFICATION

I, *Ao Zhang*, hereby declare that this thesis submitted in fulfilment of the requirements for the conferral of the degree Doctor of Philosophy (PhD), from University of Wollongong, Australia, is my own work. Any contribution made to the research by others, with whom I have worked, is explicitly acknowledged in the thesis. This thesis is being submitted under a joint PhD programme between University of Wollongong and the Victoria University of Wellington, New Zealand. This degree will be conferred as a single degree. Therefore, this thesis has also been submitted to Victoria University of Wellington for PhD examination. This document has not been submitted for qualification at any other academic institution.

Ao Zhang
Date: 22/04/2021

LIST OF PUBLIFICATIONS

During the course of this thesis, one journal article and one conference paper have been published. Several passages, figures and tables that were included in these published papers have been directly reused in this thesis. A list of publication is given below:

Journal Article:

- A. Zhang, B. J. Monaghan, R. J. Longbottom, M. Nusheh, and C. W. Bumby, "Reduction Kinetics of Oxidized New Zealand Ironsand Pellets in H_2 at Temperatures up to 1443 K," *Metall. Mater. Trans. B*, vol. 51, pp. 492-504, 2020.

Conference Paper:

- A. Zhang, R. J. Longbottom, M. Nusheh, C. W. Bumby, and B. J. Monaghan, "Hydrogen Reduction of New Zealand Titanomagnetite Pellets," in *Iron Ore Conference 2019 Proceedings*, Perth, Australia, pp. 472-478.

- A. Zhang, R. J. Longbottom, M. Nusheh, C. W. Bumby, and B. J. Monaghan, "Reduction of Titanomagnetite Pellets by Hydrogen Gas," in *8^{th} International Congress on Science and Technology in Ironmaking.* Vienna, Paper ID: 282.

LIST OF ABBREVIATIONS

NZ = New Zealand

BF = Blast furnace

DR = Direct reduction

RPCC = Reduced primary concentrate and char

EAF = Electric arc furnace

TTM = Titanomagnetite phase

TTH = Titanohematite phase

H_2 = Hydrogen gas

CO = Carbon monoxide

CH_4 = Methane gas

Ar = Argon gas

SCM = Shrinking core model

PSB = Pseudobrookite Fe_2TiO_5

TGA = Thermogravimetric analysis

ND = Neutron diffraction

XRD = X-ray diffraction

XRF = X-ray fluorescence

LOI = Loss on ignition

VUW = Victoria University of Wellington

UOW = University of Wollongong

SEM = Scanning electron microscopy

EDS = Energy dispersive spectroscopy

ANSTO = Australia Nuclear and Science Technology Organisation

NOMENCLATURE

t = Time (min)

ρ_B = Molar density of the solid reactant (mole/cm^3)

$X_a(X)$ = Reduction degree (dimensionless)

C_{Ag} = Gas concentration at the gas stream (mole/cm^3)

C_{As} = Gas concentration at the pellet surface (mole/cm^3)

C_{Ac} = Gas concentration at the reaction interface (mole/cm^3)

C_{Ae} = Equilibrium gas concentration at the reaction interface (mole/cm^3)

k_g = Mass transfer coefficient (cm/min)

k_s = Reaction rate constant (cm/min)

k_s' = Apparent reaction rate constant (cm/min)

D_e = Effective diffusion coefficient (cm^2/min)

D_e' = Apparent effective diffusion coefficient (cm^2/min)

$R(r)$ = Radius (cm)

$D50\%$ = Average particle size (μm)

w_0 = Initial weight of pellets before reduction (mg)

w_t = Weight of pellets after reduced for *t* mins (mg)

m_o = Mass of oxygen (mg)

M = Molar mass (g/mol)

$vol\%$ = Volume fraction (dimensionless)

$wt\%$ = Weight percentage (dimensionless)

$at\%$ = Atomic percentage (dimensionless)

τ = Characterisation time (50wt% metallic Fe) (min)

$I(X_a)$ = Interfacial chemical reaction dependence (dimensionless)

$D(X_a)$ = Diffusion dependence (through product layer) (dimensionless)

R = Universal gas constant = 8.314 (J/(mol·K))

E_A = Activation energy (J/mol)

x_0 = Initial stoichiometric of Ti in TTM (dimensionless)

y_0 = Initial stoichiometric of Ti in TTH (dimensionless)

δ = Enrichment of Ti in TTM (dimensionless)

n = Molar fraction (dimensionless)

ΔG = Gibbs free energy (kJ/mol)

Q = Equivalent flow rate (ml/min)

CONTENTS

LIST OF FIGURES

LIST OF TABLES

Chapter 1
Introduction

1.1 Background of the study

In New Zealand (NZ), large deposits of titanomagnetite ironsand are found along the west coast of the North Island, both onshore and offshore [1]–[4]. Ever since these deposits were found, they have been the only local source of iron ore for the iron/steel production, constituting an important mineral in NZ [5]. However, compared to internationally-found non-titaniferous magnetite ores, NZ titanomagnetite ironsand contains slightly less iron (Fe, ~60wt%). In addition, other elements such as titanium (Ti, at equivalent to ~8 wt% TiO_2) and vanadium (V, at equivalent to ~0.5wt% V_2O_5) are also present in the ironsand.

There are many factors highlighting the importance and advantages of utilising NZ titanomagnetite ironsand for steelmaking. Firstly, it can be easily mined as it deposits as sand dunes along the coast [6]. More than 1.2 million tonnes of ironsand are mined annually in NZ [7]. Secondly, the ironsand is also regarded as a cheap source of iron units for steel making [8]. Aside from the local utilisation to produce iron/steel to meet the New Zealand's national demand [9], the ironsand is also exported to other countries such as China, Japan and Australia [10]. The mining and utilisation of the ironsand not only directly contributes to New Zealand's GDP, but also helps the local economy by creating jobs [11], [12]. Finally, there is also possible value in co-production of TiO_2 and V_2O_5 minerals found within the titanomagnetite ironsand [13], [14].

Despite the advantages of employing NZ ironsand, there are challenges around the ironsand reduction process. Due to the presence of Ti in the ironsand, the internationally dominant iron reduction process used in most steel industries, the Blast Furnace (BF), is not applicable [15]. This is because during reduction of titanomagnetite ironsand in a BF, the carbon from the coke combines with the Ti in the ironsand to form a slag layer which has a high viscosity. This slag layer does not flow well and can block the tap holes, making it difficult to withdraw the molten Fe and slag from the furnace.

Today, NZ Steel applies a direct reduction (DR) process using coal to reduce NZ ironsand. This integrated ironmaking plant has the capacity to produce 650,000 tonnes molten iron per

year [15]. This process reduces the ironsand in two stages. The ironsand concentrate is initially mixed with coal and heated in the multi-hearth furnaces. The heated mixture is then blended with limestone and partially reduced in a rotary kiln via a solid-state carbothermic reduction process. Afterwards, the partially reduced product (Reduced Primary Concentrate and Char - RPCC) is smelted in an electric furnace, to complete the reduction process and produce molten iron.

Although the NZ Steel process is industrially proven for the production of iron/steel from NZ ironsand, this solid state carbothermic process consumes lots of energy and emits a large amount of carbon dioxide (CO_2). These emissions represent ~55% of industrial greenhouse gas emissions in NZ [16]. However, NZ has launched a target for net zero emissions of all greenhouse gases (other than biogenic methane) by 2050 [17]. This target urgently requires a cleaner and more sustainable iron/steel producing industry. Therefore, investigating and developing new alternative processes for ironsand reduction, which can enable high iron/steel production rates with low greenhouse gas emissions, is of great importance.

In recent years, gas-based DR has become increasingly recognised as a promising alternative process for titanomagnetite ore reduction [18]–[20]. Gas-based DR processes do not require the coking process required for conventional BF ironmaking. As a result the advantages of gas-based DR include reduced greenhouse gas emissions, reduced energy consumption and reduced overall capital cost [21]–[23]. Amongst the various commercial gas-based DR processes in operation today, the Midrex process is one of the most developed. This process utilises lump or pelletised ores as the charge in a vertical shaft furnace. It reduces the ores at temperatures (generally at ~1173 K) below the melting point of iron (~1803 K) by using syngas or natural gas [24]. The final product of the reduced iron is normally referred to as sponge iron due to its porous structure. This is then melted in an electric arc furnace (EAF) for steel making, which are generally used to recycle high-quality scrap.

There is also the possibility to design gas-based reduction processes which employ H_2 gas as a reductant (instead of CO or methane). This is attracting increasing attention as a potential route to realise a zero-carbon footprint for the iron/steel making processes [25]–[27]. In recent times, NZ has been investigating heavily in H_2 research and development. Today, 85% of NZ's electricity is generated from renewable sources. The abundance of renewable energy could be used to produce 'Green H_2' as a next generation fuel, thus help to build a robust energy platform

to decarbonise NZ [28]. Therefore, to fulfil the target of net zero greenhouse gas emissions from the iron/steel industry in NZ, a H_2-based DR process has been proposed for the reduction of NZ ironsand. One such process could reduce pellets formed from NZ titanomagnetite ironsand in a vertical shaft furnace fed with H_2 gas.

However, when compared to the relatively comprehensive knowledge of DR characteristics of the conventional iron ores in CO, methane or syngas, the reduction behaviour of titanomagnetite ironsand pellets in H_2 gas has not been fully investigated. While the presence of Ti is reported to affect the reduction process of the titanomagnetite ore [29], this effect is not fully understood. Moreover, the influence of Ti on the reaction pathway and phase evolution which occurs during reduction has also not been studied in detail. And finally, the kinetics and mechanisms for the H_2 reduction of NZ ironsand pellets has not previously been determined. Accordingly, the work presented in this thesis aims to investigate the behaviour and properties of the NZ titanomagnetite ironsand pellets during direct reduction in H_2 gas. It is hoped that conclusions drawn from this work may have implications for any future industrial application of this type of process

1.2 Aim of the study

The ultimate aim of this study is to understand the reduction mechanisms for NZ titanomagnetite ironsand pellets in H_2 gas. To fulfil this aim, the following objectives have been set:

1. To develop a pelletising approach for producing pellets (Ar-sintered and pre-oxidised), which are mechanically strong at high temperatures in reducing gas atmosphere;
2. To characterise the reduction behaviours of these pellets at high temperatures;
3. To examine the morphological changes of these pellets during reduction;
4. To determine the phase evolution of these pellets during reduction; and
5. To establish an analytical kinetic model to describe the reduction behaviours (2) and morphological changes (3), as well as analyse the phase evolutions (4) during reduction.

The findings of this study should contribute to the understanding of the reductions of the NZ titanomagnetite ironsand pellets in H_2 gas at high temperatures.

1.3 Structure of thesis

The structure of the thesis is shown in **Figure 1.1**.

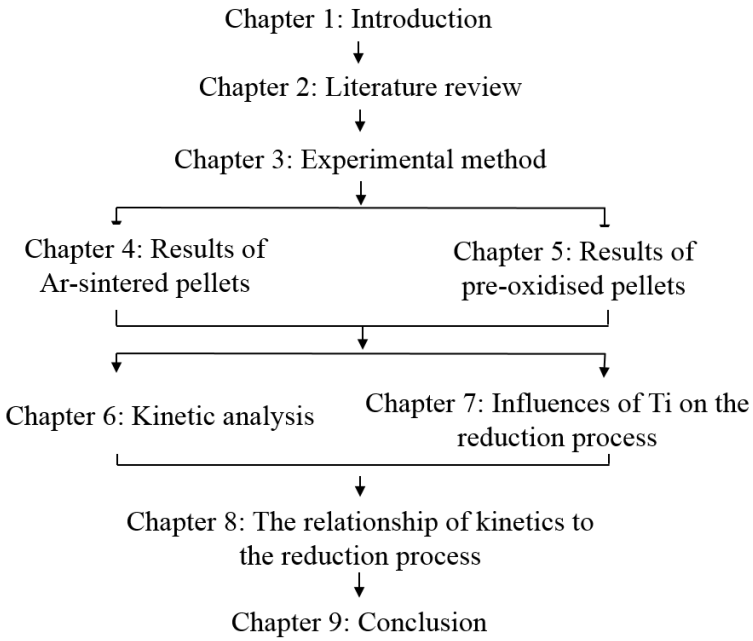

***Figure 1.1** – A flowchart showing the structure of the thesis*

As such, the following chapters are included in this thesis:

Chapter 1: An introduction of the thesis

Chapter 2: A survey of the existing literature, determining the knowledge gap in the reduction of the NZ titanomagnetite ironsand pellets

Chapter 3: Descriptions of the experiment set ups and procedures, to achieve the objectives of the study of pellet reduction

Chapter 4: The results of the reduction behaviour, phase evolution and morphological evolution of the Ar-sintered pellets

Chapter 5: The results of the reduction behaviour, phase evolution and morphological evolution of the pre-oxidised pellets

Chapter 6: The application of a pellet-scale shrinking-core model (SCM) to describe the reduction process

Chapter 7: Analysis of the phase evolution at 1223 K, especially on the influence of Ti on the reaction pathway

Chapter 8: Analysis of the phase evolution at varying temperatures, and interpretation in terms of findings from the SCM analysis

Chapter 9: Conclusion of the findings from this work and recommendations for further future investigations

Chapter 2
Literature review

A reasonably large amount of literature reporting the properties of the NZ titanomagnetite ironsand has been published, reflecting the industrial significance of this type of ironsand. Driven by the demands for creating a sustainable iron/steel production industry, the volume of literature regarding the gas-based DR process of other iron ores, has also been increasing. However, studies on the gas-based DR behaviour and mechanisms of the NZ titanomagnetite ironsand, especially in the form of pellets, are comparatively rare.

In this chapter, a literature survey is presented which examines previous related studies in order to provide some initial insight into the expected gas-based DR behaviour of the NZ titanomagnetite ironsand pellets. This work is subdivided into the following sections:

- **Section 2.1**: An introduction to NZ titanomagnetite ironsand
- **Section 2.2**: Pelletising process
- **Section 2.3**: Kinetics of gas-based DR of iron ore
- **Section 2.4**: Gas-based DR characteristics of titanomagnetite iron ores.
- **Section 2.5**: Summary of the literature review

2.1 An introduction to NZ titanomagnetite ironsand

In NZ, titanomagnetite ironsand deposits were formed 2.5 million years ago from the erosion of andesitic volcanic rocks which erupted from the Taranaki volcanoes [30]–[32]. Over time, the ironsand was transported by ocean currents and finally deposited on beaches, forming dunes [33]. Currently, these ironsands are commercially mined at Taharoa and Waikato North Head. Many previous studies have investigated the properties of the ironsands obtained from these two deposits [4], [34]–[39]. Their overall chemical compositions are summarised in **Table 2.1**. In this table, some selected titanomagnetite ores from around the world are also presented for comparison [13], [40]–[43]. As can be seen, the titanomagnetite ores from international deposits have quite different chemical compositions to NZ ironsand. In NZ ironsand, the proportion of Fe^{2+} (denoted as equivalent wt% of 'FeO' in this table) is generally ~30wt% which is higher than other international ores. Moreover, the NZ ironsands also contain Ti levels

equivalent to about 7wt% to 8wt% TiO_2, which is significantly lower than most other internationally reported titanomagnetite ores.

***Table 2.1**– Chemical composition (wt%) of the NZ titanomagnetite ironsands from different deposits, alongside some selected international titanomagnetite ores. Note that the values stated in the table stand for the equivalent wt% assuming all the cations are in their equivalent oxide phase (i.e. Fe^{2+} as FeO)*

Deposit	Reference	FeO	Fe_2O_3	TiO_2	MgO	MnO	Al_2O_3	V_2O_5	Other
Waikato North Head	[4]	30.6	52.5	8	3.3	0.6	3.5	0.4	1.2
	[34]	30	52.4	8	3	0.6	4	0.4	1.5
	[37], [38]	Total Fe: 59.3		7.9	2.8	0.6	3.6	0.5	
Taharoa	[4]	31.9	51.5	7.9	3.2	0.7	3.3	0.4	1.1
	[36]	26.1	47.1	7.4	4	0.6	5	0.3	14.4
China	[13]	18.4	42.1	21.5	0.7	0.7	1.8	0.1	14.7
	[43]	Total Fe: 52.3		12.9	3.1	0.3	3.1	0.3	
Indonesia	[40]	Total Fe: 57.3		11.4	2.7	0.4	2.9		
Russia	[41]	23.3	49.4	11.3	2.4	0.1	3.7	0.7	9.1
South Africa	[42]	15	63.2	13.7	1.2	0.3	3.2	1.6	

The morphologies of the particles in NZ titanomagnetite ironsand has also been previously analysed [4], [34], [35], [44]. Beneficiated ironsand is typically observed to contain two different types of particles. Typical examples of these two types of particles in the light microscopy are shown in **Figure 2.1** [44].

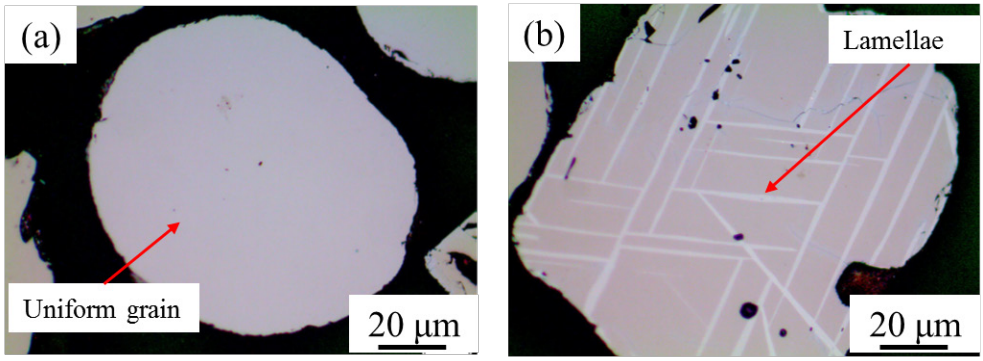

***Figure 2.1**– Light microscopy images showing the two typical types of the particles found in the NZ titanomagnetite ironsand based on [44]*

In NZ titanomagnetite ironsand, the majority of particles are homogeneous in appearance, as shown in **Figure 2.1(a)**. These particles have been referred to as 'uniform' titanomagnetite particles as they contain mainly the titanomagnetite phase (TTM). TTM is a solid solution of magnetite (Fe_3O_4) and ulvospinel (Fe_2TiO_4). It has a cubic spinel structure and the stoichiometry can be expressed as $Fe_{3-x}Ti_xO_4$. For NZ ironsand, x has a typical value of 0.27 ± 0.02 [44]. The other type of the particles in NZ ironsand show lamellar structures within the homogeneous background matrix, as illustrated in **Figure 2.1(b)**. These lamellar structures are typically found to be enriched in Ti compared to their surroundings, and are believed to be exsolved titanohematite formed by partial oxidation [45]. Titanohematite (TTH) is a solid solution of hematite (Fe_2O_3) and ilmenite ($FeTiO_3$). It has a rhombohedral structure and its stoichiometry can be expressed as $Fe_{2-y}Ti_yO_4$. In both types of particles, it has been found that other elements such as magnesium (Mg), aluminium (Al), and manganese (Mn) are also in solid solution within the TTM phase. However silicon (Si) typically is only found in separate silicate particles [44].

To conclude, NZ titanomagnetite ironsand is compositionally different from other international titanomagnetite ores, and it normally contains two types of particles. These features make the properties of the NZ titanomagnetite ironsands unique from conventional non-titaniferous ores as well as from other international deposits of titanomagnetite ores.

2.2 Pelletising process

To perform a gas-based DR process in a vertical shaft furnace, iron ore is normally charged in the form of pellets [46]. This requires that fines such as NZ ironsand must be consolidated into pellets prior to processing. Pelletisation ensures enhanced performance of the DR process, enabling advanced permeability for gas transport (between pellets), and faster heat transfer inside the furnace [47]–[50].

The disc pelletising process is one of the most widely applied pelletising technologies [51], [52]. **Figure 2.2** schematically illustrates a laboratory disc pelletiser [53]. As the disc rotates, feed material is charged to the bottom of the disc and water is added. When the powdered material makes contact with water, the nucleation of the pellet seeds starts to occur. This forms initial small pellets. With the addition of more feed material, the size of these pellets increases. By controlling the amount of feed material and pelletising time, green pellets of the desired size range are produced. Moreover, pelletising variables, such as the diameter of the disc pelletiser, the set vertical angle, the rotation speed and the amount of added water, can all affect the final pellet properties [51], [52].

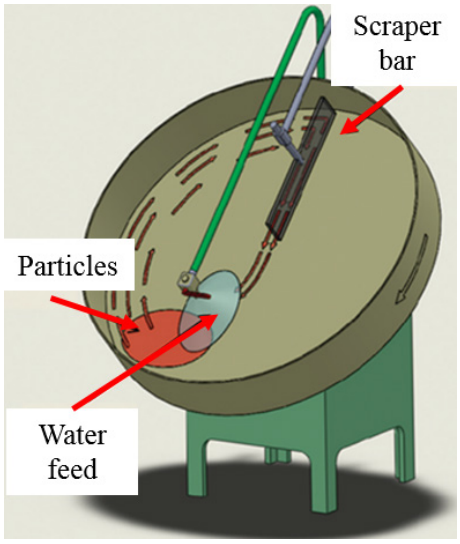

***Figure 2.2**– Schematic of a laboratory disc pelletiser based on [53]*

During disc pelletisation, feed particles are converted into pellets via several steps [54]. Firstly, the solid particles are covered by a water film, which bridges between particles and forms agglomerates. The movement of the disc densifies these agglomerates, leading to the

production of ‘green’ pellets. It is important to note that ‘green’ pellets produced directly from the disc pelletiser are mechanically weak and could not survive compression under high weight loads in a vertical shaft reactor. Hence before reduction, the pellets are normally sintered at high temperature in order to develop significantly increased strength through the formation of sintered solid-to-solid bonds [55].

The feed material for disc pelletising in the iron/steel industries are mostly iron ore fines. In order to improve the process and enhance the bonding strength of both ‘green’ and ‘sintered’ pellets, binders are also introduced and mixed in small quantities with the iron ore fines [56]. The effects of mineral and organic polymer-based binders on the properties of the pellets have been extensively studied [57]–[64]. Some common binder materials, and their advantages and disadvantages to the pelletisation process are summarised in **Table 2.2** [64].

Table 2.2*– Some common binder materials and their properties [64]*

Types of binder material	Advantages	Disadvantages
Clay - Bentonite	➢ Easily spread in the particle mixtures ➢ High capacity of absorbing water ➢ Smooth and uniform pellets ➢ Relatively cheap	➢ Adding silica to the pellets
Organic – Carbon based polymers	➢ Silica free ➢ Can be specifically designed to meet the properties ➢ Highly reproducible characteristics	➢ Relatively high cost
Cementitious binders – Lime	➢ Silica free ➢ Irreversible bonding action ➢ Can be self-fluxing and readily available	➢ Relatively long curing time

2.3 Kinetics of gas-based DR of iron ore

Kinetic models can be used to describe the reduction rate of iron ore pellets in a gas reductant. Such models can help develop understanding of the rate-limiting mechanisms for reactions occurring between the gas reductant and solid reactant.

2.3.1 Summary of the kinetic analysis

Since the development of gas-based DR processes, kinetic analysis has been conducted for the reduction of many conventional non-titaniferous iron ores [65]–[113]. Such studies have simulated reductions in industrial shaft furnaces [72], [76], [79], [101], [114], as well as the Fluidized Bed system and Flash Reduction [84], [102], [115], [116]. For all these processes, CO, methane (CH_4) and H_2, were the most commonly studied reducing gases [65]–[113]. Models based on either mathematical equations or numerical simulation methods have been applied to determine the kinetic behaviour [106], [117]. Some studies developed a multi-stage mechanism that accounted for all of the separate reaction steps participating in the process [72], [81]. However, many other works have assumed a single overall reaction step which describes the whole process. In each case, kinetic analyses have been used to describe the experimental results and provide fundamental understanding which is important to the design of industrial gas-solid reaction reactors. However, compared to the studies regarding the kinetics of reducing the non-titaniferous iron ores, the knowledge on the mechanisms of reducing titanomagnetite ores was relatively scarce [19], [20], [118]–[130].

This thesis considers the H_2 direct reduction of ironsand pellets. Thus, the kinetic modelling of iron ore pellets during gas reduction requires review. A summary of critical works on this topic are listed in **Table 2.3**. It is noted that most of the studies utilised a shrinking core model (SCM) to describe the reduction progress of the pellet. This model will be discussed in more detail in **Subsection 2.3.2**.

***Table 2.3**- Summary of key literature reporting kinetic analyses of the gas-based reduction of iron ore pellets*

Reference	Ore type	Experiment conditions	Model type	Rate-limiting step
[77]	Iron oxide pellets from Arcelor Mittal and LKAB	Isothermal reduction from 708 K to 1183 K by H_2-CO mixture	A modified three-interface Shrinking Core Model (Fe_2O_3/Fe_3O_4; Fe_3O_4/FeO; FeO/metallic Fe)	Interfacial chemical reaction of FeO → metallic Fe
[79]	Hematite pellets	Isothermal reduction from 1123 K to 1323 K by H_2	Single interface (FeO/metallic Fe) SCM	Interfacial chemical reaction of FeO → metallic Fe
[86]	Hematite pellets	Isothermal reduction from 1073 to 1273K by H_2-CO mixture	Single interface (FeO/metallic Fe) SCM	Interfacial chemical reaction at beginning and then a mixed control (interfacial chemical reaction and pore diffusion of gases) and pore diffusion of gases at later reduction stages
[88]	Iron oxide pellet	Isothermal reduction from 1073 K to 1373 K by H_2-CO mixture gas	A mathematical time-dependent model based on the grain model with a finite volume fully implicit technique	The reaction rate of FeO is much slower than other iron oxide components
[94]	Hematite pellets from Sidor Steelmaking Plant	Isothermal reduction at 1123 K by H_2, CO and Midrex Gas	An approximated single interface (FeO/metallic Fe) Grain Model	For H_2 and CO: mix of interfacial chemical reaction and pore diffusion of gases at the beginning and then purely pore diffusion of gases For Midrex Gas: mixed control through the whole process
[100]	Hematite pellets from Arcelor-Mittal	Isothermal reduction at 1123 K by H_2-CO mixture gas	Single interface (FeO/metallic Fe) SCM	Interfacial chemical reaction at initial stage and pore diffusion of gases at later stage

Table 2.3 *- Summary of key literature reporting kinetic analyses of the gas-based reduction of iron ore pellets (continued)*

Reference	Ore type	Experiment condition	Model type	Rate limiting step
[103]	Hematite pellets	Isothermal reduction from 1089 K to 1477 K by H_2 with different flow rates	Model type not specified	Interfacial chemical reaction of H_2 gas with iron oxide at reaction interface
[104]	Hematite pellets from Sweden	Isothermal reduction from 1123 K to 1273 K by a H_2-CO-N_2 gas mixture	Single interface numerical modelling - A well-developed mathematical model involving a series of heterogeneous chemical reactions, heat transfer and mass transfer	First-order reactions controlled by a mix of interfacial chemical reaction and pore diffusion of gases
[106]	Industrial hematite pellets with 96wt% Fe_2O_3	Isothermal reduction at 1073 and 1123 K by pure H_2	Single-interface (Fe_2O_3/metallic Fe) finite element modelling - 2-Dimensional model in COMSOL Multiphysics 5.1 Software	Mix of gas transport in gas stream and solid phases and interfacial chemical reaction in the reaction zone
[131]	Hematite pellets	Isothermal reduction from 1123 K to 1323 K by biomass syngas	A single interface (interface not specified) SCM	Interfacial chemical reaction
[122]	Indonesia oxidised titanomagnetite pellets with 55.5 wt% Fe and equivalent 9.6 wt% TiO_2	Isothermal reduction from 1073 to1273 K by pure H_2	A single interface (interface not specified) SCM	Below 1123 K, interfacial chemical reaction control at the beginning of the reduction, then a mixed control to the end of the reduction; Above 1173 K, interfacial chemical reaction control at beginning of the reduction, then a mixed control, and finally pore diffusion of gases control at later stage

Table 2.3 *- Summary of key literature reporting kinetic analyses of the gas-based reduction of iron ore pellets (continued)*

Reference	Ore type	Experiment condition	Model type	Rate limiting step
[126]	Oxidized High Chromium-Vanadium-titanomagnetite pellets with 59.5 wt% Fe and equivalent 4.5 wt% TiO_2	Non-isothermal reduction by H_2-CO-CO_2 mixture gas	A modified three-interface SCM (Fe_2O_3/Fe_3O_4; Fe_3O_4/FeO; FeO/metallic Fe)	Not specified
[127]	Oxidized Vanadium-titanomagnetite pellets with 45.5 wt% Fe and equivalent 13.4 wt% TiO_2	Isothermal reduction from 1223 K to 1373 K by H_2-CO mixture gas	A single interface (interface not specified) SCM	Interfacial chemical reaction control at early stage and gas diffusion through the product layer control at later stage
[128]	Oxidized High – Chromium-Vanadium-titanomagnetite pellets with 59.4 wt% Fe and equivalent 4.5 wt% TiO_2	Isothermal reduction from 1223 K to 1373 K by H_2-CO mixture gas	A single interface (interface not specified) SCM	Mix of interfacial chemical reaction and gas diffusion at early stage and purely gas diffusion through the product layer control at later stage
[130]	Oxidised Vanadium-titanomagnetite pellets with 54.27 wt% Fe and equivalent 12.5 wt% TiO_2	Isothermal reduction from 1173 K to 1323 K by H_2-CO mixture gas	A single interface (interface not specified) SCM	Interfacial chemical reaction at early stage and gas diffusion through the product layer at later stage

One of the main kinetic parameters obtained from the kinetic models is the activation energy. It is generally used to determine the rate of the reduction, which can optimise the reactor design [68], [132]. Activation energies have been determined in a number of studies reducing conventional non-titaniferous ores, and the values reported have varied over a large range, from 9 kJ/mol to 120 kJ/mol [93], [96], [101], [133]–[136]. This difference in the activation energy has been associated with the many different experimental conditions used in different studies, such as: impurities in the ores [137], types of reducing gas and gas composition [98], [136], and pre-treatment of the ore [111]. In general, it has been reported that reductions in H_2 gas show a decrease in the activation energy compared to CO gas [99]. This represents another potential advantage of utilising H_2 gas as the reducing agent.

However, there are only few reports on the determination of the activation energy for the reduction of titanomagnetite ores in H_2 gas [108], [118], [125]. These studies and the corresponding determined activation energies are listed in **Table 2.4**. The activation energy determined was generally within a similar range to conventional non-titaniferous ores. However, discrepancies in these three reports are also clear, which again are expected to be related to the experimental conditions applied in different works. It should be noted that, to date there have been no published reports determining the activation energy for gas-based reduction of NZ ironsand pellets.

***Table 2.4** – Summary of key literature reporting activation energies for the gas-based reduction of titanomagnetite ores*

Refer-ence	Sample	Experimental conditions	Controlling step	Activation energy
[108]	Titanomagnetite ore (~200 µm, 3 g, 55.6 wt% Fe and equivalent 11.4 wt% TiO_2)	H_2-Ar gas mixture 1073 K to 1273 K	Raw ironsand: mix of nucleation and growth, 1st order chemical reaction, and 3-dimensional gas diffusion; Pre-oxidised ironsand: Interfacial chemical reaction control	Raw ironsand: 50 to 105 kJ/mol; Pre-oxidised ironsand: 67 kJ/mol
[118]	Titanomagnetite ore (~150 to 160 µm, 100 mg, 56.9 wt% Fe and equivalent 9.0 wt% TiO_2)	H_2-Ar gas mixture 967 K to 1173 K	Interfacial chemical reaction for $FeO + FeTiO_3 \rightarrow Fe +$ Ti-containing phases	115 kJ/mol
[125]	Titanomagnetite briquette (~108 - 422 µm, 15 g, 55.6 wt% Fe and equivalent 11.4 wt% TiO_2)	Graphite 1423 K to 1623 K	Diffusion of the ions through the product layer	170 kJ/mol

2.3.2 Single interface Shrinking Core Model (SCM)

Description of the model

As listed in **Table 2.3**, the shrinking core model (SCM) is the most widely applied kinetic model used to describe the gas-based reduction of iron ore pellets [79], [86], [100], [122], [127], [128], [130], [131]. Commonly, the SCM is applied by assuming only one rate-limiting reaction interface. Based on Levenspiel [138], the single interface SCM can be used to describe a gas-solid reduction process which proceeds through five successive steps. The effects of these five steps on the gaseous reduction of a spherical pellet/particle are schematically illustrated in **Figure 2.3**. These five steps are [138]:

Step 1: Diffusion of the reducing gas through the gas film surrounding the outer surface of the pellet/particle;

Step 2: Diffusion of the reducing gas through an outer solid product layer until it reaches the surface of the unreacted shrinking core. This surface is commonly referred as the reaction interface;

Step 3: Chemical reaction at the surface of the shrinking core between the reducing gas and solid reactant, which generates both solid and gaseous products. This is commonly referred to as the interfacial chemical reaction;

Step 4: Diffusion of the gaseous products back through the outer solid product layer until reaching the surface of the pellet/particle;

Step 5: Diffusion of the gaseous product back through the gas film and hence into the surrounding gas stream.

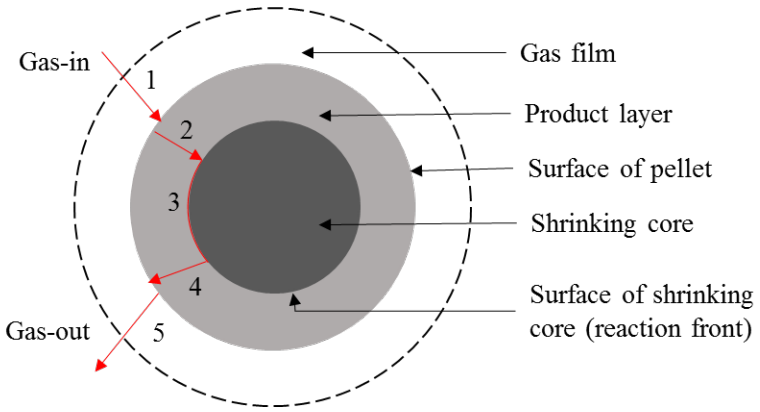

Figure 2.3 *- Illustration of the five steps described by the single interface SCM for the reduction of a spherical iron ore (pellet/particle). Step 1 and 5 illustrate the gas diffusion in the gas stream; Step 2 and 4 illustrate the gas diffusion in the product layer; and Step 3 illustrates the interfacial chemical reaction at the reaction interface [138]*

During reduction, the step which proceeds at the slowest rate will directly limit the reduction process [138]. Often, step 1 is combined with step 5 and referred to as the diffusion of gases through the gas film [138]. Similarly, step 2 is coupled with step 4 and referred to as the diffusion of gases through the product layer [138]. Therefore, in the gaseous reduction of spherical pellet/particle, there are usually three possible controlling mechanisms [138]: (1) the diffusion of gases through the gas film, (2) the diffusion of gases through the solid product layer and (3) the interfacial chemical reaction at the reaction front. Among these three controlling mechanisms, the slowest one will limit the overall reduction rate, and is referred to as the rate-limiting step.

Each controlling step leads to a different contribution of gas concentration within the pellet/particle. This is schematically represented in **Figures 2.4** to **2.6**. Note that here these digrams have been drawn assuming that diffusion of the reducing gas contributes to the rate-limiting mechiansm, but diffusion due to the product gas distribution is also possible. In all the figures, C_{Ag} represents the concentration of the reducing gas in the main gas stream; C_{As} represents the concentration of the reducing gas at the surface of the pellet; C_{Ac} represents the concentration of the reducing gas at the reaction front; C_{Ae} represents the equilibrium gas concentration at the reaction interface; R represents the radius of the pellet/particle; and r represents the radius of the shrinking core.

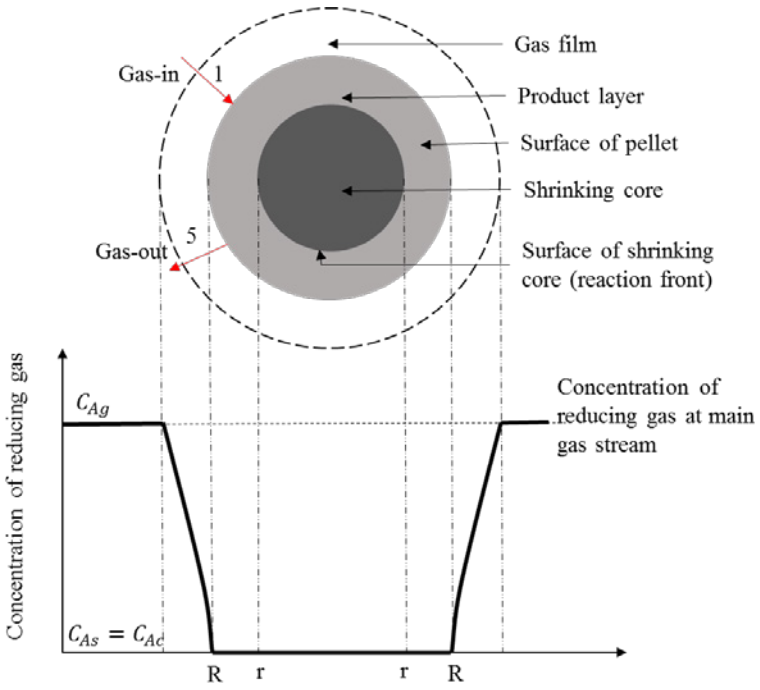

***Figure 2.4**- Schematic illustration of the mechanism of diffusion of gases through the gas film (step 1 and step 5) based on [138]*

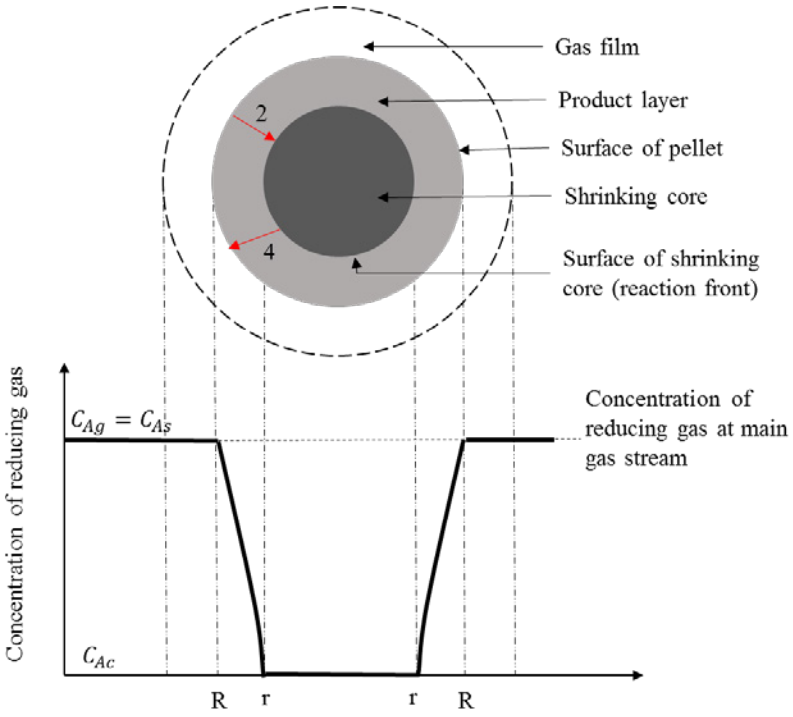

Figure 2.5*- Schematic illustration of the mechanism of diffusion of gases through the product layer (step 2 and step 4) based on [138]*

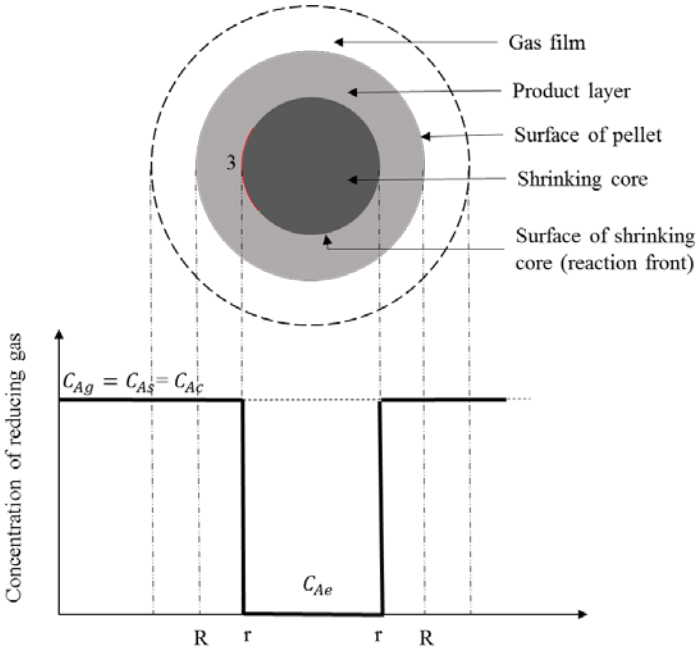

Figure 2.6*- Schematic illustration of the mechanism of the chemical reaction at the reaction front (step 3) based on [138]*

Mathematical equations for the SCM

A general gas-solid reaction can be simply expressed as [138]:

$$A\ (gas) + bB\ (solid) \leftrightharpoons cC\ (gas) + dD\ (solid) \qquad \textbf{(2.1)}$$

The SCM kinetic model provides mathematical equations which describe the expected reduction rate for each controlling mechanism in a shrinking core gas-solid reaction [138]. These are summarised in **Table 2.5**. In all the equations, ρ_B stands for the molar density of the solid reactant; b stands for the stoichiometry as listed in equation **2.1**; X_a stands for the reduction degree; k_g stands for the mass transfer coefficient of gas in the gas stream; k_s stands for the reaction rate constant; and D_e stands for effective diffusion coefficient of gas in the product layer.

***Table 2.5**- Mathematical equations which describe each rate-limiting step for the single-interface SCM [138]*

Rate-limiting step	Derived mathematical equation
Diffusion of gases through the gas film	$t = \frac{\rho_B R}{3bk_g(C_{Ag}-C_{As})}[1-(\frac{r}{R})^3] = \frac{\rho_B R}{3bk_g(C_{Ag}-C_{As})}\ X_a$ **(2.2)**
Diffusion of gases through the solid product layer	$t = \frac{\rho_B R^2}{6bD_e(C_{Ag}-C_{As})}[1-3(\frac{r}{R})^2+2(\frac{r}{R})^3] = \frac{\rho_B R^2}{6bD_e(C_{Ag}-C_{Ac})}\ [1-3(1-X_a)^{\frac{2}{3}}+2(1-X_a)]$ **(2.3)**
Interfacial chemical reaction	$t = \frac{\rho_B}{bk_sC_{Ag}}[R-r] = \frac{\rho_B R}{bk_sC_{Ag}}\ [1-(1-X_a)^{\frac{1}{3}}]$ **(2.4)**

Note that: ρ_B is the molar density of the solid reactant (mol./cm^3); $X_a$stands for the reduction degree (dimensionless); C_{Ag} is the gas concentration at the gas stream (mol./cm^3); C_{As} is the gas concentration at the pellet surface (mol./cm^3); C_{Ac} is the gas concentration at the reaction interface (mol./cm^3); k_g is the mass transfer coefficient (cm/min); k_s is the reaction rate constant (cm/min); D_e is the effective diffusion coefficient (cm^2/min); R is the pellet radius (cm); and r is the shrinking core radius (cm).

When utilising these equations to determine the mechanisms of a reduction process, experimental conditions should be correlated. For example, the mechanism of the diffusion of gases through the gas film can be eliminated by increasing the flow rates of the reducing gas

above a minimum ‘critical flow rate’. This is because increasing the flow speed of gases around the solid surface, increases the rate of mass transfer through the gas film [103].

At the beginning of most reduction processes, diffusion of gases through the solid product layer is rarely a rate-limiting step, as an intact product layer has not yet been formed. However, this mechanism can become the rate-limiting step during later stages of reduction. The properties of the product layer play a significant role. If the product layer is porous, it is relatively easy for gas to diffuse through it, however if the product layer is dense diffusion rates can be slow and hence the overall reduction rate can be limited by this mechanism.

Table 2.3 shows that the interfacial chemical reaction mechanism has often been identified as the rate-limiting step for the gas-based reduction of iron ore pellets. However, in most of these cases, the reduction studied involves not a single reaction but multiple reaction steps with intermediate phases being generated and consumed as the reaction progresses. For example, this is the case for the reduction of Fe_2O_3 (which typically proceeds via the pathway: $Fe_2O_3 \rightarrow Fe_3O_4 \rightarrow FeO \rightarrow Fe$ [77], [86], [105], [139]–[141]). Therefore, in this case it is also necessary to define a rate-limiting reaction step – which is the slowest reaction step taking place and hence defines the single interface for the shrinking core process.

In summary, the single interface SCM has previously been successfully applied to the gaseous reduction of various types of iron ore pellets, and therefore may be relevant to the reduction of the ironsand pellets studied in this thesis.

2.4 Gas-based DR characteristics of the titanomagnetite iron ores

This section summarises the reduction behaviour of various titanomagnetite ores described in the existing literature. Firstly, the effects of pre-oxidation on the DR of the titanomagnetite iron ores are presented (**Subsection 2.4.1**). Then the effects of the experimental conditions on the reduction are summarised (**Subsection 2.4.2**), as well as the reported phase evolution during reduction (**Subsection 2.4.3**). Finally, the morphologies of the pellets during reduction is displayed (**Subsection 2.4.4**).

2.4.1 The effects of pre-oxidation on the DR of the titanomagnetite iron ores

It is well known that conventional hematite and magnetite ores present different reducibility, with hematite ores displaying a much faster reduction rate [142]. Without any pre-treatment, magnetite ores are seldom used directly in the industrial DR shaft furnace. Instead, magnetite ores are normally pre-oxidised to convert them into hematite prior to the reduction process [133]. This pre-oxidation of magnetite to hematite leads to a significant increase in the reduction rate of the ore, and this is ascribed to an increase in surface area and gas permeability of the particles. This is a result of micro-cracks formed during the conversion of the crystal structure from rhombohedral Fe_2O_3 to cubic Fe_3O_4, which occurs at the beginning of the reduction of the pre-oxidised ores. These micro-cracks form due to the large internal stresses imposed by the volume increase associated with this transformation.

A similar phenomenon has also been observed in reducing pre-oxidised titanomagnetite ores, and this has also been attributed to the same effects caused by transformation of the crystal structure [143], [144]. Longbottom *et al.* [144] compared the reduction rates of NZ titanomagnetite ironsand in both raw and pre-oxidised states, using a mixture of 55vol% H_2, 35vol% CH_4 and 10vol% Ar at 1023 K. Results from this work are shown in **Figure 2.7**. As can be seen, with pre-oxidation, the reduction rate of the ironsand increased greatly, and approached a similar rate to the reduction of conventional hematite ore.

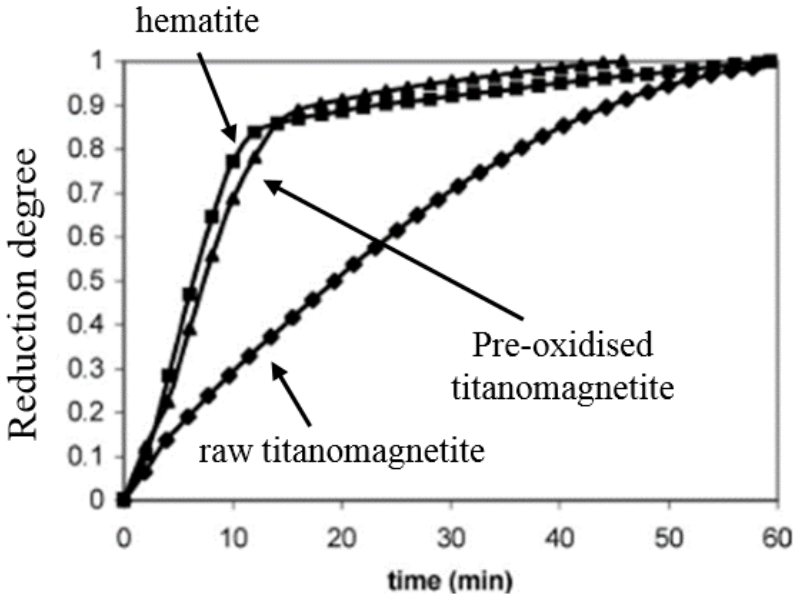

Figure 2.7*- Reduction degree curves of reducing NZ raw titanomagnetite ironsand, pre-oxidised ironsand and conventional hematite ore by gas (55vol% H_2, 35vol% CH_4 and 10vol% Ar) at 1023 K based on [144]*

In addition to investigating the effect of pre-oxidation on reduction rate, the phase evolution during oxidation of titanomagnetite ores has also been studied. During isothermal oxidation of the NZ titanomagnetite ironsand, Park *et al.* [143] summarised its oxidation path, as shown in **Figure 2.8**. TTM was firstly oxidised to TTH. With further oxidation, parts of TTH were converted to pseudobrookite (PSB, Fe_2TiO_5). During non-isothermal oxidation, TTM was found to not be directly oxidised to TTH between 873 and 1073 K; instead, an intermediate phase of Ti-containing maghemite was found [143]. However, this intermediate Ti-containing maghemite was not observed in the work of Wang *et al.* [145], which might be due to its instability and fast transition. From the work of Wang *et al.* [145], it was also concluded that during non-isothermal oxidation, Ti gradually accumulated in the lamellar structure, while Fe and Al were mostly distributed in the uniform regions.

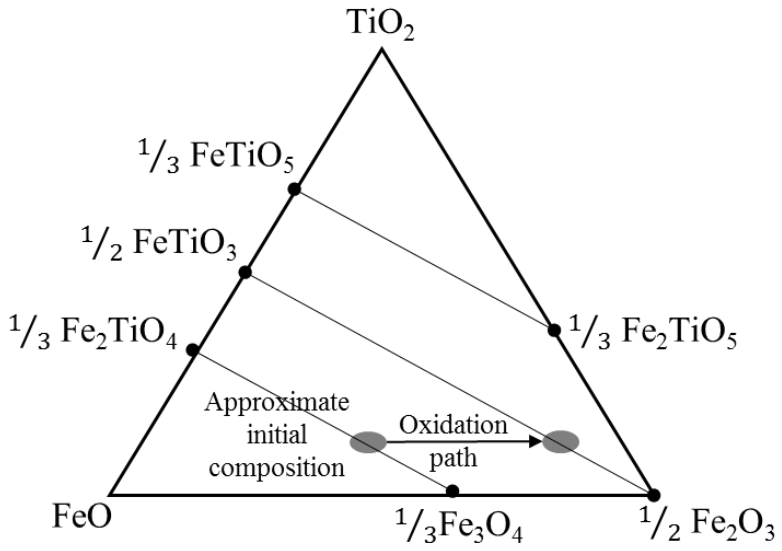

Figure 2.8*- Isothermal oxidation path of NZ titanomagnetite ironsand in the FeO-Fe_2O_3-TiO_2 ternary system based on [143]*

A kinetic analysis of the oxidation of the titanomagnetite ore was conducted by Han *et al.* [20]. It found that with increasing temperature, the interfacial chemical reaction rate increased, and accordingly the O_2 gas diffusion in the product layer gradually took over to rate limit the oxidation process [20].

To summarise, pre-oxidising titanomagnetite ores has been found to increase their reduction rate in reducing gases. This approach has also been shown to have an effect on NZ ironsand.

2.4.2 The effects of experimental conditions on the DR of the titanomagnetite ores

Within this subsection, the effects of varying experimental conditions on the reduction behaviour of titanomagnetite ores are discussed. Such experimental conditions include the types of reducing gases, reduction temperature, and the composition of the ores. Each of these conditions has been shown to have an effect on the reduction rate of titanomagnetite ores [129], [146]–[151].

For the gaseous reduction of iron ores, CO, CH_4 and H_2 are the most commonly studied reducing agents [129], [146]–[150]. **Table 2.6**. summarises the typical results reported for the reduction of titanomagnetite ores using these different gases.

***Table 2.6**- Summary of the effects of different reducing gases on the reduction of the titanomagnetite ore*

H_2/CO	The extent of reduction or metallization of the titanomagnetite ores increased with the increasing amount of reducing gases in gas mixtures (H_2 in H_2-Ar mixture or CO in CO-CO_2-Ar mixture) [129], [146]–[150].
	At 1373 K, the reduction of titanomagnetite ores containing 57.2wt% Fe and equivalent 7.43wt% TiO_2 in a fixed bed reactor was found to proceed faster by using H_2 than for reduction by CO [146].
CH_4	CH_4 content in H_2-CH_4-Ar mixture was found to have no effect on the reduction rate of the NZ titanomagnetite ore containing 57.2wt% Fe and equivalent 7.42% TiO_2 at 1173 K, but it contributed to cementite (Fe_3C) formation [144]; However, a different paper has reported that CH_4, combined with H_2 and CO, promoted the reduction of the titanomagnetite iron ores [152]
	The cementite formation rate of the pre-oxidised NZ titanomagnetite ore was slower than that of the hematite ores, but it was in general more stable [153].

As summarised in **Table 2.6**, the reduction rate of the titanomagnetite ores by H_2 gas is faster than when using either CO or CH_4 [146]. This may be caused by the thermodynamic differences between the reduction reactions for the different gases, as illustrated by the Baur-Glaessner diagram in **Figure 2.9** [154]. This diagram shows that at higher temperatures (> 843 K), the reduction potential of H_2 gas is better than that of CO, meaning that a higher gas utilisation rate can be achieved. Moreover, because the reduction of iron ores by H_2 gas is an endothermic reaction, reduction at high temperatures also further promotes the reduction rate [147]. Due to its low viscosity and small molecule size, H_2 gas diffuses more easily than other reducing gases, which can also improve the reduction rate [25]. As a result, the reduction of the titanomagnetite ores by H_2 has the fastest rate. In addition H_2 gas does not cause carburization of the reduced iron ores, but this is observed in studies that have used CO or CH_4 as the reducing agent [19], [143], [151], [152].

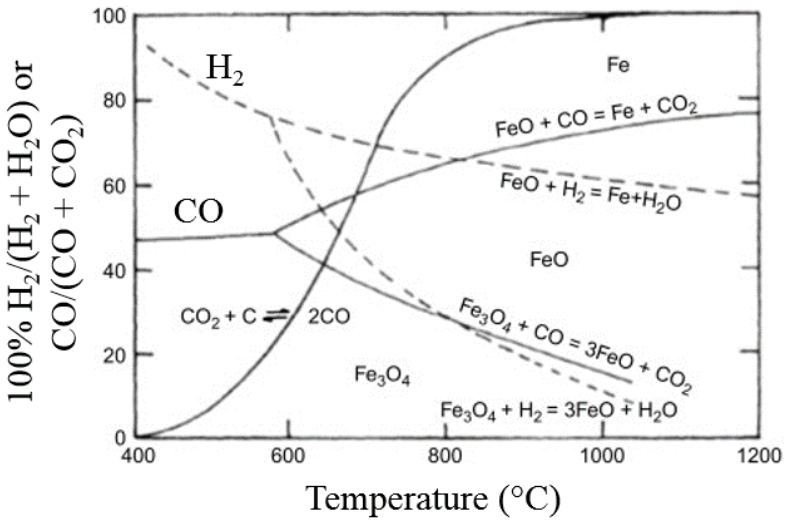

Figure 2.9*- The Baur-Glaessner diagram for the reduction of iron ores by both H_2 and CO [154]*

In addition to the effects of using different types of reducing gases on the reduction rate, the concentration of the reducing gas in a gas mixture further affects the reduction progress, and the distribution of phases present in the reduced ores. Park *et al.* [147] reduced the NZ titanomagnetite ironsand in a laboratory fixed bed reactor using gas mixtures containing different ratios of CO/CO_2. It was found that TTM was only completely reduced to metallic Fe and titanium oxides when the concentration of CO was higher than 96.5vol%. Moreover, the distribution of the Ti-containing phases at the end of the experiment (~90 minutes) was also related to the ratio of CO/CO_2. Below 90vol% CO, Fe_2TiO_4 was the main Ti-carrying phase, while for 90vol% to 95vol% CO, $FeTiO_3$ was detected in the final product. However, above 95vol% CO, titanium oxides were observed as the only final Ti-containing phase.

The effects of reduction temperature on the reduction rate of the titanomagnetite ores have also been investigated. In general, the reduction rate increases with increasing temperature [129], [146]–[150]. Park *et al.* [146] investigated the temperature effects on the reduction rate of the NZ titanomagnetite ironsand in a fixed bed reactor using a 25vol% H_2-Ar gas mixture. These results indicated a significant temperature dependence to the reduction process, and are shown in **Figure 2.10**.

However, in previous literature, it has also been pointed out that when the reduction temperature becomes too high (> 1373 K), sintering of pellets or formation of low-melting-point slags within the titanomagnetite ore may hinder the reduction process [34]. What is more,

in terms of the reduction of titanomagnetite pellets, higher temperatures may promote the sticking phenomenon which would impede further reduction [155].

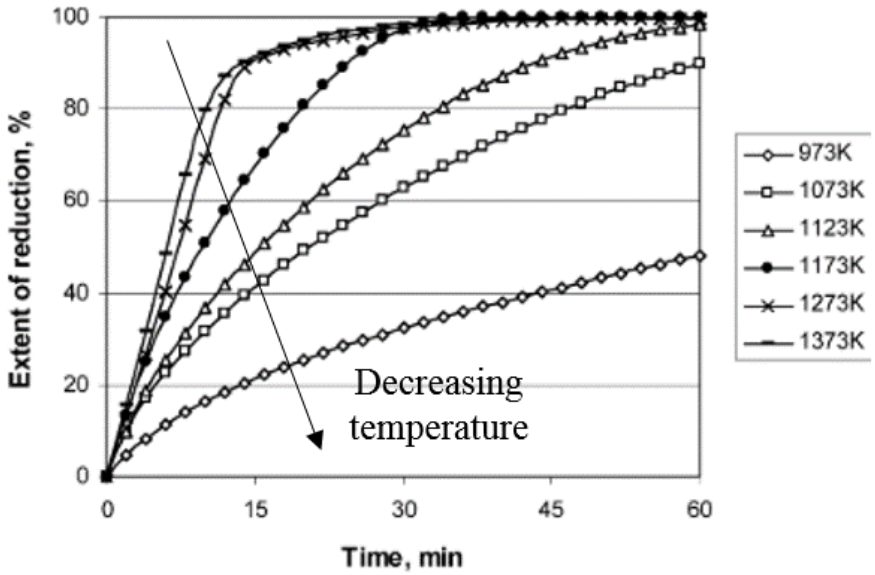

Figure 2.10 *- Temperature effects on the reduction rate of the NZ titanomagnetite ironsand by a 25vol% H_2-Ar gas mixture based on [146]*

Similarly to the effects of the concentration of the reducing gas, temperature also influenced the distribution of the phases present in the reduced ironsand. Park *et al.* [146] concluded that after 2 hours reduction, TTM was only completely consumed at temperatures higher than 1073 K. For other Ti-containing phases, $FeTiO_3$ was only present in the final product at reduction temperatures below 1173 K. Above 1173 K, $FeTiO_3$ was no longer detected, and instead TiO_2 appeared.

In summary, literature suggests that to achieve efficient gaseous reduction of titanomagnetite ores, a high temperature and high concentration of reducing gas should be applied. Furthermore, H_2 gas reductions are expected to proceed significantly more quickly than for reductions using CO or CH_4.

2.4.3 Phase evolution during DR of the titanomagnetite iron ores

It is widely accepted that the reduction of Fe_2O_3 to metallic Fe is a multistep reaction process [77], [86], [105], [139]–[141]. Above 843 K, its reduction path follows: $Fe_2O_3 \rightarrow Fe_3O_4 \rightarrow FeO \rightarrow Fe$; while below 843 K, no FeO is formed, and the reduction path follows: $Fe_2O_3 \rightarrow$

$Fe_3O_4 \rightarrow Fe$. The reactions involved in the reduction path by using H_2 gas include (where the gaseous phase is indicated by *g* and the solid phase is indicated by *s*):

$$3Fe_2O_3(g) + H_2(g) \rightarrow 2Fe_3O_4(s) + H_2O(g) \quad (\mathbf{2.5})$$

$$Fe_3O_4(s) + H_2(g) \rightarrow 3FeO(s) + H_2O(g) \quad (\mathbf{2.6})$$

$$FeO(s) + H_2(g) \rightarrow Fe(s) + H_2O(g) \quad (\mathbf{2.7})$$

However, the reduction of TTM has been reported to be more complicated, due to the evolution of various Fe-Ti-O phases [118], [119], [143], [146], [147], [150], [156].

The general view suggested in the previous literature, is that the reduction of the titanomagnetite ores in equilibrium state proceeds through the following path [146], [157], [158]:

$$Fe_{3-x}Ti_xO_4 \rightarrow FeO + Fe_2TiO_4 \rightarrow Fe + Fe_2TiO_4 \rightarrow Fe + FeTiO_3 \rightarrow Fe + TiO_2 \quad (\mathbf{2.8})$$

The associated reactions in this path by H_2 gas include:

$$Fe_{3-x}Ti_xO_4(s) + (1-x)H_2(g) \rightarrow 3(1-x)FeO(s) + xFe_2TiO_4(s) + (1-x)H_2O(g) \quad (\mathbf{2.9})$$

$$FeO(s) + Fe_2TiO_4(s) + H_2(g) \rightarrow Fe(s) + Fe_2TiO_4(s) + H_2O(g) \quad (\mathbf{2.10})$$

$$Fe_2TiO_4(s) + H_2(g) \rightarrow Fe(s) + FeTiO_3(s) + H_2O(g) \quad (\mathbf{2.11})$$

$$FeTiO_3(s) + H_2(g) \rightarrow Fe(s) + TiO_2(s) + H_2O(g) \quad (\mathbf{2.12})$$

This reaction path has been determined in the previous literature mainly through *ex-situ* XRD analysis. Park *et al*. [143] reduced the pre-oxidised NZ ironsand in a fixed bed by 75vol% CO and 25 vol% Ar gas mixture non-isothermally to 1373 K, and the *ex-situ* XRD results are shown in **Figure 2.11**. TTH started to be reduced to TTM at 637 K. Metallic Fe was initially detected at 873 K. Other Ti-containing phases ($FeTiO_3$ and TiO_2) were also found above 1073 K. On the other hand, FeO was not detected during the whole reduction process. Despite this intermediate phase not being detected, it was expected in the work that it was still generated from TTM but was then rapidly reduced to metallic Fe and hence measurable quantities were not present in the sample. However, in other studies of the titanomagnetite ores reduced isothermally at 1173 K [159] and 1373 K [147], FeO has been detected in partially reduced samples.

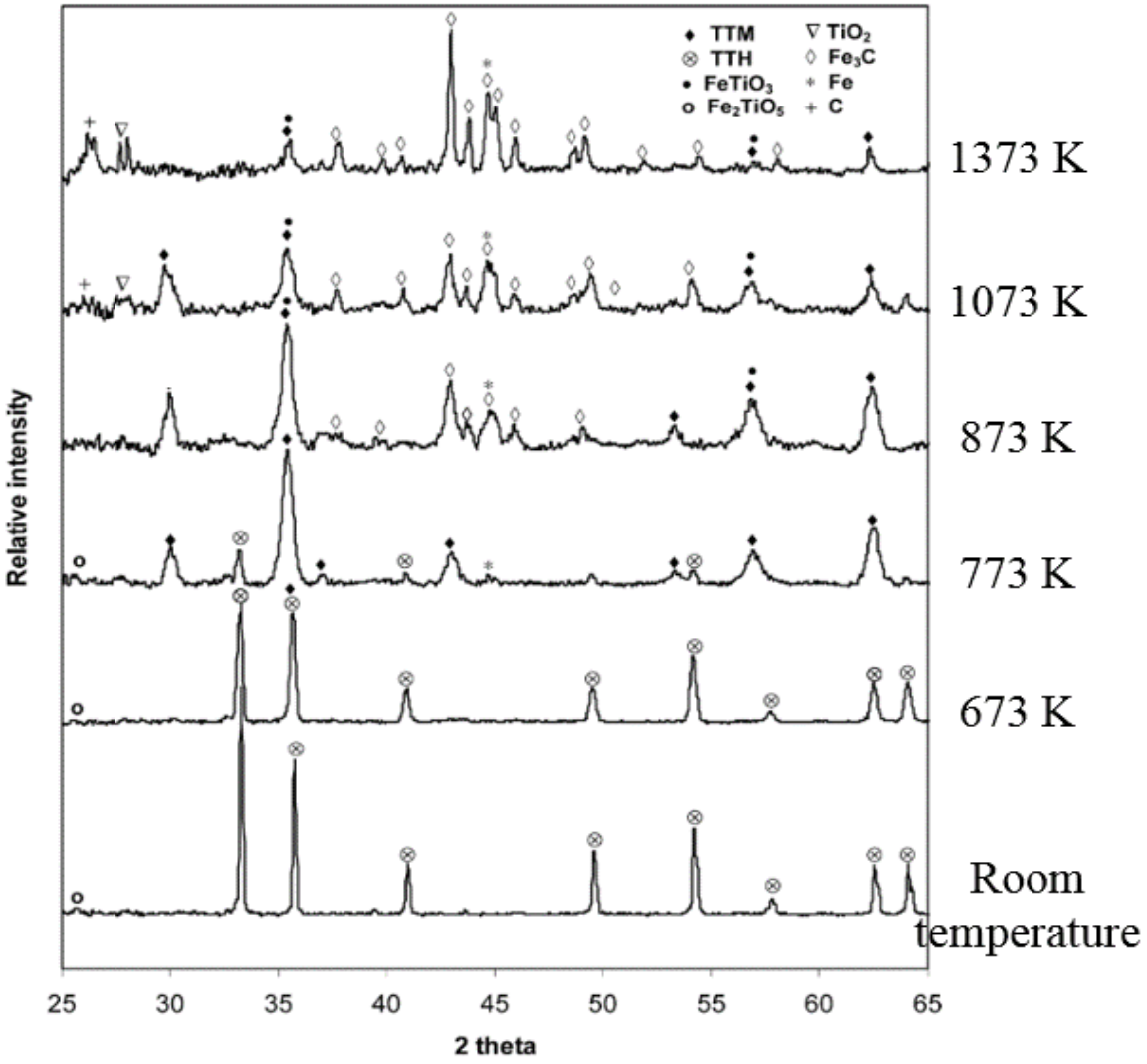

***Figure 2.11**- XRD patterns of the pre-oxidised NZ titanomagnetite ironsand by 75vol% CO and 25 vol% Ar gas mixture non-isothermally to 1373 K based on [143]*

Another very recent paper has reported the phase evolution of NZ titanomagnetite ironsand undergoing isothermal reduction in H_2-Ar gas mixtures at 1223 K. These experiments were performed in a Fluidised Bed system by Prabowo *et al.* [156], and the phase evolution during reduction was determined by quantitative *ex-situ* XRD analysis of quenched samples. Typical results are illustrated in **Figure 2.12**. Contrary to the results reported by Park [143], in this work FeO was found to be present as an intermediate phase during the reduction of TTM. A further unusual feature of the results in this work was that the reduction of TTM significantly slowed down after FeO was observed to reach its maximum concentration. This was attributed to the accumulation of Ti in the remaining TTM, which could decrease the thermodynamic driving force for the generation of FeO [156].

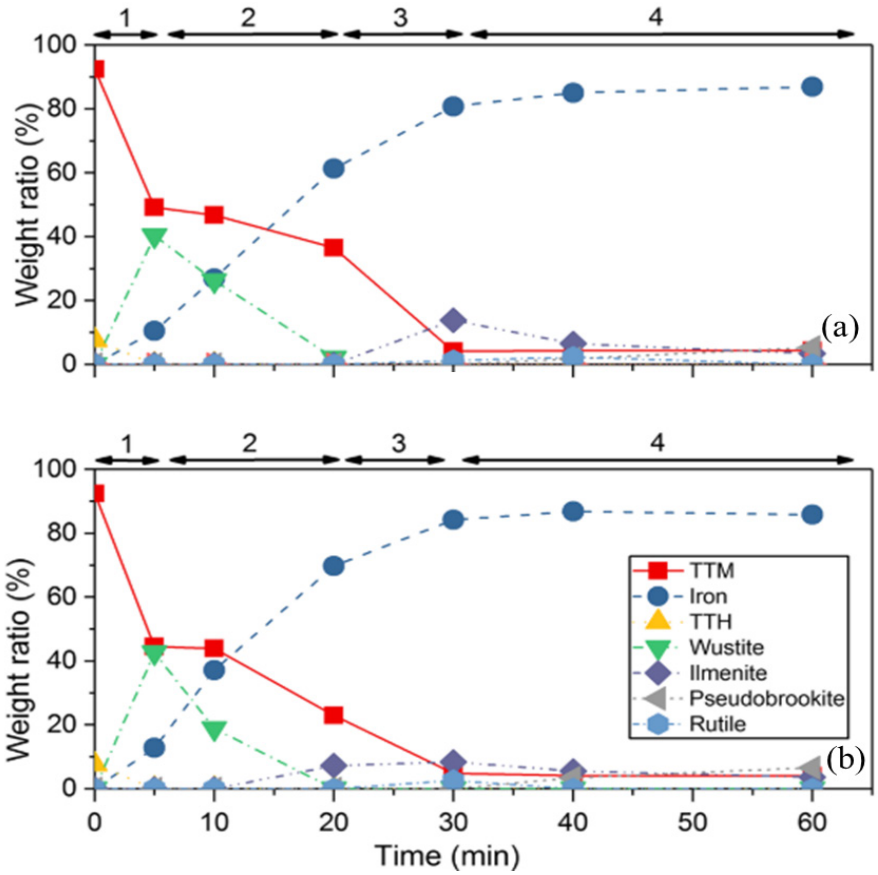

***Figure 2.12**- The evolution of the amount of each detected phase of reducing NZ titanomagnetite ironsand by a H_2-Ar gas mixture at 1223 K in a Fluidized Bed system. (a) 80vol% H_2 – 20vol% Ar; (b) 100vol% H_2 based on [156]*

In summary, previous literature reports of phase evolution during the reduction of titanomagnetite ores have presented differing results and conclusions. However, it is clear that the existence of Ti is expected to significantly affect the phase evolution during reduction of TTM.

2.4.4 Microstructure analysis during DR of the titanomagnetite iron ores

The morphological evolution of the titanomagnetite ores during reduction has also been reported in a few papers. Park *et al.* [146] examined the microstructure of NZ titanomagnetite ironsand during reduction by a 25vol% H_2-Ar gas mixture at 1173 K in a fixed bed reactor. The morphological changes are illustrated in **Figure 2.13**. The generation of metallic Fe was topochemical, with a particle-scale shrinking core formed inside the interface between the metallic Fe and the unreduced TTM. However, the morphologies of intermediate phases (such as FeO) were not reported. After completion of the reduction, metallic Fe occupied most of the particles. That work [146], also reported that the morphology of the metallic Fe in the fully

reduced ores depended on temperature. At lower temperatures, metallic Fe was observed in the form of feathered whiskers, but with increasing temperature, a fine structured metallic Fe was formed [146].

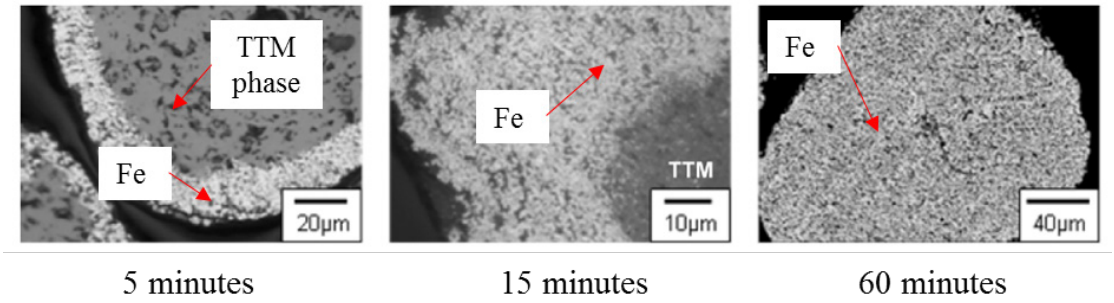

***Figure 2.13**- Morphology of the NZ titanomagnetite ironsand at different time points during reduction by a 25vol% H_2-Ar gas mixture at 1173 K based on [146]*

In another work, Sun *et al.* [150] presented the morphological changes which occurred for non-uniform particles (containing TTH) in South African titanomagnetite ores during reduction by a 50vol% CO-N_2 gas mixture at 1223 K. Examples of these microstructures are shown in **Figure 2.14**. In this case a shrinking core phenomenon was not observed. Instead, it seemed that metallic Fe was first generated at the edge of lamellar structures, and then gradually grew to consume the remaining unreduced areas.

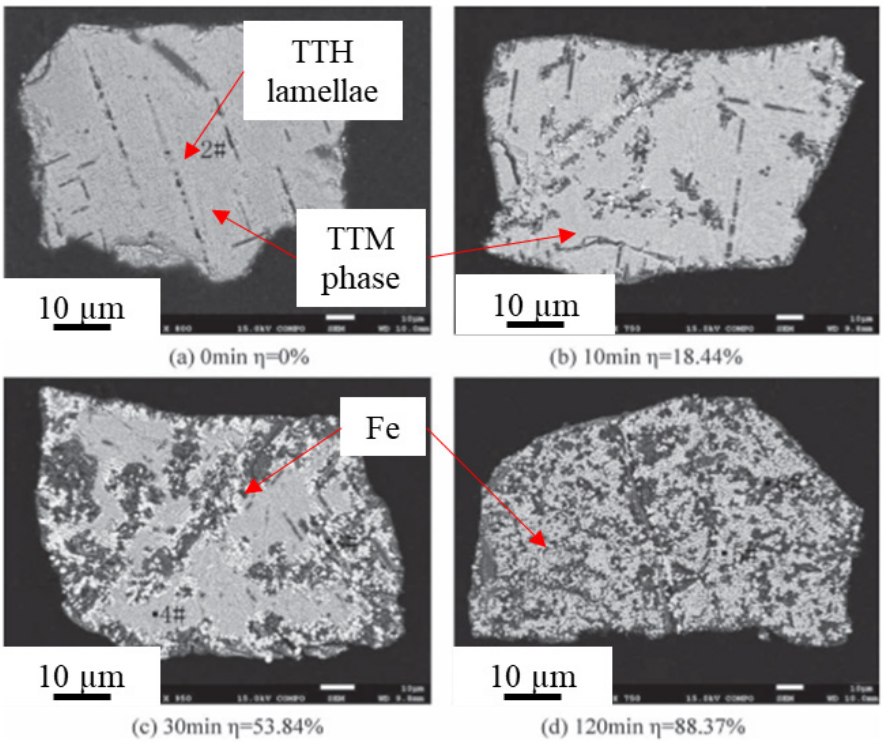

***Figure 2.14**- Morphological changes of the particles with intrusions in the South African titanomagnetite ores during the reduction by a 50vol% CO-N_2 gas mixture at 1223 K. η stands for metallisation degree based on [150]*

The morphologies of pre-oxidised Chinese titanomagnetite pellets has also been reported. Li *et al.* [148] reduced these pellets using 70vol% H_2-CO gas mixture at 1323 K. The microstructures of the pellets at each reduction stage are illustrated in **Figure 2.15**. A change in structure was observed when TTH was reduced to TTM, with damage to the particle structure (cracks and fractures). As the reduction progressed, metallic Fe was found to nucleate throughout the whole particles. Upon the completion of the reduction, a uniform area was formed which was advantageous for subsequent melting process [148].

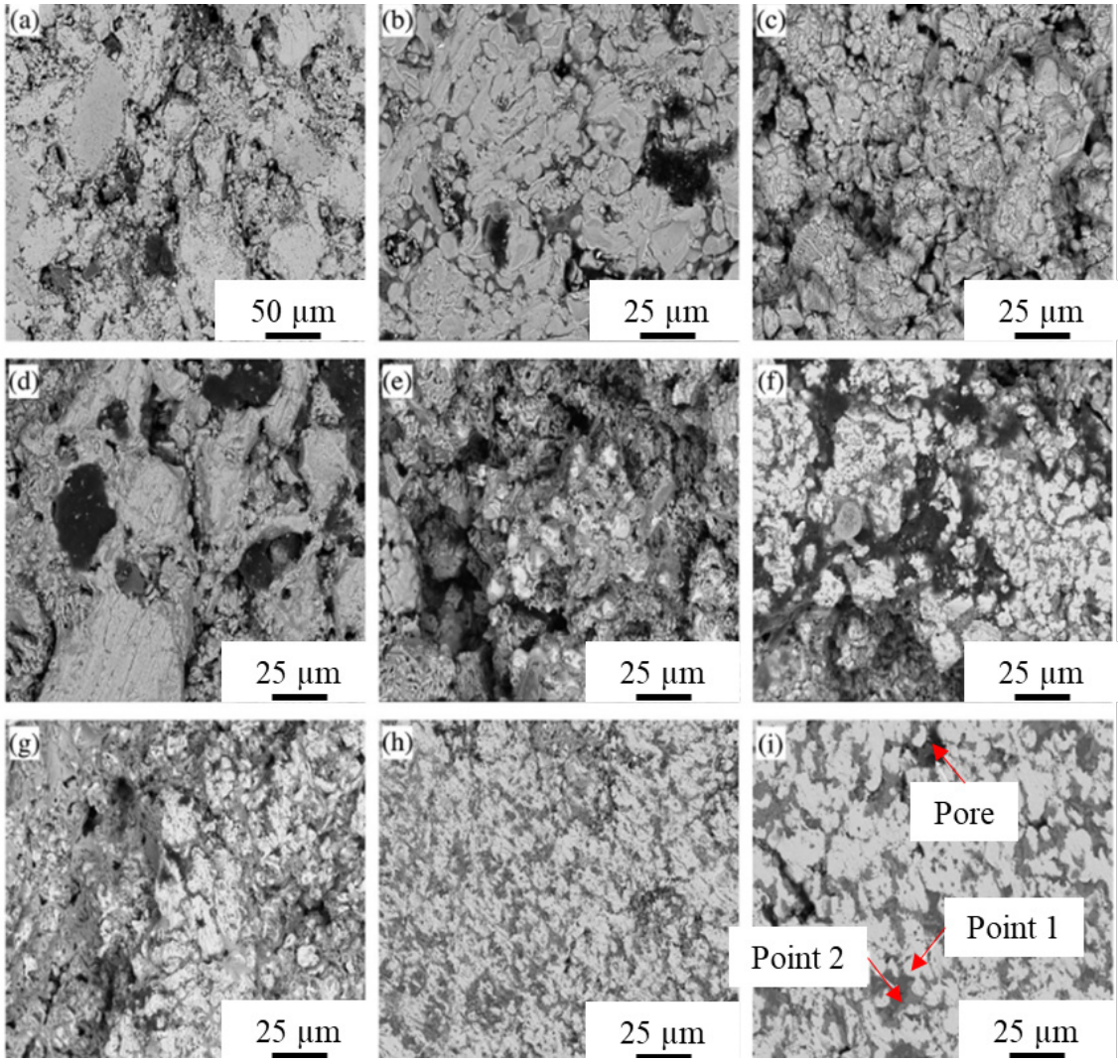

***Figure 2.15**- Morphologies of the pre-oxidised Chinese titanomagnetite pellet at different stages during reduction by a H_2-CO (2.5:1) gas mixture at 1323 K. (a) 0 min; (b) 1min; (c) 3 min; (d) 5min; (e) 10min; (f) 15min; (g) 25 min; (h) 35 min; and (i) 60 min. Point 1 in (1) indicates metallic Fe and point 2 indicates impure oxides based on [148]*

To summarise, morphology evolution during gas-based DR of some types of titanomagnetite ores has been previously reported. Significant variation between different types of particles in the titanomagnetite ore have been observed. In particular, it appears that pre-oxidation of the titanomagnetite ores significantly affects the morphologies which occur during reduction [148].

2.5 Summary

In this chapter, a literature survey was presented of the properties of the NZ titanomagnetite ironsand and the gas-based DR behaviour of various titanomagnetite ores. The key findings from these previous studies can be summarised as follows:

- In NZ titanomagnetite ironsand, most of the particles are uniform titanomagnetite, but a small portion is non-uniform t particles with a lamellar structure (titanohematite).
- The reduction rate of the titanomagnetite ores is usually found to be slower than that of conventional magnetite ores. However, pre-oxidation can significantly increase the reduction rate.
- The reduction conditions affect the reduction rate of the titanomagnetite ores. In general, increasing either temperature and/or reductant gas concentration, causes the reduction rate to increase. Reduction in H_2 gas is reported to procced more quickly than for the equivalent conditions using CO or CH_4.
- The phase evolution during reduction of titanomagnetite ores has been studied using *ex-situ* techniques such as XRD analysis.
- Microstructure analysis during reduction of some titanomagnetite ores has been reported, and illustrates different features for different types of ores and particles.
- A small number of previous works have reported kinetic analysis of the gaseous reduction of various titanomagnetite ores through applying a single interface SCM. In these studies, this model is reported to describe the experimental data reasonably well.

Much of the existing literature has studied the reduction of international titanomagnetite ores. However, NZ titanomagnetite ironsand differs from other internationally reported titanomagnetite ores due to its lower Ti concentration. There is limited knowledge of the reduction behaviour of NZ ironsand, especially in the form of pellets. In particular:

- Most of the previous literature is focused directly on gas reduction of unpelletised titanomagnetite ores as powders. Studies on the reduction of the pellets are rare.
- There is limited knowledge of the mechanisms which control the reduction kinetics of NZ titanomagnetite pellets, and these are not fully understood. In particular, although a few previous studies have successfully applied a single interface SCM to describe the reduction

of various forms of titanomagnetite ores, the controlling reaction steps at the interface have not been clearly identified.

- Morphology studies in the former literature have mostly focussed on the generation of metallic Fe in the particles. The morphological evolution which occurs during the generation and consumption of the intermediate phases (such as FeO), are seldom discussed.
- Research on the phase evolution during reduction of ironsands and other titanomagnetite ores has been performed using *ex-situ* XRD analysis. There are limitations to this approach as it only provides discontinuous data, and there is the possibility for phase changes to occur during cooling. Therefore, an *in-situ* investigation of the phase evolution during the reduction of pellets is desired in order to more clearly understand the reaction pathway, and especially for analysing the fate of Ti during the reduction process.

The work presented in this thesis attempts to fill in some of the missing knowledge outlined above. It aims to investigate the reduction behaviours of the NZ titanomagnetite ironsand pellets at higher temperatures, determine the phase evolution during reduction, and develop an analytic kinetic model which can describe the reduction progress of ironsand pellets at different reduction temperatures.

Chapter 3
Experimental method

The aim of this thesis is to obtain a comprehensive understanding of the reduction characteristics and mechanisms for the reduction of NZ titanomagnetite ironsand pellets in H_2 gas. To achieve this, the experimental methodology shown in **Figure 3.1** was followed. The experimental techniques used, and their key purposes are given in **Table 3.1**.

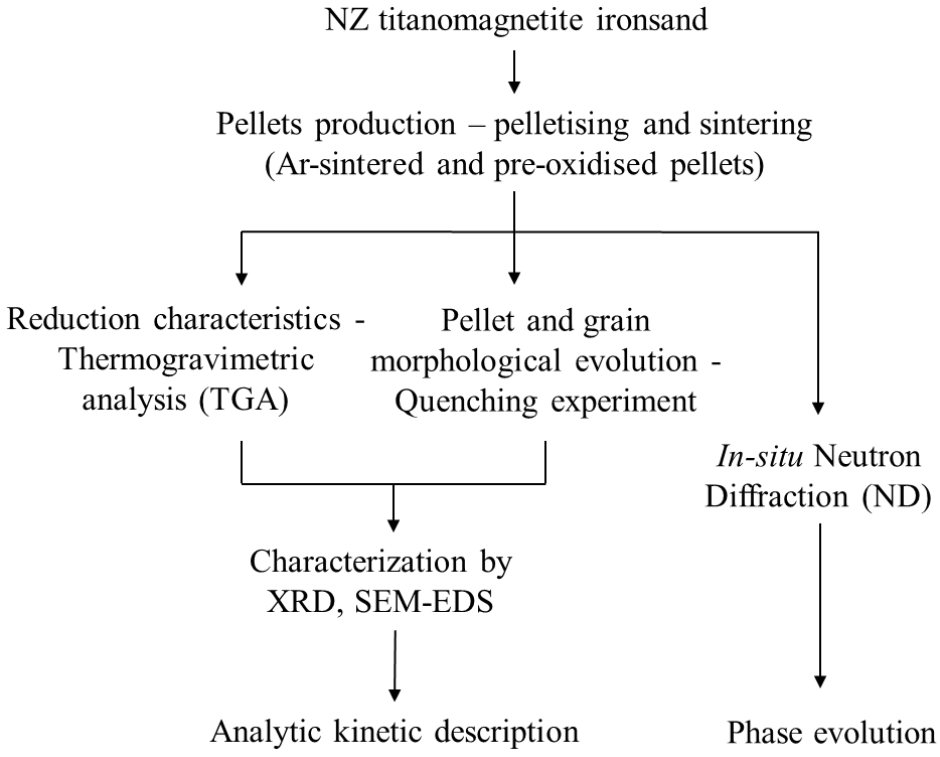

Figure 3.1 – *A schematic showing the experimental methodology used in this research*

This chapter is divided into the following sections:

- **Section 3.1**: Summary of the properties of the experimental materials
- **Section 3.2**: Description of the pelletising and sintering process of generating both the Ar-sintered and pre-oxidised pellets
- **Section 3.3**: Establishment of the Thermogravimetric analysis (TGA) measurement procedure
- **Section 3.4**: Description of the quenching reduction experiments
- **Section 3.5**: Description of *ex-situ* methods used to characterise the reduced pellets
- **Section 3.6**: Description of the methodology for the reduction experiments monitored by *in-situ* neutron diffraction analysis (ND)

Table 3.1**– The experimental techniques and their purpose for each of the methods shown in **Figure 3.1

	Techniques	Purpose
Sample preparation	Grinding, pelletising, sintering and pre-oxidising	To generate pellets for reduction
Reduction experiment in H_2 gas	High temperature reduction experiment in TGA (Mettler TA1 Thermobalance)	To characterise the reduction behaviours of the pellets at high temperatures
	Reduction of the pellets to desired reduction extent and quenching to reserve the morphologies	To observe the pellet and particle morphologies of the partially reduced pellets
	Reduction of the pellets while applying *in-situ* ND analysis for a direct measurement of the phases present in the pellets at each reduction time (ANSTO Wombat)	To determine the phase evolution *in-situ* during the reduction of the pellets
ex-situ characterisation experiment	Light Microscopy (Nikon Eclipse LV100NDA)	To observe the pellet morphology of unreduced, partially reduced and fully reduced pellets
	SEM - EDS (JEOL JSM-6490LV and Quanta)	To observe the pellet and particle morphologies and identify the phases present in the pellets
	XRD (Bruker D8)	To determine the crystalline phases in the pellets

3.1 Experimental materials – NZ titanomagnetite ironsand

In this study, the material investigated was NZ titanomagnetite ironsand. The as-received ironsand was obtained from the Waikato North Head, NZ mine. Its composition, as determined using XRF analysis, is given in **Table 3.2**. The equivalent TiO_2 content is ~8wt%.

Table 3.2 *– Chemical composition of the as-received NZ titanomagnetite ironsand from Waikato North Head mine*

FeO	Fe_2O_3	TiO_2	Al_2O_3	MgO	SiO_2	MnO	CaO	V_2O_5	Rest	LOI
28.1	54.1	7.9	3.7	2.8	2.0	0.6	0.5	0.5	0.5	-3.0

Note: The as-received ironsand does not actually contain wustite (FeO) or hematite (Fe_2O_3) as crystalline phases. Here, the stoichiometric notation describes the Fe^{2+} and Fe^{3+} content of the ironsand. The Fe^{2+} content of the ironsand was established using the Potassium Dichromate titration method based on ISO-9035 and found to be 21.9 wt% (equivalent to 28.1 wt% FeO). The Fe^{3+} content was determined by subtracting the Fe^{2+} content from the total Fe content measured by XRF (after accounting for oxidation mass gain after roasting the ironsand sample at 1273 K).

The size distribution of the as-received ironsand particles was measured using a laser-scattering particle size analyser (Mastersizer 3000, UK). The results are shown in **Figure 3.2**. As can be seen, most of the particles are in the range of 100 µm to 300 µm, with an average particle size of 200 µm.

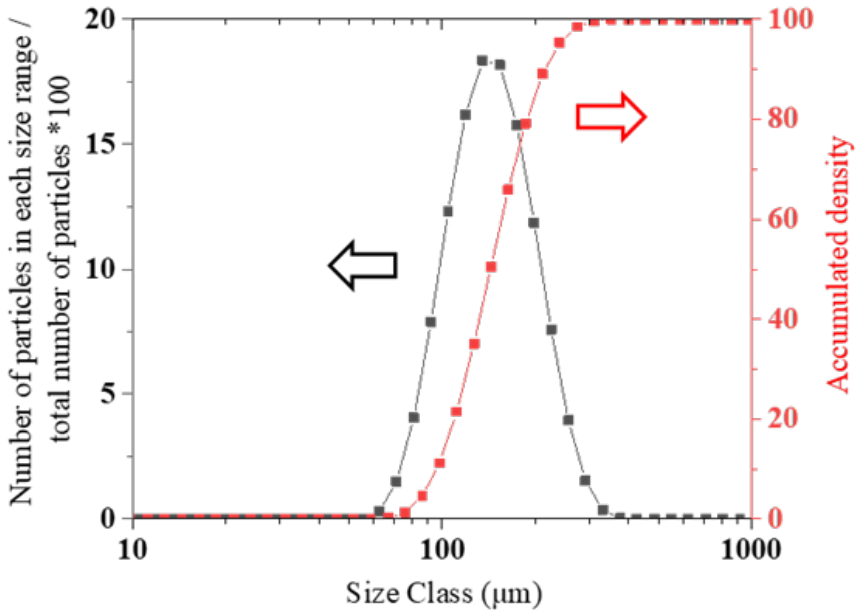

Figure 3.2*– Size distribution of the as-received ironsand from the particle size analyser*

3.2 Preparation and production of ironsand pellets

3.2.1 Milling of the as-received ironsand

The particles needed to be milled to an average particle size of <80 µm prior to pelletisation. This was necessary to enable pellets to be formed in the disc pelletiser, and to ensure adequate green strength [160], [161]. The milling was performed in water using a rolling-jar ball mill (Pascal Engineering UK, No. 20582). The conditions of the wet milling process are listed in **Table 3.3**. After wet milling and drying, the ironsand was then riffled to produce a representative small sample for particle size analysis. The size distribution of the milled particles depends on the time and rotation speed of the mill. The average particle size (D50%) after milling was measured by the laser-scattering particle size analyser. The relationship between the measured average particle size and the milling conditions is plotted in **Figure 3.3**.

Table 3.3 *– Conditions of wet-milling process and drying conditions after milling*

Jar volume	Milling medium – stainless steel balls	Weight of ironsand per mill	Ball-to-powder mass ratio	Water used per mill	Drying conditions
5 L	7.5 kg	2 kg	3.75 : 1	0.7 L	363 K, 24 h

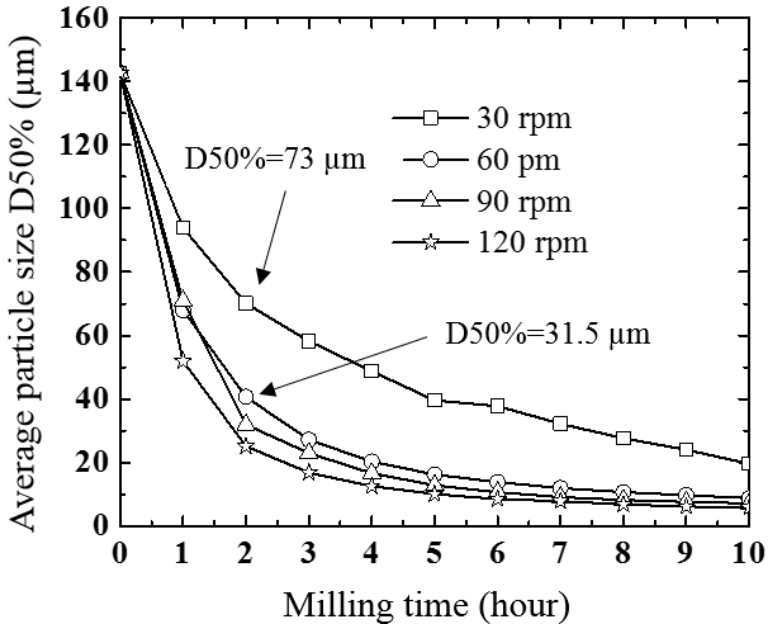

Figure 3.3 *– Average particle size (D50%) after wet-milling at each milling condition*

All pellets used in this work were produced from particles wet milled at 90 rpm for 2 hours (D50%=32 µm) and at 30 rpm for 2 hours (D50%=73 µm). The detailed particle size distributions are shown in **Figure 3.4(a)** and **(b)** respectively.

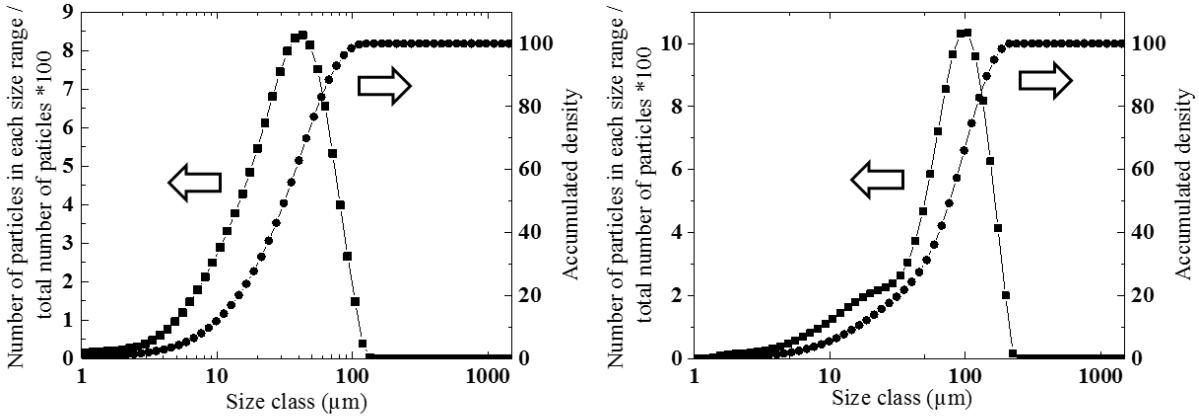

***Figure 3.4** – Specific particle size distributions of the ironsand after wet milling at (a) 90 rpm for 2 hours [162] and (b) 30 rpm for 2 hours*

3.2.2 Pelletising, sintering and pre-oxidising

Pellets were produced from the dried milled ironsand, which was pre-mixed with 1wt% bentonite. The composition of bentonite used (after roasting in air), is listed in **Table 3.4**, as determined by XRF. To generate the pellets, a Lurgi-type disc pelletiser (see in **Figure 3.5(a)**) was used. This disc pelletiser has a diameter of ~35 cm and was set to an angle of 45°. During pelletisation, the disc pelletiser rotated at a speed of 35 rpm. At the same time, tap water was manually sprayed into the particle mixture until spherical 'green' pellets began to form. At this point, no further water was added, and the 'green' pellets were then removed from the pelletiser and dried in an oven at 363 K for 2 hours. Examples of the 'green' pellets are shown in **Figure 3.5(b)**. In the pelletising process, a range of pellets with diameters from 3 to 12 mm were obtained. In this study, mid-size pellets of a defined diameter (from 5.5 to 8.5 mm) were selected for various experiments.

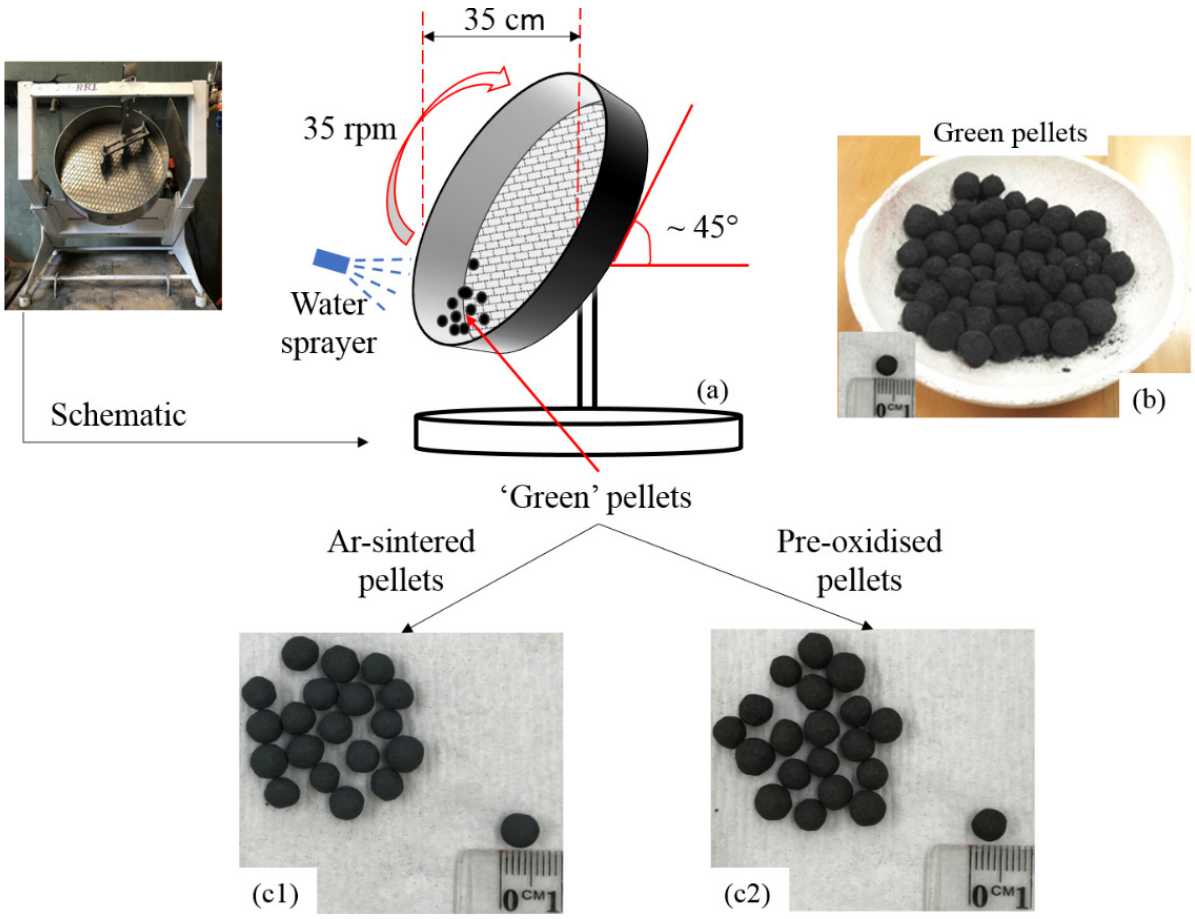

Figure 3.5 – *(a) A photo and schematic of the laboratory Lurgi-type disc pelletiser. Examples of pellets (b) directly obtained from the pelletiser ('Green' pellets), (c1) after sintering in Ar gas (Ar-sintered pellets) and (c2) after sintering in air (pre-oxidised pellets)*

Table 3.4 *– The composition of bentonite after roasting in air, as determined by XRF [162]*

SiO_2	Al_2O_3	Fe_2O_3	MgO	Na_2O	CaO	TiO_2	LOI	Balance
70.2	15.5	3.6	1.7	1.6	1.5	0.1	4.7	1.1

The 'green' pellets obtained directly from the pelletiser are generally too mechanically weak to be used directly in reduction experiments. Therefore, they were sintered in either Ar gas or air to generate either Ar-sintered or pre-oxidised pellets respectively. Examples of these pellets are given in **Figure 3.5(c1)** and **(c2)** respectively. These sintered pellets were used for the reduction experiments.

Production of the Ar-sintered pellets

Ar-sintered pellets were obtained by heating the 'green' pellets at 1473 K under Ar gas at a flowrate of 65 ml/min for 2 hours in a tube furnace. After placing the dried 'green' pellets in the hot zone of the furnace, the furnace was initially heated to 773 K at a rate of 5 K/min in Ar

gas. Then, it was further heated to 1473 K at a rate of 10 K/min, and kept at 1473 K for 2 hours. After sintering, the pellets were analysed by XRD to determine the phases present. **Figure 3.6** compares the XRD patterns from both the 'green' and Ar-sintered pellets. It can be seen that there was no significant change in the phase distribution in the pellet after sintering, with TTM remaining the dominant phase. It should be noted that the small TTH peaks in both pellets originate from the lamella within the non-uniform particles in the as-received ironsand (results see in **Section 4.3**).

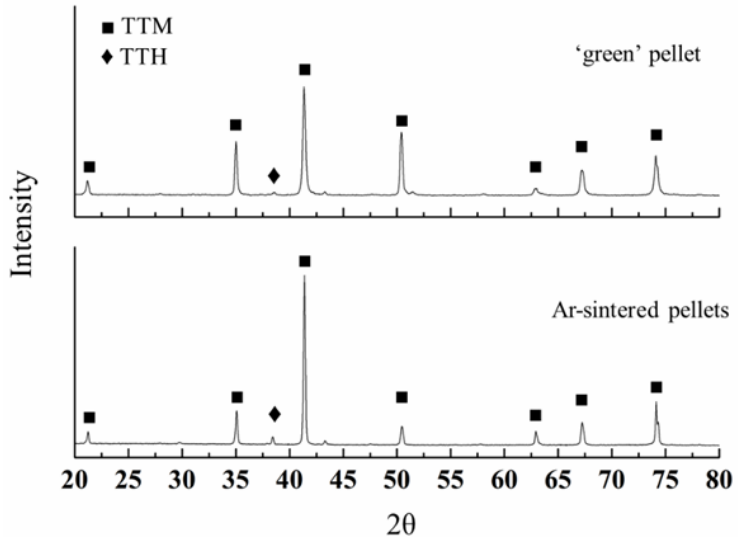

***Figure 3.6** – XRD patterns obtained from 'green' pellets and Ar-sintered pellets following 2 hours of heating at 1473 K in Ar gas*

Production of the pre-oxidised pellets

The pre-oxidised pellets were produced by oxidative sintering of the 'green' pellets at 1473 K for 2 hours in a muffle furnace with a static air atmosphere. After placing the dried 'green' pellets in the hot zone of the furnace, it was heated to 1473 K at a rate of 10 K/min, and kept at 1473 K for 2 hours. These pre-oxidised pellets were also analysed by XRD to determine the phases present. **Figure 3.7** shows and compares the XRD patterns obtained from both the 'green' and pre-oxidised pellets. Following this oxidative sintering process, all of the TTM present in the 'green' pellets was fully oxidised to TTH.

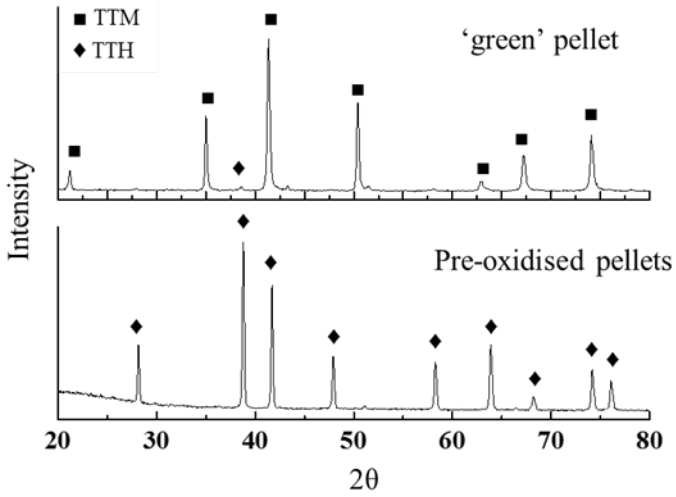

***Figure 3.7** – XRD pattern obtained from 'green' and pre-oxidised pellets following 2 hours oxidative sintering at 1473 K with a static air atmosphere [162]*

The reduction swelling index (RSI) at 1343 K and the compressive strength of both types of pellets are also determined. They are shown in **Appendix A.1**.

It should be noted that the porosity and its effect on the reduction rate of the pellets are beyond the scope of the thesis. In the current experimental set up for pelletising and sintering, it is not practically feasible to produce pellets with different porosities without changing other parameters (such as the choice of binders, or sintering conditions). Instead, this study focuses on the pellets with controlled porosity. It is confirmed that the properties of the pellets for the reduction experiments are similar to each other, as shown in **Section 3.3.1** experiment set up of the reproducibility of the reduction experiments in **Figure 3.9**.

3.3 H_2 gas reduction of NZ ironsand pellets in a TGA system

H_2 gas reduction in a TGA system (at Callaghan Innovation) was conducted to study the reduction behaviours of the pellets at high temperatures. These experiments measured the weight loss of the pellets versus reaction time. The reduction degree was then calculated from the weight loss.

3.3.1 Experiment set up

A schematic of the experiment set up is shown in **Figure 3.8**. The furnace can be raised for loading and unloading samples. To form a sealed reaction chamber, an outer alumina sheath (~4.5 cm diameter) is used. Inside the chamber, an alumina crucible is placed on top of a vertical sheathed B-type thermocouple. The bottom of the thermocouple sheath is connected to a balance located outside of the furnace hot zone, which allows *in-situ* weight recordings during reduction. To ensure good contact between the pellets and the reducing gas, a capillary, acting as a gas inlet, is installed next to the crucible.

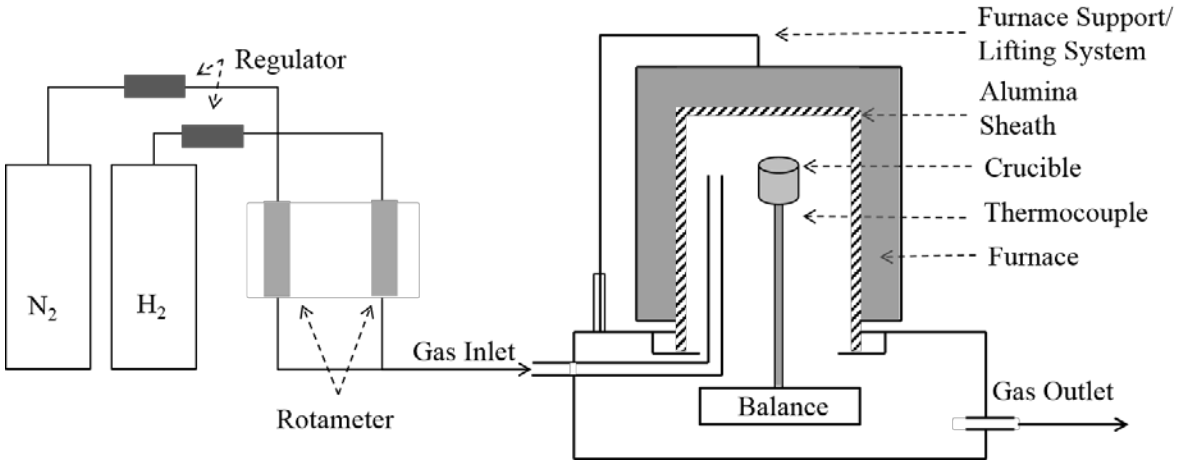

***Figure 3.8** – Schematic of the TGA experimental arrangement used in this work at Callaghan Innovation, which employed a modified Mettler (USA) TA1 Thermobalance [162]*

For each experimental run, a single pellet (~7 mm diameter) was used, produced from milled ironsand with an average particle size of 32 µm. This was placed in the middle of the crucible. To maintain an inert atmosphere inside the system before reduction, the chamber was first evacuated then backfilled with N_2 gas until atmospheric pressure was reached. The furnace was then heated to the required experimental temperature (993 K to 1443 K) at a ramp rate of 15

K/min under N_2 at a gas flow rate of 35 ml/min. Once the target temperature was achieved, the system was allowed to thermally stabilise for 10 or 30 minutes. Once stabilised, the gas flow was switched to 100vol% H_2 gas, marking the beginning of the reduction experiment. During the experiment, the mass of the pellet was recorded every 1 or 10 seconds, depending on the reduction rate. Measurement proceeded until there was no further measurable weight loss of the pellet. The N_2 gas was then switched back into the furnace, and the system cooled to room temperature at a rate of 40 K/min. Post experiment, the fully reduced pellets were characterised by SEM and XRD to establish the composition, microstructure and phase evolution.

The reduction degree *X*, was calculated based on the weight loss resulting from the removal of oxygen in the system.

For the Ar-sintered pellets, *X* is calculated by equation **3.1**:

$$X = \frac{w_0 - w_t}{0.23 * w_0} * 100\% \quad \textbf{(3.1)}$$

For the pre-oxidised pellets, *X* is calculated by equation **3.2**:

$$X = \frac{w_0 - w_t}{0.26 * w_0} * 100\% \quad \textbf{(3.2)}$$

In both equations, w_0 is the initial weight of the pellet, and w_t is the pellet weight after time *t*. The factors 0.23 in equation **3.1** and 0.26 in equation **3.2** stands for the total weight fraction of the removable oxygen in the Ar-sintered and pre-oxidised pellets respectively. (The determination of these values is given in **Appendix A.2**).

At the start of each TGA run, a short delay of ~0.4 minutes was observed to occur between switching the flow of H_2 gas into the chamber and the onset of weight loss. This delay was attributed to the time required for H_2 gas to flow through the inlet pipe and displace N_2 gas from the chamber. Therefore, in all of the following analyses, the onset delay time was removed and the time t=0 s considered to be the final data point collected before an initial weight loss was observed.

In order to confirm the reproducibility of the reduction measurements prior to undertaking experiments, multiple reduction runs were performed in the TGA under identical conditions:

~7 mm diameter pellets, 1343 K, and a flow of 250 ml/min 100vol% H_2 gas. The results are shown in **Figure 3.9**. It can be seen that all five reduction runs show very close agreement (at each reduction time, the mismatch of the calculated *X* in all the runs only shows a standard deviation of ~0.49 on average), providing a high degree of confidence in the reproducibility of the experimental method employed. This also confirms that the properties of each independent pellet are similar to each other.

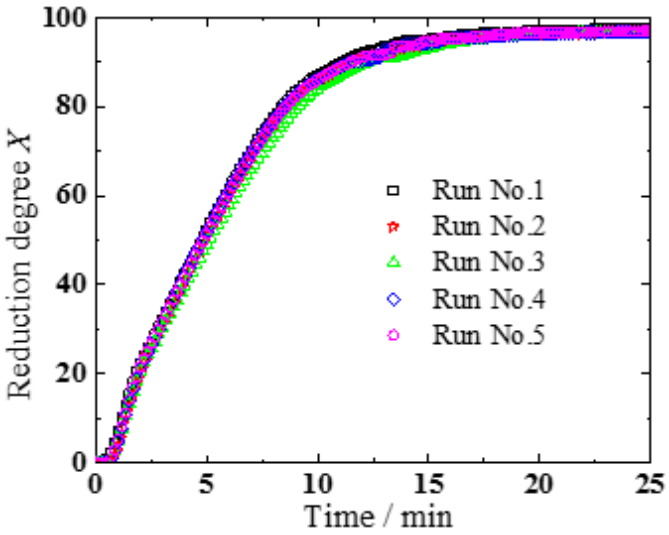

***Figure 3.9** – Plots showing data obtained during reproducibility tests of the H_2 gas reduction experiment performed in this work at Callaghan Innovation. Five sets of reduction degree data are shown, each obtained from the H_2 gas reduction of similar pre-oxidised pellets under the same condition (1343 K, 250 ml/min, ~7 mm diameter pellets) [162]*

Prior to conducting reduction experiments at different temperatures, the critical flow rates of the experiment set up for reducing both types of pellets were determined. This was done through monitoring the reduction rate for a series of increasing H_2 gas flow rates. The critical flow rate is defined as the flow rate above which there are no further effects on the reduction rate. Above the critical flow rate, gas mass transport effects are eliminated. The determination of the critical flow rate of reducing Ar-sintered and pre-oxidised pellets will be detailed in **Sections 4.1** and **5.1** respectively.

3.3.2 Experimental matrix

In the TGA experiments, the effect of temperature and pellet diameter on the reduction rate was investigated. The reduction experiments conducted for both types of pellets in this study are summarised in **Table 3.5**.

***Table 3.5** – Matrix of the experiments for reducing both types of pellets in H_2 gas in the TGA system*

	Flow rate / ml/min	Temperature / K					Pellet diameter (mm) at 1343 K			
Ar-sintered pellets	980	993	1043	1073	1093	1143	5.5	6.5	7.5	8.5
		1193	1243	1293	1343	1443				
Pre-oxidised pellets	520	1043	1143	1243	1343	1443	5.5	6.5	7.5	8.5

The pellets obtained from the highlighted reduction experiments in this table were also characterised by SEM and XRD to observe the morphologies and phase distribution in the final fully reduced pellets.

3.4 Microstructural analysis of reduced pellets from quenching experiment

To observe the microstructure of the pellets at different reduction stages, quenching experiments were carried out. Quenching experiments were conducted at both VUW and UOW, using two different set-ups. In this experiment, partially reduced pellets with desired reduction degrees were obtained. These pellets were then characterised by light microscopy and SEM-EDS analysis to establish the morphological and compositional change during reduction.

3.4.1 Experiment set up

Quenching experiments were conducted at VUW using a sliding furnace. A schematic of the experiment set up is shown in **Figure 3.10**. A quartz tube with an 8 mm inner diameter was placed inside a horizontal furnace. The furnace has four wheels, which allows it to be moved from one side to the other. This leads to rapid heating/cooling, depending on whether the sample is inside or outside the furnace cavity. The furnace temperature was controlled by an Omega-MSC controller. An N-type thermocouple was placed inside the quartz tube, close to the pellets in order to measure the sample temperature. Gases (Ar/H_2) were introduced from one end of the tube and exhausted from the other end.

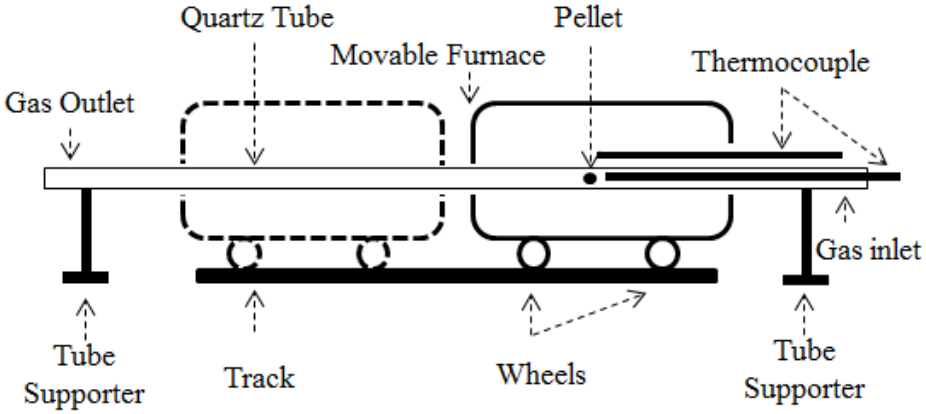

***Figure 3.10** – Schematic of the sliding furnace for obtaining the partially reduced pellets with desired reduction degrees at VUW*

For each experimental run, a single pellet (~6 mm) produced from particles with an average size of 73 µm was placed in the quartz tube. The position of the furnace was adjusted so that the pellet was placed in the hot zone. Then the furnace was heated under flowing Ar gas (340 ml/min) to the target temperature (1023 K, 1123 K or 1223 K, corresponding to the temperature

in the ND reduction experiments). After stabilising at the target temperature for 5 minutes, the gas was switched to 100vol% H_2 at a flow rate of 340 ml/min. Once the time required to obtain the desired reduction degree was reached, the furnace was immediately moved away from the sample, and H_2 gas flow was switched back to Ar gas. This process ensured that the partially reduced pellets were rapidly cooled to room temperature to reserve the pellet/particle morphologies. The quenched pellet was then removed from the quenching system and weighed. The final reduction degree was calculated using either equation **3.1** for Ar-sintered pellets or equation **3.2** for pre-oxidised pellets. Afterwards, the pellet was mounted in resin and prepared for SEM-EDS characterisation.

In addition to the 'elapsed-time' quenching experiments performed in the sliding furnace, some 'TGA-based' quenching experiments were also conducted, using a TGA system at UOW. A schematic of the experiment set up is shown in **Figure 3.11**. An alumina crucible was attached to a platinum wire, which was further extended and connected to a stainless wire. This crucible wire set-up was connected to a measuring balance at the top of the furnace. For quenching, the crucible/sample was raised to the top (cold zone) of the furnace area to cool rapidly. Before the gases (H_2 and Ar) were introduced to the furnace, they passed through drierite and ascarite to remove the water vapour and CO_2.

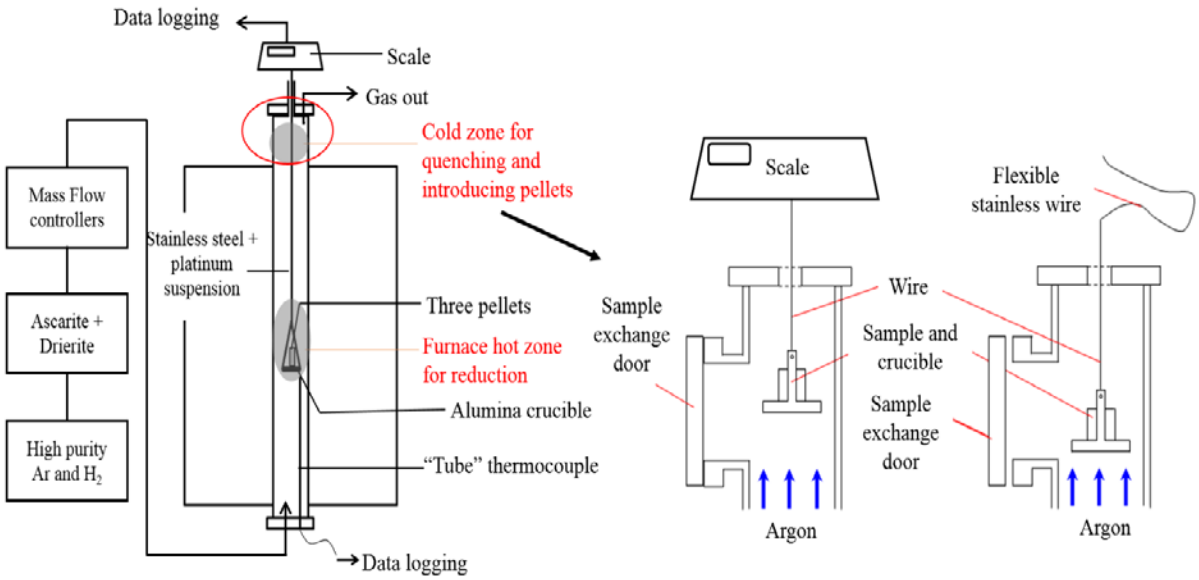

Figure 3.11 *– Schematic of the TGA system for the quenching experiments performed at UOW. During heating and reduction, the stainless steel wire is hooked at the bottom of the scale so that the pellets are in the hot zone. For quenching in Ar gas, the stainless-steel wire is unhooked and pulled up for the pellets to cool rapidly in the cold zone*

The experimental conditions are listed in **Table 3.6**. After putting three pellets in the crucible, they were initially flushed with Ar gas for 20 minutes. Then the furnace was heated up to the target temperature in Ar gas. After thermo-stabilisation for 10 minutes, the pellets were reduced in 100vol% H_2 gas. When the desired reduction degree was reached, as indicated by the weight change from the scale, the crucible was moved to the cold zone and quenched in Ar gas. Afterwards, the pellets were taken out at room temperature and prepared for characterisation. The gases used in both the UOW 'TGA-based' experiments, and VUW-based 'elapsed time' experiments were of similar grade, and the results obtained from each method were found to be consistent.

***Table 3.6** – Experimental conditions of quenching experiment conducted in the TGA system at UOW*

Pellets	Step 1: heating		Step 2: reducing	Step 3: quenching	
	Target temperature	Ar gas flow	H_2 gas flow	Quenching temperature	Ar gas flow
Diameter ~6 mm, D50%=~73 μm (Particle size)	1023 K, 1123 K, and 1223 K	1 L/min	1 L/min	~423 K	3 L/min

3.4.2 Experimental matrix

The quenching experiments conducted for both types of pellets in both the 'elapsed-time' sliding furnace at VUW and the 'TGA -based' system at UOW are summarised in **Table 3.7**.

***Table 3.7** – Matrix of experiments for reducing and quenching both types of pellets for the observation of morphologies in the partially reduced pellets with desired reduction degrees*

		Ar-sintered pellets				Pre-oxidised pellets			
Experiment set up		'TGA-based' system at UOW 1 L/min 100vol% H_2 gas flow				'elapsed-time' sliding furnace at VUW 340 ml/min 100vol% H_2 gas flow			
Temperature /K		Reduction degree obtained							
	1023	21%	50%	81%	Fully reduced	21% (1min)	55% (4mins)	79% (10mins)	Fully reduced
	1123	21%	50%	78%	Fully reduced	18% (45s)	56% (2min50s)	80% (5min40s)	Fully reduced
	1223	25%	54%	82%	Fully reduced	23% (30s)	53% (1min40s)	81% (3min20s)	Fully reduced

3.5 *Ex-situ* characterisation methods

XRD, light microscopy and SEM-EDS analysis (imaging characterisation) were used to analyse the characteristics of the as-received ironsand, unreduced pellets, partially reduced and fully reduced pellets.

3.5.1 XRD analysis

To conduct powder XRD analysis, the pellets were first crushed and ground in a mortar. The XRD analysis conducted in this study used a Bruker D8 Advance Diffractometer. Its set up is summarised in **Table 3.8**. After collecting diffraction patterns from the studied samples, they were analysed using EVA (V2) software to determine the phases present in the samples. Quantitative analysis was also conducted using Topas 4.2 software (see **Section 3.6**).

***Table 3.8** – Set up of the Bruker D8 XRD facility and the operation parameters*

Radiation source	Beam height	Detector	Voltage and current	Step interval	Count time per step
Co Kα (1.79026 Angstroms)	1 mm	Na(Tl)l scintillation counter	40 kV and 15 mA	0.05° per 2θ	5 seconds

3.5.2 Imaging characterisation

Sample preparation

Pellets and powders were prepared for microscopy imaging (light microscopy or SEM-EDS) by mounting in an epoxy resin mould. The resin applied was Struers EpoFix - a slow-curing transparent epoxy which has a high fluidity and long settling time to aid impregnation. The pellets in the uncured resin were placed in a vacuum chamber to ensure resin impregnated throughout the pores within the pellets. It took around 24 hours for the epoxy resin to harden.

Once hardened, the mounted pellets were ground roughly to their centre planes using a series of silicon-carbide papers from #250 to #2000 grit. The resulting cross-section surface was polished by a series of diamond pastes (9 µm, 3 µm and 1 µm) to remove scratches and give a

final smooth and even surface. Between each grinding and polishing step, the epoxy-mounted pellets were washed using soap, rinsed under ethanol and dried, to remove grinding dust from the surface.

For light microscopy, the polished pellets were directly used. For SEM-EDS analysis, the pellets were coated with a thin layer of carbon to provide a conductive surface.

Light microscopy

Light microscopy allows the observation of pellet-scale morphology and evolution. Light microscopy was conducted with a Nikon Eclipse LV100NDA optical microscope, equipped with a Nikon camera (AF-S Micro NIKKOR 40mm lens) and NIS-Elements photo analysis software.

SEM-EDS analysis

SEM-EDS analysis was undertaken mainly using two different microscopes: a FEI Quanta 450 and a FEI Nova. Both microscopes are equipped with an EDAX detector, which was used with the TEAM 3.1 software to provide quantitative EDS analysis. In addition, the EDS-Line scan analysis (a type of analyses as seen below) was conducted using a JEOL JSM-6490LA electromicroscope integrated with AZtecSynergy software (Aztec 4.2).

Three different types of analyses were obtained from the SEM-EDS analysis:

(1). Back-scattered SEM images. These back-scattered microstructure images show the morphologies of cross-sectioned pellets at different reaction stages. This allowed for the investigation of reduction conditions on the morphologies of the fully reduced pellets, and revealed the morphological evolution of particles distributed from the pellet surface to the pellet centre.

(2). EDS point/mapping analysis. This analysis was used to quantitatively determine the distribution of the elements at points within a back-scattered SEM image.

(3). EDS-line scan analysis. This method was adopted specifically for analysing the atomic% O/Fe ratio as a function of the location in a partially reduced pellet. This analysis is similar to

the point analysis, but is conducted by scanning along a continuous line all the way from the pellet surface to its centre. The output of the EDS-line scan is a plot of the atomic% O/Fe ratio profile along the scanned line. Due to the existence of pores and impure oxides in the pellets, the profile normally shows noise. To remove the noise while maintaining the shape of the profile, post-processing using data smoothing is applied. A 50th percentile smoothing filter with a window of 5 picks the middle point of each rolling set of 5 data points. By using this smoothing method, the noise was significantly reduced while maintaining the profile shape. The atomic% O/Fe ratio obtained from this method were externally calibrated and then checked using mineral standards of Fe_2O_3, Fe_3O_4, FeO and metallic Fe. The results are shown in **Figure 3.12**. As can be seen, the atomic% O/Fe ratios obtained from the mineral standards agree closely with the corresponding stoichiometries (stoichiometric FeO is assumed).

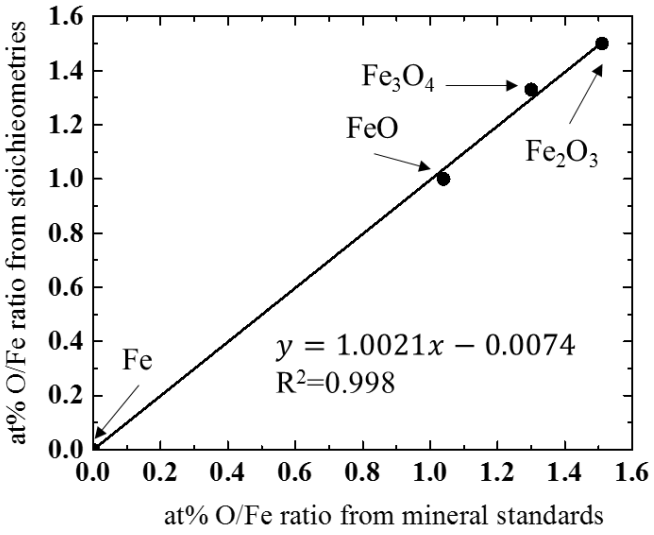

***Figure 3.12** – External calibration for performing the EDS-line scan analysis for the partially reduced pellets*

3.6 Phase evolution during reduction of pellets from *in-situ* ND experiments

A series of *in-situ* neutron diffraction (ND) experiments were performed to determine the phase evolution during reduction of the pellets. ND is a technique that allows direct elucidation of the amount of each phase generated during reduction. The principle of the method is similar to XRD, but compared to X-rays, neutrons can travel long distances in materials without being adsorbed. Their penetrating depth could reach up to several centimetres. Hence, ND technique allows the use of bulk materials such as the ironsand pellets. In these experiments, continuous diffraction patterns during reduction of the pellets across the whole process were obtained. Then, these diffraction patterns were converted to the concentration (weight proportion) of each key crystalline phase occurring during reduction for the phase evolution analysis.

3.6.1 Experiment set up

The *in-situ* ND experiments were conducted using the Wombat high-intensity diffractometer facility at the Australian Nuclear and Science Technology Organisation (ANSTO). Wombat has a large solid angle detector with position sensitive detection capabilities, enabling the collection of an entire diffraction pattern at once. The Wombat instrument is equipped with a high-temperature furnace, allowing diffraction patterns to be continuously obtained during a reaction. The operating parameters used in these experiments are summarised in **Table 3.9**.

***Table 3.9** – Operating parameters of the Wombat instrument at ANSTO for conducting the reduction experiments monitored by the in-situ ND technology*

Detector scattering angle	Wavelength	Exposure time
120°	0.241 nm	30 seconds

Schematics of the facility and the sample holder are shown in **Figure 3.13**. In each experimental run, four pellets (~6 mm diameter) produced from an average particle size of 73 µm were put in a quartz tube (ID=7 mm). This tube also acted as a gas inlet. Alumina wool was used at one end of the tube to support the pellets and facilitate gas flow. A thermocouple was inserted close to the pellets, continuously measuring the sample temperature during the experiments. The small quartz tube was then inserted into a larger diameter tube with a closed end, which sealed the reaction chamber and also acted as a gas outlet. The whole assembly was then placed inside the hot zone of the furnace. At the start of the experiment, the samples were

flushed with Ar gas before heating. Once the target temperature (1023 K, 1123 K or 1223 K) was reached under Ar gas, the system was held at this temperature for 5 minutes to allow thermal stabilisation. Once stabilised, a H_2 or H_2-Ar gas mixture was introduced, marking the beginning of the reaction. At the end of each experiment, the gas was changed back to Ar and the samples were cooled down. Diffraction patterns were collected every 30 seconds from the start until the end of the experiment. The time resolution of 30 seconds was enough to provide sufficient counts for the diffraction pattern on the Wombat instrument.

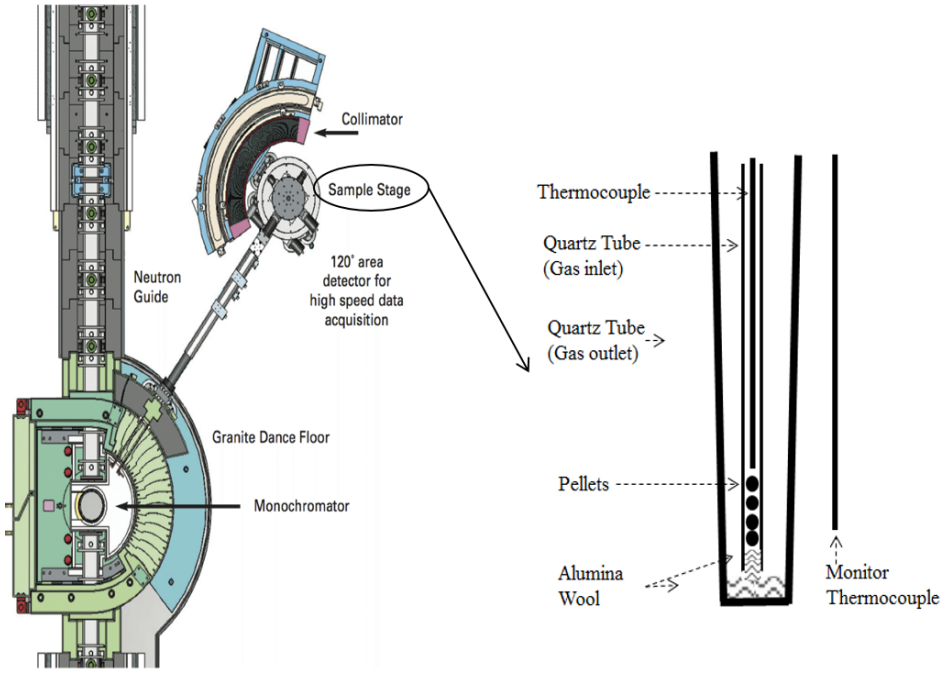

***Figure 3.13** – Illustration of the Wombat facility [163] and a schematic of the sample holder*

Data analysis was then performed to convert the diffraction patterns from each time step into the concentration of each crystalline phase. This conversion was conducted using Topas 4.2 software, and followed a similar peak fitting principle as described in Longbottom *et al*. [124]. The peak positions were determined by the size and symmetry of the unit cells for each phase. The peak widths were dominated by instrumental broadening so that the peak shape is the same for all phases at each diffraction angle. Peak intensity fitting was related to the scale factor, atom positions, site occupation and thermal vibrations. The scale factor links the peak generated by the fitting model to that from the actual diffraction pattern obtained from ND, which is used to establish a reasonable data fitting. In this work, the atom positions were fixed to their literature values, and 100% atom occupancy of the corresponding sites was assumed. In TTM, Ti only occupies octahedral Fe sites according to literature [164], so that the peak

intensity generated by the model for TTM is modified. Based on previous experience, the thermal parameter was fixed at 0.33 to provide reasonable fittings.

A typical peak-fitting result for an ND pattern is shown in **Figure 3.14**. The fitting was conducted from 2θ = 20° to 125° (No peaks are distinguished above 125°). The background of the diffraction pattern was modelled by a 4th order Chebyshev polynomial regression. A common Thompson-Cox-Hasting pseudo-Voigt (TCHZ) peak shape was applied to all the possible crystalline phases, with the peak-fitting principle as described above. The scale factor and lattice parameter of each main crystalline phase were fitted parameters for each separate pattern.

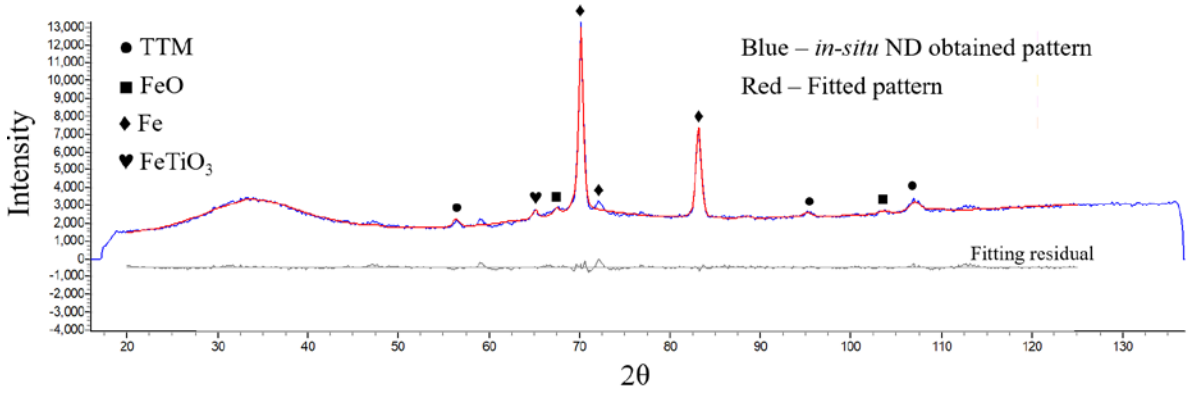

Figure 3.14 *– A typical peak-fitting results of an ND pattern obtained of reducing the pre-oxidised pellets at 1223 K at a flow of 250 ml/min 100vol% H_2 gas*

As can be seen, the peaks of TTM, FeO, Fe and $FeTiO_3$ phases were generally well represented by the fitted curves. This fitting procedure gives the final refined scale factor of each crystalline phase, allowing the concentration of each phase to be established.

These fitted concentrations can also be converted to an overall reduction degree *X*, which is defined as the fraction of O removed from the system based on equation **3.3**:

$$X = \frac{m_{o,0} - m_{o,t}}{m_{o,0}} \quad \textbf{(3.3)}$$

where $m_{o,0}$ represents the mass of O in the pellets before reduction, and $m_{o,t}$ represents the mass of O in the pellets after reduction at time *t*. However, due to the constant decrease in the pellets' mass during reduction, the absolute mass of O at any time cannot be determined. Therefore, the mass of O in the pellet is normalised against the mass of Fe. This mass ratio,

O/Fe, is used to replace the mass of O in equation **3.3**. This normalisation is shown by equation **3.4**. In this equation, *M* stands for the molar mass of each phase or element, and $\{i\}$ indicates the mass percentage (concentration) of each crystalline phase obtained from the *in-situ* ND analysis.

$$\frac{O}{Fe} = \frac{\{Fe_2O_3\}\frac{3M_o}{M_{Fe_2O_3}} + \{Fe_3O_4\}\frac{4M_o}{M_{Fe_3O_4}} + \{FeO\}\frac{M_o}{M_{FeO}} + \{FeTiO_3\}\frac{3M_o}{M_{FeTiO_3}}}{\{Fe_2O_3\}\frac{2M_{Fe}}{M_{Fe_2O_3}} + \{Fe_3O_4\}\frac{3M_{Fe}}{M_{Fe_3O_4}} + \{FeO\}\frac{M_{Fe}}{M_{FeO}} + \{FeTiO_3\}\frac{M_{Fe}}{M_{FeTiO_3}} + \{Fe\}\frac{M_{Fe}}{M_{Fe}}} \quad (\mathbf{3.4})$$

3.6.2 Experimental matrix

In the ND experiments, the effect of reduction conditions on the phase evolution were investigated. The parameters varied included: H_2 flow rates, H_2 gas concentrations and reduction temperature. The experiments undertaken at ANSTO in June 2017 are summarised in **Table 3.10**.

Table 3.10 *– Reduction experiments for both types of pellets monitored by in-situ ND technology and conducted under different reduction conditions. Experiments performed at Wombat beamline at ANSTO in June 2017*

Flow rate	Temperature	H_2 gas concentration (vol%) in H_2-Ar gas mixture (for both types of pellets)					
250 ml/min	1023 K	100% H_2	75% H_2	50% H_2			
	1123 K	100% H_2	75% H_2	50% H_2	25% H_2	10% H_2	
	1223 K	100% H_2	75% H_2	50% H_2	25% H_2	10% H_2	5% H_2

To examine the effects of gas flow rate on the phase evolution for both types of pellets, reduction experiments were also conducted at three different flow rates (62.5 ml/min, 125 ml/min and 250 ml/min) at 1223 K with 100vol% H_2 gas.

It should be noted that due to the late Australia Visa issuing for the author of this thesis, the *in-situ* ND reduction experiments were conducted by a team of scientists in Australia without the author in attendance. However, all of the analyses in the post processing of the data were conducted by the author.

In this chapter, the experiment set ups and procedures for the pellet reductions are described. To conduct these reduction experiments, several different furnaces were used. To enable effective comparison, the temperature at the sample position in the hot zone of each furnace was calibrated. This calibration is shown in **Appendix A.3**. Similarly, the purity of the gases (H_2, N_2 and Ar) used in the experiments is also summarised in **Appendix A.3**.

Chapter 4
Results of reducing Ar-sintered pellets in H_2 gas

In this chapter, a summary of experimental results obtained from reducing the Ar-sintered pellets in H_2 gas is given. These results include:

- **Section 4.1**: TGA measurements of the reduction of Ar-sintered pellets in H_2 gas
- **Section 4.2**: The evolution of crystalline phase during reduction determined by *in-situ* ND
- **Section 4.3**: The pellet- and particle-scale morphologies which occur during reduction, as captured during quenching reduction experiments
- **Section 4.4**: Summary of the results of reducing Ar-sintered pellets

Note that in this chapter, only the experimental results obtained are reported. Discussion of the analysis of these results is presented in **Chapters 6**, 7 and **8**.

4.1 Reduction of the Ar-sintered pellets in the TGA system

In this section, the DR characteristics of the Ar-sintered pellets in H_2 gas flow were investigated. Key experimental variables examined were the effect of H_2 gas flow rate, reduction temperature and pellet diameter on the pellet reduction rate.

4.1.1 Determination of critical flow rate

In **Figure 4.1**, the effect of H_2 gas flow rate on the reduction of the pellets reduced at 1343 K is shown. The reduction progressed faster with increasing flow rate from 330 ml/min to 850 ml/min. Further increase on the flow rate had no additional effects on the reduction rate. This implies that the critical flow rate of this experiment is below 850 ml/min. To ensure that mass transport effects in the gas stream were excluded, the highest tested flow rate of 980 ml/min was chosen for all the following reduction experiments.

It should be noted that reducing 1 mole Fe_3O_4 stoichiometrically requires 4 mole of H_2 gas. In the current experiment, 0.65 g pellet was reduced, which has a stoichiometric requirement of only 250 ml H_2 gas. This is much less than used in these experiments. This is because excess H_2 is needed to exceed the thermodynamic limits of the reactions. In addition, a high flowrate

is also required to sweep away water vapour and maintain a local $[H_2]/[H_2O]$ ratio that is favourable to iron production. In a practical industrial process, wastage of excess H_2 gas can be avoided by recycling unused H_2 gas from the exhaust gas (after first condensing and removing the water vapour). This also applies to the reduction of pre-oxidised pellets reported in **Section 5.1**.

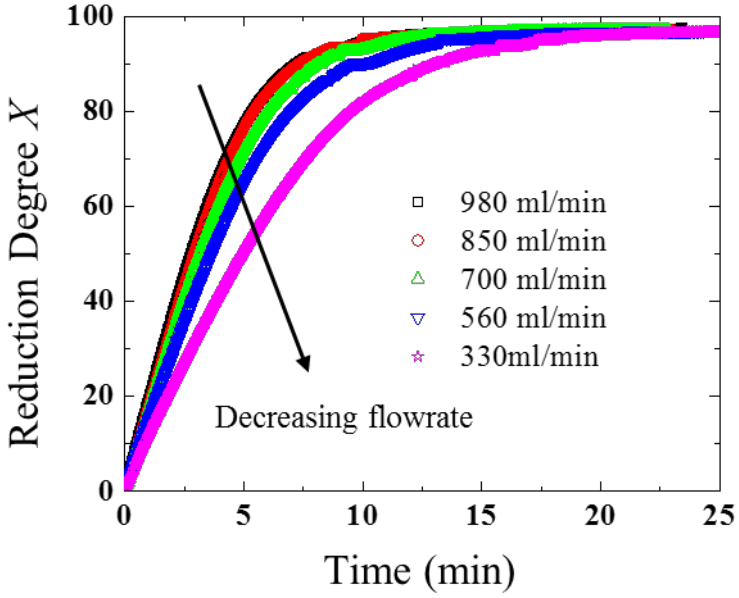

Figure 4.1 *– The effect of changing H_2 gas flow rate on the reduction rate of reducing Ar-sintered pellets (~7 mm) at 1343 K in the TGA system at Callaghan Innovation*

4.1.2 The effect of temperature on reduction rate

Results of the TGA experiment of reducing Ar-sintered pellets in 980 ml/min flowing H_2 gas are shown in **Figure 4.2**. As can be seen, the reduction rate increased with increasing temperatures. From 993 K to 1193 K, the reduction rate increased significantly. At temperatures ≥ 1193 K, the temperature effect was still present, but less significant than at lower temperatures. At 993 K, it took almost 110 minutes for the completion of the reduction, while it took less than 20 minutes at all temperatures above 1143 K. Interestingly, it was found that the maximum reduction degree achieved at the completion of reduction varied with temperature. It increased from 93.3% to 97.4% as temperature increased from 993 K to 1443 K. The lower maximum reduction degree might result from the residual Fe-Ti-O phases. The evolution of these phases is further discussed in **Chapters 7** and **8**.

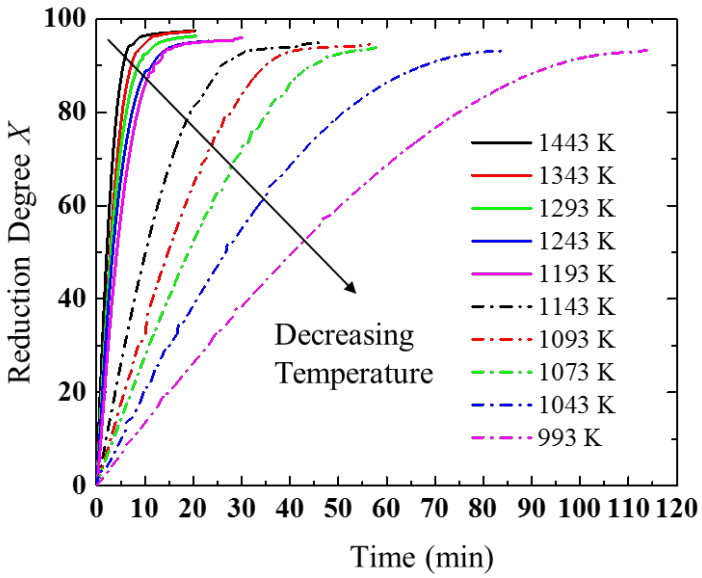

***Figure 4.2**– The effect of temperature on the reduction rate of Ar-sintered pellets (~7mm diameter) in 980 ml/min flowing H_2 gas from 993 K to 1443 K in the TGA system at Callaghan Innovation*

XRD analysis was performed on the fully reduced pellets obtained from selected TGA experiments (as shown in **Table 3.5**), and the results are given in **Figure 4.3**. From this figure it can be seen that, in addition to the major phase of metallic Fe (Peak A), several different residual Fe-Ti-O phases were also observed (Peak B to Peak D). These residual oxides were identified to be ilmenite ($FeTiO_3$), rutile (TiO_2), pseudobrookite (PSB-Fe_2TiO_5 or ferro-PSB, $FeTi_2O_5$), and a generic spinel phase (Peak E). The presence of these residual oxides is consistent with a final reduction degree of <100%. The evolution of these phases with reduction temperature is shown in **Figure 4.4**. On increasing the reduction temperature, the concentrations of both $FeTiO_3$ and TiO_2 decreased, while that of PSB/ferro-PSB increased. The spinel concentration did not change significantly with temperature.

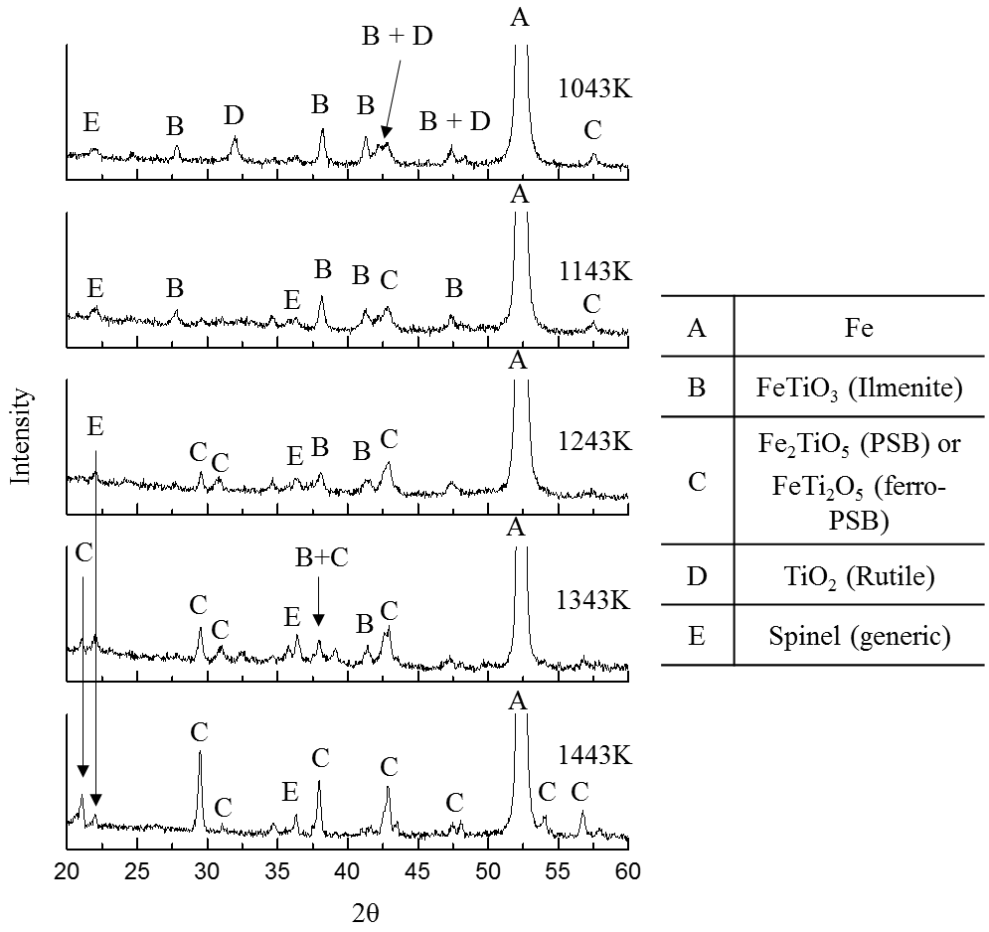

A	Fe
B	$FeTiO_3$ (Ilmenite)
C	Fe_2TiO_5 (PSB) or $FeTi_2O_5$ (ferro-PSB)
D	TiO_2 (Rutile)
E	Spinel (generic)

Figure 4.3 *- Magnified XRD diffractograms obtained from fully reduced pellets following reduction at each temperature from 1043 K to 1443 K. Note that the metallic Fe peak (A) is truncated in order to enable minor peaks to be clearly shown. The full pattern is shown in* ***Figure B.1*** *in* ***Appendix B.1***

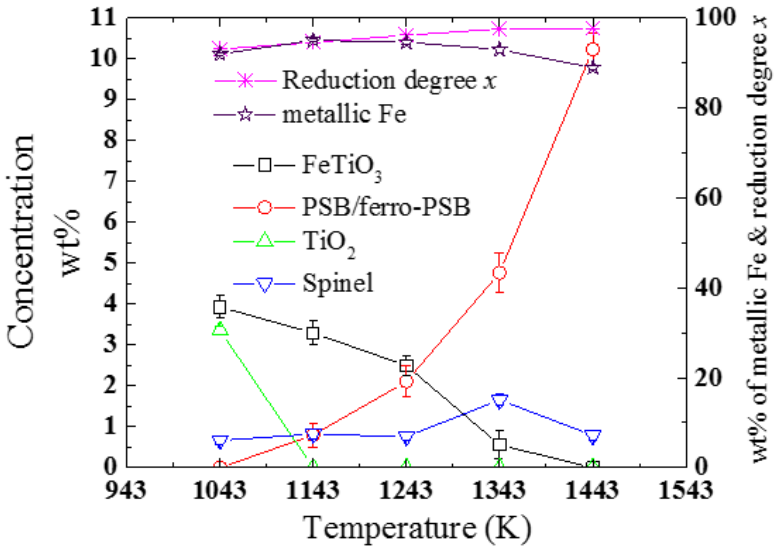

Figure 4.4 *– Changes in concentration of residual oxides (as well as metallic Fe and reduction degree) indicated in* ***Figure 4.3*** *in the fully reduced pellet at each temperature from 1043 K to 1443 K. Note the error bar of each phase concentration is generated from the peak fitting*

4.1.3 The effect of pellet size on reduction rate

The reduction behaviour of Ar-sintered pellets with diameters ranging from 5.5 mm to 8.5 mm was measured at 1343 K at a H_2 gas flow of 980 ml/min, and the results are plotted in **Figure 4.5**. As can be seen, increasing the pellet size results in a slower reduction rate.

It should be noted that 'kinks' were observed in the reduction degree curve above 90%. This has been seen in almost all the reduction experiments, which might be attributed to the reductions of the residual iron oxides (as established from the XRD analysis in **Figure 4.3**) at latest stages. These reactions are further discussed in **Chapters 7** and **8**. This suggests that smaller pellets may be desirable for practical DRI processes in order to deliver a faster reduction rate.

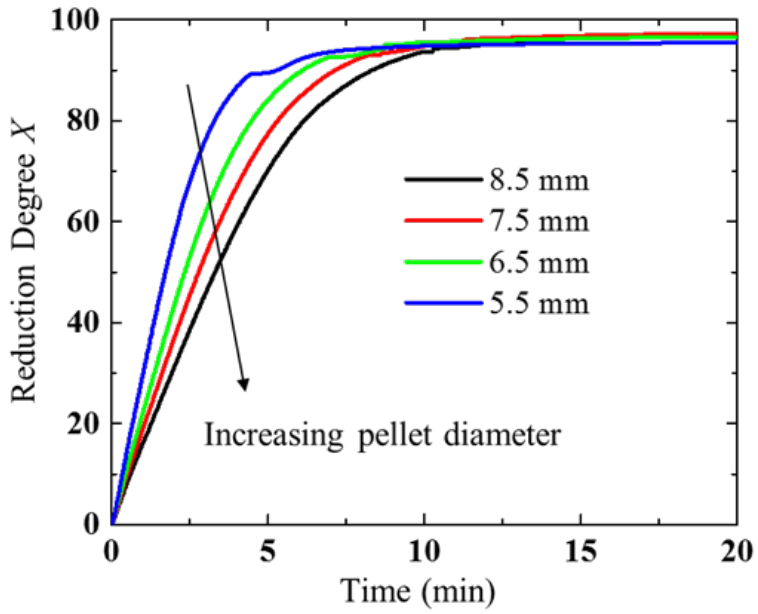

***Figure 4.5** – The effect of pellet size on the reduction rate for the Ar-sintered pellets reduced at a flow rate of 980 ml/min H_2 gas at 1343 K. (Data taken in the TGA system at Callaghan Innovation)*

4.2 Phase evolution during H_2 gas reduction of Ar-sintered pellets through *in-situ* ND measurements

In this section, results obtained from *in-situ* ND measurements of the phase evolution during H_2 gas reduction of the Ar-sintered pellets is described. The effects of H_2 flow rate, H_2 gas concentration and temperature on the phase evolution were investigated.

The *in-situ* diffraction patterns obtained were converted to crystalline phase concentrations at each point in time during a series of reduction experiments, using the approach explained in **Subsection 3.6.1**. An example phase evolution plot is shown in **Figure 4.6**, which shows results from Ar-sintered pellet reduced at 1223 K by 100vol% H_2 gas at a flow of 250 ml/min. Before reduction, the Ar-sintered pellets composed ~95wt% TTM and ~5wt% TTH. At the moment H_2 gas was introduced, TTH was rapidly consumed, and a slight increase in the concentration of TTM was observed. After this, the concentration of TTM started to decrease, and FeO was detected. The concentration of FeO first rose to a peak at about 3 mins, before dropping back down to zero. Metallic Fe first appeared at the same time as FeO. $FeTiO_3$ was detected after the concentration of FeO reached its peak. At the completion of the reduction, metallic Fe and $FeTiO_3$ were the only products observed.

It should be noted that compared to XRD, the ND technique gives broader peaks and higher background noise level. This does not allow for the identification and observation of other minority phases which may also be present, such as Fe_2TiO_4, TiO_2 and PSB. This limitation of ND measurements will be further addressed in **Subsection 4.2.4.**

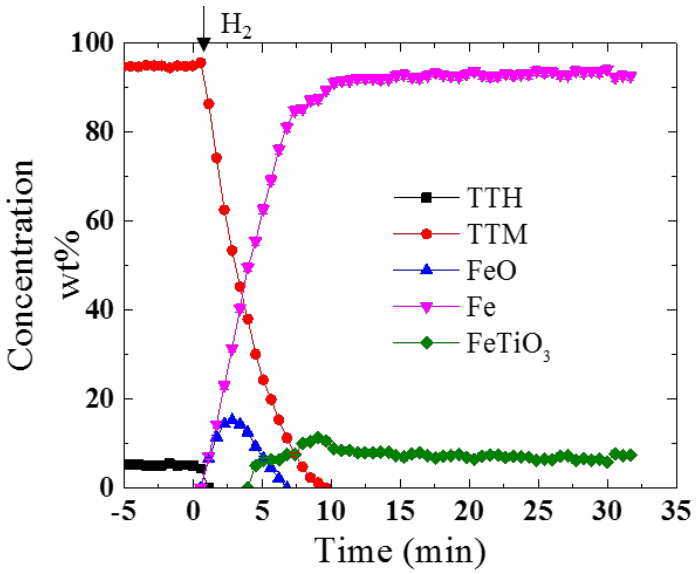

***Figure 4.6**– An example of the phase evolution obtained from the in-situ ND measurements of Ar-sintered pellets reduced at 1223 K by 100vol%H_2 at a gas flow rate of 250 ml/min*

In the *in-situ* ND experiments, the key variables investigated were different H_2 flow rates at 1223 K, H_2 gas concentrations at each temperature and reduction temperatures (1023 K, 1123 K and 1223 K). In order to compare the effects of each reduction condition on the phase evolution, it is necessary to renormalize the time axis so that each reaction can be visualised within the same axis range. To do this, a characteristic time (τ) was determined for each reaction. This was defined as the time to reach 50wt% metallic Fe.

4.2.1 The effect of H_2 flow rate on the phase evolution at 1223 K

1. Determining the critical flow rate for ND reduction experiments

At 1223 K, the Ar-sintered pellets were reduced using 100vol% H_2 gas at three different flow rates: 62.5 ml/min, 125 ml/min and 250 ml/min. Concentration curves of each crystalline phase obtained at each flow rate are shown in **Figure 4.7**. It can be seen that lower flow rate results in a slower reduction rate.

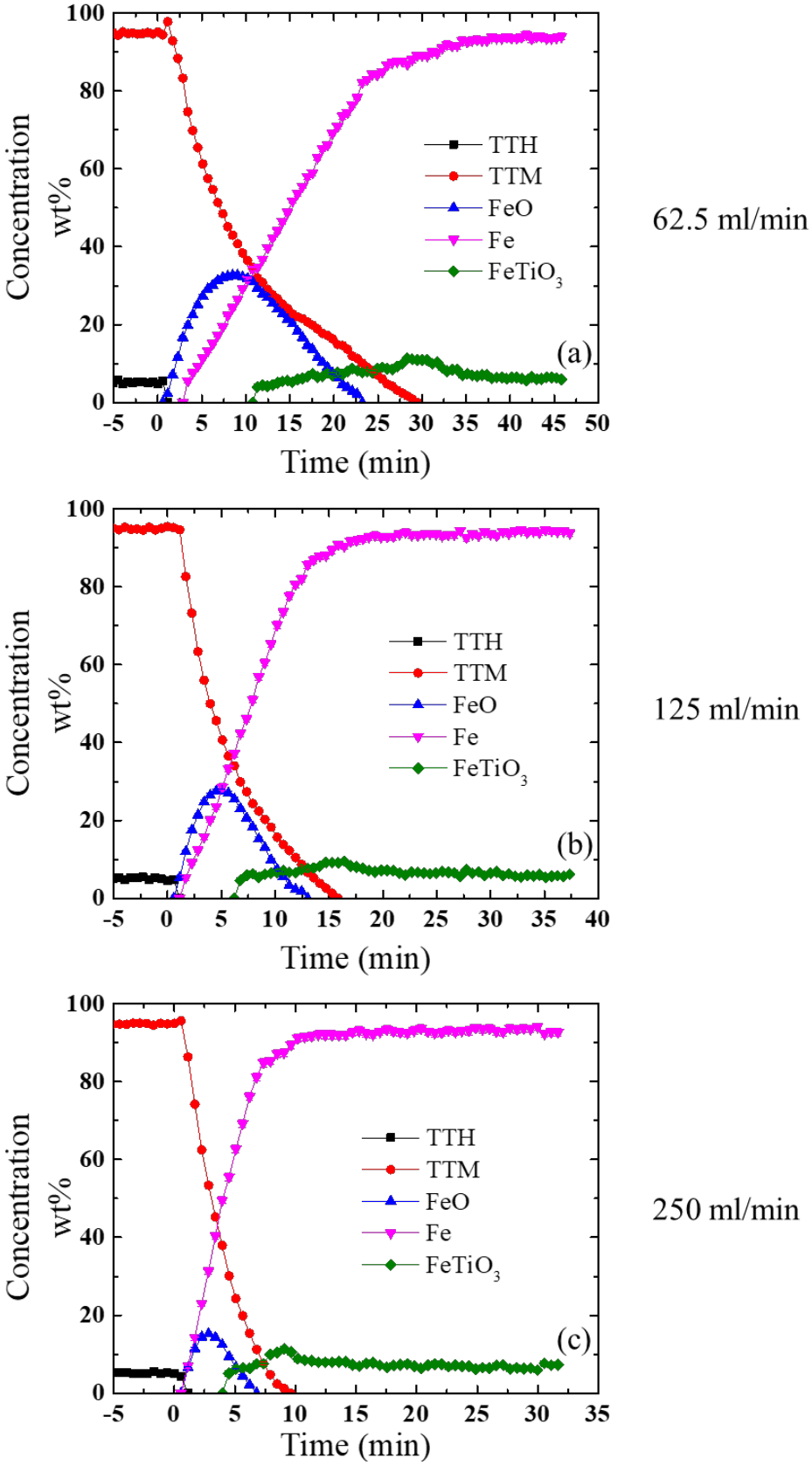

Figure 4.7 *– Concentration curves of each crystalline phase during reduction of Ar-sintered pellets by 100vol% H_2 gas at 1223 K at a flow rate of (a) 62.5 ml/min, (b) 125 ml/min, and (c) 250 ml/min*

To verify whether the highest flow rate conducted in ND reduction experiments (250 ml/min) was conducted above the critical flow rate of these experiments, ND and TGA results were compared for a similar pellet (~6 mm pellet diameter and 73 µm average particle size). The TGA experiment was performed at 1223 K at a flow of 980 ml/min 100vol% H_2 gas. (These conditions were known to be above the critical flow rate condition for Ar-sintered pellets in the TGA system at Callaghan Innovation). Reduction degree values were also calculated from the phase concentration curves obtained from the ND reduction experiments (using equations **3.3** and **3.4)**. A comparison between the ND and TGA result is shown in **Figure 4.8**. As can be seen, the ND reduction experiments conducted at a flow rate of 250 ml/min seemed closely follow the reduction rate obtained in the TGA experiment at a flow rate of 980 ml/min, indicating this experiment took place above the critical flow rate for the ND experimental apparatus at the Wombat beamline. However, the ND reduction experiments conducted at lower flow rates (62.5 ml/min and 125 ml/min) were below the critical flow rate, meaning that gas mass transport effect on the phase evolution cannot be excluded.

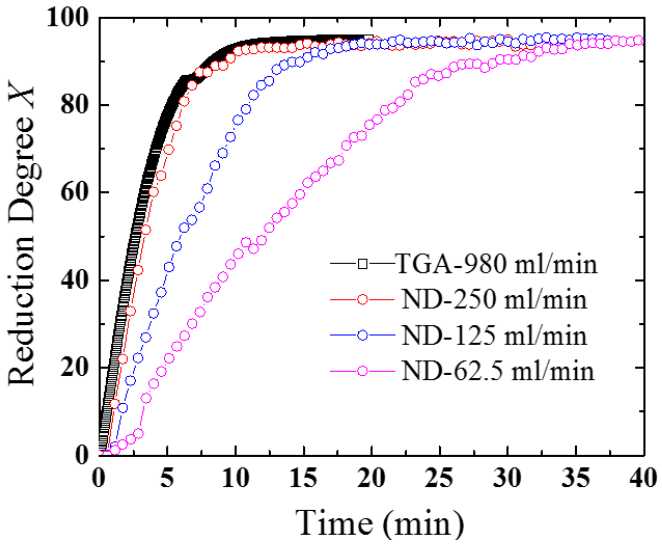

Figure 4.8 *– Comparison between the reduction degree curve obtained from the TGA experiment (Callaghan Innovation) at a flow rate of 980 ml/min, and the results obtained from the ND reduction experiments (Wombat beamline) at three different flow rates using 100vol% H_2 gas at 1223 K*

2. The effect of flow rate on the in-situ phase evolution

In **Figure 4.9(a)**, the production rate of metallic Fe during reduction at different H_2 flow rates are indicated. As can be seen, the generation of metallic Fe progressed faster with increasing flow rates. The intersection of the dashed line with each data curve shows the time, τ, at which

50% metallisation was achieved for each experiment. In **Figure 4.9(b)**, a plot of the reciprocal of each τ ($1/\tau$) against the respective flow rate shows a linear relationship passing through the origin. This linear relation implies that the generation of metallic Fe is directly proportional to H_2 flow rate over the range of flow rates studied. Note that this linear relation also indicates the flow rate of 250 ml/min applied in the ND reduction experiment is just above the critical flow rate for the Wombat beamline.

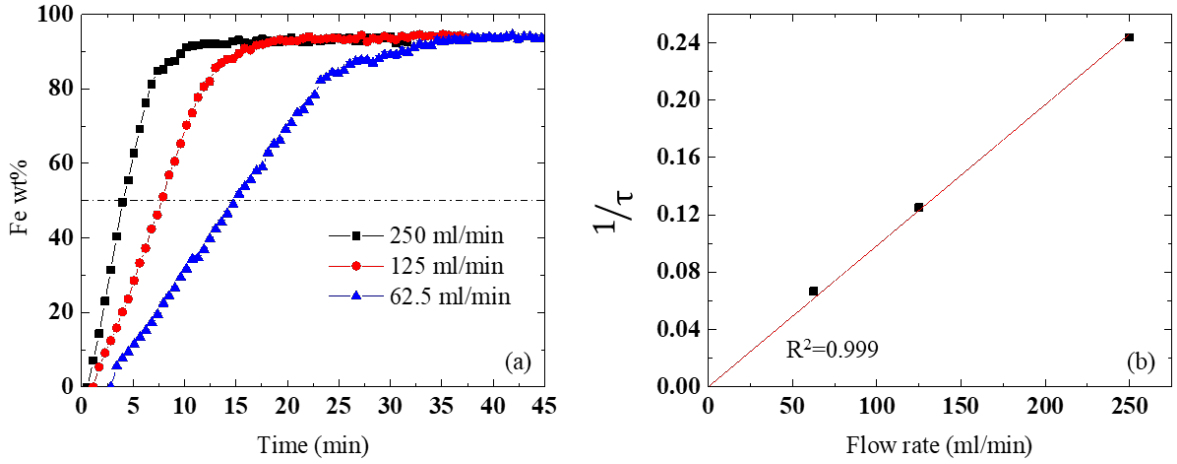

***Figure 4.9**– (a) The effect of H_2 flow rate on the changes in concentration of metallic Fe during reduction of Ar-sintered pellets at 1223 K by 100vol% H_2 at 62.5 ml/min, 125 ml/min and 250 ml/min. The dashed line indicates 50wt% metallic Fe. (b) A linear relationship between $1/\tau$ and flow rate.*

In order to compare the evolution of each crystalline phase at different H_2 flow rates on a single coordinate axis, the *x*-axis was normalised (t/τ) and the data replotted, as in **Figure 4.10(a)** to **(e)**. As can be seen, the normalised curves for TTH, metallic Fe, and $FeTiO_3$ are highly similar for the different H_2 flow rates tested. However, the peak level of the intermediate FeO phase varies significantly with different flow rates, with the maximum concentration of FeO increasing as the H_2 flow rate decreases. Some discrepancies are also observed for the TTM phase at the highest flow rate. These differences are possibly attributed to the gas mass transfer effects. It might result in a different local H_2/H_2O distribution in the pellets at different H_2 flow rates, affecting the phase evolution (especially the reduction of TTM to FeO).

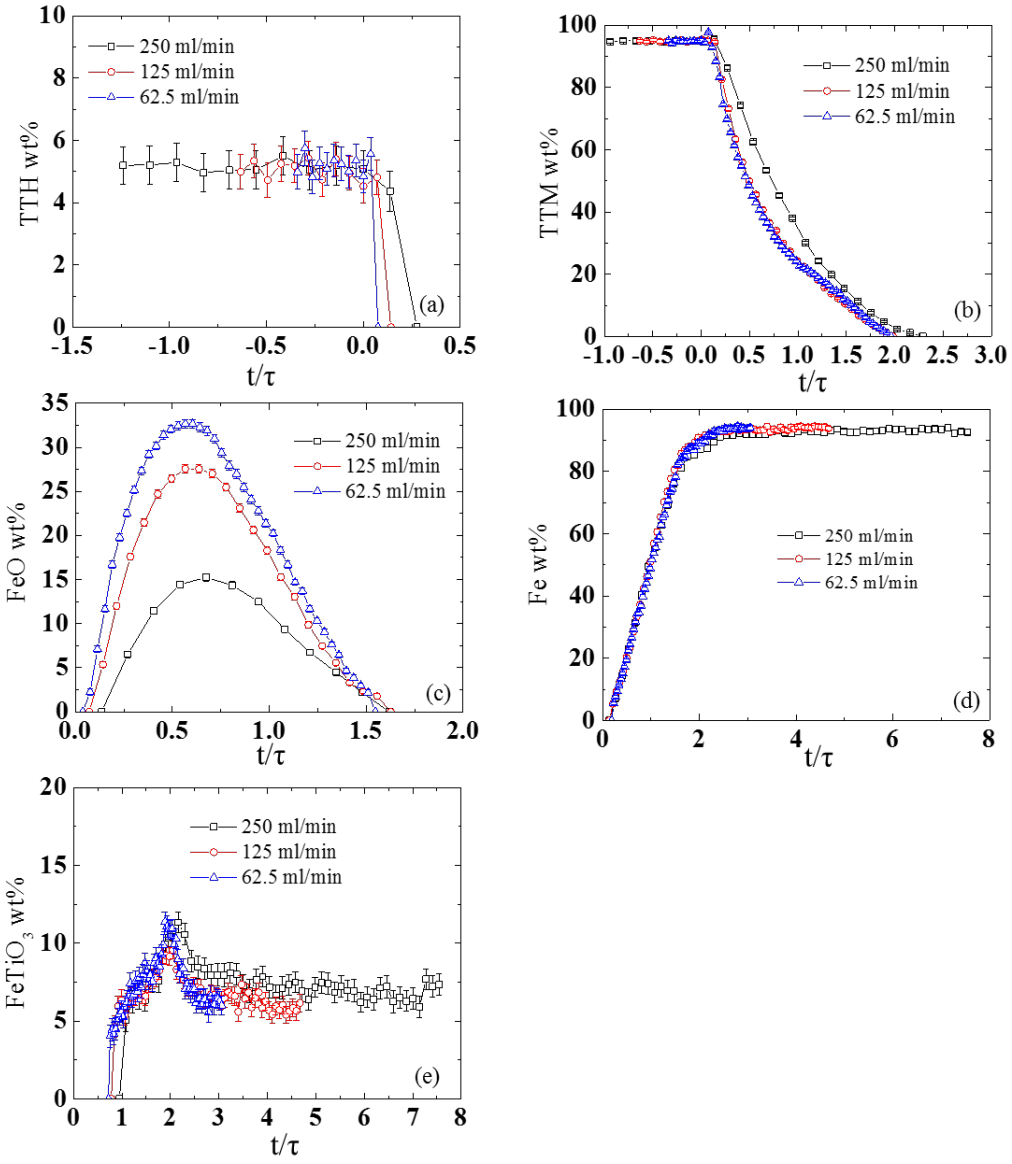

Figure 4.10 *- In-situ ND results showing the evolution of each crystalline phase during reduction of Ar-sintered pellets by 100vol% H_2 gas at 1223 K at a flowrate of 62.5 ml/min, 125 ml/min and 250 ml/min respectively at the Wombat beamline. Here, data is plotted in a single coordinate system by using a normalised dimensionless x-axis (t/τ). It should be noted each reduction started at t/τ=0. (a) TTH, (b) TTM, (c) FeO, (d) metallic Fe and (e) $FeTiO_3$*

4.2.2 The effect of H_2 gas concentration on the phase evolution at each temperature

At each temperature from 1023 K to 1223 K, reductions of the Ar-sintered pellets in a 250 ml/min flowing H_2-Ar gas mixture with H_2 gas concentrations ranging from 5vol% to 100vol% were conducted. Concentration curves for each crystalline phase during reduction at each condition at 1223 K are shown in **Figure 4.11** as examples, while the concentration curves obtained at 1023 K and 1123 K are given in **Appendices B.2** and **B.3**. It should be noted that

for the reductions at lower H_2 gas concentrations in **Figure 4.11(a)** to **(c)**, a sudden slight drop in the concentration of Fe was observed with the emergence of $FeTiO_3$. This decrease in the Fe concentration is to compensate the jump of $FeTiO_3$ concentration from zero to the amount (~5wt%) which is above the detection threshold of the ND method.

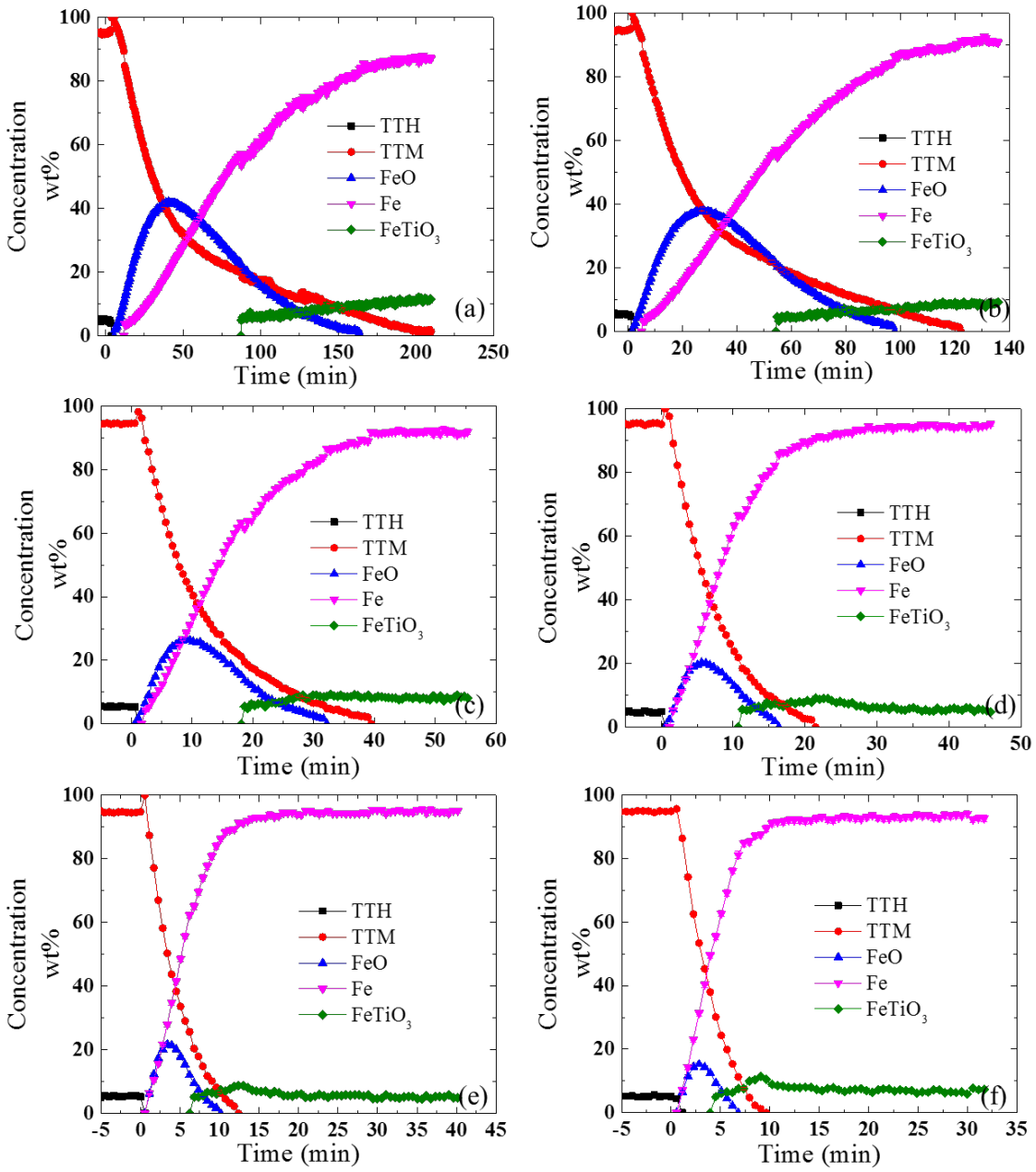

***Figure 4.11** – Concentration curves for each crystalline phase measured by in-situ ND at the Wombat beamline, during reduction of Ar-sintered pellets at a flow of 250 ml/min at 1223 K in various H_2-Ar gas mixtures. (a) 5vol% H_2, (b) 10vol% H_2, (c) 25vol% H_2, (d) 50vol% H_2, (e) 75vol% H_2, and (f) 100vol% H_2*

The production rate of metallic Fe at each different H_2 gas concentration and temperature are indicated in **Figures 4.12(a1)** to **(a3)**. At each temperature the generation of metallic Fe

progressed faster with increasing H_2 gas concentration. In the same manner as before, the reciprocal of each τ ($1/\tau$) is plotted against the respective H_2 gas concentration in **Figures 4.12(b1)** to **(b3)**. In each case this gives a linear relationship passing through the origin. This shows that at each temperature, the generation of metallic Fe is directly proportional to the delivered flow of H_2 gas.

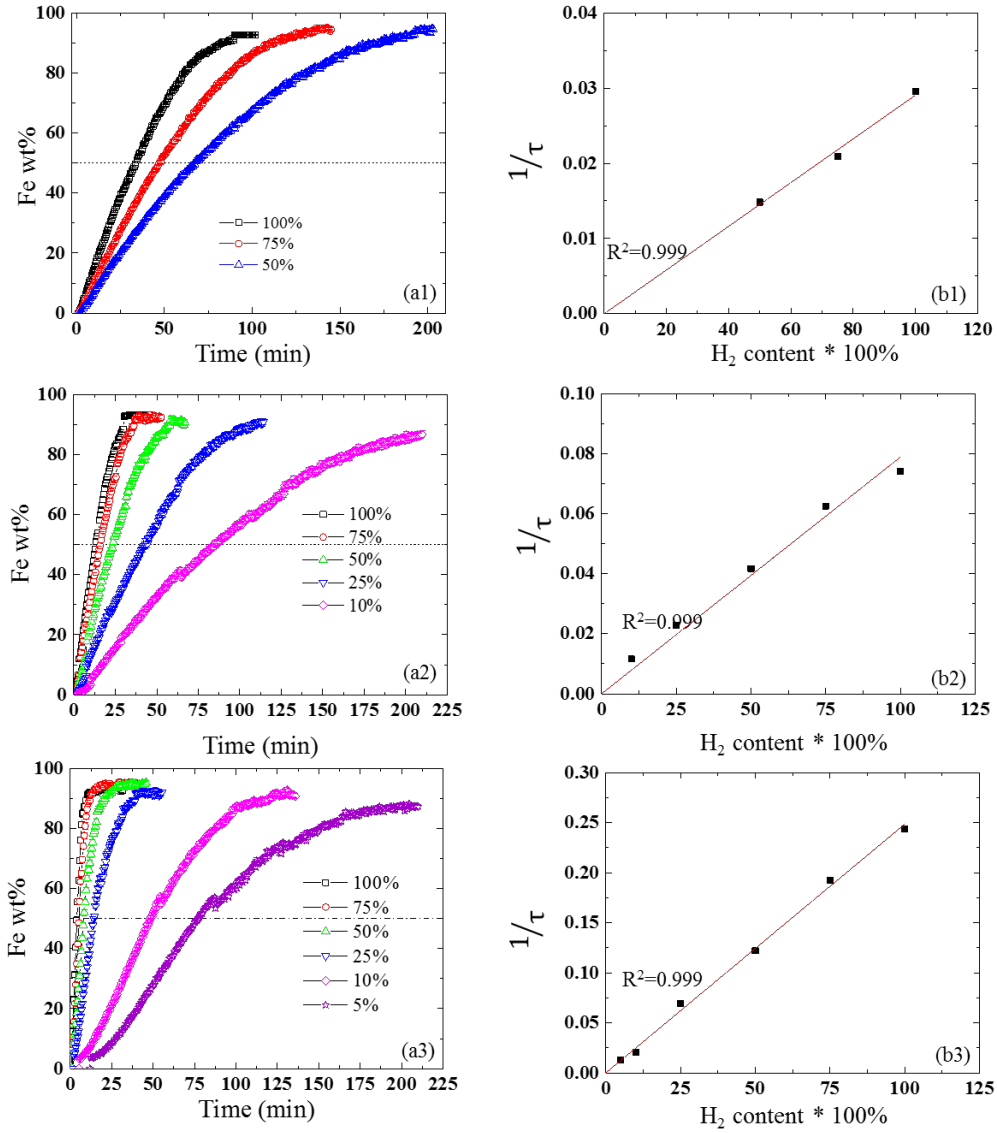

***Figure 4.12**–(a) The effect of H_2 gas concentration on the production rate of metallic Fe during reduction of Ar-sintered pellets at a flow of 250 ml/min gas mixture with different H_2 gas concentrations at (a1) 1023 K, (a2) 1123 K, and (a3) 1223 K. The dashed line indicates 50wt% metallic Fe. (b) The linear relationship between $1/\tau$ and H_2 gas concentration at (b1) 1023 K, (b2) 1123 K, and (b3) 1223 K (Results obtained from ND experiments performed at the Wombat beamline)*

Comparisons of the evolution of each crystalline phase at each temperature and H_2 gas concentration are shown in **Figure 4.13**, where the *x*-axis is normalised time (t/τ). As for the comparison among flow rates, most of the phase concentration curves are similar across all

different H_2 gas concentrations at each temperature. However, some differences can be observed for both the TTM phase and FeO at 1223 K, as well as for $FeTiO_3$ at both 1123 K and 1223 K. A discussion of these observations is presented later in **Section 7.3**.

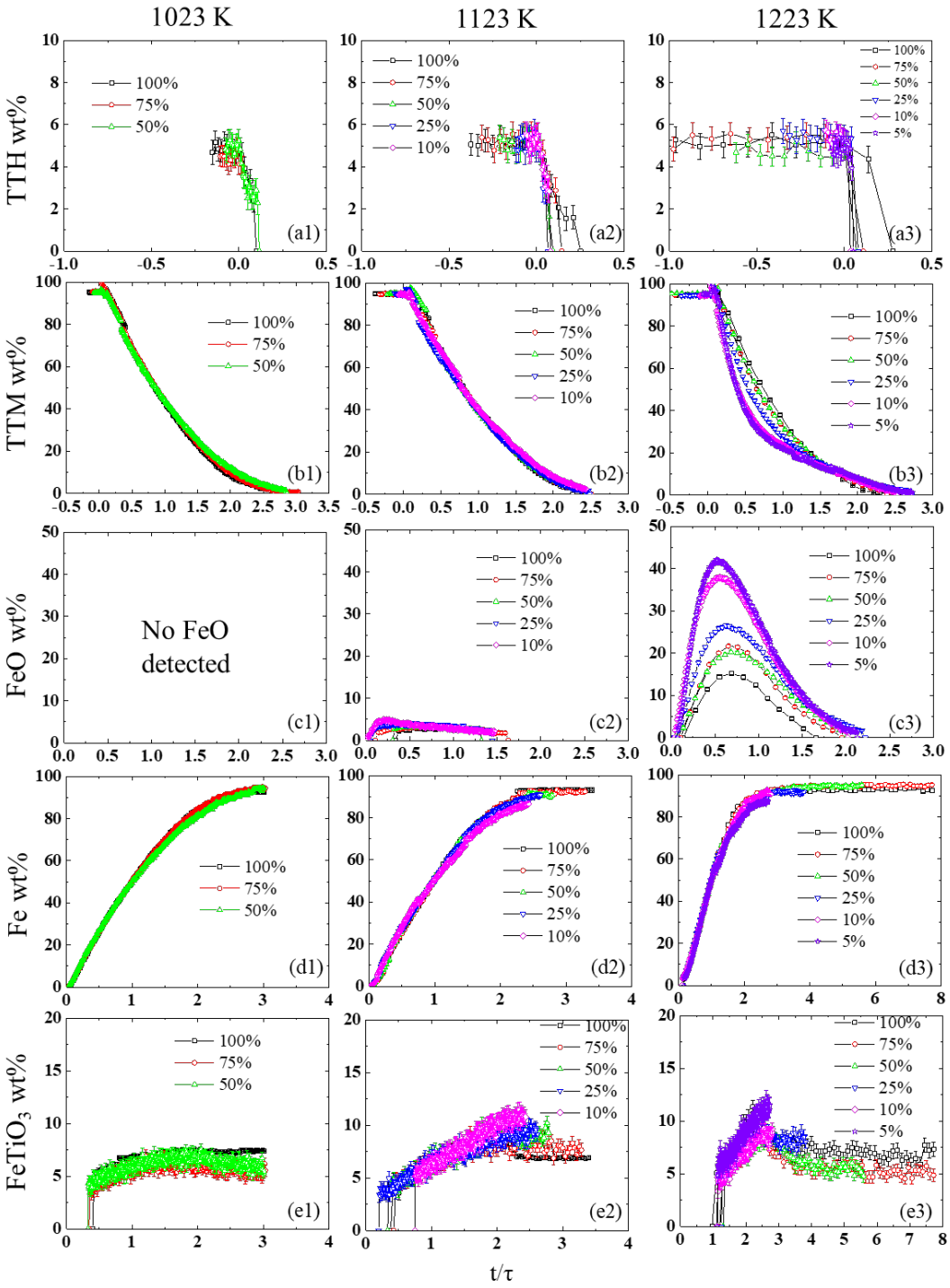

***Figure 4.13**– The evolution of each crystalline phase during reduction of Ar-sintered pellets in a 250 ml/min flow gas at different H_2 gas concentrations at each temperature. These data are plotted in single coordinates with normalised dimensionless x-axis (t/τ) at (1) 1023 K, (2) 1123 K and (3) 1223 K. Note that the reductions started at $t/\tau=0$ (a) TTH, (b) TTM, (c) FeO, (d) Metallic Fe and (e) $FeTiO_3$ (Results from in-situ ND performed at the Wombat beamline)*

4.2.3 The effect of temperature on phase evolution

Figures 4.12 and **4.13** also allow a comparison of the effects of temperature on the phase evolution. As illustrated in **Figure 4.12**, the generation of metallic Fe under a similar condition was faster with increasing temperatures. In **Figure 4.13**, ~5wt% TTH phase in the pellets was consumed rapidly at the beginning of reduction in all conditions. However, temperature significantly affected the evolution of TTM, and especially FeO. With decreasing temperature, the maximum FeO concentration decreased, and at 1023 K there was no FeO detected. Moreover, it seems that the maximum $FeTiO_3$ concentration also increased slightly with increasing temperatures.

4.2.4 Limitation of *in-situ* ND measurements

The limitation of the measurement gives an idea of the pedigree of the phase concentration data in the *in-situ* ND. As observed in **Figure 4.7** and **Figure 4.11**, the final products of the *in-situ* ND reduction experiments were only metallic Fe and $FeTiO_3$. Specifically, at the completion of the experiments, on average ~90wt% metallic Fe and 10wt% $FeTiO_3$ presented in the reduced pellets. However, based on the conservation of the elements Fe and Ti in the pellets during reduction, ~78wt% metallic Fe and 22wt% $FeTiO_3$ are expected in the reduced pellets at the completion of experiments. In addition, for almost all the concentration curves obtained, when TTM was no longer detected, the concentration of metallic Fe still experienced a slight increase while that of $FeTiO_3$ decreased. This might indicate that $FeTiO_3$ is likely to be further reduced to metallic Fe, but without the detection of other Ti-containing phases (TiO_2 and PSB).

In **Figure 4.14**, an example of an *in-situ* ND pattern is shown for Ar-sintered pellets near the completion of reduction (X=~93%). The pattern was obtained at 1223 K (as ND measurements were not obtained during cooling). It clearly shows that only the peaks of metallic Fe and $FeTiO_3$ could be distinctively identified in the ND diffraction at this reduction degree. No other Ti-containing phases (TiO_2 and PSB (ferro-PSB, Fe_2TiO_5 – $FeTi_2O_5$)) could be observed above the background signal at this time.

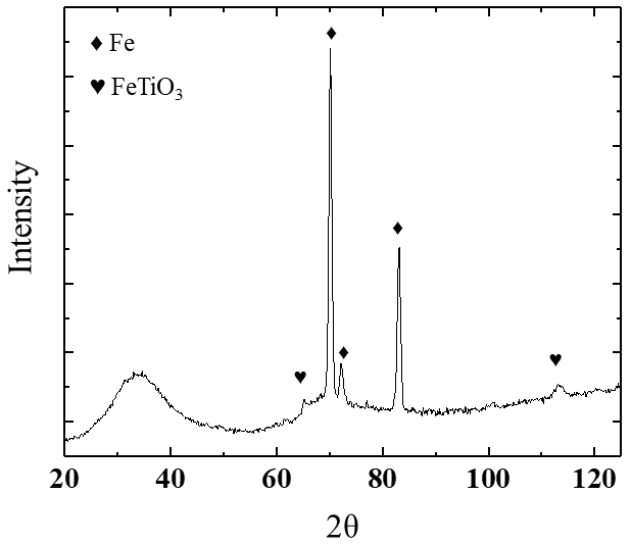

Figure 4.14- *A typical in-situ ND pattern obtained from Ar-sintered pellets reduced to X=~93%. The pattern was obtained at 1223 K at a flow of 250 ml/min 100vol% H_2 gas at the Wombat beamline.*

Nevertheless, crystalline TiO_2 and PSB (ferro-PSB, Fe_2TiO_5 – $FeTi_2O_5$) were observed for some fully reduced pellets determined by *ex-situ* XRD (**Figure 4.3**). These fully reduced pellets were obtained from the TGA reduction experiment after cooling to room temperature, as outlined in **Section 3.3**.

It seems that not all Ti-containing phases (such as TiO_2 and PSB (ferro-PSB, Fe_2TiO_5 – $FeTi_2O_5$)) are accounted for in the ND measurement. The principle reason for this could be a that the small amounts of these phases are not distinguishable above the background noise level of the ND measurement. The scattering background of a typical ND pattern is generally higher than XRD. The high incoherent neutron-scattering cross section of H_2 gas increases the background level of the ND measurements [165], thus reducing the signal to noise ratio. In addition, the ND measurements also gave broad peaks due to instrument broadening. Such broad peaks prevented an accurate calculation of the lattice constant. There is a possibility that the TiO_2 and PSB (ferro-PSB, Fe_2TiO_5 – $FeTi_2O_5$)) may have formed during cooling of the TGA experiments. This is thought to be unlikely, as the initial sample cooling was reasonably rapid, with the sample temperature falling from 1443 K to < 1223 K within 30 minutes of the conclusion of the reduction reaction.

.

In **Section 4.2**, the phase evolution obtained from the *in-situ* ND measurements for the Ar-sintered pellets is described. A discussion and analysis of these data is presented in **Chapters 7** and **8**.

4.3 Morphology development during H_2 gas reduction of Ar-sintered pellets: Results from quenching experiments

In this section, results of microscopy on the microstructure of the pellets at various stages during the reduction reaction from 1023 K to 1223 K are reported. These pellets were obtained from quenching experiments using a TGA system at UOW as outlined in **Subsection 3.4.1**. At each temperature, partially reduced pellets were quenched at reduction degrees of approximately X=~20%, 50%, 80%, and fully (maximum reduction degree as indicated in **Figure 4.2**), and then characterised to reveal their morphological evolution. These pellets were reduced under an equivalent condition as those reduced in the ND measurements. This is confirmed by a comparison of the reduction degrees of these pellets to those obtained from the ND reduction experiments (using equations **3.3** and **3.4**). The result is shown in **Figure 4.15**, which indicates a close agreement between the two experiments.

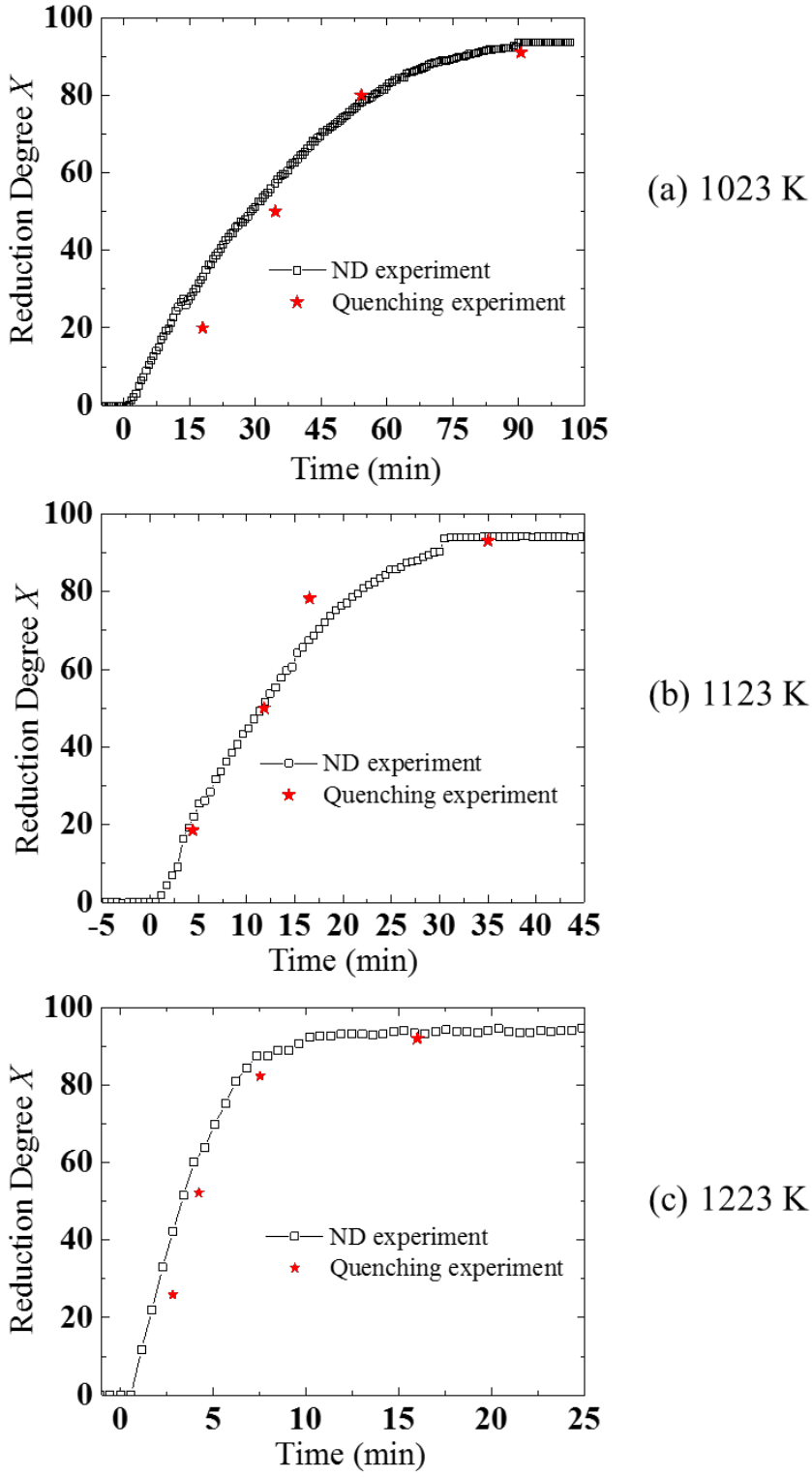

Figure 4.15 *- Comparisons of the reduction degrees of the quenched pellets to those obtained from the ND reduction experiments (equations **3.3** and **3.4**) using 100vol% H_2 gas at different temperatures (a) 1023 K, (b) 1123 K and (c) 1223 K. The quenching experiments were performed in a TGA system at a flow of 1 L/min H_2 gas at UOW. The flow rate for the ND reduction experiments at Wombat beamline is 250 ml/min*

4.3.1 Macro-morphology of the partially reduced pellets at each temperature

Optical images that illustrate cross-sections of the unreduced, partially reduced, and fully reduced Ar-sintered pellets at each temperature are shown in **Figure 4.16**. A dark core and a bright shell were observed within each partially reduced pellet, although the interface became less clear with either increasing reduction degree at each temperature, or with decreasing temperature at similar reduction degree.

Before reduction, the morphology of the Ar-sintered pellet (X=0%) was homogeneous. Note that the bright spots in the images is believed to be caused by the porosity in the pellets unfilled with resin or particles pulled out during grinding/polishing. For the X=~20% pellets reduced at 1223 K, a pellet-scale interface was observed separating two parts: a dark core and a very thin bright shell. However, this interface was not clearly observed in the X=~20% pellets reduced at 1023 K or 1123 K. For the X=~50% pellets at all temperatures, a pellet-scale interface was observed, which had moved closer to the pellet centre than seen in the X=~20% pellets. For the X=~80% pellets reduced at 1023 and 1123 K, the inner core and outer shell could still be vaguely distinguished, but not at 1223 K. For the fully reduced pellets, a homogeneous morphology was observed throughout the whole pellets. However, they presented as significantly brighter than the original unreduced pellets.

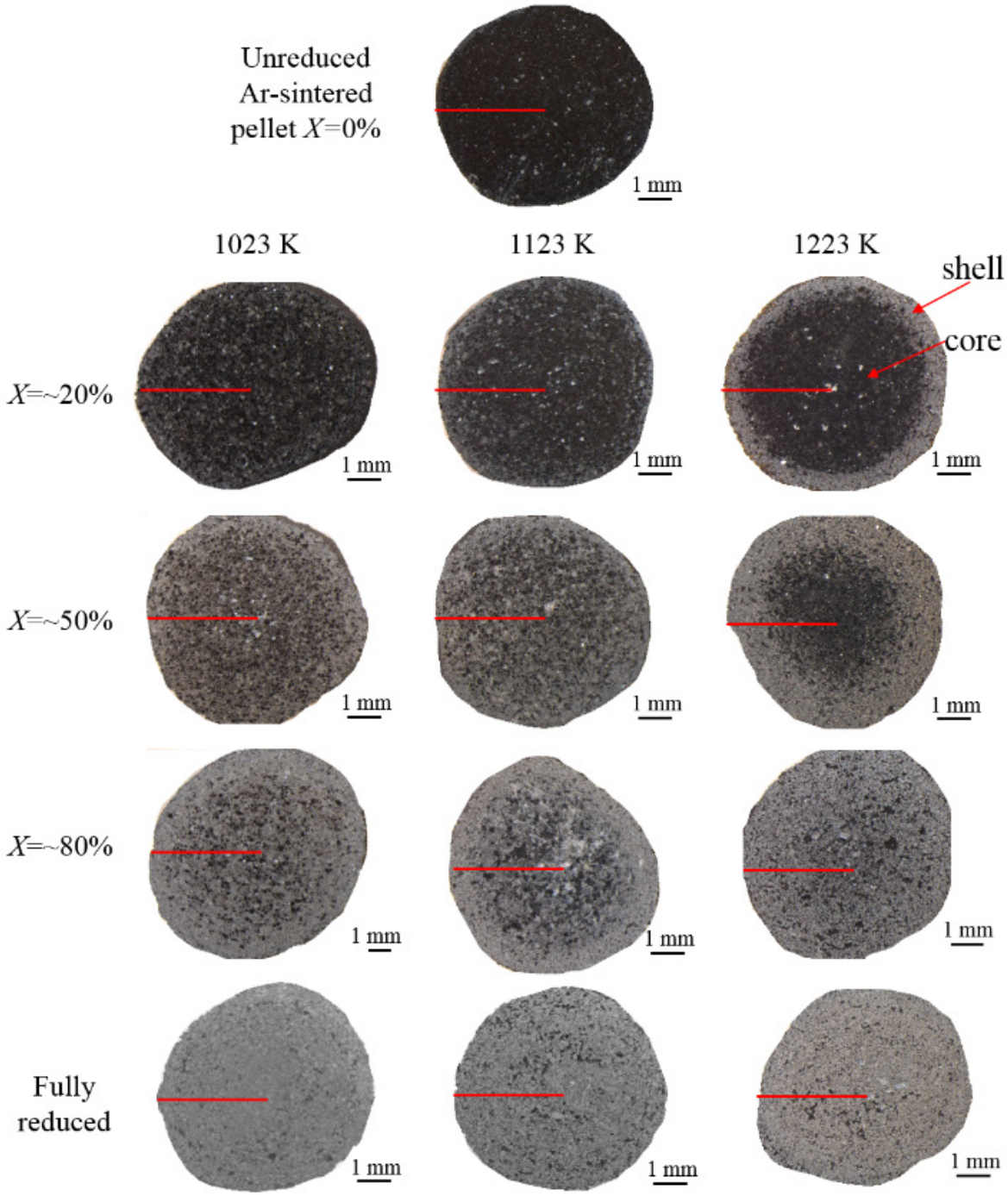

Figure 4.16– *Optical image showing macro-morphologies of the unreduced, partially reduced and fully reduced pellets. The partially and fully reduced pellets were obtained by reducing the Ar-sintered pellets in a flow of 1L/min 100vol% H_2 gas at 1023K, 1123 K and 1223 K in the TGA system at UOW. The red lines in each plot indicate the areas where EDS-line scans were conducted.*

4.3.2 Pellet-scale phase determination of the reduced pellets

EDS-line scans were applied to identify the phases in the bright shell and dark core distinguished in **Figure 4.16**. The EDS scans were conducted along a line from the pellet surface to pellet centre for each investigated pellet, as indicated by the red lines in **Figure 4.16**. These results obtained along the line were expressed as an atomic% O/Fe ratio, and plotted as a profile along the scanned line. EDS analyses of mineral standards of Fe_3O_4, FeO and metallic Fe were used to validate the atomic% O/Fe ratio profile, as established in **Subsection 3.5.2**.

EDS-line scan data from an unreduced Ar-sintered pellet (X=0%) is shown in **Figure 4.17**. The black square symbols indicate the obtained atomic% O/Fe ratio at each point along the line. The three black solid lines indicate the atomic% O/Fe ratio from the corresponding mineral standard. A red dashed line is drawn to highlight clustering in the measured data. These notations are also used in all the following figures showing the results of EDS-line scans. In the unreduced pellet, the atomic% O/Fe ratio was constant at all the positions along the line, and showed a value close to that from the mineral standard of Fe_3O_4. This is consistent with TTM being the main phase in the Ar-sintered pellets prior to reduction. It should be noted that some data scatter at higher atomic% O/Fe ratio is observed in this figure, and also in all the following figures associated with the results of the EDS-line scan. This data scatter might result from the voids between the particles in the pellets, which are filled with epoxy resin. If a scan point sits in the regions of the epoxy resin filled voids, then this point exhibited a higher O atomic% and lower Fe atomic%, resulting in a higher atomic% O/Fe ratio than a point located wholly within a particle. It should also be noted that the electron beams from the SEM-EDS analysis interact with the electron clouds of the atoms, hence the EDS analysis is also not as accurate for light elements with fewer electrons (such as O).

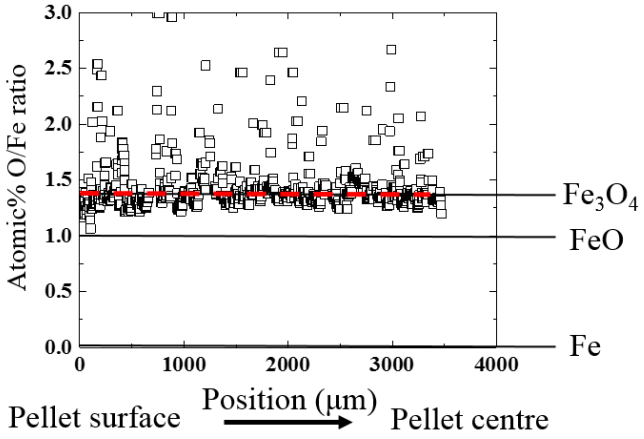

***Figure 4.17** – Atomic% O/Fe ratio profile of a cross-sectioned Ar-sintered pellet prior to reduction, measured by EDS-line scan*

The results of EDS-line scan from partially and fully reduced pellets at 1023 K, 1123 K and 1223 K are shown in **Figure 4.18**, **Figure 4.19**, and **Figure 4.20** respectively. It was found that at all temperatures, a similar trend in the change of the atomic% O/Fe ratio profile in the pellets during reduction was observed. The key features were most pronounced at 1223 K, and as such, these results are described below.

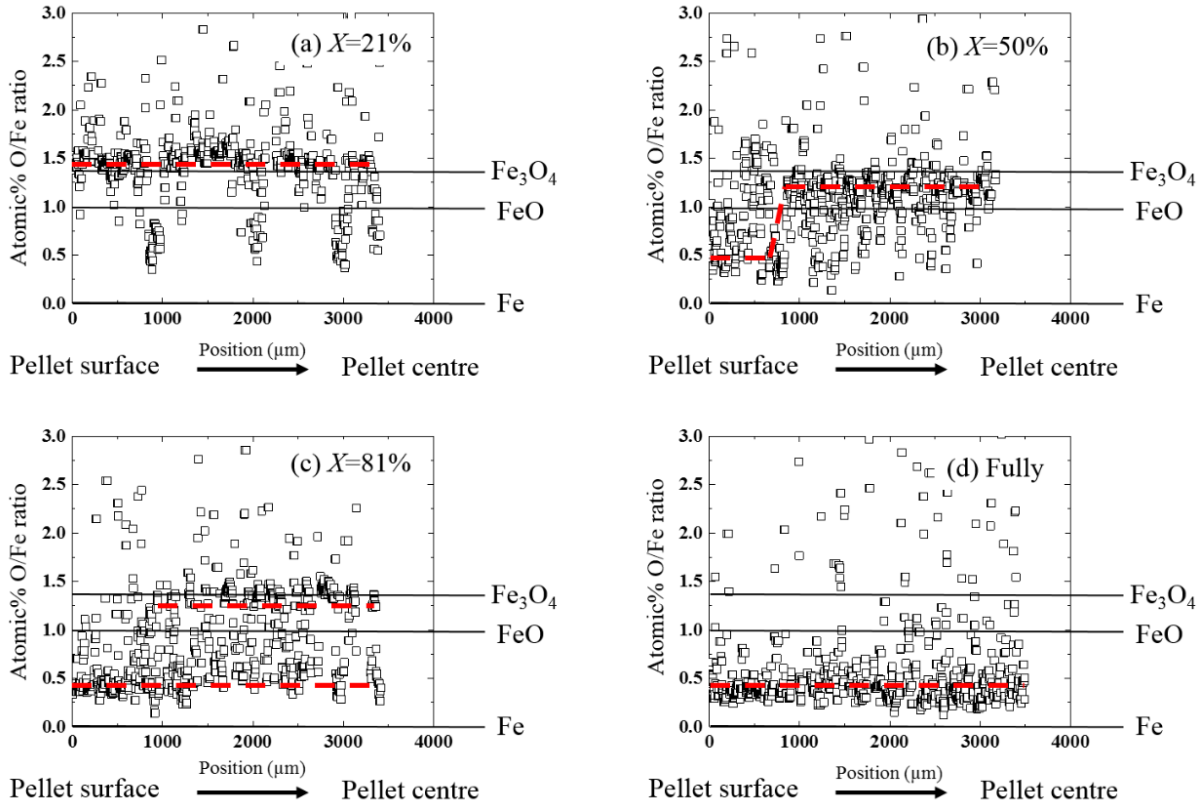

Figure 4.18 *- Atomic% O/Fe ratio profile measured by EDS-line scan of each partially and fully reduced pellet from 1023 K. (a) X=21%, (b) X=50%, (c) X=81% and (d) Fully-reduced. The three black solid lines in each figure indicate the atomic% O/Fe ratio obtained from the mineral standards of Fe_3O_4, FeO and metallic Fe. A dashed red line is drawn to highlight the trend of each profile*

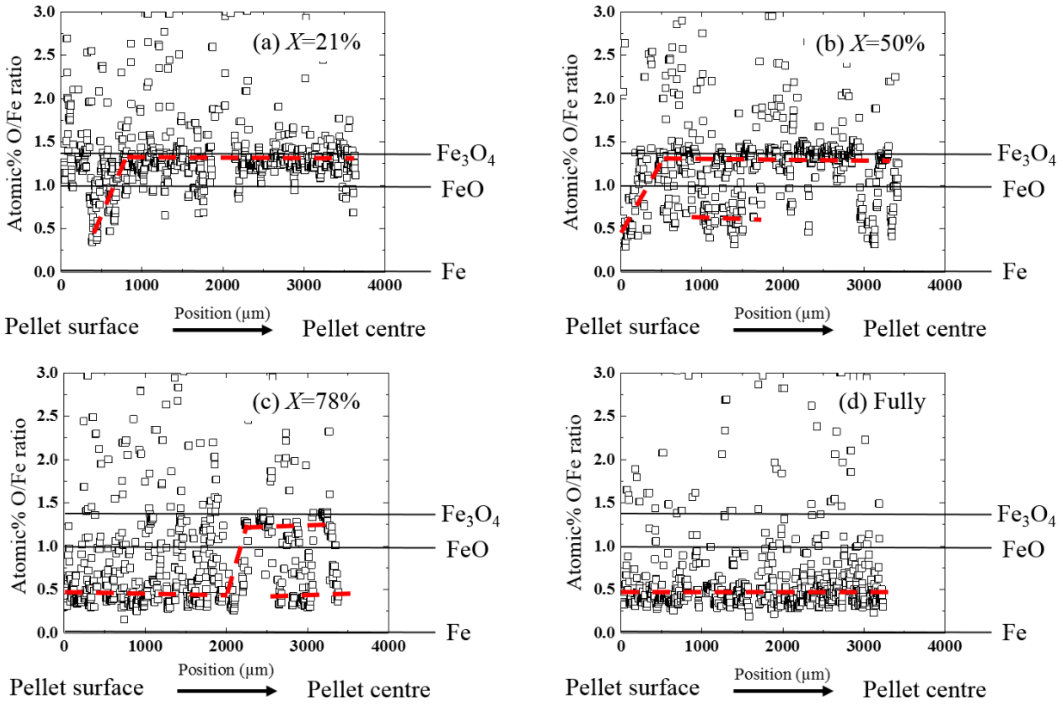

Figure 4.19 *- Atomic% O/Fe ratio profile measured by EDS-line scan of each partially and fully reduced pellet from 1123 K. (a) X=21%, (b) X=50%, (c) X=78% and (d) Fully-reduced. The three black solid lines in each figure indicate the atomic% O/Fe ratio obtained from the mineral standards of Fe_3O_4, FeO and metallic Fe. A dashed red line is drawn to highlight the trend of each profile*

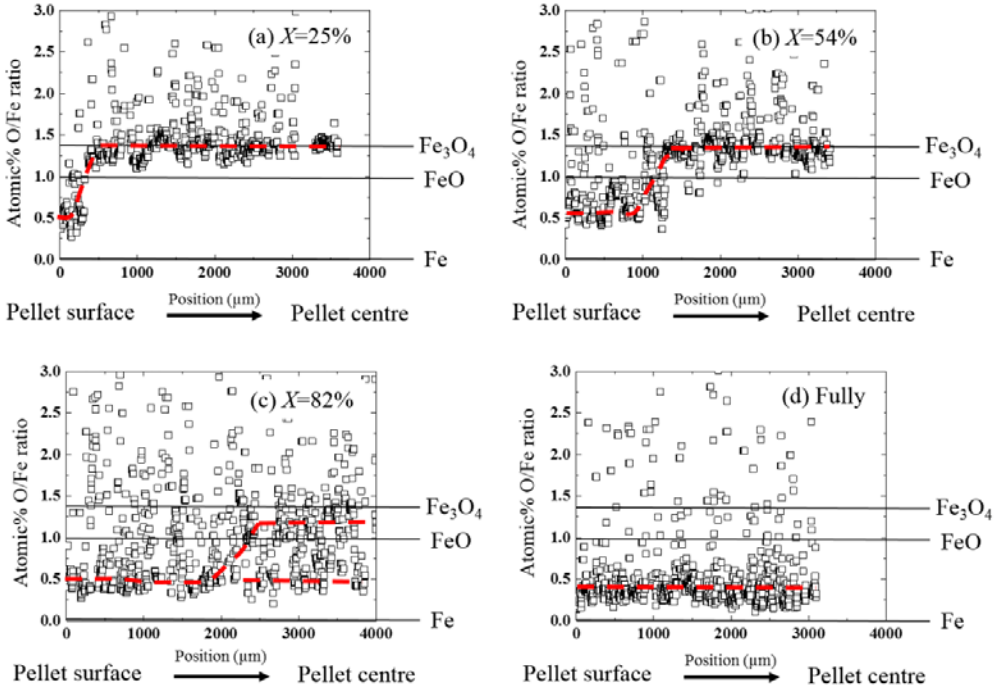

Figure 4.20 *- Atomic% O/Fe ratio profile measured by EDS-line scan of each partially and fully reduced pellet from 1223 K. (a) X=25%, (b) X=54%, (c) X=82% and (d) Fully-reduced. The three black solid lines in each figure indicate the atomic% O/Fe ratio obtained from the mineral standards of Fe_3O_4, FeO and metallic Fe. A dashed red line is drawn to highlight the trend of each profile*

The results from EDS-line scans of pellets reduced at 1223K are shown in **Figure 4.20**. For the fully reduced pellet shown in **Figure 4.20(d)**, the atomic% O/Fe ratio has a constant value of ~0.4 along the whole line from the pellet surface to pellet centre. This ratio is slightly larger than that measured from the mineral standard of metallic Fe (zero) suggesting that unreduced oxides (such as $FeTiO_3$, TiO_2 or PSB) are closely mixed with reduced metallic Fe. In addition, it might also result from the high oxygen level in the epoxy resin filled voids between the particles.

The results of the X=25% pellet is shown in **Figure 4.20(a)**. The pellet surface (at positions < ~600 μm) has an atomic% O/Fe ratio ~0.5. This value is close to that obtained throughout the completely reduced pellets (~0.4, **Figure 4.20(d)**), implying that the pellet surface has already been reduced to metallic Fe by this time. Moving inwards towards the centre of the pellet, a sharp transition in the atomic% O/Fe ratio is seen at ~600 μm, where it increases to ~1.4. This value is similar to that in the unreduced Ar-sintered pellets (**Figure 4.17**), indicating that the inner areas of the X=25% pellet remain unreduced.

For the X=54% pellet shown in **Figure 4.20(b)**, similar atomic% O/Fe ratios are observed at the surface and centre, to those found in the X=25% pellet. This again implies that the surface has been reduced to metallic Fe, while the centre remains unreduced. However, in the case of X=54% pellet, the sharp transition occurs closer to the centre the pellet, at ~1000 μm, which is consistent with this reaction interface moving inwards over time.

For the X=82% pellet shown in **Figure 4.20(c)**, the transition between pellet surface to pellet centre is not as sharply defined. Metallic Fe is again likely to be present at the pellet surface (< 2000 μm), with the atomic% O/Fe ratio being slightly below 0.5. However, at positions > 2000 μm, there is a spread of data which is bounded by the two trend lines shown. In this central region, some scan points presented an atomic% O/Fe ratio of ~1.2, which corresponds to a possible mixture of TTM and FeO. However, other points showed a much lower ratio of ~0.5, which can only be achieved if metallic Fe is present. This data scattering implies the transition interface is no longer distinct, and instead localised metallisation might be occurring at the pellet centre.

Overall the atomic% O/Fe ratio profiles obtained at 1223K are generally consistent with a single interface shrinking core process, where metallic Fe is initially generated at the pellet

surface and the reaction interface then moves inwards to the pellet centre. However, at the later stages of the reduction, the shrinking core interface is not clearly apparent and more complex localised reductions seem to occur instead.

The atomic% O/Fe ratio line-scans for pellets reduced at 1023 K and 1123 K show similar features to those at 1223 K, but with more data scatter so that the transition interface was less well-defined. The data scatter is probably due to a broadening of the interface at lower temperature, and to complex reductions in the particles, which will be displayed later in back-scattered SEM images of particle morphologies at different temperatures.

4.3.3 Particle morphology of the reduced pellets at each temperature

In this subsection, back-scattered SEM images are reported to show the evolving particle-scale micro-morphologies of phases during reduction. Based on these observations, schematic graphics have then been generated which illustrate the main morphological features and their evolutions over time. In addition, summary tables are produced to list the key features observed in the particle morphologies of the 'green' pellets, unreduced Ar-sintered pellets, partially reduced pellets and completely reduced pellets at each temperature. It should be noted that the properties of the 'green' pellets are similar to those in the as-received ironsand, as the generation of 'green' pellets have not been through any chemical treatment such as high temperature reduction/oxidation (**Subsection 3.2.2**).

1. As-received ironsand and unreduced Ar-sintered pellets

The morphology of the as-received NZ ironsand was characterised by light microscopy and SEM-EDS analysis. In both the light microscopy image (**Figure 4.21(a)**) and the back-scattered SEM image (**Figure 4.21(b)**), two types of particles are present in the as-received ironsand. One type of particle appears uniform throughout, whereas the other is non-uniform in character and contains intrusions in the form of lamellae. In both images, the uniform particles are a similar colour to the regions surrounding the lamellar structures in the non-uniform particles. However, under light microscopy, the lamellar structures are brighter than the surrounding regions. While they appear darker in the back-scattered SEM image, indicating a lower electron density (also a lower average atomic number) and indicative of higher levels of oxygen. The elevated oxygen content in the lamellae structure was confirmed by EDS point

analysis given in **Table 4.1** of the points marked in **Figure 4.21(b)**. The matrix composition in both the uniform and non-uniform particles (points 1 and 2 respectively) are both determined to contain ~24wt% O, 66wt% Fe and 4.4wt% Ti. This composition is broadly consistent with TTM. By contrast, the lamellar structures had significantly higher Ti content (~16wt%) and lower Fe content (~54wt%) (see points 3 and 4 in **Table 4.1**). These lamellae are expected to be TTH. Other elements such as Al and Mg were also observed in the matrix but were less concentrated in the lamellae.

It is observed that most of the particles are the uniform particles in the pellets, while the non-uniform particles account for ~10% of the total particle population. This estimated value was obtained from particle counting within a 5x optical image, taken at a randomly selected position on the cross section of a 'green' pellet. All incomplete particles at the edge of the image were excluded from the counting, as were a small number of dark silica-like gangue particles or particle tails smaller than ~10 μm. The remaining particles were all clearly identifiable as either uniform particles or non-uniform particles. A total of 203 particles were counted, of which 22 particles were non-uniform, and 181 were uniform.

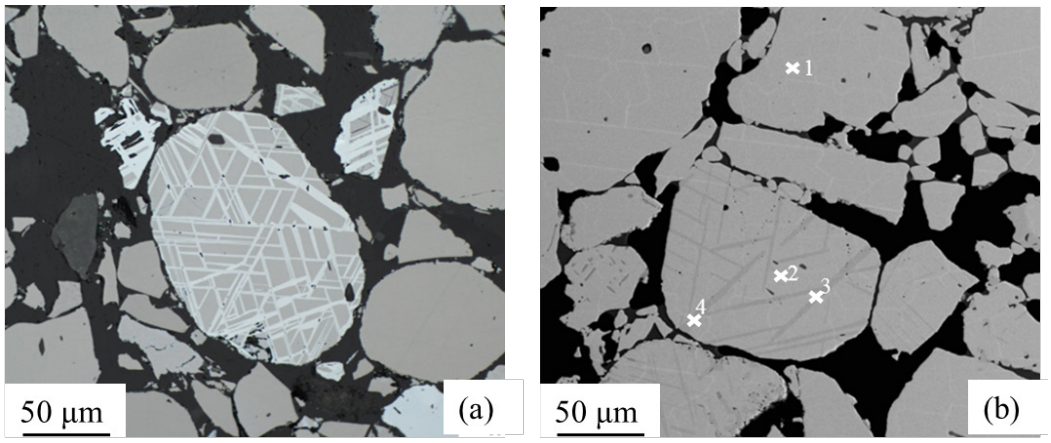

Figure 4.21 *– Micrographs of the as-received NZ titanomagnetite ironsand. (a) Light microscopy and (b) back-scattered SEM image. Note this figure has already been published in a paper from the author [162]*

***Table 4.1**– EDS point analysis (wt%) from the numbered positions given in the SEM micrograph of the as-received ironsand (**Figure 4.21(b)**). Note this table has already been published in a paper from the author [162]*

	points	O	Fe	Ti	V	Al	Mg	Mn	O/(Fe+Ti)
wt%	1	24.4	66.0	4.4	0.3	2.5	2.0	0.5	0.3
	2	24.3	68.4	4.5	0.3	1.7	-	0.7	0.3
	3	27.7	54.0	16.0	0.4	0.6	1.0	-	0.4
	4	27.2	55.0	16.3	0.5	-	-	-	0.4
at%	1	51.1	39.6	3.1	0.2	3.1	2.7	0.3	1.2
	2	52.0	41.9	3.2	0.2	2.2	-	0.4	1.2
	3	55.7	31.0	10.7	0.2	0.7	1.4	-	1.3
	4	55.7	32.3	11.2	0.4	-	-	-	1.3

After sintering in Ar gas, there was no apparent change in element distribution in the pellets (shown in **Figure 3.6**). In addition, most of the particles in the Ar-sintered pellets remained uniform (see later in **Figure 4.23(a)** as an example).

Since the majority of the particles in the Ar-sintered pellets are uniform particles, the following schematics are only focused on the morphological evolution of these particles. On the other hand, the morphological evolution of the non-uniform particles is only described in the summary table at each temperature.

In the following pages, particle morphological evolution is reported for the Ar-sintered pellets obtained from the quenching reduction experiments at 1023 K, 1123 K, and 1223 K respectively. In each case, illustration of the results starts with a schematic graphic. This schematic graphic is constructed from the collection of representative back-scattered SEM images shown in **Appendices B.5** to **B.7**. The phases observed in the particle-scale back-scattered SEM images were initially identified by determining the elemental compositions using an SEM-EDS point analysis from specific representative images. An example is shown in **Figure 4.22**, with SEM-EDS point analysis data for the corresponding areas in the image listed in **Table 4.2**. Based on the analyses, it is concluded that, the grey areas indicate TTM, the light grey areas indicate FeO, and the bright areas indicate metallic Fe. Utilising this phase identification approach, key features that represent the changes in the particle morphologies during reduction are summarised.

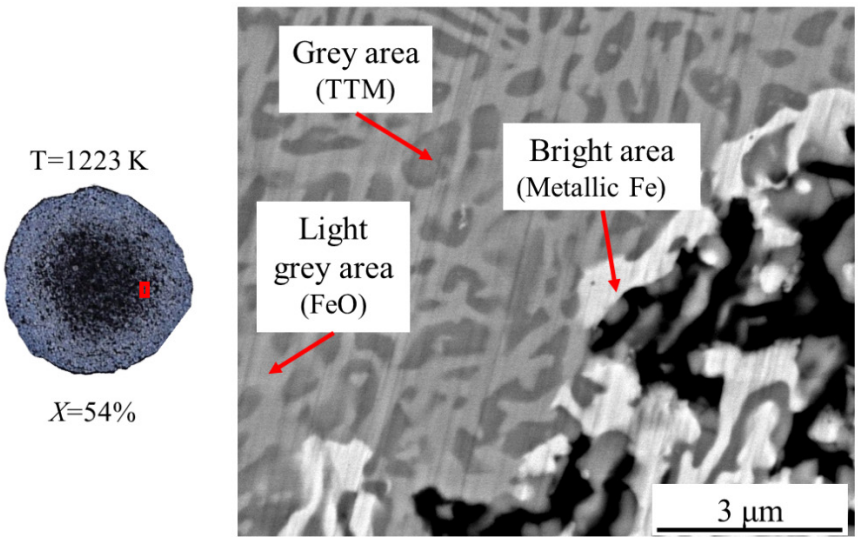

Figure 4.22 *—An example of back-scattered-SEM images of a representative particle depicting the different contrast of phases observed inside individual particles within partially reduced pellets. The representative particle is in the region of the pellet-scale reaction interface of the X=54% pellets reduced at 1223 K from quenching experiment by the TGA system at UOW*

Table 4.2 *– Atomic% of the corresponding areas shown in* ***Figure 4.22*** *obtained from the SEM-EDS point analysis to identify phases, each value is an average of three points for each feature*

Area	Fe	Ti	O	Mg	Al	Phase identification
Grey area	39.1	2.9	52.3	2.5	3	TTM
Light grey area	41.6	2.1	50.5	3.9	1.8	FeO
Bright area	68.8	3.1	20.5	4.8	3.3	Fe

Using the information in **Table 4.2**, different iron oxide phases were then identified in the back-scattered SEM images from their relative contrast. A selection of example images used as a key to illustrate the relationship between the schematic graphics and the original back-scattered SEM images are displayed in **Figure 4.23** and **Figure 4.24**. Here, TTM shows as a grey colour as in **Figure 4.23(a)**. In all cases, metallic Fe is generated from the particle surface to its centre, but the specific morphology is seen to vary with temperature. For example, at 1023 K (in **Figure 4.23(c)**), metallic Fe spots form a thin layer at the surface of the particles, while metallic Fe whiskers occupy the inner areas. However, at 1123 K (in **Figure 4.23(e)**), metallic Fe shows both a trellis structure at the particle surface and small whiskers at particle centre. Furthermore, at 1223 K (in **Figure 4.24(c)**), metallic Fe shows an intertwined channel-like structure

occupying almost the whole particle. It should be noted that following local reduction, the remaining residual oxides are illustrated as black. FeO is only observed in the particles reduced at higher temperatures. At 1123 K (in **Figure 4.23**(**d**)), FeO exhibits a fine and sparse trellis-like structure. However, at 1223 K (in **Figure 4.24**(**a**) and (**b**)), a network of broader FeO channels are seen to develop within the particles. The schematics of the particle morphology at each temperature and reduction stage seek to illustrate all of these features, making the actual particle morphological evolution simpler to be displayed. It should be noted that throughout the following graphics, if the total amount of a phase present increases as the reduction progresses, more of the corresponding features are added to the diagram.

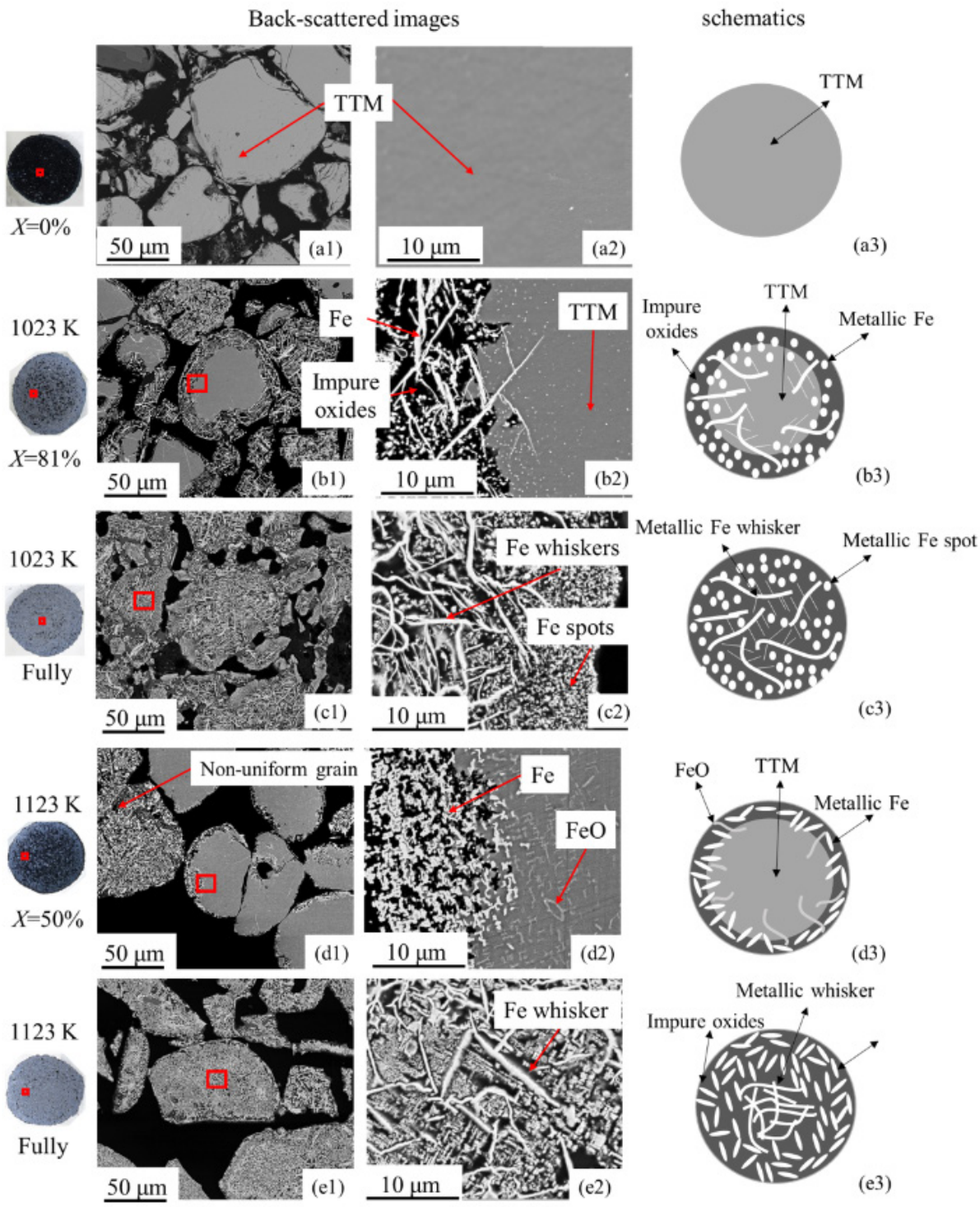

***Figure 4.23**- Examples illustrating the relationship between the schematic graphics constructed as a key to depict features of the particle morphologies, and the original back-scattered SEM images. (a) unreduced Ar-sintered pellet, (b) and (c) reduced pellets at 1023 K, and (d) and (e) reduced pellets at 1123 K. (1) shows the morphologies of the particles indicated at different areas in the corresponding pellets (at left) at lower magnification, (2) shows the morphologies of the areas as highlighted in (1) at higher magnification, and (3) shows the schematic graphics illustrating the features in (2)*

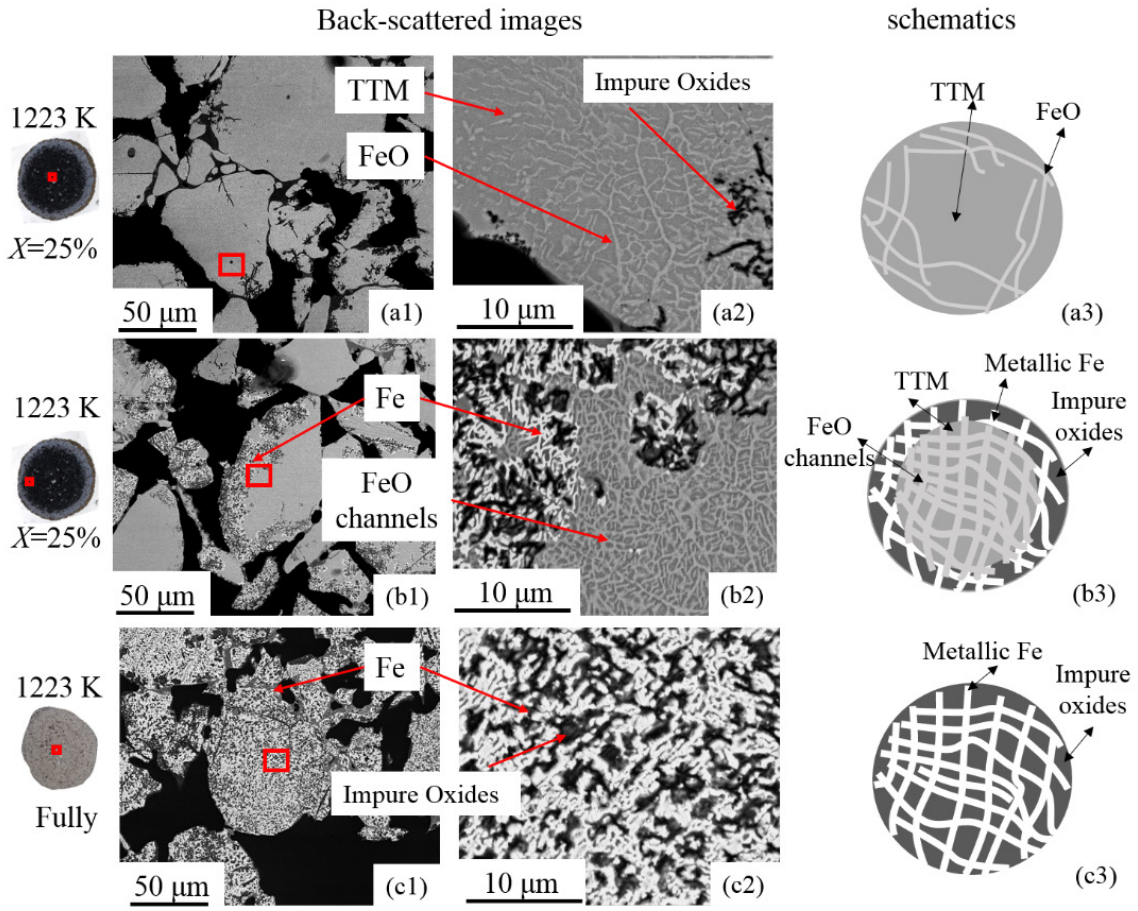

Figure 4.24 *- Examples illustrating the relationship between schematic graphics constructed as a key to depict features of the particle morphologies, and the original back-scattered SEM images of reduced pellets at 1223 K. (1) shows the morphologies of the particles indicated at different areas in the corresponding pellets (at left) at lower magnification, (2) shows the morphologies of the areas as highlighted in (1) at higher magnification, and (3) shows the schematic graphics illustrating the features in (2)*

2. Particle morphologies within pellets partially reduced at 1023 K

In **Figure 4.25**, a schematic graphic is shown which illustrates the morphological evolution of particles at different positions within the pellet during reduction at 1023 K (The original back-scattered SEM images from which this schematic has been constructed are shown in **Appendix B.5)**. As can be seen, metallic Fe is generated gradually from pellet surface to pellet centre, which is broadly consistent with the results obtained from the EDS-line scans shown in **subsection 4.3.2**.

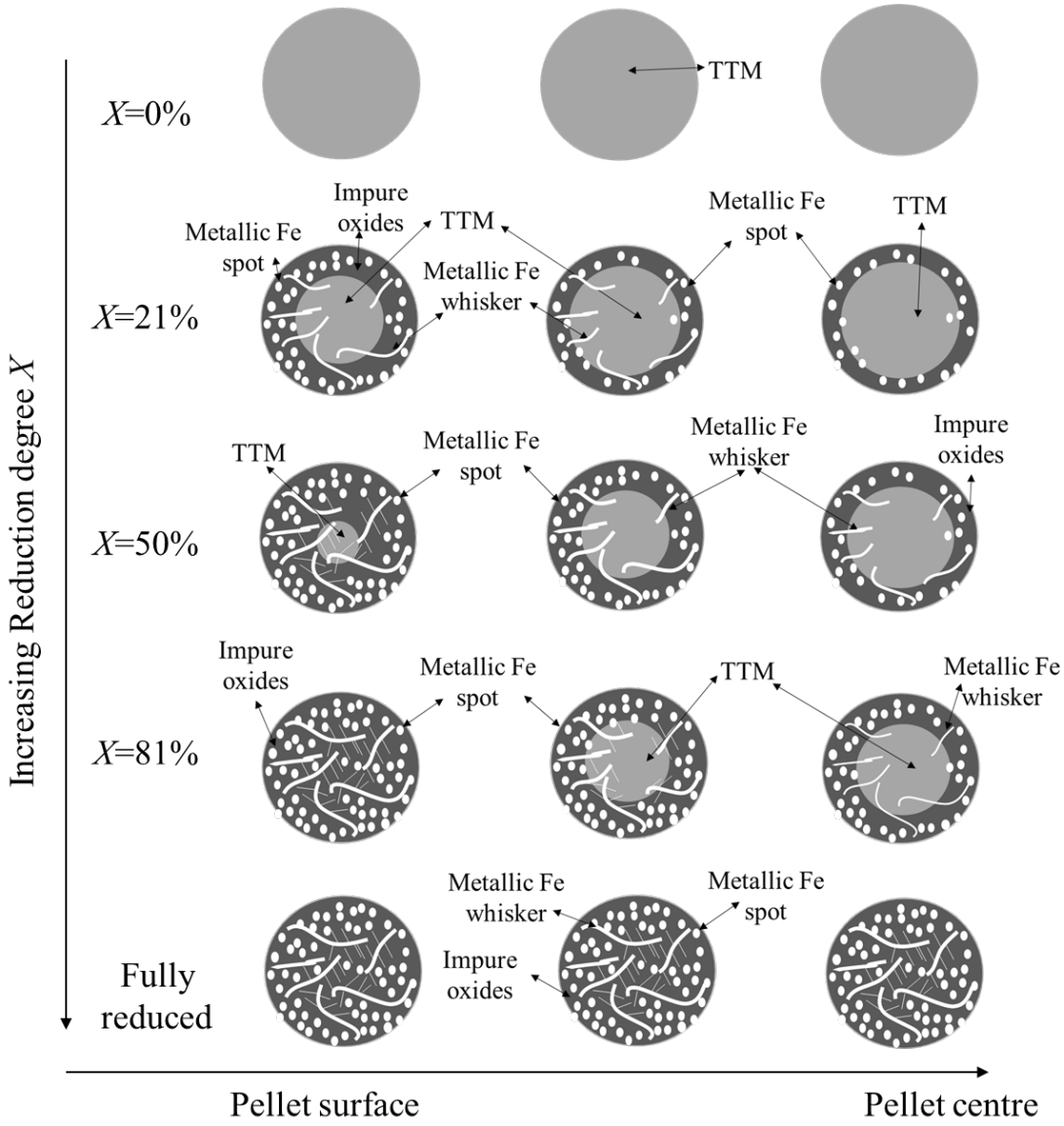

Figure 4.25– *Schematic graphic of particle morphological evolution during reduction of the Ar-sintered pellets at 1023 K*

Descriptions of the key particle-scale morphological features that observed during reduction at 1023 K are summarised in **Table 4.3**

***Table 4.3**– Summary of the main features of the particle morphologies in the 'green' pellets, unreduced Ar-sintered pellets and reduced pellets investigated at 1023 K*

Scale	'Green' pellets (Ground raw particles pelletised with 1wt% Bentonite)	Ar-sintered ('Green' pellets sintered in Ar for 2 hours at 1473 K)	Quenched from 1023 K, 100vol% H_2, 1 L/min			
			21%	50%	81%	Fully
Pellet	1. The morphologies of the particles are homogeneous.	1. There is no obvious change in the morphologies or elements distribution. TTM remains as the major phase in the particles.	1. It is difficult to observe a pellet-scale reaction interface.	1. A pellet-scale reaction interface is also not clear.	1. Similar to 50% #1, a pellet-scale reaction interface is vaguely observed.	1. The morphology of the pellet is homogeneous but shows brighter than that of the unreduced one.
Particle	2. The particle sizes are randomly distributed. 3. Most particles are smooth at the surface with a light grey colour. 4. Fine lamellar structure (enriched with Ti) can be observed in ~10% of the particles. 5. A small amount of silicate particles which are smaller than ~30 μm are present.	2. The size distribution of the particles is similar to 'Green' #2. 3. The morphologies are similar to 'Green' #3, but show evidence of sintering. 4. Fine lamellar structure which is enriched with Ti is also observed, similar to 'Green' #4.	2. The size distribution of the particles is similar to Ar-sintered #2. 3. In the surface of the particles at the pellet centre, metallic Fe is observed to form in the structure of spots directly from TTM. The generation of metallic Fe seems to follow the particle-scale shrinking core phenomenon. The unreduced TTM in the particle centre is similar to Ar-sintered #3. FeO is barely observed in the particles. 4. In the areas closer to pellet surface, a similar particle morphology is observed as in #3, with more metallic Fe spots generated and a smaller unreduced TTM core. Moreover, metallic Fe whiskers starts to be found at inner areas of the particle. 5. At the pellet surface, the particle morphology is similar to #4. However, more metallic Fe is generated, and the whiskers develops longer.	2, 3, 4 and 5 are similar to 21% #2, 3, 4, and 5 respectively, but with more metallic Fe observed in the particles. 6. In the pellets at X=21% and 50%, it was found that the non-uniform particles throughout the whole pellets are reduced much faster than the uniform particles. The generation of metallic Fe no longer follows the particle-scale shrinking core phenomenon. Instead, FeO is initially observed at the vicinity of the lamellae, and then metallic Fe is observed from FeO throughout the whole particle.	2, 3, and 4 is similar to 50% #2, 3, and 4 respectively, but with more metallic Fe observed in the particles. 5. At pellet surface, the particles are fully reduced to metallic Fe. At the particle surface, a thin layer of metallic Fe spots is observed. While at the particle inner areas, metallic Fe is observed in the structure of whiskers.	The morphologies of the fully reduced particles throughout the whole pellets are similar to 81% #5.

3. Particle morphologies within pellets partially reduced at 1123 K

In **Figure 4.26**, a schematic graphic is presented which illustrates the morphological evolution of particles at different positions within the pellet during reduction at 1123 K (The original back-scattered SEM images from which this schematic has been constructed are shown in **Appendix B.6)**. A key difference to the results reported in the previous section is that at 1123 K a fine structure of FeO was also observed. Moreover, metallic Fe was initially in the form of spots but gradually develop into short-sectioned trellises as reduction progressed. At the particle centre, metallic Fe whiskers were also observed.

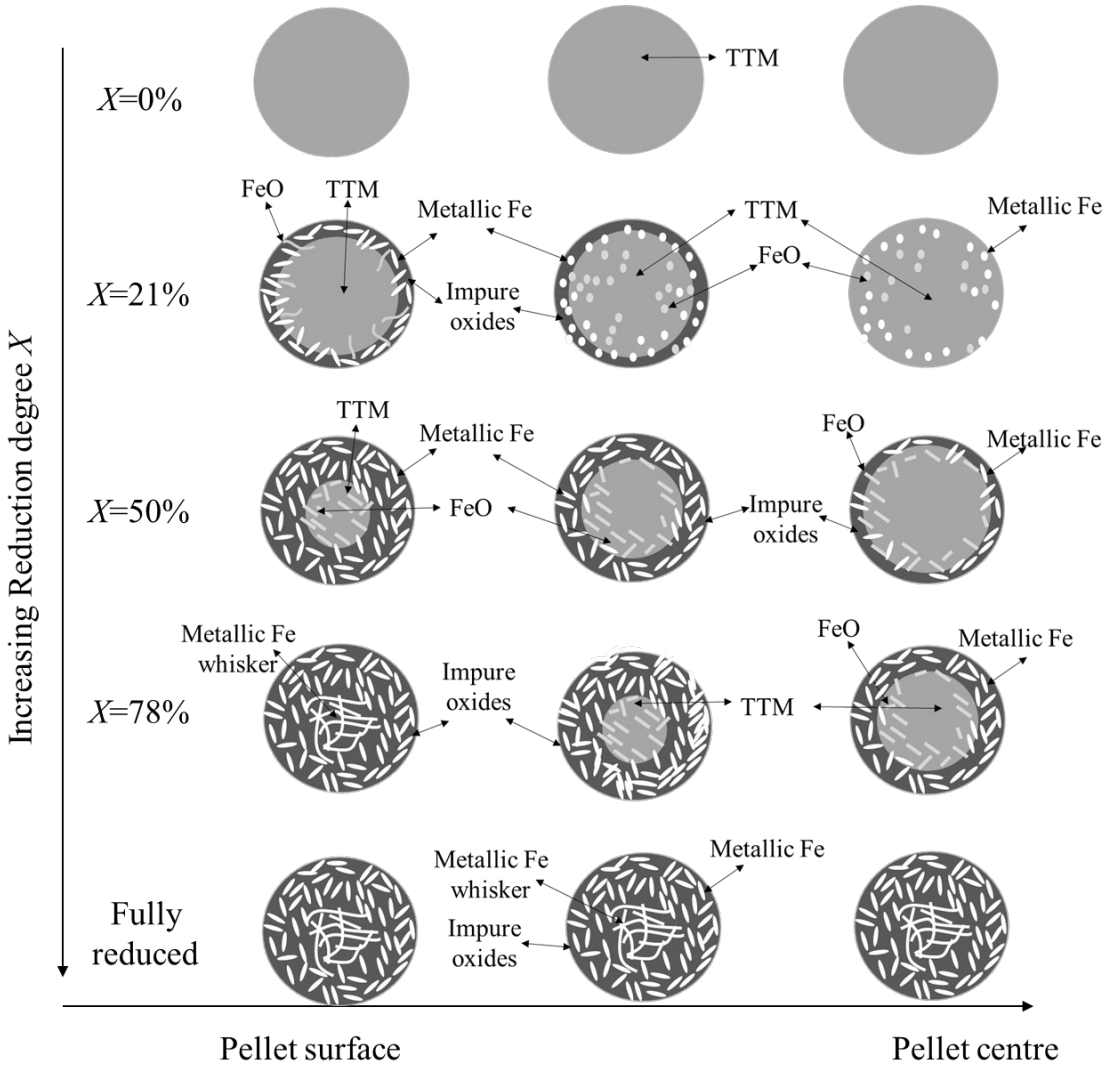

***Figure 4.26**- Schematic graphic of particle morphological evolution during reduction of the Ar-sintered pellets at 1123 K*

Descriptions of the key particle-scale morphological features that observed during reduction at 1123 K are summarised in **Table 4.4**.

Table 4.4 *- Summary of the main features of the particle morphologies in the 'green' pellets, unreduced Ar-sintered pellets and reduced pellets investigated at 1123 K*

Scale	'Green' pellets (Ground raw particles pelletised with 1wt% Bentonite)	Ar-sintered ('Green' pellets sintered in Ar for 2 hours at 1473 K)	Quenched from 1123 K, 100vol% H_2, 1 L/min			
			21%	50%	78%	Fully
Pellet	1. The morphologies of the particles are homogeneous.	1. There is no obvious change in the morphologies or elements distribution. TTM remains as the major phase in the particles.	1. It is difficult to observe a pellet-scale reaction interface.	1. A pellet-scale reaction interface is vaguely observed.	1. Similar to 50% #1, a pellet-scale reaction interface is vaguely observed.	1. The morphology of the pellet is homogeneous, but shows brighter than that of the unreduced one.
Particle	2. The particle sizes are randomly distributed. 3. Most particles are smooth at the surface with a light grey colour. 4. Fine lamellar structure (enriched with Ti) can be observed in ~10% of the particles. 5. A small amount of silicate particles which are smaller than ~30 μm are present.	2. The size distribution of the particles is similar to 'Green' #2. 3. The morphologies are similar to 'Green' #3, but show evidence of sintering. 4. Fine lamellar structure which is enriched with Ti is also observed, similar to 'Green' #4.	2. The size distribution of the particles is similar to Ar-sintered #2. 3. At the pellet centre, small FeO and Fe spots are observed. Both the generations of FeO and metallic Fe follow a particle-scale shrinking core phenomenon. The unreduced TTM shows a similar morphology as in Ar-sintered #3. 4. In the areas closer to pellet surface, a similar particle morphology is observed as in #3, with more metallic Fe and FeO observed and a smaller unreduced TTM core. 5. At the pellet surface, the particle morphology is similar to #4. However, Both the metallic Fe and FeO are observed to develop into small trellises.	2. Similar to 21% #2. 3, 4, and 5 is similar to 21% #5. However, as reduction progresses, more metallic Fe and FeO in the form of trellises are observed with a gradually shrinking unreduced TTM core. 6. Similar to 1023 K 50% #6, the non-uniform particles throughout the whole pellets are reduced faster than that of the uniform particles.	2, 3, and 4 is similar to 21% #2, 3, and 4. 5. At the pellet surface, the particles are fully reduced to metallic Fe. Trellises metallic Fe formed a layer at the particle surface, while in the inner areas of the particles, metallic Fe whiskers are observed. However, these whiskers are found to be smaller in size as observed at 1023 K.	The morphologies of the fully reduced particles throughout the whole pellets are similar to 78% #5.

4. Particle morphologies within pellets partially reduced at 1223 K

In **Figure 4.27**, a schematic graphic is shown which illustrates the morphological evolution of particles at different positions within the pellet during reduction at 1223 K (The original back-scattered SEM images from which this schematic has been constructed are shown in **Appendix B.7)**. At this temperature, FeO was observed to form a network of broader channels. Moreover, the subsequent generation of metallic Fe from FeO seems to follow these channels, until finally metallic Fe occupies most of the particle, interspersed with the residual unreduced oxides.

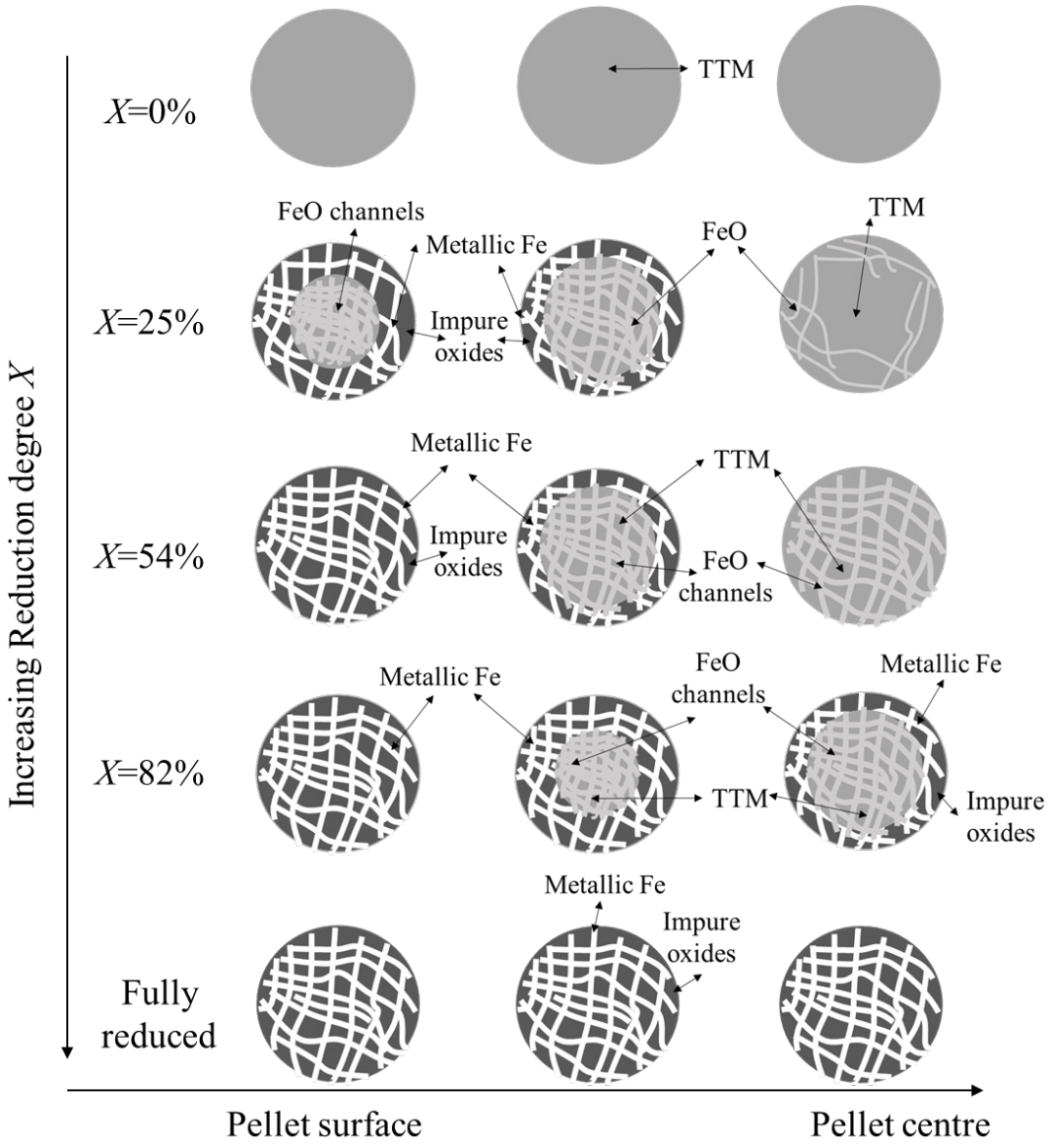

Figure 4.27*- Schematic graphic of particle morphological evolution during reduction of the Ar-sintered pellets at 1223 K*

Descriptions of the key particle-scale morphological features that observed during reduction at 1223 K are summarised in **Table 4.5**.

***Table 4.5**- Summary of the main features of the particle morphologies in the 'green' pellets, unreduced Ar-sintered pellets and reduced pellets investigated at 1223 K*

Scale	'Green' pellets (Ground raw particles pelletised with 1wt% Bentonite)	Ar-sintered ('Green' pellets sintered in Ar for 2 hours at 1473 K)	Quenched from 1223 K, 100vol% H_2, 1 L/min			
			25%	54%	82%	Fully
Pellet	1. The morphologies of the particles are homogeneous.	1. There is no obvious change in the morphologies or elements distribution. TTM remains as the major phase in the particles.	1. A pellet-scale reaction interface is observed.	1. A pellet-scale reaction interface is observed.	1. It is difficult to observe the pellet-scale reaction interface.	1. The morphology of the pellet is homogeneous, but shows brighter than that of the unreduced one.
Particle	2. The particle sizes are randomly distributed. 3. Most particles are smooth at the surface with a light grey colour. 4. Fine lamellar structure (enriched with Ti) can be observed in ~10% of the particles. 5. A small amount of silicate particles which are smaller than ~30 µm are present.	2. The size distribution of the particles is similar to 'Green' #2. 3. The morphologies are similar to 'Green' #3, but show evidence of sintering. 4. Fine lamellar structure which is enriched with Ti is also observed, similar to 'Green' #4.	2. Similar to Ar-sintered #2. 3. At the pellet centre, thin FeO channels are sparsely distributed. The unreduced TTM in the inner areas of the particles is similar to Ar-sintered #3. 4. In the particles at the pellet-scale reaction interface, a particle-scale shrinking core phenomenon is observed. In the core, FeO is developed into channels, and occupies most of the particles with unreduced TTM 'islands' in-between. At the shell, metallic Fe is observed. It seems metallic Fe is generated along the FeO channels, forming a similar morphology. 5. At the pellet surface, the particle morphology is similar to #4, however, more metallic Fe is generated with a smaller unreduced core.	2. Similar to Ar-sintered #2. 3. At the pellet centre, FeO channels are observed to occupy most of the particles. 4. At the pellet-scale reaction interface, the particle morphology is similar to 25% #4. 5. At the pellet surface, the particles are fully reduced to metallic Fe. The morphology of the metallic Fe seems to follow the pattern of FeO, forming intertwined channels, with impure oxides in-between. 6. The non-uniform particles are reduced at a similar rate to the uniform particles. However, their morphologies during reduction is similar to 1123 k 50% #6.	2, 3, 4, and 5 is similar to 54% #2, 4, and 5.	The morphologies of the fully reduced particles throughout the whole pellets are similar to 82% #5.

4.3.4 Particle morphologies of fully reduced pellets at higher temperatures

In addition to the quenching experiments conducted between 1023 K and 1223 K, completely reduced pellets were also produced from the TGA experiments (at Callaghan Innovation) at higher temperatures up to 1443 K. The particles morphologies in those fully reduced pellets were also characterised to examine the effects of temperature on the morphology of metallic Fe. It should be noted that these pellets were not quenched after complete reduction, but instead were subject to controlled cooling in the TGA furnace at a rate of 40 K/min.

Back-scatter SEM images showing the representative particle morphologies from 1043 K to 1443 K from the TGA experiments are shown in **Figure 4.28(a)** to **(e)**. At lower temperatures (1043 K and 1143 K, **Figure 4.28(a)** and **(c)**), the morphology of the metallic Fe showed a similar structure to those observed in the partially reduced pellets investigated from quenching. As the reduction temperature increased, the structure of metallic Fe coarsened, forming bulbous clusters (**Figure 4.28(d) and (e)**). This is consistent with an increased mobility of Fe atoms at elevated temperatures.

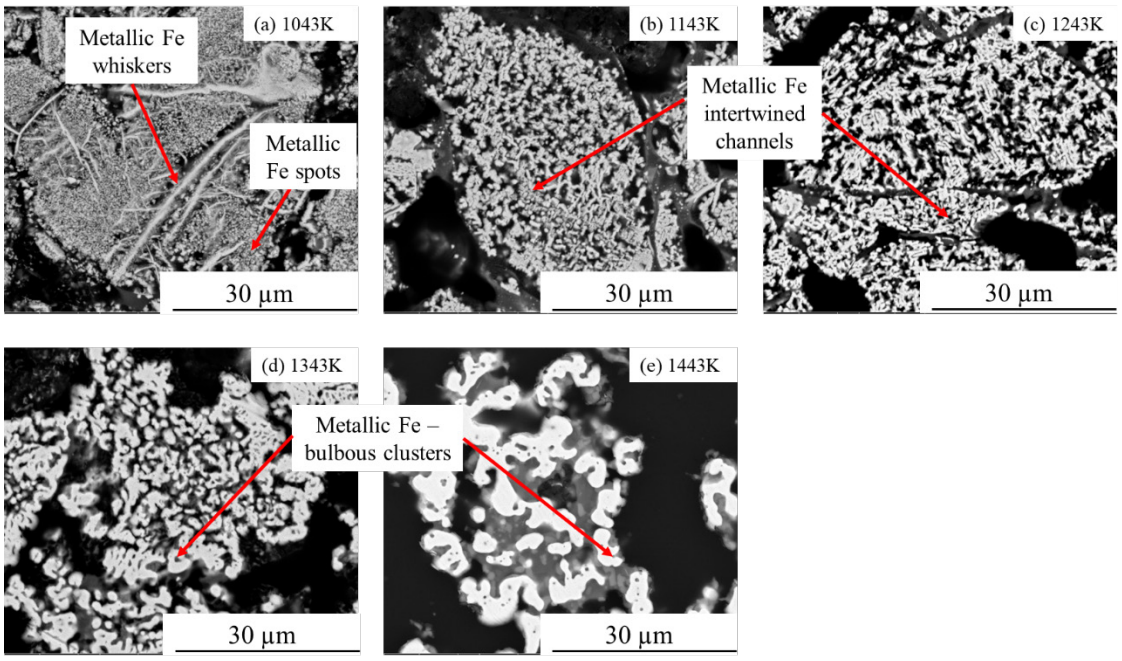

***Figure 4.28** - Backscatter-SEM images of cross-sectioned fully reduced pellets from the TGA experiment (Callaghan Innovation) showing the final morphologies of particles at each reducing temperature studied. (a) 1043K, (b) 1143 K, (c) 1243 K, (d) 1343 K and (e) 1443 K*

4.4 Summary

In this chapter, the results of the Ar-sintered pellets reduced in H_2 gas have been reported. Detailed discussion and analysis of these results follows in **Chapters 6**, 7 and **8**. In general, it was found that the reduction rate increased with increasing temperature, H_2 gas flow rates, H_2 gas concentrations, and decreasing pellet size (studied only at 1343 K).

In-situ ND measurements (Wombat beamline) during H_2 gas reduction of the Ar-sintered pellets were performed at the Wombat facility at ANSTO, and analysed to determine the phase evolution during the reaction. For all the reduction conditions studied, the initial ~5wt% of TTH was rapidly consumed in the early reduction stages. Following this, TTM was reduced. FeO was only observed as an intermediate phase when the temperature was above 1123 K. Metallic Fe and some residual $FeTiO_3$ were the final products observed. A characteristic time, τ, was defined for these experiments, which allowed comparison of the phase evolution during reactions which proceeded at different conditions. Reduction conditions significantly affected the observed evolution of FeO. At high temperature, a decreasing H_2 flow rate or gas concentration, led to an increase in the peak concentration of FeO observed. However, as temperature decreased from 1223 K to 1023 K, the maximum concentration of FeO decreased, and there was no FeO detected at 1023 K.

The evolution of pellet-scale and particle-scale morphologies within the reduced pellets were also investigated. From the macro-morphologies, a pellet-scale reaction interface distinguishing a bright shell and a dark core were observed in most of the reduced pellets. EDS-line scans confirmed the initial generation of metallic Fe at the pellet surface and a reaction interface that moved towards the pellet centre over time, implying a pellet-scale single interface shrinking core mechanism. However, these results also imply that later stage reactions (X>80%) in the pellet occur after the disappearance of the shrinking core, and might be more complex involving particle-scale reductions, which will be discussed in more detail in **Chapter 8**.

It should be noted that temperature significantly affected the morphological evolution of FeO within the pellet particles. At 1023 K, FeO was not observed, but it appeared with increasing temperature. At 1123 K, FeO formed fine and sparse trellis structures, while a network of

broader FeO channels were formed at 1223 K. The effects of the different morphology of FeO at different temperatures on the reduction process is further discussed in **Chapters 7** and **8** .

Similarly, at 1023 K and 1123 K metallic Fe formed small spots at each particle surface and whiskers at the particle centre. At temperatures where FeO was observed to form a network of channels at 1223 K, it was then reduced to metallic Fe which followed the same morphology. However, fully reduced pellets formed at temperatures above 1223 K, did not show a linear whisker or channel structure. Instead, pellets cooled from these temperatures exhibited metallic Fe formed into more bulbous clusters, which may reflect an increased local mobility of Fe atoms at elevated temperatures.

Chapter 5
Results of reducing pre-oxidised pellets in H_2 gas

In this chapter, a summary of results from reducing the pre-oxidised pellets in H_2 gas is presented. These results include:

- **Section 5.1**: TGA measurements of the reduction of pre-oxidised pellets in H_2 gas
- **Section 5.2**: The evolution of crystalline phases during reduction determined by *in-situ* ND
- **Section 5.3**: The pellet- and particle-scale morphologies which occur during reduction, as captured during quenching experiments
- **Section 5.4**: Summary of the results of reducing pre-oxidised pellets

This chapter reports only the experimental results obtained. Note that some of the contents have already published in a paper of *the* author [162]. *Discussion* of the analysis of these results in presented in **Chapters 6**, 7 and **8**.

5.1 Reduction of pre-oxidised pellets in the TGA system

In this section, the DR characteristics of the pre-oxidised pellets in H_2 gas flow are presented. Key experimental variables examined were the effect on the pellet reduction rate of: H_2 gas flow rate, reduction temperature and pellet diameter.

5.1.1 Determination of critical flow rate

In **Figure 5.1**, the effect of H_2 gas flow rate on the reduction rate of the pellets reduced at 1343 K is shown. The reduction progressed faster when the flow rate was increased from 152 ml/min to 330 ml/min. However, further increase in the flow rate to 380 ml/min had no additional effect on the reduction rate. This indicated that the critical flow rate for this experiment was $\leq$ 330 ml/min. Note that this critical flow rate is much smaller than that of reducing Ar-sintered pellets ($\leq$ 850 ml/min as shown in **Figure 4.1**). To ensure that mass transport effects in the gas stream were excluded, a higher flow rate of 520 ml/min was chosen for all following reduction experiments on the pre-oxidised pellets.

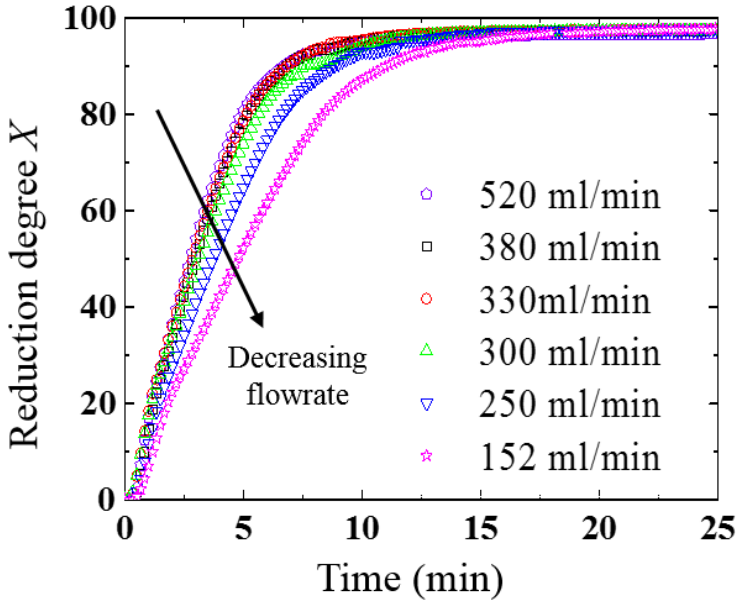

Figure 5.1 *– The effect of changing H_2 gas flow rate on the reduction rate of reducing pre-oxidised pellets at 1343 K. (Data taken using the TGA system at Callaghan Innovation)*

5.1.2 The effect of temperature on reduction rate

Results of the TGA experiments in which pre-oxidised pellets were reduced in 520 ml/min flow of H_2 gas are shown in **Figure 5.2**. Experiments were performed at temperatures from 1043 to 1443 K, at 100 K intervals. As can be seen, the reduction rate increased with increasing temperature, and a similar maximum reduction degree of 97% ± 0.8% was achieved at all temperatures. At 1043 K, it took ~40 minutes to reach the maximum reduction degree, while it took less than 20 minutes to achieve a similar maximum reduction at all the other temperatures. The reduction rate presented here is similar to that of Ar-sintered pellets above 1043 K, while it becomes much faster at lower temperature (compared with **Figure 4.2**). The reasons behind this phenomenon are discussed in **Chapters 6** and **7**.

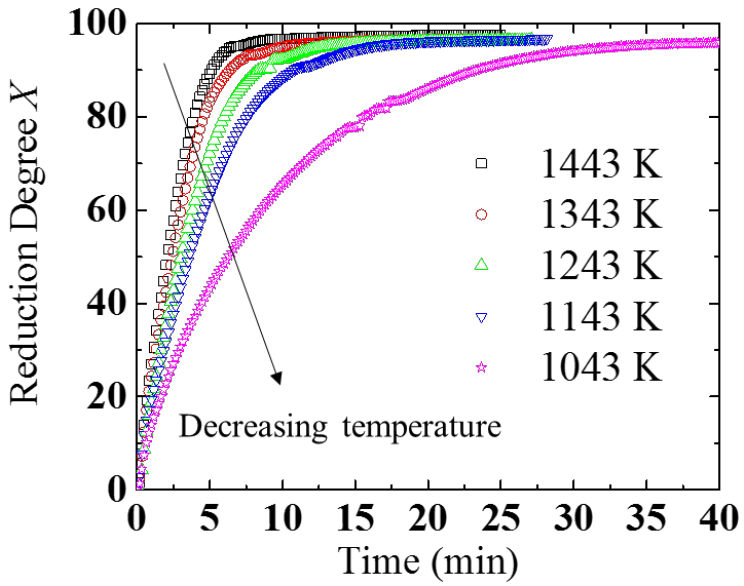

***Figure 5.2**– The effect of temperature on the reduction rate of the pre-oxidised pellets in 520 ml/min flowing H_2 gas, at temperatures from 1043 K to 1443 K. (Data taken using the TGA system at Callaghan Innovation) [162]*

XRD analysis was performed on the fully reduced pellets obtained from each TGA experiment, and the results are given in **Figure 5.3**. From this figure it can be seen that, in addition to the major phase of metallic Fe (Peak A), several different residual Fe-Ti-O phases were also observed (Peak B to Peak D). These residual oxides were identified to be $FeTiO_3$, TiO_2, Fe_2TiO_5 (PSB, or $FeTi_2O_5$ as ferro-PSB), and a generic spinel phase (Peak E). The presence of these residual oxides is consistent with a final reduction degree of <100%.

The evolution of these residual oxides with reduction temperature is shown in **Figure 5.4**. On increasing the reduction temperature, both the concentrations of $FeTiO_3$ and TiO_2 decreased while that of PSB increased. The spinel concentration did not change significantly with temperature. These observations are similar to those found in the Ar-sintered pellets shown in **Figures 4.3** and **4.4**.

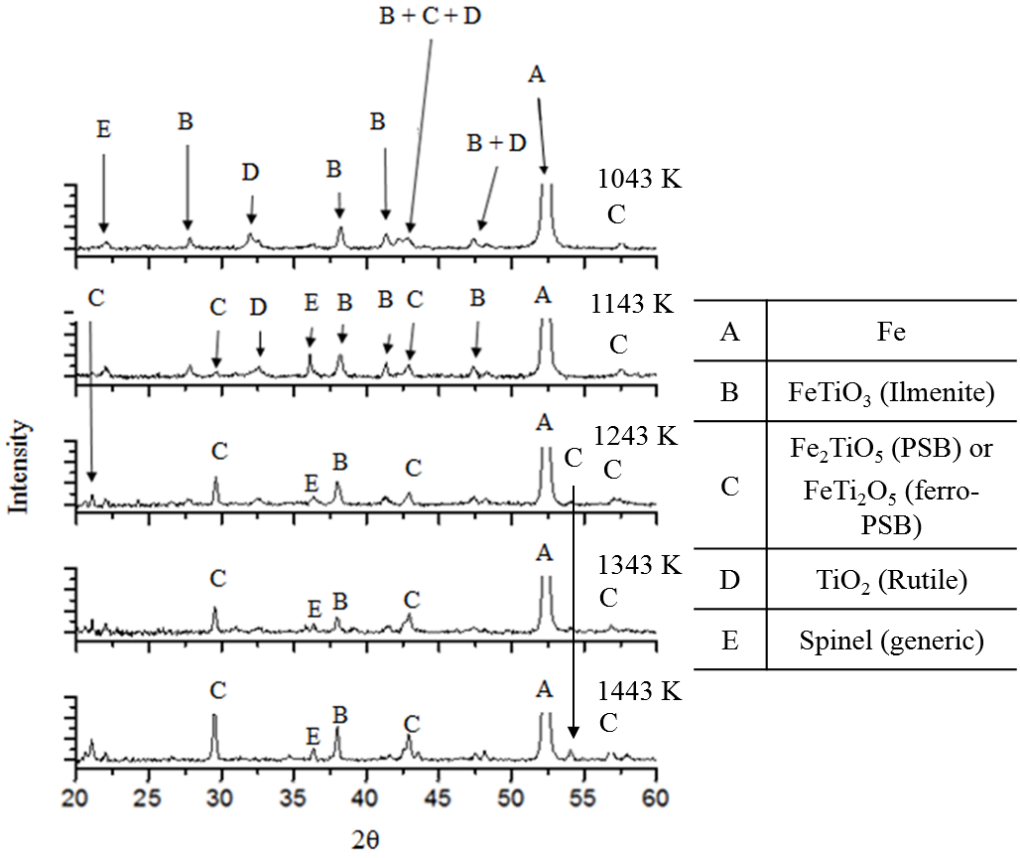

Figure 5.3 *– Magnified XRD diffractograms obtained from fully reduced pellets following reduction at each temperature from 1043 K to 1443 K. Note that the metallic Fe peak (A) is truncated in order to enable minor peaks to be clearly shown. The full pattern is shown in* ***Figure C.1*** *in* ***Appendix C.1*** *[162]*

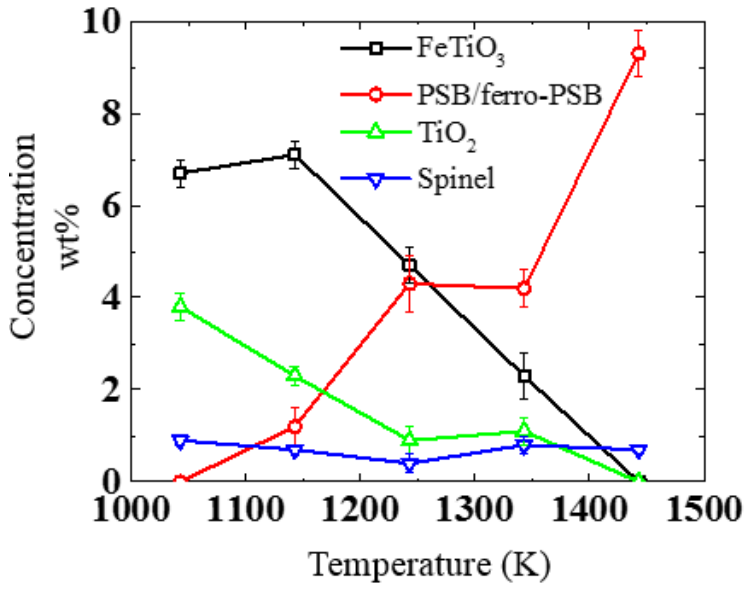

Figure 5.4*- Changes in concentration of residual oxides indicated in* ***Figure 5.3*** *in the fully reduced pellet at each reduction temperature. Note the error bar of each phase concentration is generated from the peak fitting [162]*

5.1.3 The effect of pellet size on reduction rate

The reduction behaviour of the pre-oxidised pellets ranging from 5.5 mm to 8.5 mm were measured at 1343 K at a H_2 gas flow of 520 ml/min, and the results are plotted in **Figure 5.5**. From this figure it indicates that, increasing pellet size results in a slower reduction rate. This is also similar to the pellet size effect on reduction rate of the Ar-sintered pellets at 1343 K above the critical flow rate (**Figure 4.5**), once again indicating that smaller pellets are desirable for practical DRI processes.

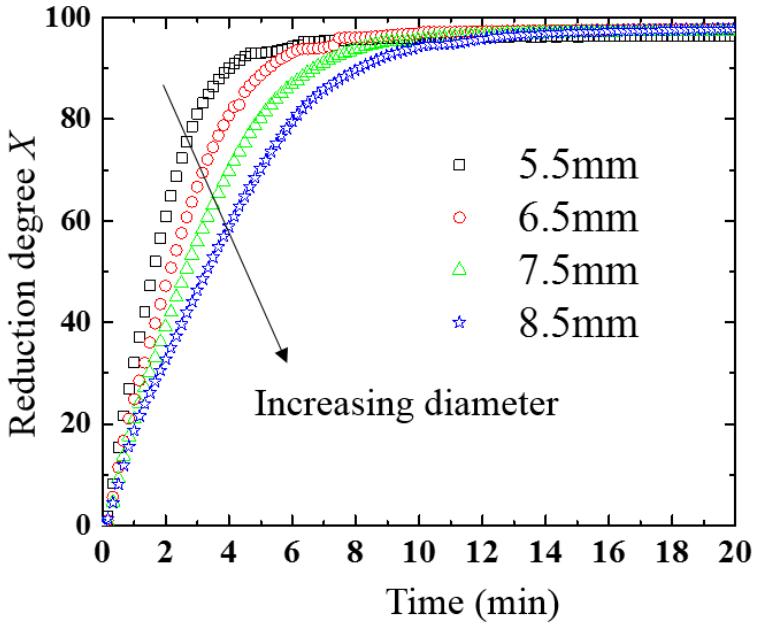

***Figure 5.5**– The effect of pellet size on the reduction rate for the pre-oxidised pellets reduced at a flow rate of 520 ml/min H_2 gas at 1343 K. (Data taken in the TGA system at Callaghan Innovation) [162]*

5.2 Phase evolution during H_2 gas reduction of pre-oxidised pellets through *in-situ* ND experiment

In this section, results from *in-situ* ND measurements of the phase evolution during H_2 gas reduction of the pre-oxidised pellets are presented. The effects of H_2 flow rate, H_2 gas concentration and temperature on the phase evolution were also investigated in these experiments.

The *in-situ* diffraction patterns obtained were converted to crystalline phase concentrations at each point in time during a series of reduction experiments, using the method outlined in **Subsection 3.6.1**. An example phase evolution plot is shown in **Figure 5.6**, which shows results from pre-oxidised pellets reduced at 1223 K by 100vol% H_2 gas at a flow of 250 ml/min. As can be seen, before reduction, the pre-oxidised pellets were solely composed of TTH. At the moment H_2 gas was introduced, the amount of TTH started rapidly decreasing and reached zero within a few minutes. As TTH was reduced, TTM and FeO started to form. The concentrations of both TTM and FeO first rose to a peak, before dropping back down to zero. Metallic Fe started to appear slightly later than FeO. Detectable levels of $FeTiO_3$ appeared only after the concentration of FeO reached its peak. At the completion of the reduction, metallic Fe and $FeTiO_3$ were the only crystalline products observed. Note that, due to the limitations of the ND technique (see **Subsection 4.2.4)**, other expected phases (Fe_2TiO_4, TiO_2 or PSB) were not detected.

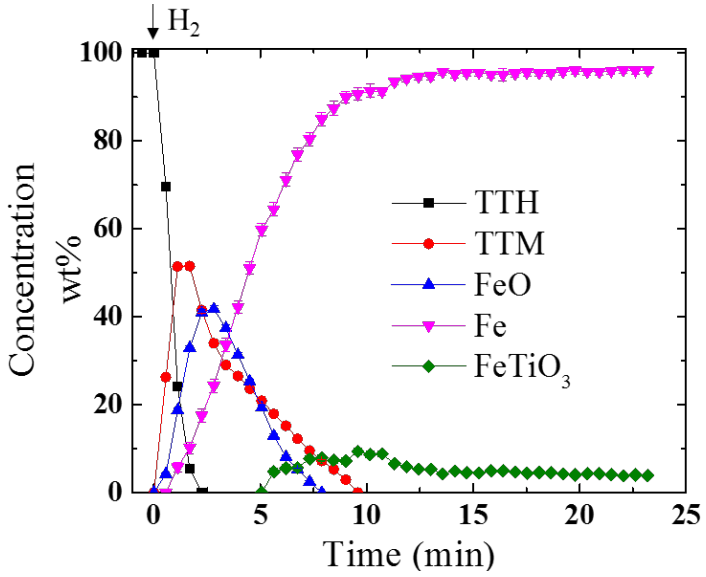

***Figure 5.6**- An example of the phase evolution obtained from in-situ ND measurements during reduction of pre-oxidised pellets at 1223 K by 100vol%H_2 at a gas flow rate of 250 ml/min*

In the *in-situ* ND experiments, the key variables investigated were effect of H_2 flow rates at 1223 K, various H_2 gas concentrations, and temperatures (1023 K, 1123 K and 1223 K). Similar to the Ar-sintered pellets (**Section 4.2**), a characteristic time (τ) was determined in order to compare the effects of each reduction condition on the phase evolution. This was defined as the time to reach 50wt% metallic Fe.

5.2.1 The effect of H_2 flow rate on the phase evolution at 1223 K

1. Determining the critical flow rate for ND reduction experiments

At 1223 K, the pre-oxidised pellets were reduced using 100vol% H_2 gas at three different flow rates: 62.5 ml/min, 125 ml/min and 250 ml/min. Concentration curves for each crystalline phase obtained at each flow rate are shown in **Figure 5.7**. Slower reaction rates were observed at the lower flow rates.

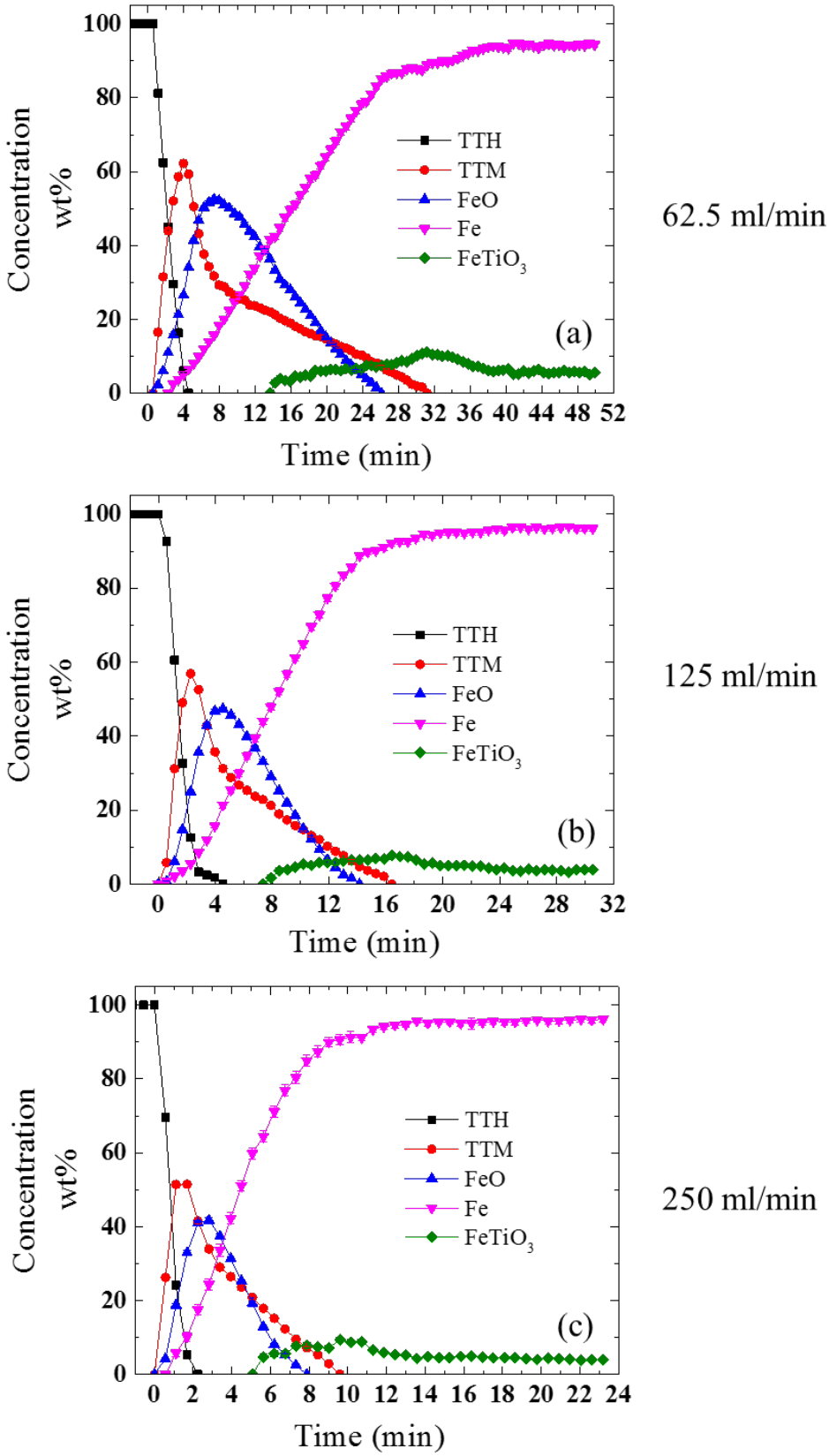

Figure 5.7 *– Concentration curves of each crystalline phase during reduction of pre-oxidised pellets by 100vol% H_2 gas at 1223 K at a flow rate of (a) 62.5 ml/min, (b) 125 ml/min and (c) 250 ml/min*

In order to verify whether the highest flow rate achievable in the ND experiments (250 ml/min) was conducted above the critical flow rate, ND and TGA results were compared for similar pellets (~6 mm diameter and ~73 µm average particle size). The TGA experiment was performed at 1223 K at a flow of 520 ml/min 100vol% H_2 gas. (These conditions were known to be above the critical flow rate condition for pre-oxidised pellets in the TGA system at Callaghan Innovation). Reduction degree values were also calculated from the phase concentration curves obtained from the ND reduction experiments (using equations **3.3** and **3.4**). A comparison between the TGA and ND results is shown in **Figure 5.8**. As can be seen, the ND reduction experiments conducted at a flow rate of 250 ml/min closely follow the reduction rate observed in the TGA experiment at a flow rate of 520 ml/min, indicating this experiment took place above the critical flow rate for the ND experimental apparatus at the Wombat beamline. However, the ND reduction experiments conducted at lower flow rates (62.5 ml/min and 125 ml/min) were likely below the critical flow rate, meaning that gas mass transport effect on the phase evolution cannot be excluded.

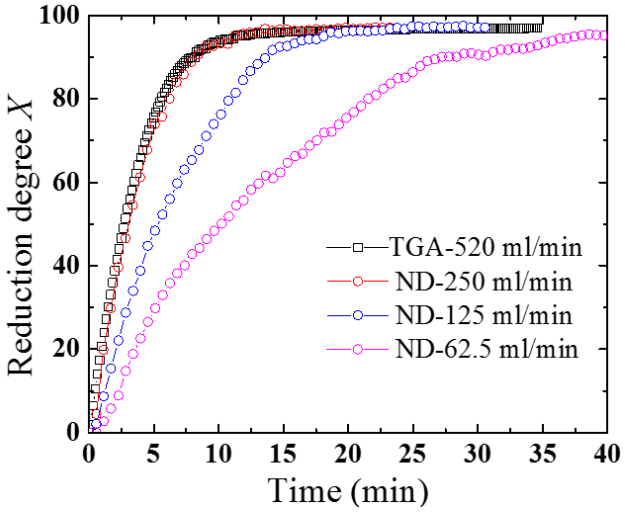

***Figure 5.8** – Comparison between the reduction degree curve obtained from the TGA experiment (Callaghan Innovation) at a flow rate of 520 ml/min, and the results obtained from the ND reduction experiments (Wombat beamline) at three different flow rates using 100vol% H_2 gas at 1223 K*

2. The effect of flow rate on the in-situ phase evolution

In **Figure 5.9(a)**, the production rate of metallic Fe in the ND experiments at different H_2 gas flow rates are indicated. As noted above, the generation of metallic Fe was faster with increasing flow rates. The intersection of the dashed line with each data curve shows the time,

τ, at which 50% metallisation was achieved for each experiment. In **Figure 5.9(b)**, a plot of the reciprocal of each τ ($1/\tau$) against the respective flow rate shows a linear relationship passing through the origin. This linear relation indicates that the generation of metallic Fe is directly proportional to H_2 flow rate over the range of flow rates studied. It should be noted that this linear relation also implies that the flow rate of 250 ml/min applied in the ND reduction experiment is just above the critical flow rate for the Wombat beamline.

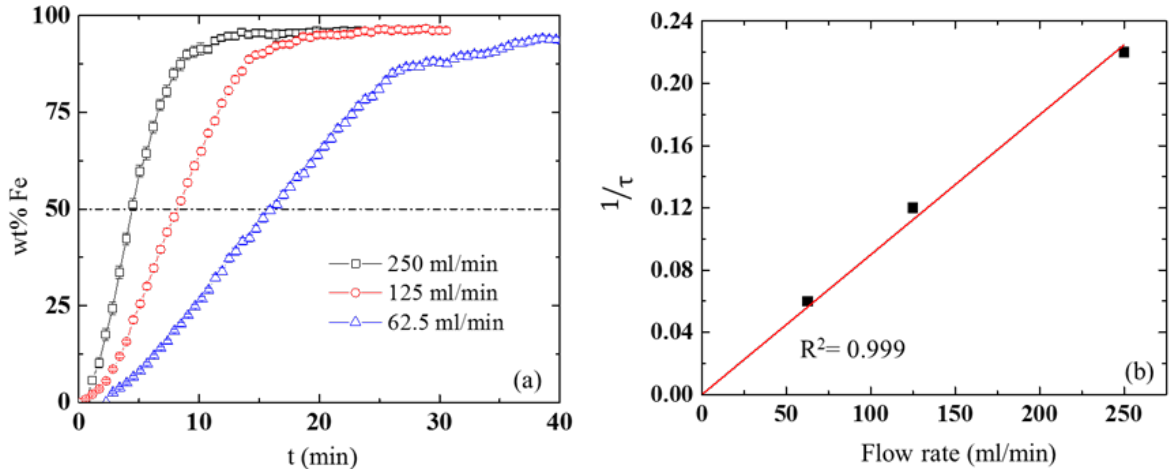

Figure 5.9 *- (a) The effect of flow rate on the changes in concentration of metallic Fe during reduction of pre-oxidised pellets at 1223 K by 100vol% H_2 gas at 62.5ml/min, 125 ml/min and 250 ml/min. The dashed line indicates 50wt% metallic Fe. (b) A linear relationship between $1/\tau$ and flow rate*

In order to compare results from experiments at different H_2 flow rates on a single coordinate axis, the *x*-axis was normalised to (t/τ) and the data replotted, as in **Figure 5.10(a)** to **(e)**. The normalised curves for TTH, metallic Fe and $FeTiO_3$, are highly similar for the different H_2 flow rates tested. However, the peak level of the intermediate FeO varies with different flow rates, with its maximum concentration increasing slightly as H_2 flow rate decreases. Small discrepancies are also observed for TTM. Similar to the effects of flow rate on the reduction of Ar-sintered pellets (**Subsection 4.2.1**), the differences might be caused by the gas transfer effect, which results in a different distribution of H_2/H_2O in the pellets at different flow rates.

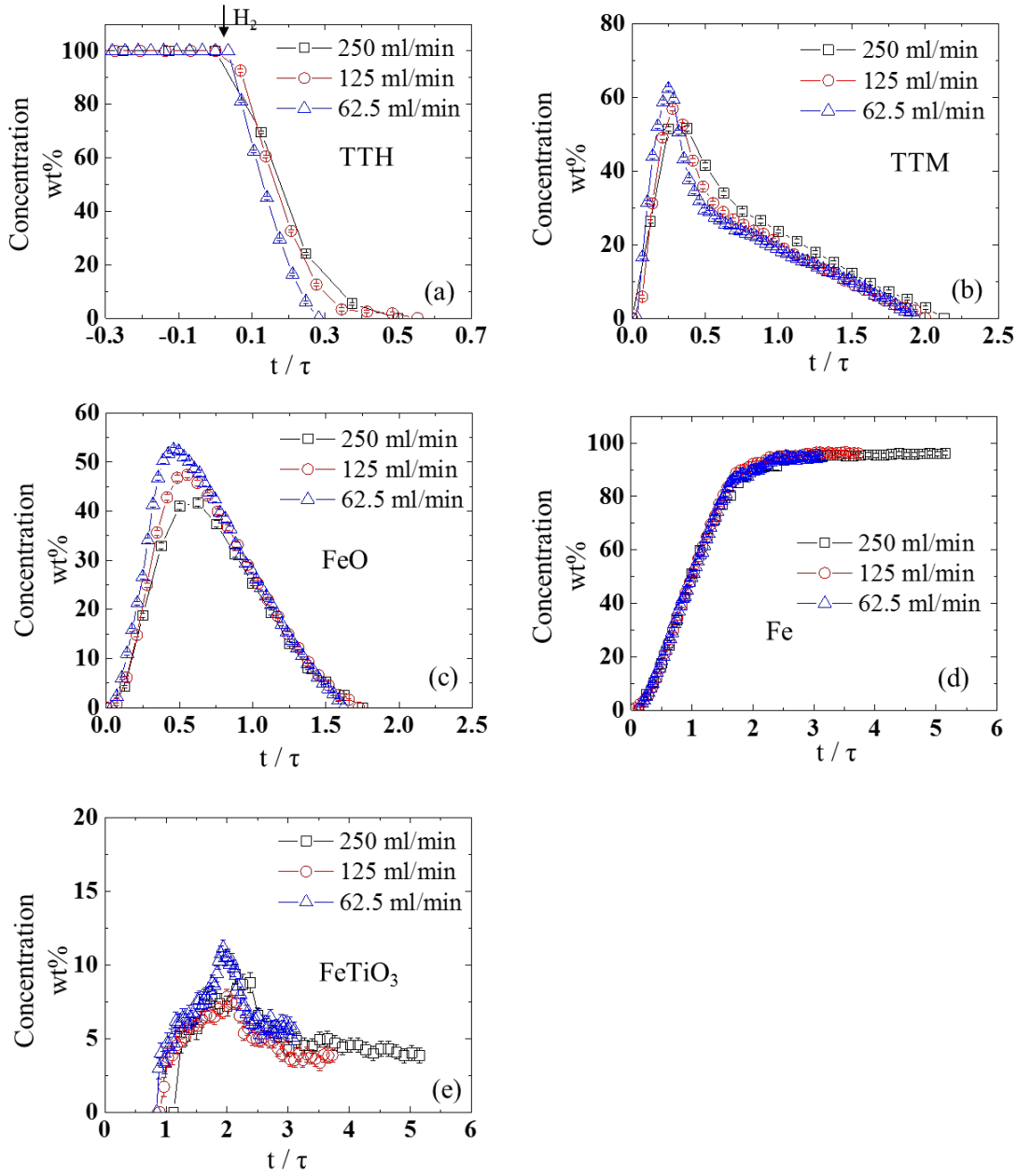

***Figure 5.10**– In-situ ND results showing the evolution of each crystalline phase during reduction of pre-oxidised pellets by 100vol% H_2 gas at 1223 K at a flowrate of 62.5 ml/min, 125 ml/min and 250 ml/min respectively at the Wombat beamline. Here, data are plotted in a single coordinate system by using a normalised dimensionless x-axis (t/τ). It should be noted each reduction started at t/τ=0. (a) TTH, (b) TTM, (c) FeO, (d) metallic Fe and (e) $FeTiO_3$*

5.2.2 The effect of H_2 gas concentration on the phase evolution at each temperature

At each temperature, the reduction of the pre-oxidised pellets in a 250 ml/min flowing H_2-Ar gas mixture with H_2 gas concentrations ranging from 5vol% to 100vol% was studied. Concentration curves for each crystalline phase during reduction at each condition at 1223 K are shown in **Figure 5.11** as examples. The concentration curves obtained at 1023 K and 1123

K are given in the **Appendices C.2** and **C.3**. An important feature to note in **Figure 5.11**, is that there is a slowdown in the consumption of TTM once the concentration of FeO has reached its peak, especially at lower H_2 gas concentrations (**Figure 5.11(a)** and **(b)**). This observation is discussed in more detail later in **Section 7.2**. Moreover, similarly to the Ar-sintered pellets (**Subsection 4.2.2**), a sudden drop in the Fe concentration was observed when $FeTiO_3$ started to be detected.

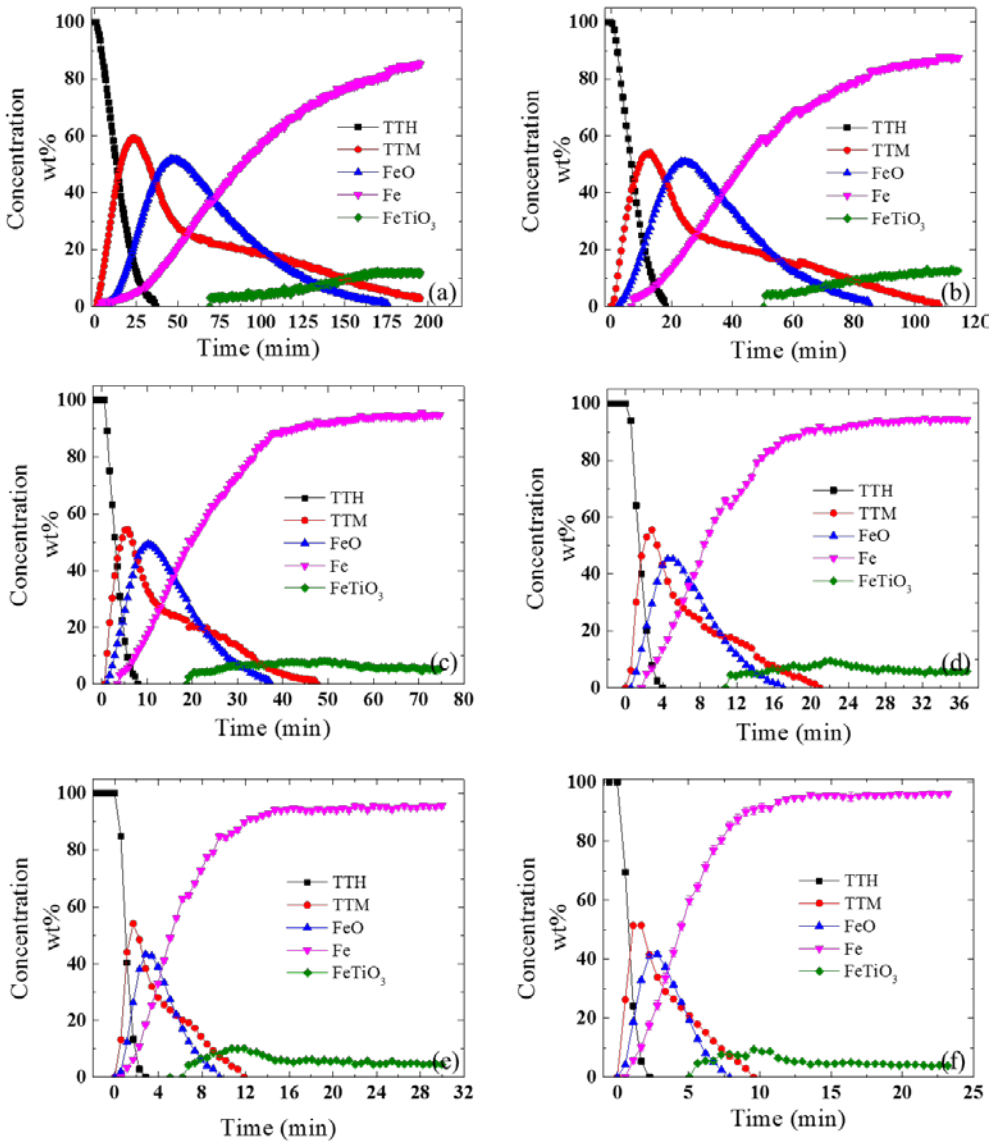

***Figure 5.11** - Concentration curves of each crystalline phase measured by ND at the Wombat beamline, during reduction of pre-oxidised pellets at a flow of 250 ml/min at 1223 K in various H_2-Ar gas mixtures. (a) 5vol% H_2, (b) 10vol% H_2, (c) 25vol% H_2, (d) 50vol% H_2, (e) 75vol% H_2, and (f) 100vol% H_2*

The production rate of metallic Fe at each different H_2 gas concentration and temperature are indicated in **Figures 5.12(a1)** to **(a3)**. At each temperature the generation of metallic Fe progressed faster with increasing H_2 gas concentration. In the same manner as before, the

reciprocal of each τ ($1/\tau$) is plotted against the respective H_2 gas concentration in **Figure 5.12(b1)** to **(b3)**. In each case this gives a linear relationship passing through the origin. This shows that at each temperature, the generation of metallic Fe is directly proportional to the delivered flow of H_2 gas. This effect of H_2 gas concentration on the generation rate of metallic Fe is similar to that of Ar-sintered pellets (**Subsection 4.2.2)**

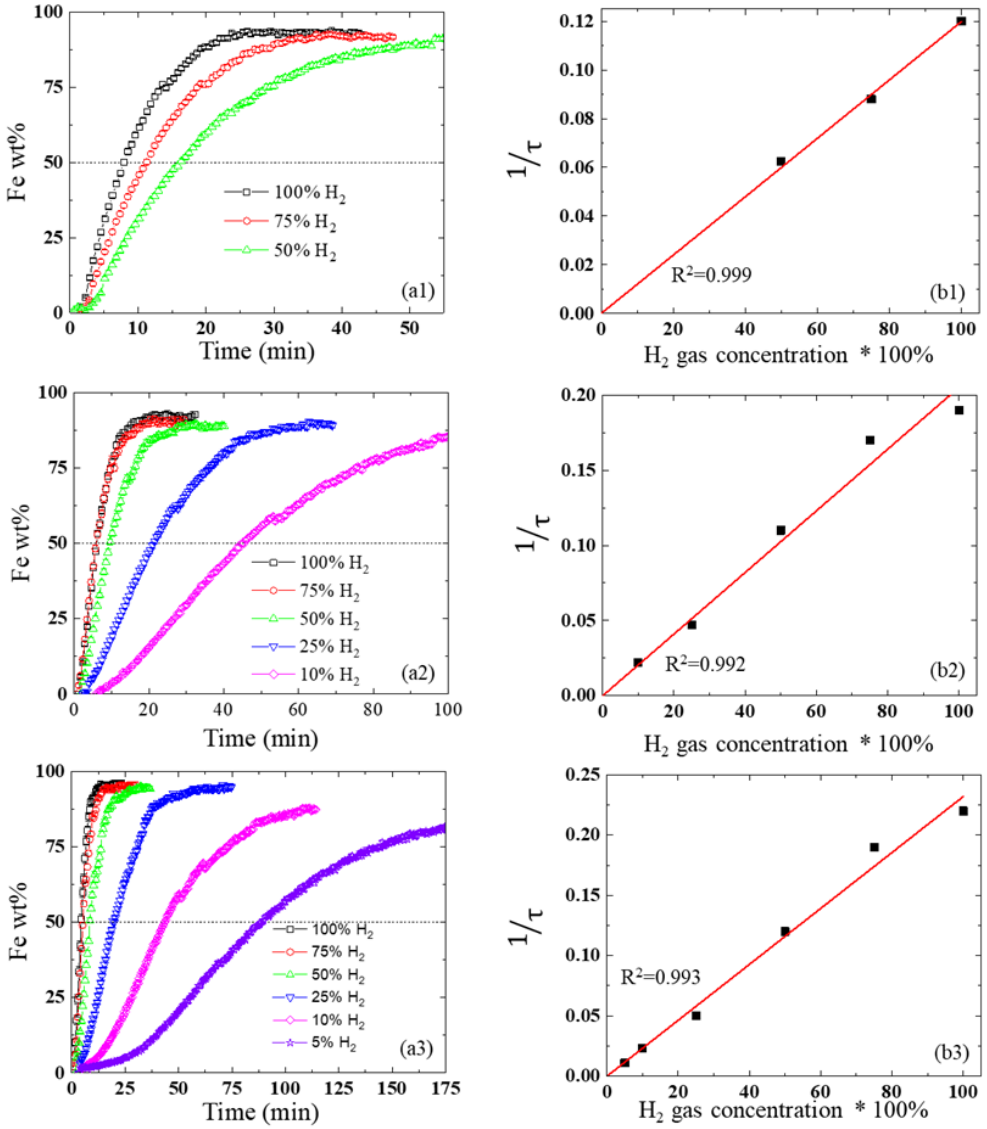

***Figure 5.12**- (a) The effect of H_2 gas concentration on the production of metallic Fe during reduction of pre-oxidised pellets at a flow of 250 ml/min gas mixture with different H_2 gas concentrations at (a1) 1023 K ,(a2) 1123 K, and (a3) 1223 K.. The dashed line indicates 50wt% metallic Fe. (b) The linear relationship between 1/τ and H_2 gas concentration at (b1) 1023 K, (b2) 1123 K, and (b3) 1223 K. (Results from the ND experiments performed at the Wombat beamline)*

The comparisons of the evolution of each crystalline phase at each temperature and H_2 gas concentration is shown in **Figure 5.13** , where the *x*-axis is normalized time (t/τ). As with the flow rate comparison, most of the phase concentration curves are seen to be highly similar

across all of the studied H_2 gas concentrations and temperatures. However, some differences can be observed for TTM and FeO at 1123 K, as well as for $FeTiO_3$ at both 1123 K and 1223 K. A discussion of these differences is presented later in **Section 7.3**.

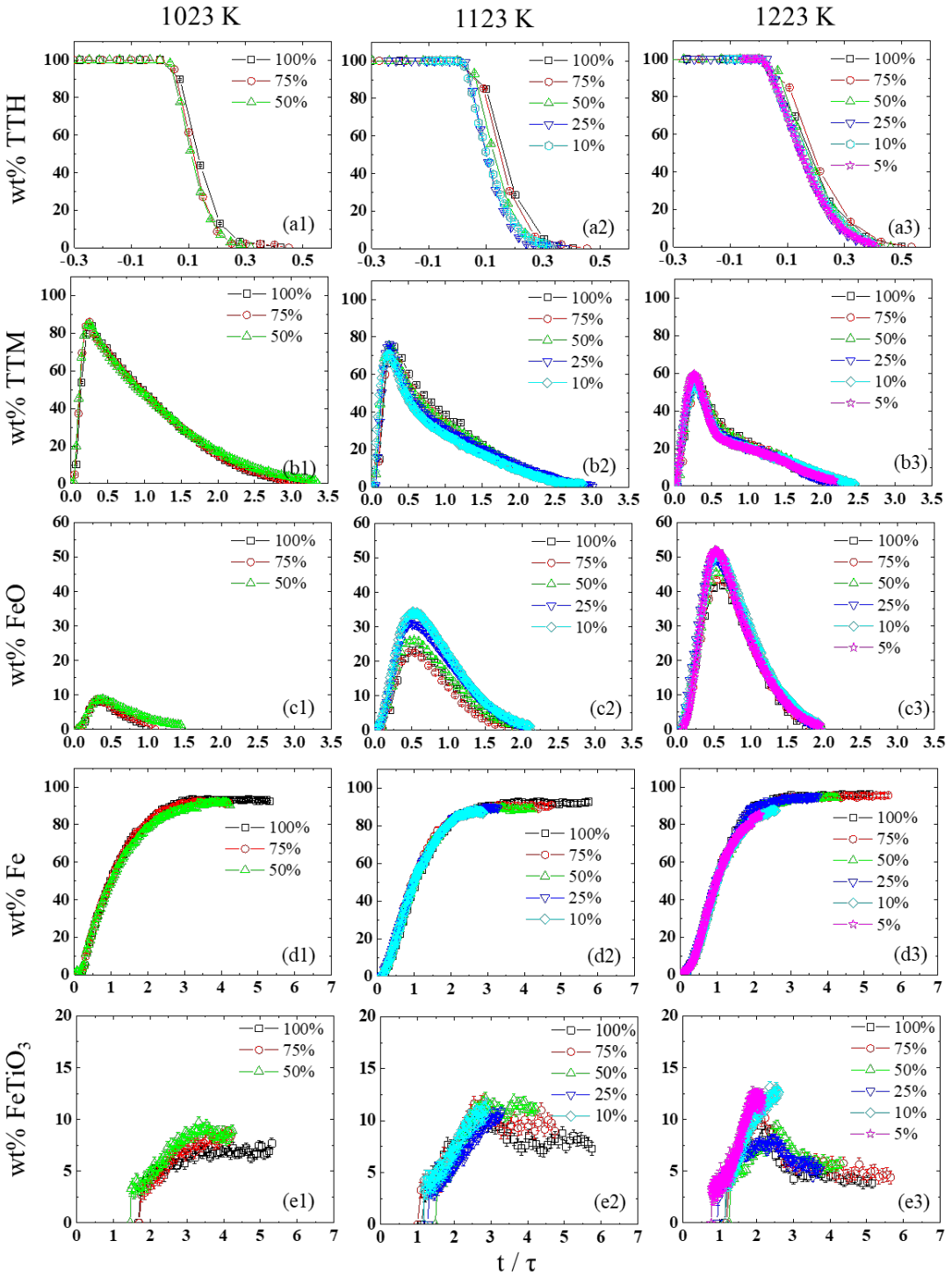

***Figure 5.13**– The evolution of each phase during reduction of pre-oxidised pellets at a 250 ml/min flow H_2-Ar gas mixture with different H_2 gas concentrations at each temperature. These data are plotted in single coordinates with normalised dimensionless x-axis (t/τ) at (1) 1023 K, (2) 1123 K and (3) 1223 K. It should be noted the reductions started at $t/\tau=0$ (a) TTH, (b) TTM, (c) FeO, (d) Metallic Fe and (e) $FeTiO_3$. (Results from the ND experiments performed at the Wombat beamline)*

5.2.3 The effect of temperature on the phase evolution

Figures 5.12 and **5.13** also allow a comparison of the effect of temperature on the phase evolution. As illustrated in **Figure 5.12**, the generation of metallic Fe was slower at lower temperatures. As shown in **Figure 5.13**, at the beginning of reduction, TTH in the pellets was consumed rapidly at all temperatures. However, temperature significantly affected the evolution of TTM and FeO. With increasing temperature, the maximum TTM concentration decreased, while that of FeO increased. Moreover, it seems that the maximum concentration of $FeTiO_3$ also increased slightly with increasing temperatures, especially when H_2 gas concentration is low. It seems that at higher temperatures, H_2 gas concentration might affect the reactions associated with $FeTiO_3$. These reactions, and their effects on the reduction are discussed later in **Sections 7.1** and **8.1**.

This section (**Section 5.2**) has described the crystalline phase concentration results obtained from the *in-situ* ND reduction experiments. Analysis and discussion of this data and its implications are presented in **Chapters 7** and **8**.

5.3 Morphology development during H_2 gas reduction of pre-oxidised pellets: Results from quenching experiments

In this section, results of microscopy on the microstructure of the pellets at various stages during the reduction reaction from 1023 K to 1223 K are reported. These pellets were obtained from quenching reduction experiments using a sliding furnace at VUW as shown in **Subsection 3.4.1**. To enable comparison of these results with those from the *in-situ* phase evolution in **Section 5.2**, these quenching experiments were conducted at a flow of 340 ml/min 100vol% H_2 gas. This flow rate was determined to be equivalent to a flow rate of 250 ml/min in the ND reduction experiment. This calculation is shown in equation **5.1**, ensuring the velocity of the gas passing the pellets is comparable at each experiment.

$$\frac{Q_{ND}}{A_{ND}} = \frac{Q}{A} \tag{5.1}$$

where $A = \pi r^2$ denotes the area of the cross section of the reaction tube (r represents the tube radius: r_{ND} = 3.5 mm for ND experiment as in **Subsection 3.6.1**, and r = 4 mm for quenching experiment as in **Subsection 3.4.1**), and Q stands for the equivalent flow rate applied in each experiment.

At each temperature, partially reduced pellets were quenched at reduction degrees of approximately X=~20%, 50%, 80% and fully reduced (~97%, the maximum reduction degree obtained as shown in **Figure 5.2**). A comparison of the reduction degrees of these pellets to those obtained from the ND reduction experiments (using equations **3.3** and **3.4**) is shown in **Figure 5.14**. In general, a reasonable agreement was observed at each temperature. However, there was discrepancy at higher temperatures. This is probably attributed to the extra unaccounted time required to purge H_2 gas out of the tube and gas lines by Ar gas at the start of quenching step. During this gas changing time, further reactions might occur. Moreover, due to a faster reduction rate at high temperatures (**Subsection 5.2.3**), more reductions might take place, but the time during which the reactions take place are not taken into consideration. As a result, this leads to a slightly higher reduction degree than expected at a desired time. After quenching, each pellet was then cross-sectioned and imaged to reveal the morphological evolution at that point in the reduction reaction.

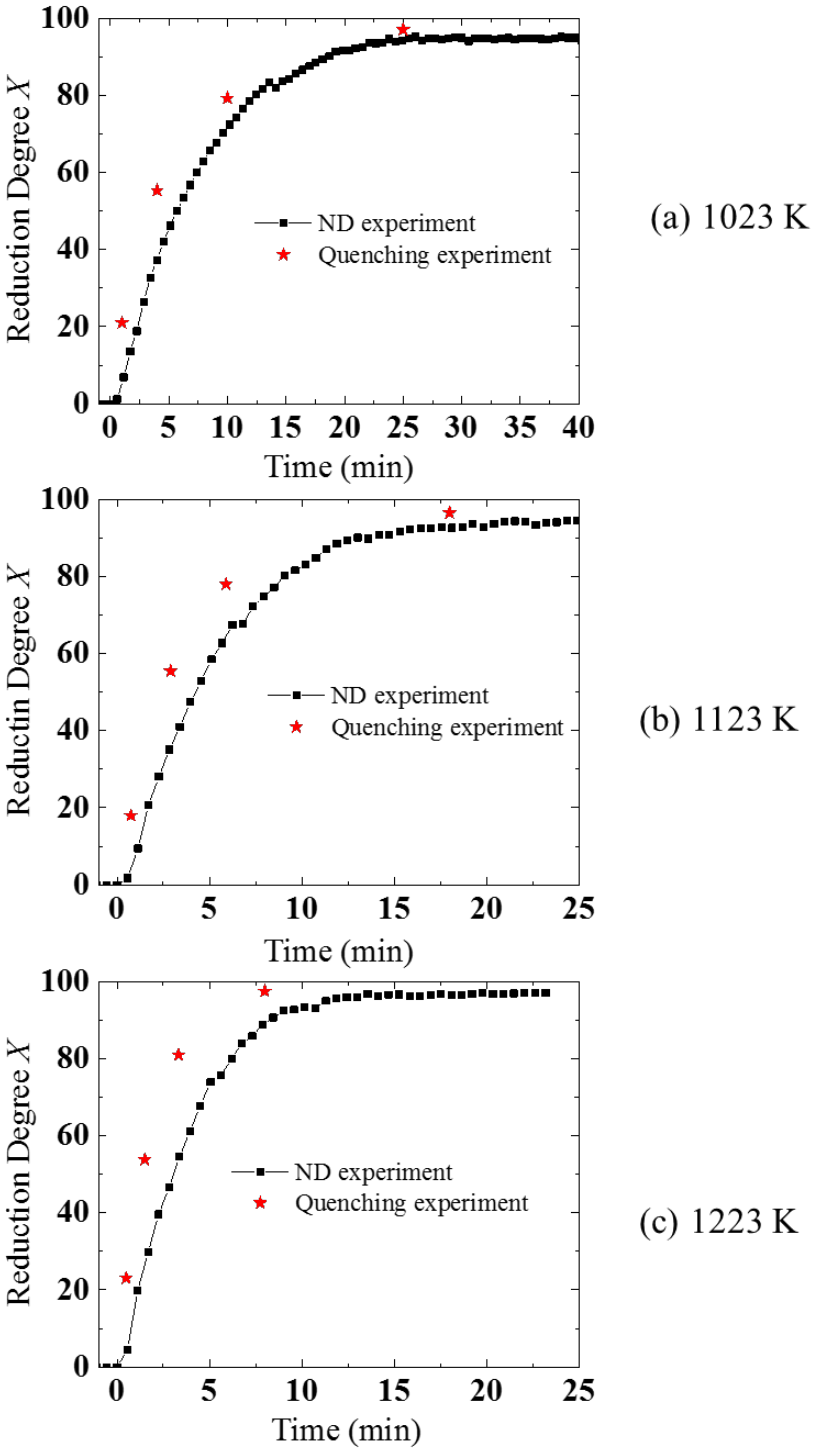

Figure 5.14 *– Comparisons of the reduction degrees of the quenched pellets to those obtained from the in-situ ND reduction experiments (by equations **3.3** and **3.4**) using 100vol% H_2 gas at different temperatures (a) 1023 K, (b) 1123 K and (c) 1223 K. The flow rate for the in-situ ND reduction experiments at Wombat beamline is 250 ml/min. The flow rate for the quenching experiments of the sliding furnace (at VUW) is 340 ml/min, which is calculated by equation **5.1** to ensure an equivalent flow condition to that in ND reduction experiments*

5.3.1 Macro-morphology of the reduced pellets at each temperature

Optical images that show cross-sections of the unreduced, partially reduced, and fully reduced pre-oxidised pellets at each temperature are exhibited in **Figure 5.15**. A dark core and a bright shell were observed within each partially reduced pellet, although the interface became less clear with increasing reduction degree (at each temperature), or with decreasing temperature (at similar reduction degree).

Before reduction, the morphology of the pre-oxidised pellet (X=0%) was homogeneous. Note that the bright spots in the images is believed to be caused by the porosity in the pellets unfilled with resin or particles pulled out during grinding/polishing. For the X=~20% pellets reduced at 1223 K, a single pellet-scale interface was observed separating two parts: a dark core and a very thin bright shell. However, a distinct interface was not clearly observable in the X=~20% pellets reduced at 1023 K or 1123 K. For the X=~50% pellets reduced at all temperatures, a pellet-scale interface was observed, and this had moved closer to the pellet centre than seen in the X=~20% pellets. For the X=~80% pellets reduced at all temperatures, the inner core and outer shell were difficult to distinguish. For the fully reduced pellets, a homogeneous morphology was observed throughout the whole pellet. However, they were significantly brighter in colour than the original unreduced pellets.

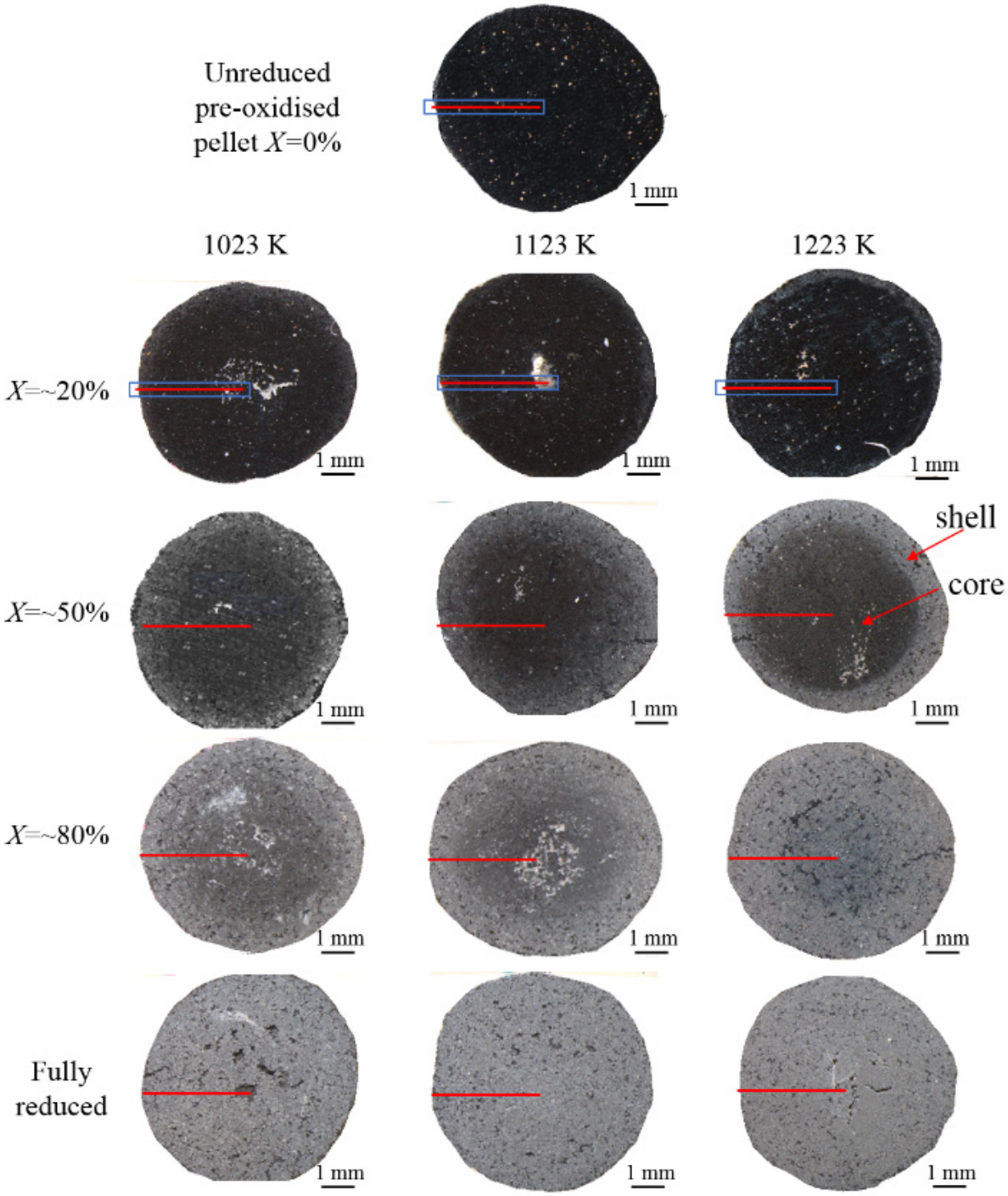

Figure 5.15– *Optical images showing macro-morphologies of the unreduced, partially reduced and fully reduced pellets. The partially and fully reduced pellets were obtained by reducing pre-oxidised pellets at a flow of 340 ml/min 100vol% H_2 gas at 1023K, 1123 K and 1223 K. The red lines in each plot indicate the areas where EDS-Line scans were conducted. The blue sectioned area in the X=~20% pellets indicate the areas where the optical microscopy at higher magnification were conducted*

According to the *in-situ* ND reduction experiment, TTH was reduced to TTM rapidly in the earliest reduction stage for all the temperatures tested. This fast reduction is difficult to observe

in the low magnification images shown in **Figure 5.15**, as there is only a small difference in optical contrast between TTH and TTM. Therefore, to examine this reduction, higher magnification optical microscopy was used to obtain images from the *X*=~20% pellets reduced at each temperature (as highlighted in blue sectioned areas in **Figure 5.15**). To enable comparison, similar images were also obtained from the Ar-sintered pellets, and the pre-oxidised pellets prior to reduction. These results are shown in **Figure 5.16**.

As can be seen, under light microscopy, TTM reflected a slightly brown colour (as seen in the unreduced Ar-sintered particles), while TTH was a brighter grey (as seen in the unreduced pre-oxidised particles). For the pre-oxidised pellets reduced to *X*=~20% at 1123 and 1223 K, most of the particles at the pellet surface appeared a similar colour to the TTM particles, whilst the particles at the pellet centre, appeared similar to the TTH particles. This implies that the reaction of TTH to TTM proceeds inwards from the pellet surface to its centre. However, at 1023 K, the pellet-scale TTH core was not as clear and could not be easily distinguished. In some cases, partially reduced individual particles could also be observed in which TTM has been generated at the particle surface and a clear TTH/TTM interface is apparent, moving inwards while retaining the particle shape. It seems that the reduction of TTH to TTM follows both a pellet-scale and particle-scale shrinking core phenomenon.

From **Figure 5.16**, it seems that at *X*=20%, more particles have been participated in the reduction of TTH to TTM at lower temperatures. However, to compensate a similar weight loss ratio of the reductions at higher temperatures, TTM in some particles at the pellet surface were reduced further to FeO and metallic Fe. This is shown later in **Figures 5.25** and **5.26**. The phenomenon of more TTM observed in the *X*=~20% pellets at lower temperatures is consistent with the concentration data measured from *in-situ* ND.

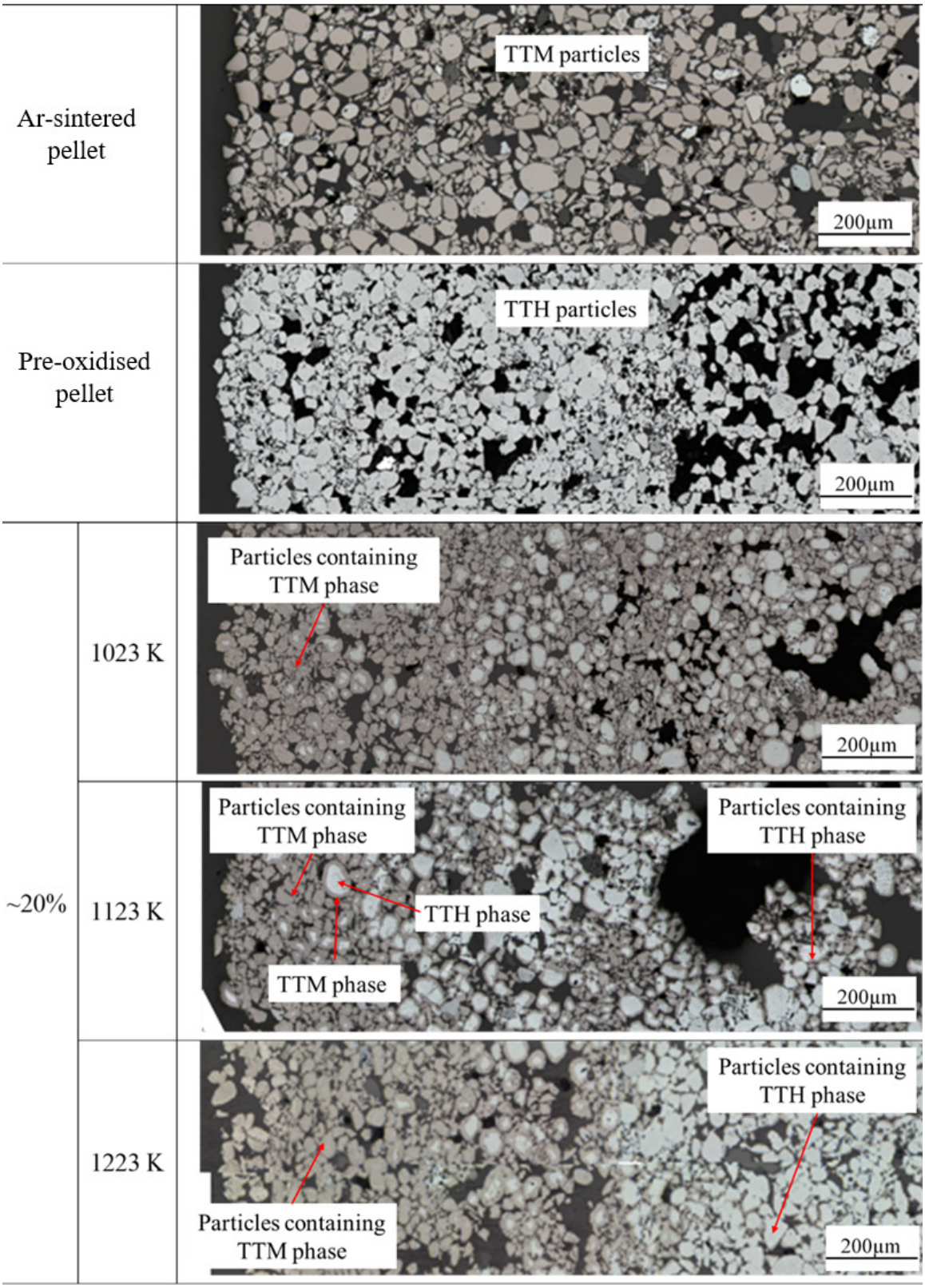

Figure 5.16– *Optical microscopy images taken from the surface to centre of each pellet, showing morphologies of X=~20% reduced pre-oxidised pellets at each temperature. The areas are shown in blue sectioned areas in* ***Figure 5.15****. The pre-oxidised pellets were reduced in a flowing of 340 ml/min 100vol% H_2 gas. Equivalent images for unreduced Ar-sintered pellets and pre-oxidised pellets are also shown for comparison*

5.3.2 Pellet-scale phase determination of the reduced pellets

EDS-line scans were applied to determine the phases present in the bright shell and dark core identified in **Subsection 5.3.1**. The EDS scans were conducted along a line from the pellet surface to pellet centre for each pellet, as indicated by the red lines in **Figure 5.15**. These results were expressed as an atomic% O/Fe ratio and plotted versus position. EDS analyses of mineral standards of Fe_2O_3, Fe_3O_4, FeO and metallic Fe were used to validate the measured atomic% O/Fe ratios, as detailed in **Subsection 3.5.2**.

The results from an EDS-line scan of an unreduced pre-oxidised pellet (X=0%) is shown in **Figure 5.17**. The black square symbols indicate the obtained atomic% O/Fe ratio at each point along the line. The four black solid lines indicate the atomic% O/Fe ratio from the corresponding mineral standards. A red dashed line is drawn to highlight clustering in the measured data. These notations are also used in all the following figures showing the results of EDS-line scans. As can be seen, in the unreduced pellet the atomic% O/Fe ratio was constant at all the positions along the line. The measured ratio (~1.8) is slightly higher than that of the Fe_2O_3 mineral standard (~1.5), this is likely attributed to levels of oxygen associated with the impure element (Ti, Al and Mg) in the pellets and the epoxy resin filled voids between particles. However, this is still consistent with TTH being the main phase in the pre-oxidised pellets before reduction. Again, as previously explained in **Subsection 4.3.2**, the scatter in the data at higher atomic% O/Fe ratio results from measurements in the regions of voids filled with epoxy resin.

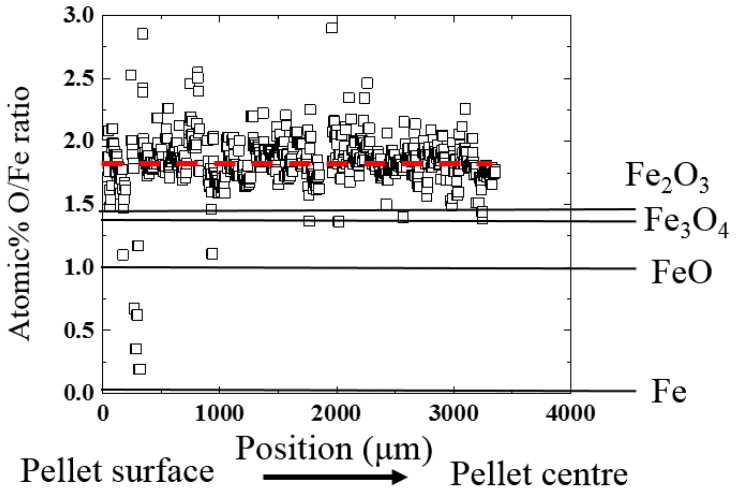

***Figure 5.17**– Atomic% O/Fe ratio profile of a cross-sectioned pre-oxidised pellet prior to reduction, measured by EDS-line scan*

EDS-line scans from partially and fully reduced pellets at 1023 K, 1123 K and 1223 K are shown in **Figure 5.18**, **Figure 5.19** and **Figure 5.20** respectively. It was found that at all temperatures, a similar trend in the change of the atomic% O/Fe ratio profile in the pellets during reduction was observed. The key features were most pronounced at 1223 K, and as such, these results are described below.

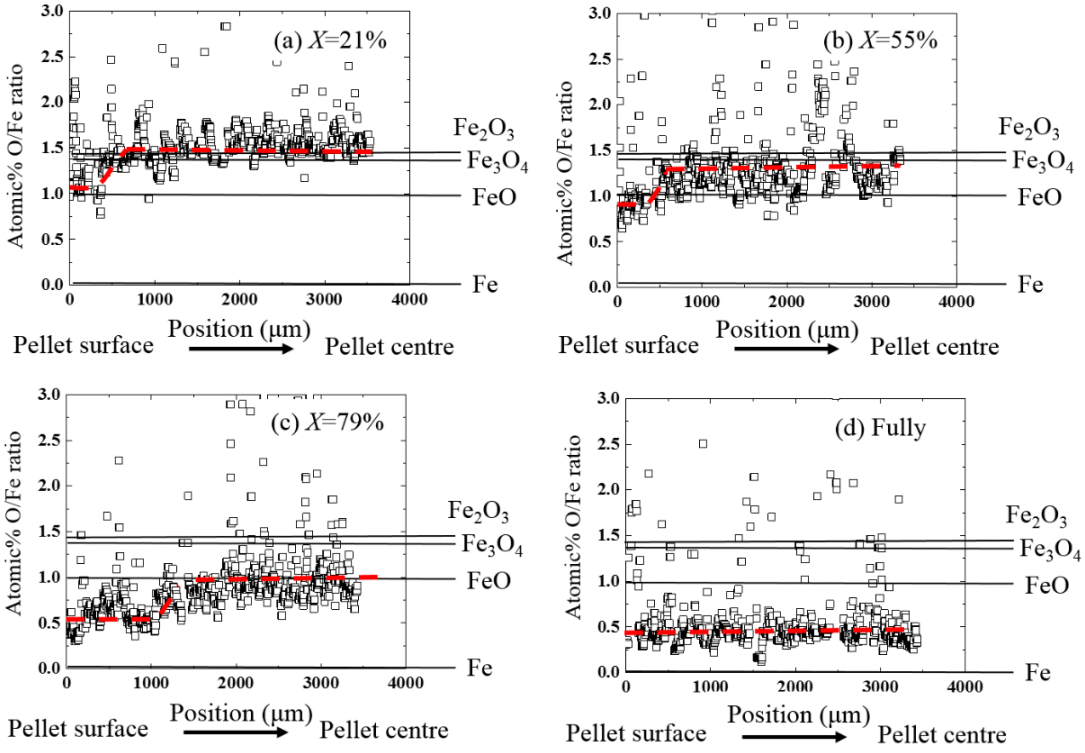

***Figure 5.18**– Atomic% O/Fe ratio profile measured by EDS-line scan of each partially and fully reduced pellet at 1023 K. (a) X=21%, (b) X=55%, (c) X=79% and (d) Fully-reduced. The four black solid lines in each figure indicate the atomic% O/Fe ratio obtained from the mineral standards of Fe_2O_3, Fe_3O_4, FeO and metallic Fe. A dashed red line is drawn to highlight the atomic% O/Fe ratio trend*

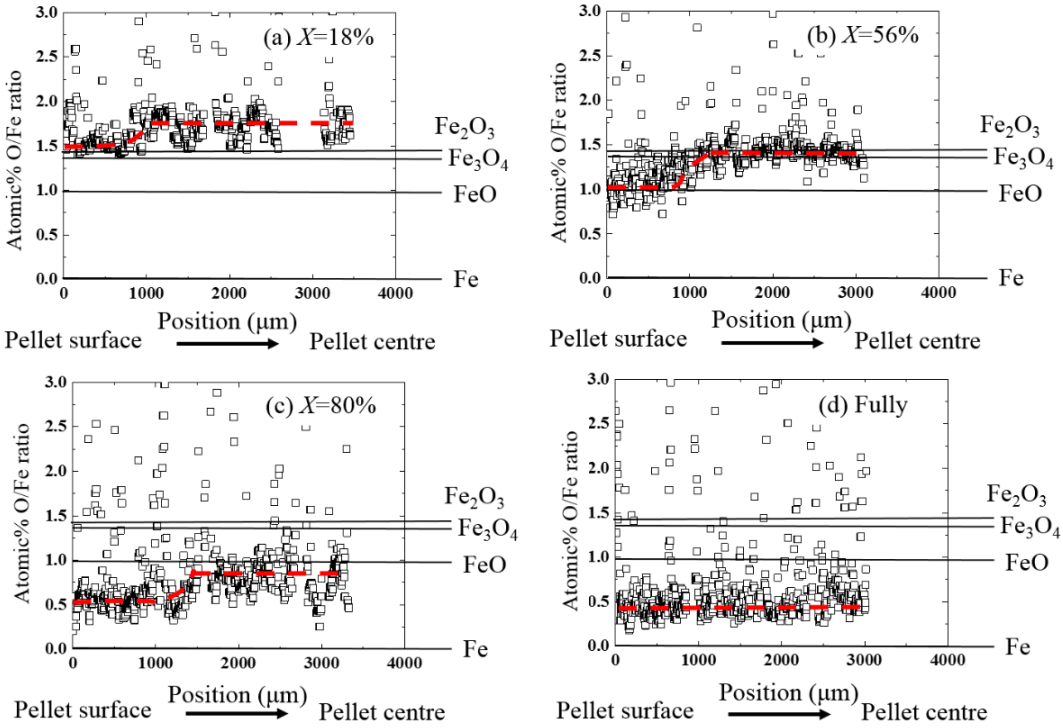

***Figure 5.19**– Atomic% O/Fe ratio profile measured by EDS-line scan of each partially and fully reduced pellet at 1123 K. (a) X=18%, (b) X=56%, (c) X=80% and (d) Fully-reduced. The four black solid lines in each figure indicate the atomic% O/Fe ratio obtained from the mineral standards of Fe_2O_3, Fe_3O_4, FeO and metallic Fe. A dashed red line is drawn to highlight the atomic% O/Fe ratio trend*

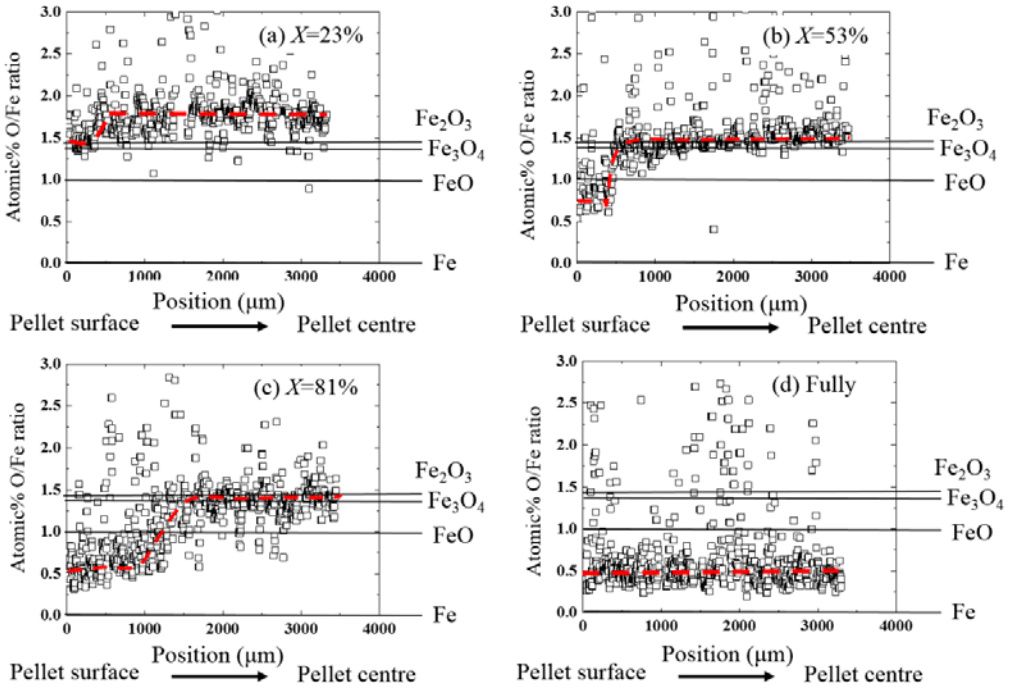

***Figure 5.20**– Atomic% O/Fe ratio profile measured by EDS-line scan of each partially and fully reduced pellet at 1223 K. (a) X=23%, (b) X=53%, (c) X=81% and (d) Fully-reduced. The four black solid lines in each figure indicate the atomic% O/Fe ratio obtained from the mineral standards of Fe_2O_3, Fe_3O_4, FeO and metallic Fe. A dashed red line is drawn to highlight the atomic% O/Fe ratio trend*

The results from EDS-line scans of pellets reduced at 1223 K are shown in **Figure 5.20**. For the fully reduced pellet shown in **Figure 5.20(d)**, the atomic% O/Fe ratio had a constant value of ~0.4 along the whole line from the pellet surface to pellet centre. This ratio is slightly larger than that measured from the mineral standard of metallic Fe (zero). This is likely due to the presence of some unreduced oxides, (such as $FeTiO_3$, TiO_2 or PSB) that are closely mixed with the metallic Fe, and again also the oxygen contained within the epoxy resin in the voids between the particles.

The line scan from the *X*=23% pellet is shown in **Figure 5.20(a)**. At the pellet inner areas (positions > ~500 μm), the atomic% O/Fe ratios were ~1.7. This value was similar to, but slightly smaller than, that obtained in the unreduced pre-oxidised pellets (~1.8) shown in **Figure 5.17**, implying that the inner areas of the *X*=23% pellet almost remained unreduced. This is consistent with the conclusion drawn from the optical microscopy images shown in **Figure 5.16**. By contrast, near the pellet surface (positions < ~500 μm), the ratios dropped slightly to ~1.4. This is consistent with TTH having been reduced to TTM at the pellet surface, although once again the measured ratio was slightly higher than that from the mineral standard of Fe_3O_4 (~1.3).

For the *X*=53% pellet shown in **Figure 5.20(b)**, a sharp transition is observed between the ratios measured near the surface of the pellets and the ratios at the centre. At the pellet surface the average atomic% O/Fe ratio was ~0.6. This value was slightly higher than the fully reduced pellet (~0.4 as shown in **Figure 5.20(d)**), indicating a mixture of metallic Fe and other unreduced iron oxides. Moving inwards, at position of ~600 μm the ratio increased to ~1.5, implying that at the pellet centre TTM (perhaps mixed with FeO) is likely to be the main phase. This is also consistent with the ND data which indicated that TTH had been completely reduced to TTM by this stage of the reduction.

For the *X*=81% pellet shown in **Figure 5.20(c)**, similar atomic% O/Fe ratios are observed at the surface and centre, as those found in the *X*=53% pellet. This again implies that the surface has been reduced to metallic Fe, while the centre remains unreduced iron oxides. However, in the case *X*=81%, the transition occurs closer to the pellet centre, at ~1200 μm. This is as expected for a reaction interface moving inwards over time.

Overall the atomic% O/Fe ratio profiles obtained at 1223 K appear generally consistent with a single interface shrinking core process, where metallic Fe is initially generated at the pellet surface, and then the reaction interface (metallic Fe/iron oxides) moves inwards to the pellet centre.

The atomic% O/Fe ratio profile for the pellets reduced at 1023 K and 1123 K show similar features to those at 1223 K. However, the transitions between higher and lower atomic% O/Fe ratio are less distinct than those observed at 1223 K. These results are similar to those obtained from the Ar-sintered pellets presented in **Subsection 4.3.2**.

5.3.3 Particle morphology of the reduced pellets at each temperature

In this subsection, back-scattered SEM images are presented which show the evolving particle-scale micro-morphologies during pellet reduction. Based on these observations, schematic graphics have been generated which illustrate the main morphological features and their evolution over time. In addition, summary tables have been produced which list the key features observed in the particle morphologies of 'green' pellets (based on the results shown in **Subsection 4.3.3**), unreduced pre-oxidised pellets, partially-reduced pellets and fully-reduced pellets at each temperature.

1. Unreduced pre-oxidised pellets

Prior to reduction, the majority of particles within the pre-oxidised pellets were uniform in appearance (see later in **Figure 5.22(a)** as an example), and only contained TTH phase (**Figure 3.7**). Non-uniform particles made up only ~15% of the total particle population (based on particle counting from light microscopy images using a similar approach outlined in **Subsection 4.3.3**). However, during reduction, it was found that these non-uniform particles showed broadly similar reduction features to those uniform ones. That being so, the particle features of the non-uniform particles are not described separately, instead, the schematics and summary tables are mainly focused on morphological evolution of the uniform particles during reduction.

In the following pages, particle morphological evolution is reported for the pre-oxidised pellets obtained from the quenching reduction experiments at 1023 K, 1123 K and 1223 K respectively.

In each case, illustration of these results starts with a schematic graphic. This schematic graphic is constructed from the collection of representative back-scattered SEM images shown in **Appendices C.5** and **C.7** for each temperature. The phases observed in the particle-scale back-scattered SEM images were initially identified by determining the elemental compositions using an SEM-EDS point analysis from representative images. Examples are shown in **Figure 5.21(a)** and **(b)**, with SEM-EDS point analysis data for corresponding areas in these images listed in **Table 5.1**. These data were an average of three points for each feature. Based on these analyses, it is concluded that, the dark grey areas indicate TTH, the grey areas indicate TTM, the light grey areas indicate FeO, and the bright areas indicate metallic Fe.

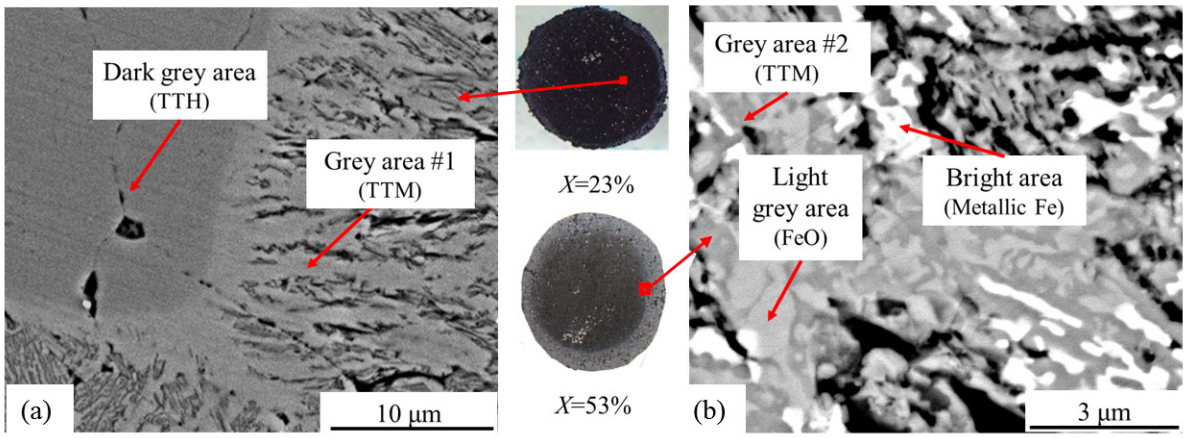

Figure 5.21 *– Example back-scattered SEM images of representative particles depicting the different contrast of phases observed inside individual particles within partially-reduced pellets obtained from quenching experiments by the sliding furnace at VUW. (a) A particle from the inner of the X=23% pellet at 1223 K. (b) a particle from the region close to the pellet-scale reaction interface in the X=53% pellet at 1223 K*

Table 5.1 *– Atomic% of the corresponding areas shown in* ***Figure 5.21*** *obtained from the SEM-EDS point analysis to identify phases. Each value is an average of three points for each feature*

Area	Fe	Ti	O	Mg	Al	Phase identification
Dark grey area	33.8	3.6	57.9	2.5	2.4	TTH
Grey area #1	37	3.7	54.1	2.5	2.7	TTM
Grey area #2	40	2.8	51.7	2.8	2.6	
Light grey	42.9	2.2	50.3	2.8	1.8	FeO
Bright	65.3	2	28	2.3	2.3	Fe

Using the information in **Table 5.1**, different iron oxide phases were then identified in the back-scattered SEM images from their relative contrast. A selection of example images is displayed in **Figures 5.22** and **5.23**, and used as a key to relate with schematic graphics (constructed to depict the morphology of each phase). Here, TTH shows a dark grey colour as in **Figure 5.22(a)**. TTM presents a grey colour, and its formation typically follows a particle-scale shrinking core process with the co-generation of micro-cracks. These micro-cracks have beneficial effects on the reduction processes, which are discussed in **Section 7.3**. Based on the back-scattered SEM images shown in **Appendices C.5** and **C.7**, this formation of TTM has been observed in the pellets reduced at early stage (X=~20%) at all temperatures studied. These features are shown in **Figure 5.22(b)** (at 1223 K) as an example. Similarly, it is found that the fully reduced particles at each temperature also present a similar morphology. Metallic Fe has grown to occupy most of the particle but coexists with some impure oxides. The metallic Fe presents a morphology of disordered branches coming off larger central spines in the fully reduced particles, as shown in **Figure 5.22(c)** (at 1123 K) as an example.

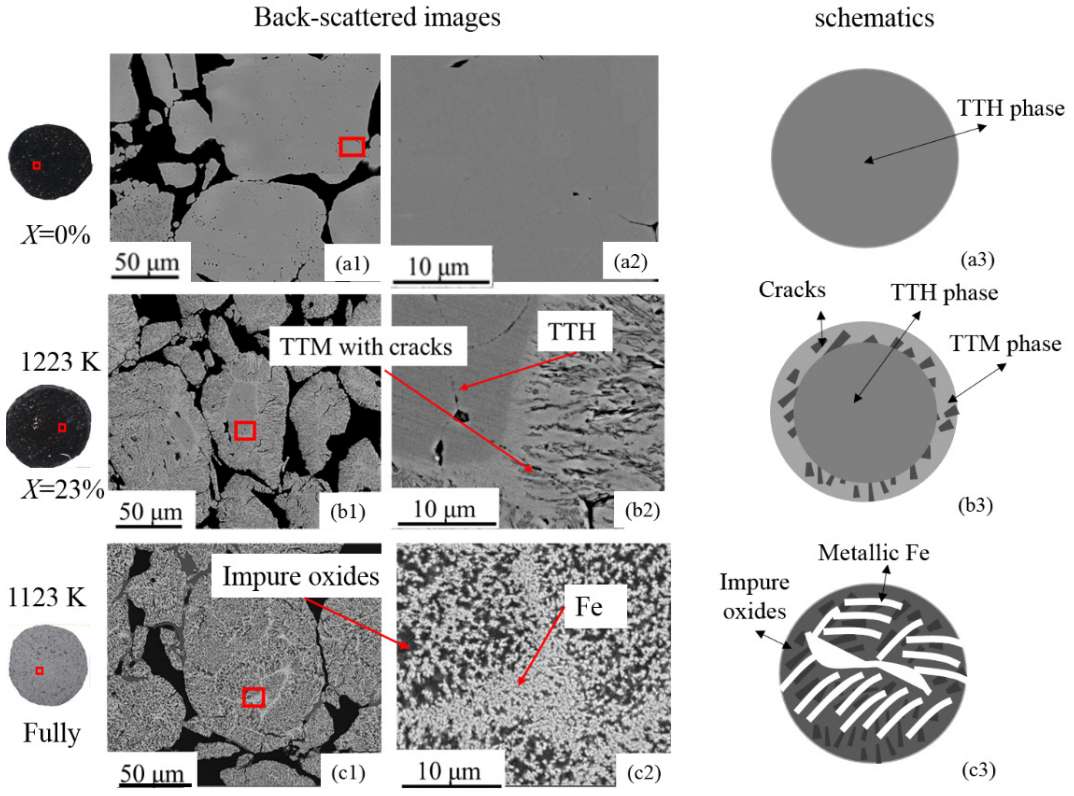

Figure 5.22 *– Examples illustrating the relationship between the schematic graphics constructed as a key to depict features of the particle morphologies, and the original back-scattered SEM images. (a) unreduced pre-oxidised pellets, (b) X=23% pellet reduced at 1223 K and (c) fully reduced pellet at 1123 K. (1) shows lower magnification back-scattered SEM images from the respective area in the corresponding pellet (at left). (2) shows higher magnification back-scattered SEM images of the phase morphologies from the highlighted areas in (1). (3) shows the schematic graphics constructed to illustrate the key features in (2)*

However, FeO shows different features in the particles at different temperatures. FeO is difficult to be observed in the particles at 1023 K. Instead, small amounts of metallic Fe are directly found from TTM (in **Figure 5.23(a)**). On the other hand, FeO is observed in the particles reduced at 1123 K and 1223 K, but the morphology changes with temperature. At 1123 K, FeO nucleates throughout the whole particle (in **Figure 5.23(b)**), while at 1223 K, FeO occupies most of the particle with unreduced TTM shrinking into small 'islands' (in **Figure 5.23(c)**). At both temperatures, metallic Fe is initially found in small spots along FeO, which then slowly occupies most of the particle, again creating the morphology in **Figure 5.22(c**).

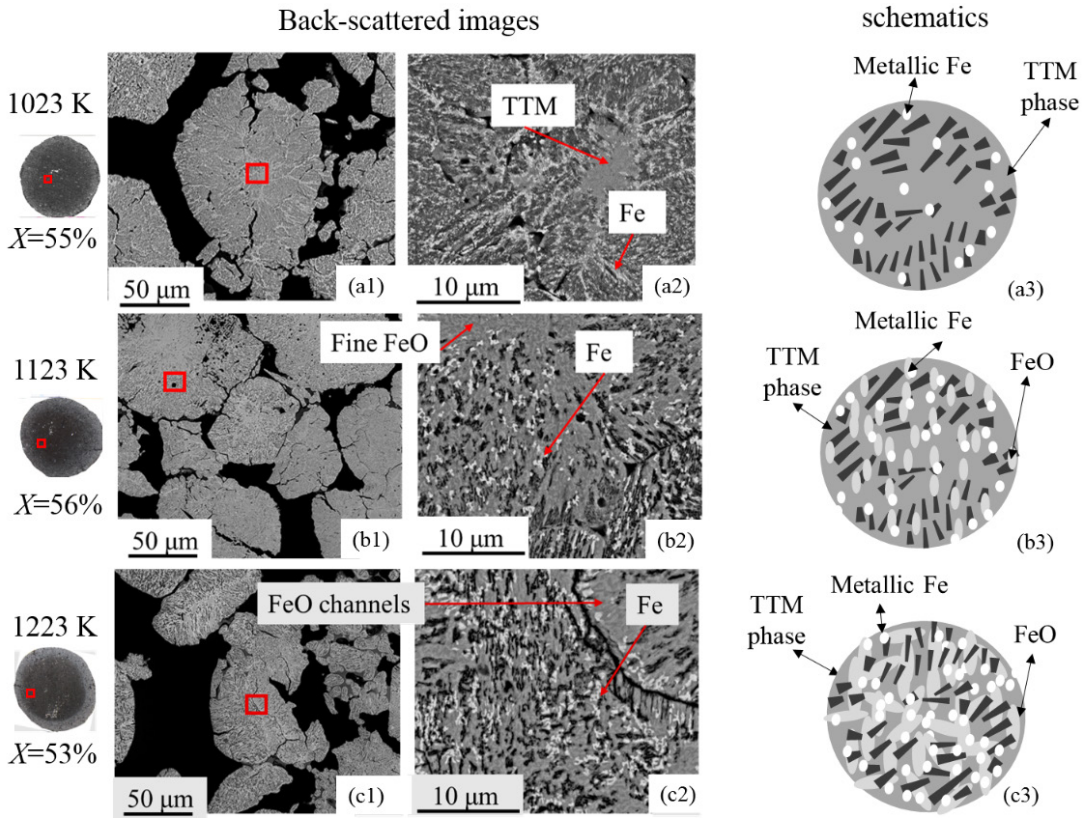

***Figure 5.23** – Examples illustrating the relationship between the schematic graphics constructed as a key to depict features of the particle morphologies, and the original back-scattered SEM images. (a) X=55% pellet reduced at 1023 K, (b) X=56% pellet reduced at 1123 K and (c) X=53% pellet reduced at 1223 K. (1) shows lower magnification back-scattered SEM images from the respective area in the corresponding pellet (at left). (2) shows higher magnification back-scattered SEM images of the phase morphologies from the highlighted areas in (1). (3) shows the schematic graphics constructed to illustrate the key features in (2)*

The schematic graphics of the particle morphology at each temperature and reduction stage is to illustrate all of these features. It should be noted that throughout the following graphics, if the total amount of a phase present increases as the reduction progresses, more of the corresponding features are added to the diagram.

2. Particle morphologies of the partially reduced pellets from 1023 K

In **Figure 5.24**, a schematic graphic is presented which illustrates the morphological evolution of the particles at different positions during reduction at 1023 K. (The original back-scattered SEM images from which this schematic has been constructed are shown in **Appendix C.5**). As can be seen, metallic Fe is generated gradually from the pellet surface to pellet centre, which is broadly consistent with the results obtained from the EDS-line scans shown in **subsection 5.3.2**. It should be noted that although the concentration of FeO showed a maximum value of ~10 wt% from the results of the *in-situ* ND (see in **Figure 5.13**) at X= ~32%, it is difficult to observe any FeO in the particle-scale back-scattered SEM images.

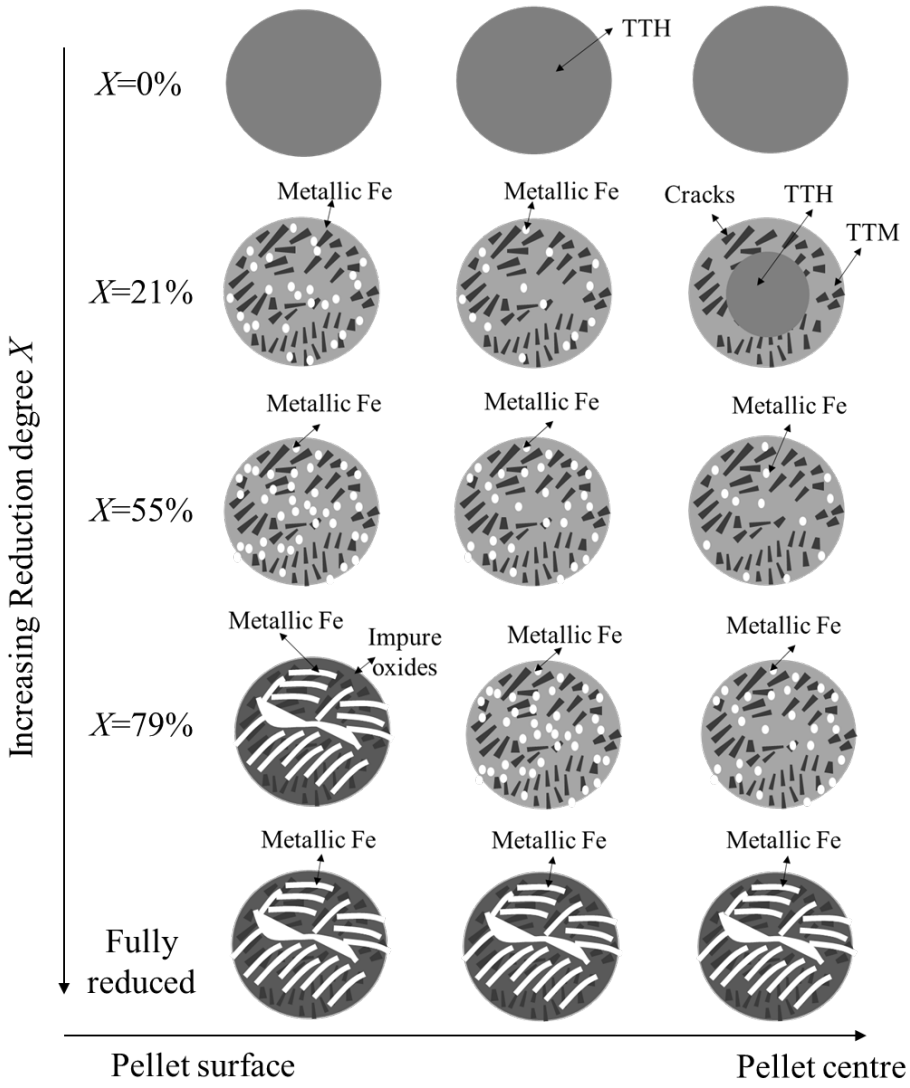

***Figure 5.24**– Schematic graphic of particle morphological evolution during reduction of the pre-oxidised pellets at 1023 K*

Descriptions of the key particle-scale morphological features that occurred during reduction at 1023 K are summarised in **Table 5.2**.

***Table 5.2**– Summary of the main features of the particle morphologies in the 'green' pellets, unreduced pre-oxidised pellets and reduced pellets investigated at 1023 K*

Scale	'Green' pellets (Ground raw particles pelletised with 1wt% Bentonite)	Pre-oxidised pellets ('Green' pellets sintered in air for 2 hours at 1473 K)	Quenched from 1023 K, 100vol% H_2, 340 ml/min			
			21% (1min)	55% (4mins)	79% (10mins)	Fully (25mins)
Pellet	1. The morphologies of the particles are homogeneous.	1. TTM is transformed into TTH. The morphologies of the particles are homogeneous.	1. It is difficult to observe a pellet-scale reaction interface.	1. A pellet-scale reaction interface is vaguely observed.	1. A pellet-scale reaction interface is vaguely observed.	1. The morphology of the pellet is homogeneous, but shows brighter than that of the unreduced one.
Particle	2. The particle sizes are randomly distributed. 3. Most particles are smooth at the surface with a light grey colour. 4. Fine lamellar structure (enriched with Ti) can be observed in ~10% of the particles. 5. A small amount of silicate particles which are smaller than ~30 μm are present.	2. The particle size distribution is similar to 'Green' #2. 3. The morphologies of most particles are slightly darker than in 'Green' #3, as the main phase is TTH. 4. Compared to 'Green' #4, there are three different non-uniform particles. Two of them contain a higher Ti content: one with a blobby structure and the other with a discontinuous lamellar structure. The third type has a hatched morphology, which contains up to 8 to 10wt% Mg and Al.	2. The particle size distribution is similar to 'Green' #2. 3. The morphology of the unreduced particles at the centre of the pellets is similar to Pre-oxidised #3. 4. For the reduced particles, TTM is generated following both pellet and particle-scale shrinking core phenomena. In addition, micro-cracks are also observed in the particles. After TTH is reduced to TTM, the particles show a structure with disordered branches off a central spine. 5. It is difficult to observe the FeO morphologies in the particles. 6. In the particles at pellet surface, metallic Fe spots are observed. The generation of metallic Fe starts close to the cracks throughout the whole particles.	2, 3, 4 and 5 are similar to 21% #2, 3, 4, and 5 respectively. 6. In the particles at the pellet surface, more metallic Fe spots are observed. However, small metallic Fe spots are also found in the particles at the centre of the pellet. This shows that, the generation and growth of metallic Fe starts from the particles at pellet surface and then to the particles at pellet centre, forming a pellet-scale gradient.	2, 3, 4 and 5 are similar to 21% #2, 3, 4, and 5 respectively. 6. The generation of metallic Fe is similar to 55% #6. Moreover, the particles at the pellet surface are fully reduced to metallic Fe. The generated metallic Fe seems to replace TTM by following its structure as in 21% #4.	The morphologies of the fully reduced particles throughout the whole pellets are similar to 79% #6.

2. Particle morphologies of the reduced pellets from 1123 K

In **Figure 5.25**, a schematic graphic is presented which illustrates the morphological evolution of the particles at different positions during reduction at 1123 K. (The original back-scattered SEM images from which this schematic has been constructed are shown in **Appendix C.6**). The particle morphological evolution at this temperature is in general similar to that at 1023 K (as shown in **Figure 5.24**), however the morphology of FeO was observed to be very fine within the particles during the 1123 K reduction.

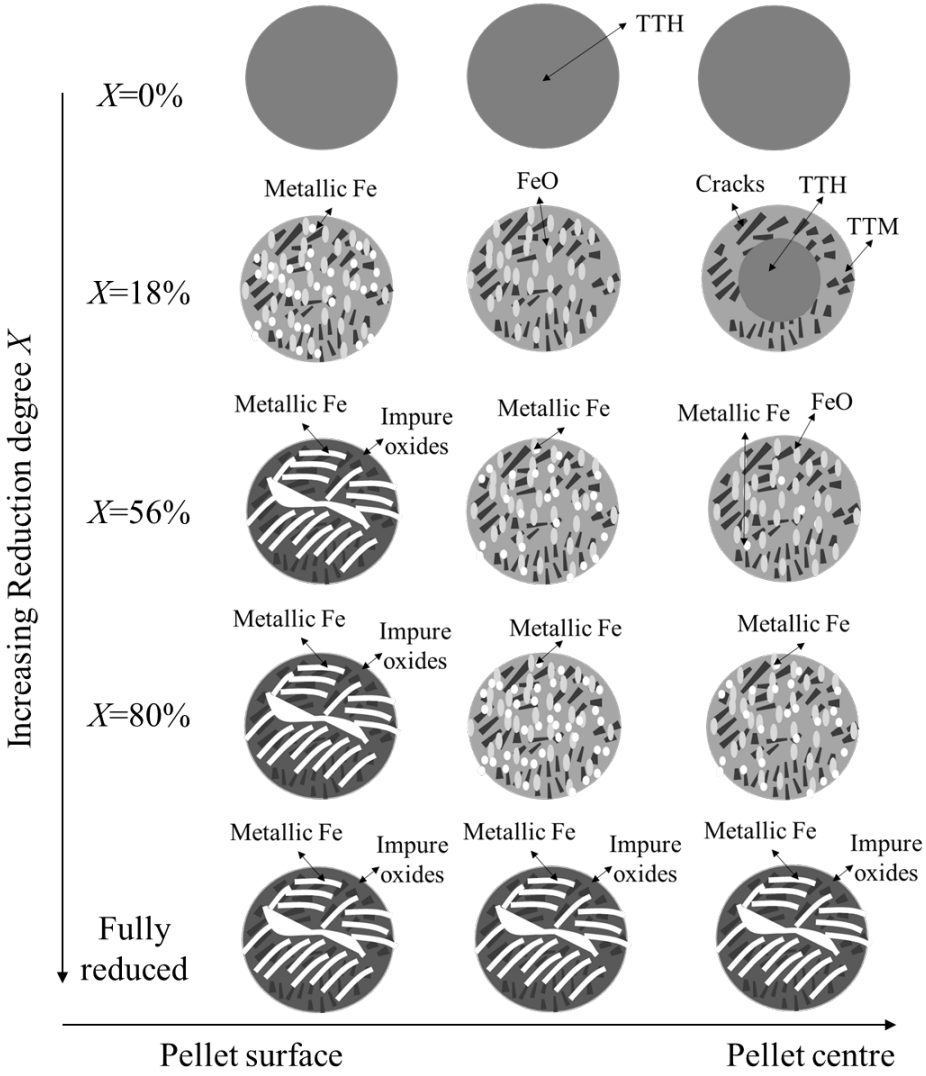

***Figure 5.25**- Schematic graphic of particle morphological evolution of the pre-oxidised pellets reduced at 1123 K*

Descriptions of the key particle-scale morphological features that occurred during reduction at 1123 K are summarised in **Table 5.3**.

***Table 5.3**– Summary of the main features of the particle morphologies in the 'green' pellets, unreduced pre-oxidised pellets and reduced pellets investigated at 1123 K*

Scale	'Green' pellets (Ground raw particles pelletised with 1wt% Bentonite)	Pre-oxidised pellets ('Green' pellets sintered in air for 2 hours at 1473 K)	Quenched from 1123 K, 100vol% H_2, 340 ml/min			
			18% (45s)	56% (2min50s)	80% (5mins40s)	Fully (18mins)
Pellet	1. The morphologies of the particles are homogeneous.	1. TTM is transformed into TTH. The morphologies of the particles are homogeneous.	1. Similar to 1023 K 21% #1, it is hard to observe a pellet-scale reaction interface.	1. A pellet-scale reaction interface is observed.	1. A pellet-scale reaction interface is observed.	1. The morphology of the pellet is homogeneous, but shows brighter than that of the unreduced one.
Particle	2. The particle sizes are randomly distributed. 3. Most particles are smooth at the surface with a light grey colour. 4. Fine lamellar structure (enriched with Ti) can be observed in ~10% of the particles. 5. A small amount of silicate particles which are smaller than ~30 μm are present.	2. The particle size distribution is similar to 'Green' #2. 3. The morphologies of most particles are slightly darker than in 'Green' #3, as the main phase is TTH. 4. Compared to 'Green' #4, there are three different non-uniform particles. Two of them contain a higher Ti content: one with a blobby structure and the other with a discontinuous lamellar structure. The third type has a hatched morphology, which contains up to 8 to 10wt% Mg and Al.	2,3, and 4 is similar to 1023 K 21% #2, 3 and 4. 5. In the particles at the pellet surface, FeO nucleates are observed. The generation of FeO in the particles seems to start close to the micro-cracks throughout the whole particles. Less FeO is observed in the particles at the pellet inner area. It seems that the generation of FeO presents a pellet-scale gradient with the particle closer to the pellet surface reduced faster than particles at pellet centre 6. The metallic Fe spots in the particles is initially found from the fine FeO throughout the whole particles.	2,3, 4, and 5 is similar to 18% #2, 3, 4, and 5. 6. The particles at the pellet surface are almost fully reduced to metallic Fe, which has a similar morphology as in 1023 K 79% #6.	2,3, 4, 5, and 6 is similar to 56% #2, 3, 4, 5, and 6.	The metallic Fe in the fully reduced particles is similar to 1023 K Fully.

3. Particle morphologies of the partially reduced pellets from 1223 K

In **Figure 5.26**, a schematic graphic is presented which illustrates the morphological evolution of the particles at different positions during reduction at 1223 K. (The original back-scattered SEM images from which this schematic has been constructed are shown in **Appendix C.7**). A key difference to the results presented at lower temperatures is that, at 1223 K, FeO nucleates developed throughout the whole particles. Moreover, the generation of metallic Fe seems to follow FeO as the reduction progresses.

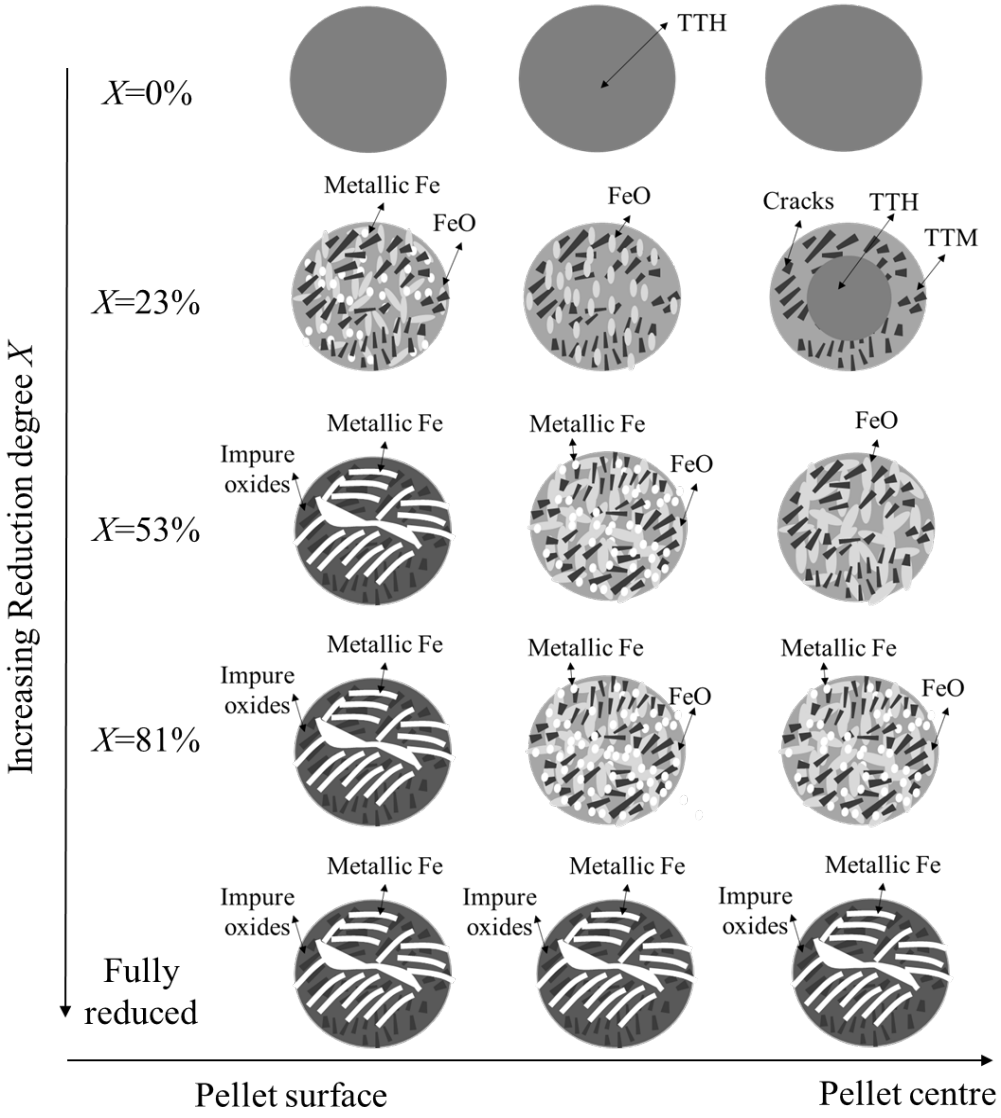

***Figure 5.26**- Schematic graphic of particle morphological evolution of the pre-oxidised pellets reduced at 1223 K*

Descriptions of the key particle-scale morphological features that occurred during reduction at 1123 K are summarised in in **Table 5.4**.

***Table 5.4**– Summary of the main features of the particle morphologies in the 'green' pellets, unreduced pre-oxidised pellets and reduced pellets investigated at 1223 K*

Scale	'Green' pellets (Ground raw particles pelletised with 1wt% Bentonite)	Pre-oxidised pellets ('Green' pellets sintered in air for 2 hours at 1473 K)	Reduced and quenched from 1223 K, 100vol% H_2, 340 ml/min			
			23% (30s)	53% (1min40s)	81% (3mins20s)	Fully (8mins)
Pellet	1. The morphologies of the particles are homogeneous.	1. TTM is transformed into TTH. The morphologies of the particles are homogeneous.	1. A pellet-scale reaction interface is observed.	1. A pellet-scale reaction interface is observed.	1. A pellet-scale reaction interface is vaguely observed.	1. The morphology of the pellet is homogeneous, but shows brighter than that of the unreduced one.
Particle	2. The particle sizes are randomly distributed. 3. Most particles are smooth at the surface with a light grey colour. 4. Fine lamellar structure (enriched with Ti) can be observed in ~10% of the particles. 5. A small amount of silicate particles which are smaller than ~30 µm are present.	2. The particle size distribution is similar to 'Green' #2. 3. The morphologies of most particles are slightly darker than in 'Green' #3, as the main phase is TTH. 4. Compared to 'Green' #4, there are three different non-uniform particles. Two of them contain a higher Ti content: one with a blobby structure and the other with a discontinuous lamellar structure. The third type has a hatched morphology, which contains up to 8 to 10wt% Mg and Al.	2. 3. and 4 is similar to 1023 K 21% #2, 3 and 4. 5. FeO is also observed in the particles. Compared to the morphology at 1123 K, more FeO nucleates in the particles at 1223 K are developed. 6. In the particles at the pellet surface, the metallic Fe morphology is similar to 1123 K 18% #6. The generation of metallic Fe is initially observed along FeO.	2. 3. and 4 is similar to 1023 K 21% #2, 3 and 4. 5. The morphology of the FeO is similar to 23% #5. However, with a combination of FeO nucleates growth and generation of more FeO nucleates, FeO seems to occupy most of the particles with remaining un-reduced TTM shrinking to small 'islands'. 6. The particles at the pellet surface are almost fully reduced to metallic Fe, which has a similar morphology as in 1123 K 56% #6.	2,3, 4, 5, and 6 is similar to 53% #2, 3, 4, 5, and 6.	The metallic Fe in the fully reduced particles is similar to 1023 K Fully.

5.3.4 Particle morphologies of the fully reduced pellets at higher temperatures

In addition to the quenching reduction experiments performed between 1023 K and 1223 K, fully-reduced pellets were also produced from the TGA experiments at temperatures up to 1443 K. The particle morphologies in those fully reduced pellets were also characterised to examine the effects of temperature on the morphology of metallic Fe. It should be noted that these pellets were not quenched after complete reduction, but were subject to controlled cooling in the TGA furnace (at Callaghan Innovation) at a rate of 40 K/min.

Back-scattered SEM images showing the representative particle morphologies from 1043 K to 1443 K from the TGA reduction experiments are shown in **Figure 5.27(a)** to **(e)**. At lower temperatures (1043 K and 1143 K, **Figure 5.27(a)** and **(b)**), the morphology of the metallic Fe showed a similar structure to those observed in the partially reduced pellets investigated from quenching. As the reduction temperature increased, the structure of metallic Fe coarsened, forming more bulbous clusters (**Figure 5.27(d) and (e)**). This coarsening effect is similar to that of the Ar-sintered pellets reduced at higher temperatures (**Figure 4.27(d)** and **(e)**), which is attributed to an increased mobility of Fe atoms at higher temperatures.

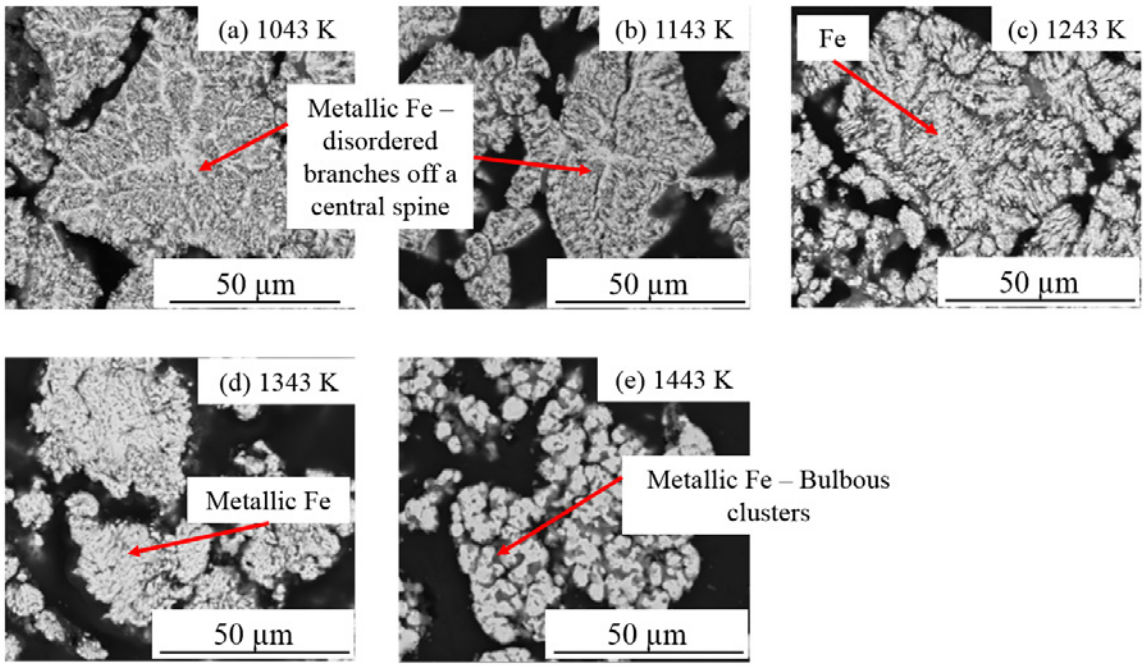

***Figure 5.27**- Back-scatter SEM images of cross-sectioned fully reduced pellets from the TGA experiment (Callaghan Innovation) showing the final morphologies of particles at each reducing temperature studied. (a) 1043 K, (b) 1143 K, (c) 1243 K, (d) 1343 K and (e) 1443 K [162]*

5.4 Summary

In this chapter, the results of the pre-oxidised pellets reduced in H_2 gas have been reported. Detailed discussion and analysis of these results is presented in the following **Chapters 6**, 7 and **8**. Similar to the results of Ar-sintered pellets in **Chapter 4**, it was found that with increasing temperature, H_2 gas flow rates, H_2 gas concentrations, and decreasing pellet size (studied only at 1343 K), the reduction rate increased.

The H_2 gas reduction of the pre-oxidised pellets was monitored by the *in-situ* ND measurements at the Wombat facility at ANSTO, and the results were analysed to determine the phase evolution during the reaction. For the reduction conditions studied, TTH was rapidly consumed in the early reduction stages. Following this, TTM and FeO were both generated and then consumed. Metallic Fe and some residual $FeTiO_3$ were the final products observed. A characteristic time, τ, was defined for these experiments, which allowed comparison of the phase evolution during reduction at different conditions. It was found that temperature significantly affected the observed evolution of TTM and FeO. As the temperature increased from 1023 K to 1223 K, the maximum concentration of TTM decreased, while that of FeO increased.

Changes in the pellet and particle-scale morphologies within the pellets during reduction were also studied. The results of the macro-morphologies indicate a pellet-scale reaction interface in most of the reduced pellets. This reaction interface distinguishes a bright shell and a dark core. EDS-line scans confirmed the initial generation of metallic Fe at the pellet surface. A reaction interface was observed that moved towards the pellet centre over time, implying a single interface shrinking core mechanism. However, these results also imply that the later stage reductions in the pellet (X > 80%) occur after the shrinking core has disappeared, and the particle-scale effects on the reactions is likely to be pronounced, which will be analysed in **Section 8.2**.

It should be noted that the reduction temperature significantly affected the morphological evolution of FeO. At 1023 K, it was difficult to observe FeO in the particles. With increasing temperature, the morphology of FeO nucleates was found at 1123 K, but gradually occupies most of the particles as temperature further increased to 1223 K.

Similarly, the metallic Fe generated in the particles at lower temperatures showed a structure with disordered branches coming off larger central spines. At 1223 K metallic Fe follows the morphology of FeO, and then slowly grows into a similar structure as observed at lower temperatures. However, at temperatures significantly above 1223 K, completely reduced pellets did not show the morphology of disordered branches. Instead, pellets quenched from these temperatures exhibited metallic Fe formed into more bulbous clusters. This, again, may reflect an increased local mobility of Fe atoms at elevated temperatures.

Chapter 6
Kinetic analysis of reducing Ar-sintered and pre-oxidised pellets in H_2 gas

The results presented in **Chapters 4** and **5** indicate that reduction of both the Ar-sintered and the pre-oxidised pellets in H_2 gas display similar characteristics:

1. From the TGA reduction experiments above the critical flow rate (at Callaghan Innovation) in **Sections 4.1** and **5.1**, the reduction rate of both types of pellets was found to be strongly dependent on the reaction temperature and pellet diameter (at 1343 K). The dependence on pellet diameter (at 1343 K) indicates that a pellet-scale process must in part play a role in controlling the reduction.
2. From the microstructure analysis of each partially reduced pellet, only one dark core and one bright shell are observed (**Figures 4.15** and **5.15**). This is despite the reduction of both types of pellets being complex processes evolving multiple phases simultaneously. Moreover, these observations also showed that metallic Fe was first generated in the particles at the pellet surface, and then a reaction front progressed towards the pellet centre. Hence, for a simple analysis of the kinetics, it is arguable to just consider a single reaction step during reduction, i.e. the generation of metallic Fe from the iron oxide. This assumption has been successfully applied in many previous studies of the gas-based iron ore reduction (as listed in **Table 2.3**).

Consequently, this chapter presents a discussion of the application of a single interface SCM to the reduction of both types of pellets. This model is applied to describe the experimental data obtained from the TGA reduction experiments of both types of pellets (**Sections 4.1** and **5.1**), and hence used to determine the rate-limiting mechanism. Note this analysis is carried out at flow rates above the crucial flow rate, eliminating the mass transfer in the gas species as a rate-limiting mechanism in the SCM. The chapter is divided into the following sections:

- **Section 6.1**: Determination of the rate-limiting step
- **Section 6.2**: Calculation of the activation energy
- **Section 6.3**: Establishment of the minimal critical pellet size for the model at 1343 K
- **Section 6.4**: Evaluating the accuracy of pellet reduction rate from the model
- **Section 6.5**: Summary of the kinetic analysis

Note that some of the contents have already published in a paper of the *author [162]*.

6.1 Determination of the rate-limiting step using the SCM

By considering only the interfacial chemical reaction and gas diffusion through the product layer steps in the model, equation **6.1** can be derived. (This is obtained by combining equations **2.3** and **2.4** listed in **Table 2.5**). This equation assumes that each step occurs sequentially in series, and the slowest step, i.e. the step that requires the longest time, is regarded as the rate-limiting step. In this case, the total time for the reaction is obtained from the sum of the times required for each step [138]. Note that in the following context, if it is not specified, the term 'diffusion' stands for gas diffusion through the product layer.

$$t = \frac{1}{k_s'} I(X_a) + \frac{1}{D_e'} D(X_a) \quad \textbf{(6.1)}$$

where $$I(X_a) = 1 - (1 - X_a)^{\frac{1}{3}} \quad \textbf{(6.2)}$$

and $$D(X_a) = 1 - 3(1 - X_a)^{\frac{2}{3}} + 2(1 - X_a) \quad \textbf{(6.3)}$$

and $$\frac{1}{k_s'} = \frac{\rho_B R}{b k_s C_{Ag}} \quad \textbf{(6.4)}$$

and $$\frac{1}{D_e'} = \frac{\rho_B R^2}{6 b D_e (C_{Ag} - C_{As})} \quad \textbf{(6.5)}$$

Here, $X_a = {}^{X}/_{100}$ is the reduction degree expressed as a decimal, k_s' is the apparent reaction rate constant, and D_e' is the apparent diffusion rate constant. $I(X_a)$ denotes a function which describes the interfacial chemical reaction dependence, and $D(X_a)$ denotes a function which describes the diffusion dependence. Other notations have been previously defined in **Subsection 2.3.2**. Equation **6.1** can be linearised by dividing both sides either by $I(X_a)$ or $D(X_a)$ to generate equations **6.6** and **6.7**. This enables the effects of each dependence term to be analysed by plotting the data obtained from the TGA experiment.

$$\frac{t}{I(X_a)} = \frac{1}{k_s'} + \frac{1}{D_e'} \frac{D(X_a)}{I(X_a)} \quad \textbf{(6.6)}$$

$$\frac{t}{D(X_a)} = \frac{1}{k_s'} \frac{I(X_a)}{D(X_a)} + \frac{1}{D_e'} \quad \textbf{(6.7)}$$

If linear fits are obtained by plotting $t/_{I(X_a)}$ against $D(X_a)/_{I(X_a)}$ in equation **6.6**, or $t/_{D(X_a)}$ against $I(X_a)/_{D(X_a)}$ in equation **6.7**, then the experimental data is regarded to be well described by the single interface SCM. Moreover, the slope and intercept in these linear relations provide insights to determine the rate-limiting step, and the apparent diffusion and/or reaction rate constant. As such, in equation **6.6**, the gradient $1/_{D_e'}$ describes the relative contribution of the gas diffusion component to the rate-limiting step, while the y-axis intercept determines $1/_{k_s'}$. By contrast, in equation **6.7**, the gradient $1/_{k_s'}$ describes the relative contribution of the interfacial chemical reaction component to the rate-limiting step, while the y-axis intercept determines $1/_{D_e'}$.

6.1.1 Assessing the kinetics of Ar-sintered pellets

Equations **6.6** and **6.7** were applied to the reduction degree data obtained from the TGA experiments in which the Ar-sintered pellets were reduced at a series of temperatures from 993 K to 1443 K above the critical flow rate (raw data shown in **Figure 4.2**). The resulting plots are illustrated in **Figure 6.1**. The expected relationships obtained from equation **6.6** are shown in **Figure 6.1(a)** (lower temperature data) and **(b**) (higher temperature data). Similarly, the expected relationships obtained from equation **6.7** are shown in **Figure 6.1(c)** and **(d)**.

Taken together, these figures, present strong evidence that the single interface SCM provides a good description of the reduction rate over the period during which most of the reaction occurs. It can be seen that reasonable linear fits are obtained for all data sets between X=10% and X=90%. The poorer agreement observed during the very early and very late stages of the reaction is to be expected. During the very early (initial) stages, the reaction interface will take time to develop (as it is not infinitesimally thick), while any experimental measurement errors during this period are amplified by the ratio of a short time and a small mass loss. Similarly, once the reduction degree exceeds 90% (latest stage), the morphologies observed in the microstructure analysis have become established throughout the pellets, with the remaining reactions sites interspersed within the metallic Fe such that they can no longer be considered as a single core (**Figure 5.24** to **5.26** or **Appendices B.5** to **B.7**). In addition, reactions associated with residual Fe-Ti-O phases might occur at higher reduction degrees, which may affect the fitting of the model (in **Chapter 8**). Consequently, the data obtained at both lower

and higher reduction degrees are not well described by the single interface SCM. This phenomenon of the poorer agreement at both lower and higher reduction degrees is consistent with the pellet-scale microstructure analysis shown in **Figure 4.15**– at both relatively lower and higher reduction degrees, the observation of the shrinking core became less apparent.

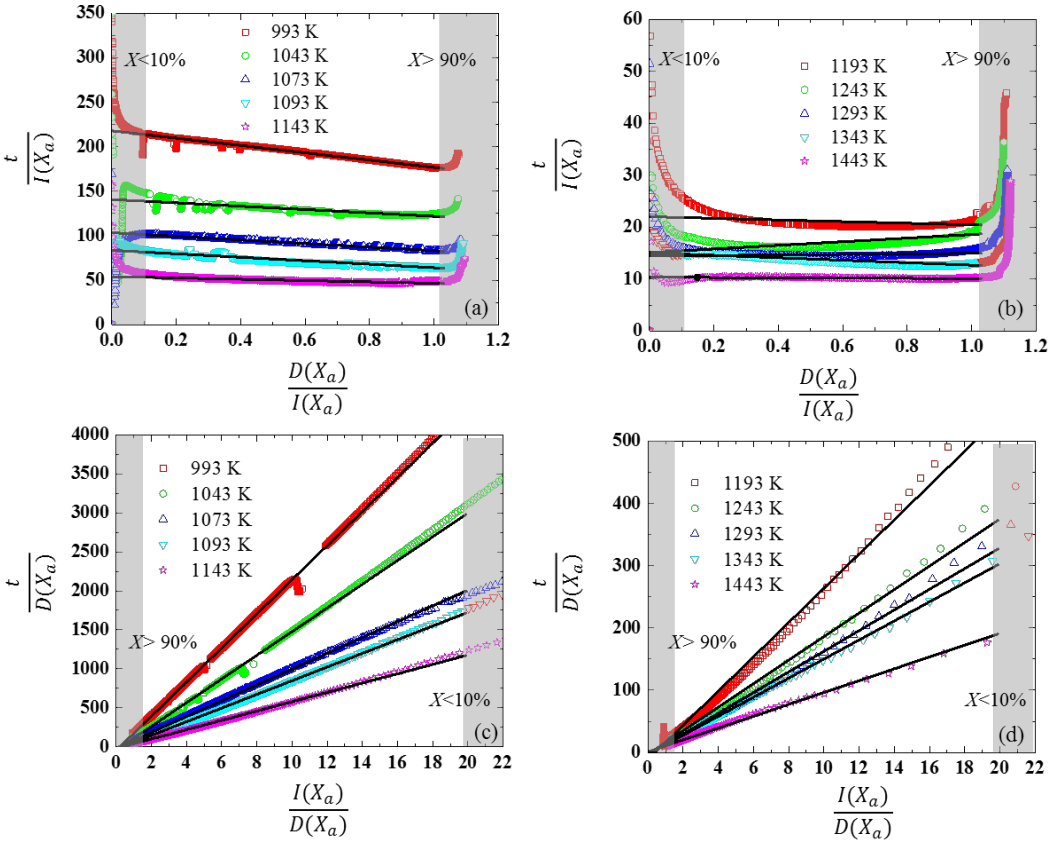

***Figure 6.1**- Plots showing correlations of the experimental TGA data from the Ar-sintered pellets with the relationships expected from equations **6.6** and **6.7**. Data were obtained from TGA experiments reducing Ar-sintered pellets (~7 mm diameter) at temperatures from 993 K to 1443 K above the critical flow rate. (a) Plots relating to equation **6.6** from 993 K to 1143 K; (b) Plots relating to equation **6.6** from 1193 K to 1443 K; (c) Plots relating to equation **6.7** from 993 K to 1143 K; and (d) Plots relating to equation **6.7** from 1193 K to 1443 K. In all figures, linear fits were made between X=10% and X=90%, and are shown extrapolated to the y-axis*

As shown in **Figure 6.1(a)** and **(b)**, almost all the plots exhibit an approximately zero gradient (except at 993 K where a slight negative gradient is observed), and a non-zero positive y-axis intercept. This indicates that the influence on the reaction rate of gas diffusion through the product layer is negligible (as $1/D_e' \approx 0$). With the positive y-axis intercept at all temperatures, it also implies that the reaction is controlled by the interfacial chemical reaction rate.

This is confirmed by the linear fits shown in **Figure 6.1(c)** and **(d)**, where non-zero positive gradients were obtained, indicating that in each case the reaction rate is at least partly controlled

by the $I(X_a)$ component. Moreover, at all temperatures, the y-axis intercept is zero, confirming that the diffusion coefficient can be neglected for the range of temperatures studied here, such that interfacial chemical reaction control is the primary rate-limiting mechanism.

6.1.2 Assessing the kinetics of pre-oxidised pellets

Equations **6.6** and **6.7** were also applied to analyse the experimental TGA data from reductions of the pre-oxidised pellets at temperatures from 1043 K to 1443 K above the critical flow rate (raw data shown in **Figure 5.2**). Following a similar approach to **Subsection 6.1.1**, the resulting plots are shown in **Figure 6.2**.

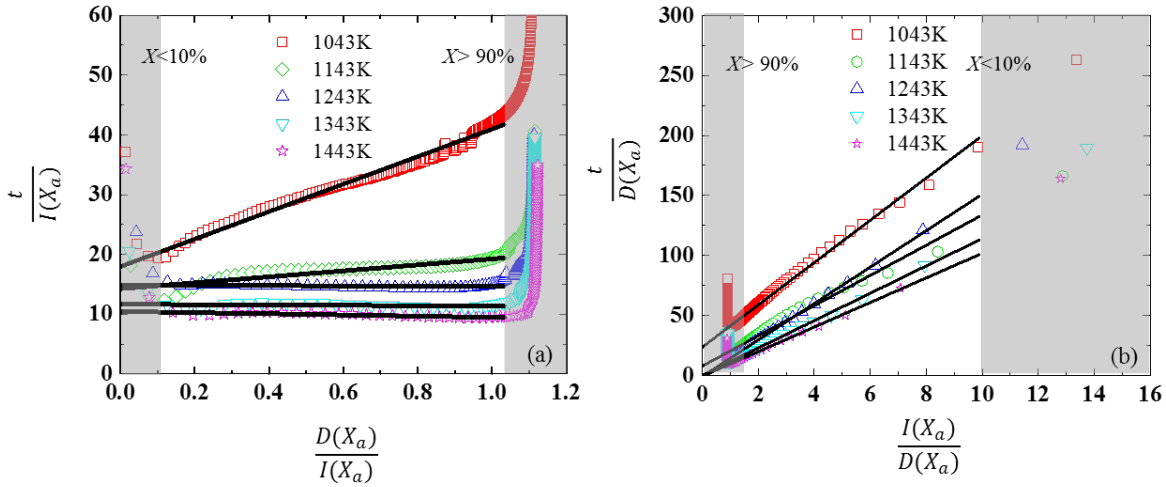

***Figure 6.2**- Plots showing correlations of the experimental TGA data from the pre-oxidised pellets with the relationships expected from equations **6.6** and **6.7**. Data were obtained from TGA experiments reducing pre-oxidised pellets (~7 mm diameter) at temperatures from 1043 K to 1443 K above the critical flow rate. (a) Plots relating to equation **6.6**; (b) Plots relating to equation **6.7**. In both figures, linear fits were made between X=10% and X=90%, and are shown extrapolated to the y-axis [162]*

As before, the linearity of the plots in **Figure 6.2** provides strong evidence that, for each of the experimentally studied temperatures, the single interface SCM provides a good description of the period during which most of the reaction occurs. Similarly to the Ar-sintered pellets, reasonable linear fits are again obtained for all data sets between X=10% and X=90%.

In **Figure 6.2(a)**, the linear fits at each temperature exhibit a non-zero y-axis intercept, but only the data at 1043 K exhibits a linear gradient that is appreciably more than zero (the other lines are all close to horizontal). This implies that at T≥1143 K the diffusion component of the rate-limiting step is zero (as $1/D'_e \approx 0$), meaning that the reaction is controlled dominantly by the interfacial chemical reaction rate at the reaction interface. However, at 1043 K, a positive

gradient and a non-zero intercept mean that mixed control is observed, in which both diffusion and interfacial chemical reaction play a role.

These conclusions are confirmed by the linear fits shown in **Figure 6.2(b)**. At all temperatures ≥1143 K, the y-axis intercept is zero, confirming that the diffusion coefficient can be neglected at these temperatures, and the interfacial chemical reaction control is dominant. It is only at 1043 K that a non-zero contribution from the diffusion component is observed. This suggests that porosity may be important to the kinetics of reducing pre-oxidised pellets at lower temperatures. Future study is needed to understand the effects of pellet porosity and density on the reduction rate.

In this section, it is analysed that for the reduction of both types of pellets at most temperatures studied is controlled by the interfacial chemical reaction, only the reduction of pre-oxidised pellets at 1043 K shows a mixed control. Nevertheless, this appears to be different from the findings in the literature for the reduction of TTM pellets above 1073 K, as listed in **Table 2.3** [122], [126], [128], [130]. These reports found that gas diffusion through the product layer seemed to play an important role in the rate-limiting step, especially at the later stages of reduction. This mismatch might arise from the different reducing gases used in those experiments. In the previous literature [122] [126]-[128] [130], almost all the experiments employed a gas mixture of H_2 and CO as the reducing agent. The molecules of CO and CO_2 are substantially larger than H_2 and H_2O molecules. Therefore, it is not surprising that gas diffusion through the product layer might be slower and hence limit the reduction rate.

On the other hand, the rate-limiting step determined in this study is consistent with literature of reducing TTM ores when H_2 gas is the dominant gas. Previous authors have found that interfacial chemical reaction rate controls the reduction process for reduction of cylindrical titanomagnetite pellets (equivalent ~10.77 wt% TiO_2) from 1173 K to 1323 K in H_2-Ar gas [121], or pre-oxidised ironsand (equivalent ~11.4 wt% TiO_2) from 1073 K to 1273 K in H_2-Ar gas [108]. Moreover, it was also reported that interfacial chemical reaction control becomes dominant with an increased ratio of $H_2/(CO+H_2)$ in the reduction of spherical pre-oxidised titanomagnetite pellets (equivalent ~12.5 wt% TiO_2) at temperatures from 1173 K to 1323 K [130]. This is also in line with the analysis discussed in this section, where the experimental data for the kinetic analysis was obtained in the reductions by 100vol% H_2 gas.

6.2 Activation energy for the interfacial chemical reaction control step

In **Section 6.1**, it was shown that interfacial chemical reaction is the rate-limiting step for the reduction of the Ar-sintered pellets at all temperatures studied (from 993 K to 1443 K), and for the pre-oxidised pellets at all temperatures above 1043 K. In these cases, an activation energy for the rate-limiting reaction can be determined using the Arrhenius equation:

$$k_s = Ae^{-E_A/(RT)} \quad \textbf{(6.8)}$$

where k_s is the reaction rate constant, R is the universal gas constant, A is a frequency factor and T is the absolute temperature in Kelvin. However, the calculation of k_s requires prior knowledge of C_{Ac} (the concentration of the reducing gas at the reaction interface, which equals to C_{Ag} shown in **Figure 2.6**). This is not easily determined. Instead, the apparent rate constant k'_s was applied. The relation between k'_s and k_s is shown in equation **6.4**, and can be simplified as:

$$\frac{1}{k'_s} = \frac{\rho_B R}{b k_s C_{Ag}} = \frac{B}{k_s} \quad \textbf{(6.9)}$$

where $B = \rho_B R / b C_{Ag}$.

In order to determine k'_s, equation **6.1** can be simplified to consider primarily the interfacial chemical reaction component:

$$t = \frac{1}{k'_s}\left[1 - (1 - X_a)^{\frac{1}{3}}\right] \quad \textbf{(6.10)}$$

By plotting t against $1 - (1 - X_a)^{\frac{1}{3}}$ for the experimental data set obtained at each temperature, k'_s can be obtained from the slope of each plot. The activation energy can then be obtained by combining equations **6.8** and **6.9**, resulting in:

$$ln\, k'_s = ln\left(\frac{A}{B}\right) - \frac{E_A}{RT} \quad \textbf{(6.11)}$$

If it is assumed that B is approximately constant with temperature, then the activation energy E_A can be obtained by plotting $\ln k'_s$ against $1/T$.

6.2.1 Reduction of Ar-sintered pellets at all temperatures

In **Figure 6.3**, linear fits of equation **6.10** are shown to the experimental TGA data obtained from reductions of the Ar-sintered pellets. Here, linear fits were generated using all data for X<90%. The R^2 values for evaluating each fit are listed in **Table 6.1**, and confirm close agreement between the fitted and experimental data in each case. The apparent reaction rate constant k'_s obtained at each temperature is also listed in **Table 6.1**. This was calculated from the reciprocal of the slope for each fitted line.

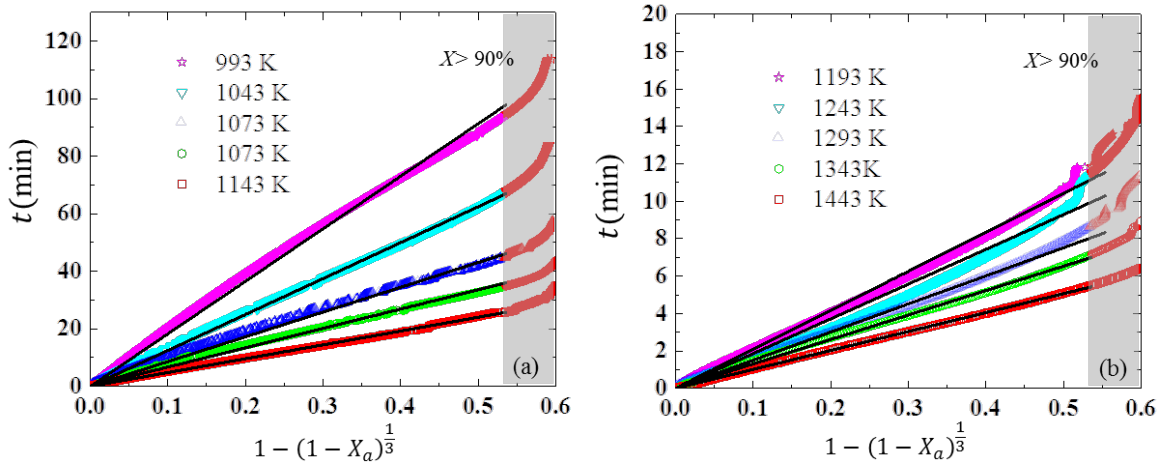

***Figure 6.3**– Fitting of equation **6.10** to the experimental data obtained from reductions of the Ar-sintered pellets at temperatures from 993 K to 1443 K. (a) Lower temperature regime, from 993 K to 1143 K; (b) Higher temperature regime, from 1193 K to 1443 K. These fits were performed using all data available up to X≤ 90%. Data for X>90% are highlighted by grey area*

***Table 6.1**– Fitted slopes, apparent reaction rate constants and R^2 values for each fit in **Figure 6.3**. (H_2 gas reduction of Ar-sintered pellets at temperatures from 993 K to 1443 K)*

T/K	993	1043	1073	1093	1143	1193	1243	1293	1343	1443
Slope = $\frac{1}{k'_s}$	182.6 ± 0.1	124.9 ± 0.1	86.8 ± 0.1	67.1 ± 0.1	48.0 ± 0.03	20.9 ± 0.03	18.6 ± 0.1	15.0 ± 0.02	13.1 ± 0.02	10.1 ± 0.01
Apparent reaction rate constant k'_s	$5.5 \times 10^{-3} \pm 6.6 \times 10^{-4}$	$8.0 \times 10^{-3} \pm 3.5 \times 10^{-4}$	$1.2 \times 10^{-2} \pm 9.7 \times 10^{-4}$	$1.5 \times 10^{-2} \pm 1.0 \times 10^{-3}$	$2.1 \times 10^{-2} \pm 6.1 \times 10^{-4}$	$4.2 \times 10^{-2} \pm 1.5 \times 10^{-3}$	$5.3 \times 10^{-2} \pm 3.8 \times 10^{-3}$	$6.7 \times 10^{-2} \pm 1.7 \times 10^{-3}$	$7.7 \times 10^{-2} \pm 1.2 \times 10^{-3}$	$9.9 \times 10^{-2} \pm 6.0 \times 10^{-4}$
R^2	0.998	0.999	0.998	0.999	0.999	0.998	0.999	0.999	0.999	0.999

In order to calculate the activation energy, $\ln k'_s$ is plotted against *1/T* in **Figure 6.4**. As can be seen, there is a discontinuity of the data over the whole temperature range, which is confirmed by conducting extra reduction experiments between each temperature at 50 K intervals. Accordingly, two independent linear lines are required to fit the data obtained in the higher and lower temperature ranges respectively. This implies that the reduction presents different activation energies in each temperature range. From 993 K to 1143 K, the activation energy calculated from the fitted blue line is found to be 89 ± 5 kJ/mol. However, from 1193 K to 1443 K, the activation energy calculated from the fitted red line drops to 41 ± 1 kJ/mol. This implies that the overall rate-limiting reaction step may be different for reduction temperatures above or below 1193 K, which is further discussed in **Section 8.1**. These activation energies obtained for reducing the Ar-sintered pellets will be compared later with the one for the pre-oxidised pellets.

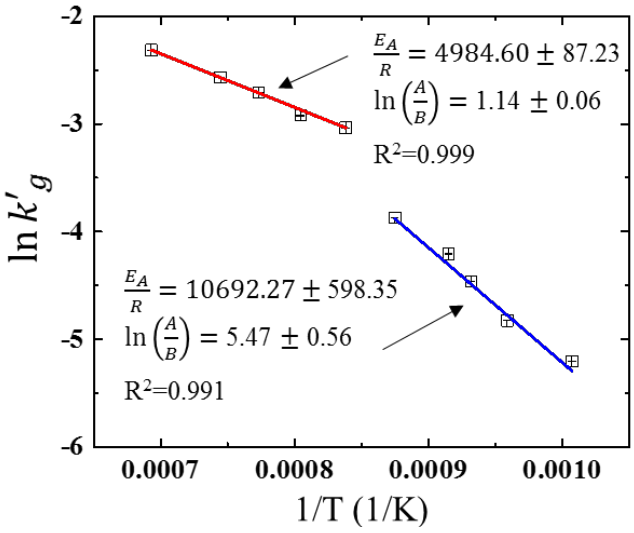

***Figure 6.4**– Arrhenius plots for determining apparent activation energy of reducing the Ar-sintered pellets reduced by 100vol% H_2 gas from 993 K to 1443 K*

6.2.2 Reduction of pre-oxidised pellets above 1043 K

Similar to **Subsection 6.2.1**, equation **6.10** was also applied to the experimental TGA data obtained from reducing the pre-oxidised pellets at temperatures from 1143 K to 1443 K. Linear fits were obtained using all data for $X \leq 90\%$, and the resulting fits are plotted in **Figure 6.5**. R^2 values for each fitted line and the apparent reaction rate constant k'_s are both listed in **Table 6.2**.

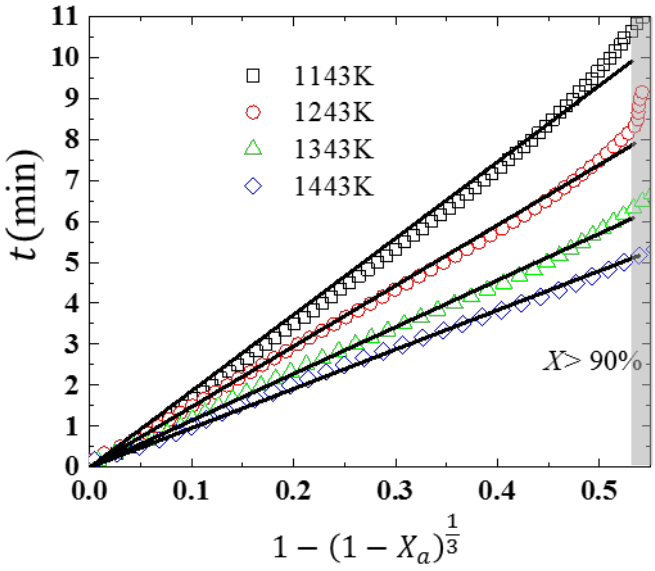

***Figure 6.5**- Fitting of equation **6.10** to the experimental data obtained from reductions of pre-oxidised pellets at temperatures from 1143 K to 1443 K. These fits were performed on all data to X≤ 90%. Data for X>90% are highlighted by grey area [162]*

***Table 6.2**- Fitted slopes, apparent reaction rate constants and R^2 values for each fit in **Figure 6.5** for the experimental data obtained reducing pre-oxidised pellets from 1143 K to 1443 K [162]*

T/K	1143	1243	1343	1443
Slope = $\frac{1}{k'_s}$	18.7 ± 0.1	14.9 ± 0.1	11.4 ± 0.1	9.6 ± 0.1
Apparent reaction rate constant k'_s	5.3×10^{-2} ± 5.9×10^{-3}	6.7×10^{-2} ± 4.7×10^{-3}	8.7×10^{-2} ± 4.4×10^{-3}	1.0×10^{-1} ± 4.2×10^{-3}
R^2	0.998	0.999	0.999	0.999

As before, the activation energy is calculated by plotting $\ln k'_s$ against $1/T$ in **Figure 6.6**. However, unlike the reduction of the Ar-sintered pellets, only one fitting line is needed to describe the data across the full range of temperatures studied (a smaller temperature range compared to the Ar-sintered pellets). The activation energy is found to be 31 ± 1 kJ/mol. This value is comparable to that obtained for the reductions of Ar-sintered pellets above 1193 K.

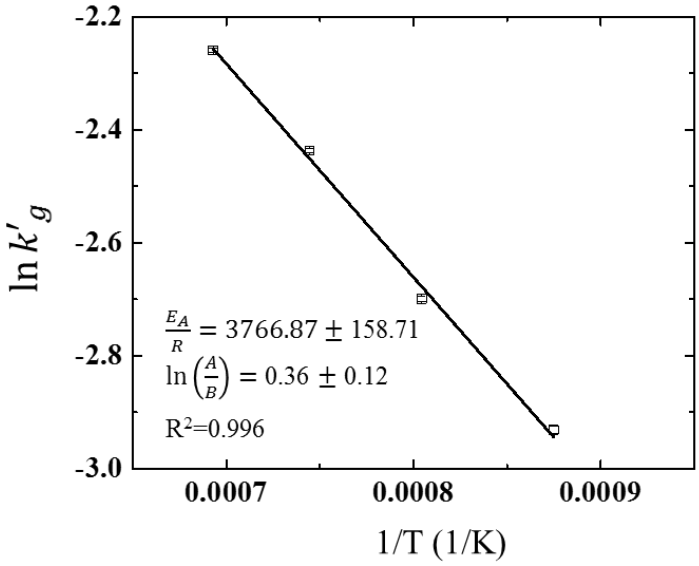

***Figure 6.6**- Arrhenius plot to determine the apparent activation energy for reducing the pre-oxidised pellets in 100vol% H_2 gas at temperatures from 1143 K to 1443 K [162]*

In this section, the activation energies calculated for both types of pellets are found in the range of the established ones among various previous studies of DR of conventional non-titaniferous ores (10 to 120 kJ/mol) [93], [96], [101], [133]–[136], as summarised in **Subsection 2.3.2**. However, discrepancies exist from the former literature of reducing titanomagnetite ores (as listed in **Table 2.4**). The activation energies obtained here are much lower than those reported by Wang *et al*. (50 to 105 kJ/mol) [108], Dang *et al*. (98 to 115 kJ/mol) [118],and Liu *et al*. (170.3 kJ/mol) [125]. This might result from a lower Ti content in the pellets, or the conditions of sintering/pre-oxidising applied in the reduction process in this thesis. It, again, emphasises the effects of experimental conditions on the activation energy, as interpreted in **Subsection 2.3.1**.

6.3 Effect of pellet diameter on the application of the model at 1343 K

In the TGA reduction experiments, reduction degree curves were also obtained for both types of pellets with different diameters from 5.5 mm to 8.5 mm reduced at 1343 K above the critical flow rate (**Figure 4.5** for Ar-sintered pellets and **Figure 5.5** for pre-oxidised pellets). Therefore, these data sets were also assessed by the single interface SCM using equations **6.6** and **6.7**.

6.3.1 Reduction of Ar-sintered pellets of different sizes at 1343 K

An investigation of the applicability of the model to the reduction degrees from different sized pellets (**Figure 4.5**) are shown in **Figure 6.7**. The relation in equation **6.6** is exhibited in **Figure 6.7(a)** while that in equation **6.7** is shown in **Figure 6.7(b)**. Again, the model was a good fit for the data for the majority of the reduction process (X=10% and X=90%). These plots show that both the gradients in **Figure 6.7(a)**, and the intercepts in **Figure 6.7(b)** are close to zero for all pellet sizes, indicating that diffusion is not the rate-limiting step in any of these experiments. Instead, interfacial chemical reaction is found to be the dominant rate controlling step for the reductions of all pellet sizes at 1343 K.

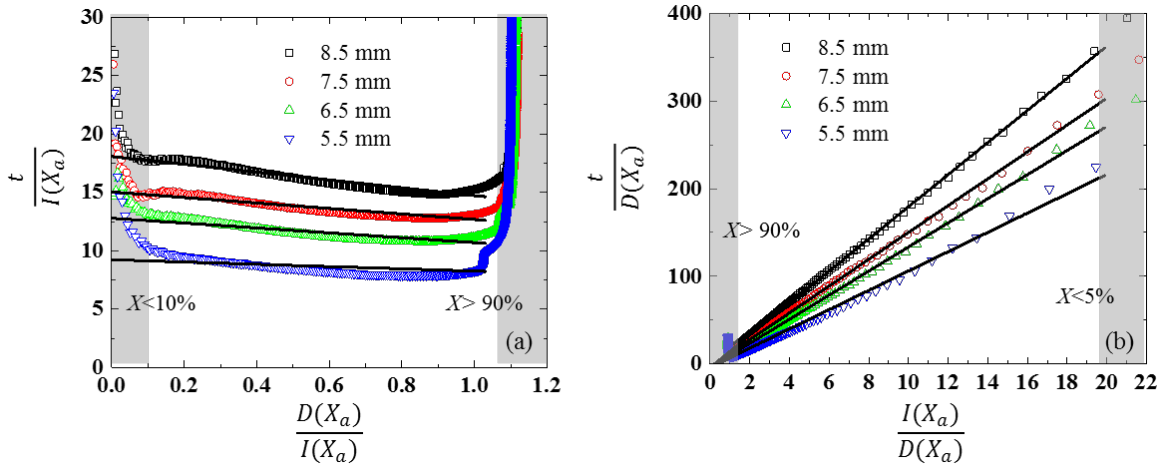

Figure 6.7*- Plots showing the relation in equations* ***6.6*** *and* ***6.7*** *of the data obtained of reducing Ar-sintered pellet with different diameters (5.5 mm, 6.5 mm, 7.5 mm and 8.5 mm) at 1343 K above the critical flow rate. In both figures, linear fits are shown between X=10% and X=90%, and are extrapolated to the y-axis. (a) Plots relating to equation* ***6.6****; (b) Plots relating to equation* ***6.7***

Consequently, equation **6.10** can also be applied to these data to determine k'_s. This approach can then be used to examine the effect of the pellet size on the reduction rate at this temperature, by applying the definition of k'_s given in equation **6.4.**

The resulting fits from equation **6.10** to the data are shown in **Figure 6.8(a)**, and the values obtained for the slopes ($1/k'_s$) of each fitted line (for each pellet diameter) are listed in **Table 6.3**. In **Figure 6.8(b)**, a plot of $1/k'_s$ against the pellet diameter from the relation in equation **6.4** is shown. While a linear correlation is observed, this line extrapolates to intercept the *x*-axis at a non-zero value of 1.5 ± 0.4 mm. This value may present a critical diameter corresponding to the development length of a pellet-scale reaction interface for the application of the model at 1343 K, which will be discussed later in this section.

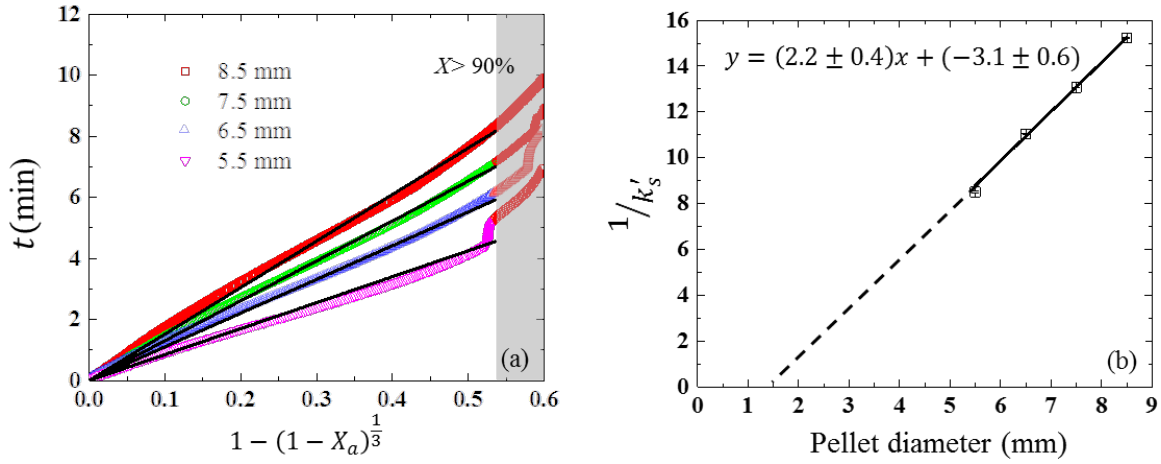

***Figure 6.8**– (a) Plots showing fits of equation **6.10** (interfacial chemical reaction control) to experimental data obtained from Ar-sintered pellets of different sizes at 1343 K above the critical flow rate. These fits were performed using data to X≤ 90%. Data for X>90% is highlighted by grey area. (b) A plot showing the linear relation between pellet diameter and the fitted slopes ($1/k'_g$) across the range of diameters studied*

***Table 6.3**– Fitted slopes and R^2 values for each fit in **Figure 6.8(a).** (Experimental data obtained from H_2 gas reductions of Ar-sintered pellets of different sizes at 1343 K)*

Diameter/mm	5.5	6.5	7.5	8.5
Slope = $\frac{1}{k'_s}$	8.50 ± 0.04	11.04 ± 0.02	13.06 ± 0.02	15.23 ± 0.02
R^2	0.995	0.999	0.999	0.999

6.3.2 Reduction of pre-oxidised pellets of different sizes at 1343 K

In **Figure 6.9(a)** and **(b)**, the relations of equations **6.6** and **6.7** to the data obtained from different sized pellets are given (raw data in **Figure 5.5**). Similar to the reductions of the Ar-sintered pellets with different sizes at 1343 K, interfacial chemical reaction is also found to be the dominant rate controlling step for all sizes of the pre-oxidised pellets.

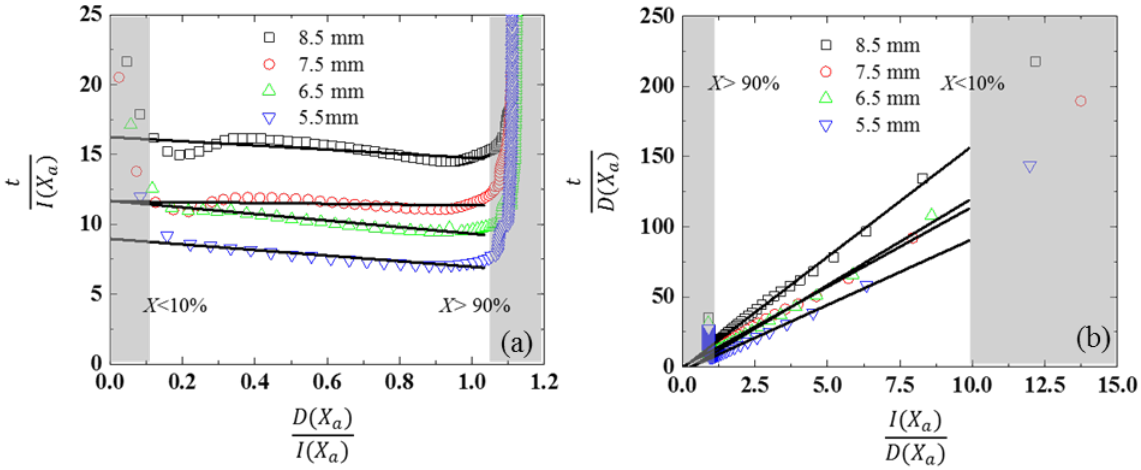

Figure 6.9*- Plots showing the relation in equations **6.6** and **6.7** of the data obtained of reducing pre-oxidised pellet with different diameters (5.5 mm, 6.5 mm, 7.5 mm and 8.5 mm) at 1343 K above the critical flow rate. In both figures, linear fits are shown between X=10% and X=90%, and are extrapolated to the y-axis. (a) Plots relating to equation **6.6**; (b) Plots relating to equation **6.7** [162]*

The analysis approach used in **Subsection 6.3.1** was also applied here for the pre-oxidised pellets. In **Figure 6.10(a)**, the plotted fits of equation **6.10** to these data are given, and the resulting values obtained for each fitted slope (at each pellet diameter) are listed in **Table 6.4**. In **Figure 6.10(b)**, a plot of $1/k'_s$ versus the pellet diameter for the range of diameters studied is shown. It is again found that the correlated linear line extrapolates to a non-zero intercept on the *x*-axis, in this case equals to 2.5 ± 0.9 mm. This value is comparable to that obtained for the Ar-sintered pellets at 1343 K (**Subsection 6.3.1**). Similarly, this value might also present the critical minimum diameter at which a definable pellet-scale reaction interface can be developed at 1343 K.

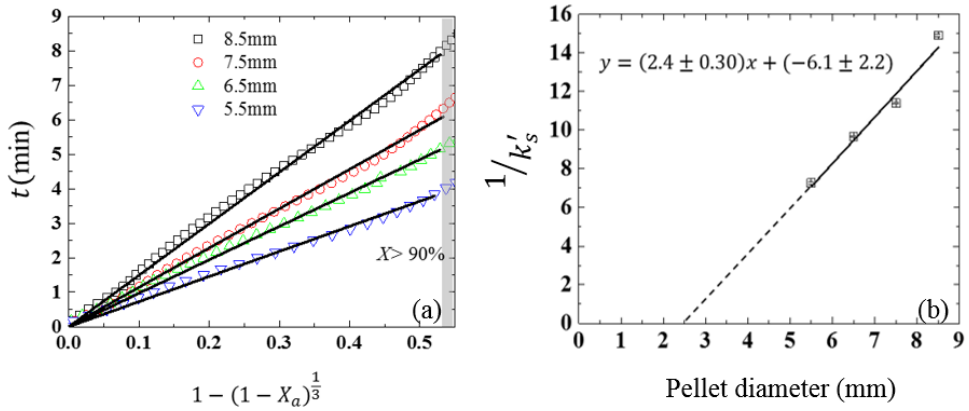

Figure 6.10*- (a) Plots showing fits of equation* ***6.10*** *(interfacial chemical reaction control) to experimental data obtained from pre-oxidised pellets of different sizes at 1343 K above the critical flow rate. These fits were performed using data to X≤ 90%. Data for X>90% is highlighted by grey area. (b) A plot showing the linear relation between pellet diameter and the fitted slopes ($1/k'_g$) across the range of diameters studied [162]*

Table 6.4*- Fitted slopes and R^2 values for each fit in* ***Figure 6.10(a)*** *for the experimental data obtained reducing pre-oxidised pellets at different sizes at 1343 K [162]*

Diameter/mm	5.5	6.5	7.5	8.5
Slope = $\frac{1}{k'_s}$	7.27 ± 0.06	9.69 ± 0.06	11.40 ± 0.04	14.91 ± 0.06
R^2	0.998	0.999	0.999	0.999

As analysed in **Section 6.3**, the intercepts in the relation of $1/k'_s$ versus the pellet diameter indicates the applicability of the model to the reductions at 1343 K. When each type of pellets with different sizes were reduced under identical experimental conditions, ρ_B, b, k_s and C_{Ag} should all be the same. Therefore, based on the definition of k'_s in equation **6.4**, a simple linear relation which passes through the origin is expected between $1/k'_s$ and pellet diameter. However, the relation between $1/k'_s$ against the pellet diameter for both types of pellets extrapolated to a non-zero x-axis intercept as shown in **Figure 6.8(b)** and **6.10(b)**. This intercept could be considered to represent the minimum critical pellet diameter at which a pellet-scale shrinking core interface will occur. At diameters less than this critical value, the pellet might be too small to accommodate the fully developed interface width, meaning that the single interface SCM may no longer be applied. That being so, when the Ar-sintered pellet is smaller than 1.5 ± 0.4 mm, or the pre-oxidised pellet is smaller than 2.5 ± 0.9 mm, the reductions can no longer be described by the single interface SCM in the pellet-scale at 1343 K. It is likely that at these smaller diameters, an alternative particle-scale model excluding a reaction interface in the pellets may be required to describe the reduction behaviour. However, such small pellets were not readily produced from the disc-type pelletiser used in this work.

6.4 Evaluating the accuracy of pellet reduction rate above the critical flow rate from the single interface SCM

An accurate analytical description of the reduction rate of the pellets in H_2 gas has potential industrial importance, as this can inform the design and optimisation of the new prototype H_2-based DR reactors. Therefore, it is important to evaluate the accuracy of the model parameters derived in the previous sections of this chapter. This can be conducted by comparing the reduction degrees calculated from the fitting parameters determined from the model to the experimental obtained ones above the critical flow rate (**Figure 4.2** and **5.2**).

For both types of pellets, reduction degree values could be calculated from the model using the fitted parameters obtained in **Figures 6.2**, **6.4**, and **6.6**. For the reductions controlled dominantly the interfacial chemical reaction, activation energy E_A and fitted $ln\left(\frac{A}{B}\right)$ (in **Figures 6.4** and **6.6**) were used to calculate k'_s by equation **6.11**. The calculated k'_s at each temperature are listed in **Tables 6.5** and **6.6** for each type of pellet respectively, and these data show close agreement to those fitted values in **Tables 6.1** and **6.2**. A reduction degree at each time point can then be calculated using k'_s in these tables by equation **6.10**, and compared with the experimental obtained ones. On the other hand, for the reduction of the pre-oxidised pellets at 1043 K (mixed control), the fitted slope and intercept obtained in **Figure 6.2** were used (listed in **Table 6.6**). These two fitted parameters were then applied in equation **6.1** to predict the time point at which a specific reduction degree is reached. The calculated time was then compared with experimental obtained data.

Table 6.5 *– Calculated k'_s from the fitted parameters obtained in* ***Figure 6.4*** *for the reduction of Ar-sintered pellets*

Parameters	$E_A = 89\ kJ/mol;\ ln\left(\frac{A}{B}\right) = 1.1$					$E_A = 41\ kJ/mol;\ ln\left(\frac{A}{B}\right) = 5.5$				
T/K	993	1043	1073	1093	1143	1193	1243	1293	1343	1443
Calculated k'_s	5.0×10^{-3}	8.4×10^{-3}	1.1×10^{-2}	1.3×10^{-2}	2.0×10^{-2}	4.8×10^{-2}	5.7×10^{-2}	6.6×10^{-2}	7.6×10^{-2}	9.9×10^{-2}
Fitted k'_s (**Tables 6.1**)	$5.5 \times 10^{-3} \pm 6.6 \times 10^{-4}$	$8.0 \times 10^{-3} \pm 3.5 \times 10^{-4}$	$1.2 \times 10^{-2} \pm 9.7 \times 10^{-4}$	$1.5 \times 10^{-2} \pm 1.0 \times 10^{-3}$	$2.1 \times 10^{-2} \pm 6.1 \times 10^{-4}$	$4.2 \times 10^{-2} \pm 1.5 \times 10^{-3}$	$5.3 \times 10^{-2} \pm 3.8 \times 10^{-3}$	$6.7 \times 10^{-2} \pm 1.7 \times 10^{-3}$	$7.7 \times 10^{-2} \pm 1.2 \times 10^{-3}$	$9.9 \times 10^{-2} \pm 6.0 \times 10^{-4}$

Table 6.6** - Calculated k'_s from the fitted parameters obtained in **Figure 6.6** for the reduction of pre-oxidised pellets from 1143 to 1443 K, and fitted parameters obtained at 1043 K in **Figure 6.2

Parameters	*slope = 23 min y-axis intercept = 18 min*	$E_A = 31\ kJ/mol;\ ln\left(\frac{A}{B}\right) = 0.4$			
T/K	1043	1143	1243	1343	1443
Calculated k'_s	-	5.3×10^{-2}	6.9×10^{-2}	8.7×10^{-2}	1.1×10^{-1}
Fitted k'_s (**Tables 6.2**)		$5.3 \times 10^{-2} \pm 5.9 \times 10^{-3}$	$6.7 \times 10^{-2} \pm 4.7 \times 10^{-3}$	$8.7 \times 10^{-2} \pm 4.4 \times 10^{-3}$	$1.0 \times 10^{-1} \pm 4.2 \times 10^{-3}$

The comparison of the reduction degree between the calculated ones (from the model fitted parameters in **Tables 6.5** and **6.6**) and experimental obtained ones is shown in **Figure 6.11(a)** to **(d).** For both types of pellet, reasonable agreement is observed up to 90% reduction degree, indicating the pellet reduction kinetics broadly consistent with the single interface SCM. However, it should be noted that as reduction degree increases (X>80%), mismatch between the calculated and experimental data are observed. This mismatch at higher reduction degrees indicates that later stages reactions (as indicated in **Chapters 4** and **5**) occurring in the pellets which limits the applicability of the model. This will be discussed further in **Chapters 7** and **8**.

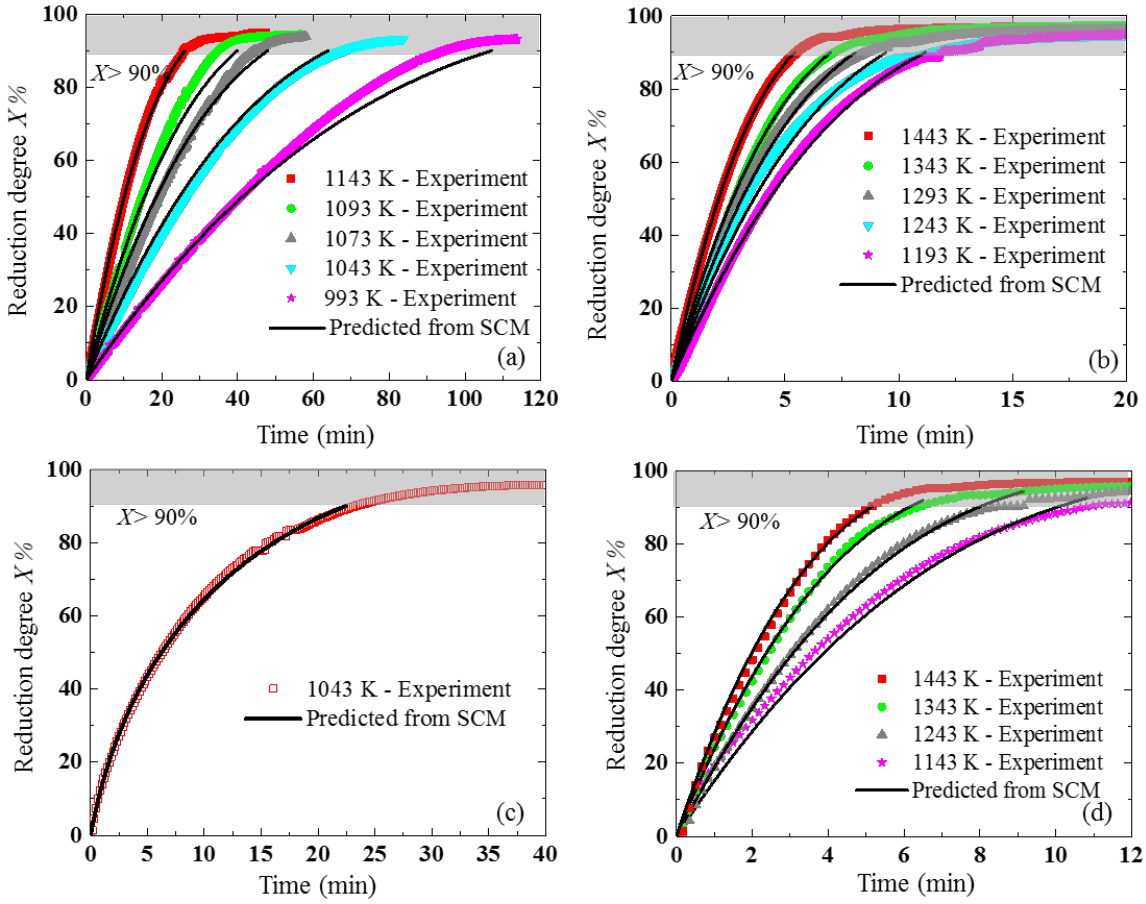

Figure 6.11– *Comparison of the model predicted and experimentally measured reduction degrees from the TGA reduction experiments. Reduction degree of X>90% are highlighted by grey area. (a) Reduction of Ar-sintered pellets from 993 K to 1143 K; (b) Reduction of Ar-sintered pellets from 1193 K to 1443 K [162]; (c) Reduction of pre-oxidised pellets at 1043 K; and (d) Reduction of pre-oxidised pellets from 1143 K to 1443 K [162]*

6.5 Summary of the kinetic analysis

In this chapter, kinetic analysis of the Ar-sintered and pre-oxidised pellets has been conducted by a single interface SCM. This analysis was performed in terms of determining the rate-limiting step, activation energy for the interfacial chemical reaction control step, minimum critical pellet size at 1343 K, and finally evaluating of the accuracy of the model to the experimental data. It was concluded that, for both types of pellets, the single interface SCM displayed a good description of the reduction progress up to $X \approx 90\%$. Poor agreement for $X>90\%$ indicates that the reductions at the latest stage of reduction may involve the dispersed Fe-Ti-O phases detected by XRD (**Figures 4.3** and **5.3**) and observed in the cross-sectioned microscopy images (**Appendices B.5** to **B.7**, and **Appendices C.5** to **C.7**). The effects of these phases on the reduction and their relationship to the model is further discussed in **Section 8.2**. In order to compare the kinetic analysis of the two types of pellets, the findings are summarised in **Table 6.7**.

***Table 6.7**– Summary of the kinetic analysis for reducing Ar-sintered and pre-oxidised pellets by the pellet-scale single interface SCM*

Kinetic analysis	Ar-sintered pellets		Pre-oxidised pellets	
	993 K - 1143 K	1193 K - 1443 K	1043 K	1143 K – 1443 K
Rate-limiting step	Interfacial chemical reaction control	Interfacial chemical reaction control	Mixed control of chemical reaction and diffusion through the product layer	Interfacial chemical reaction control
Activation energy	89 ± 5 kJ/mol	41 ± 1 kJ/mol	-	31 ± 1 kJ/mol
Minimum critical pellet size at 1343 K	1.5 ± 0.4 mm		2.5 ± 0.9 mm	

In general, pre-oxidation of the pellets increases the reduction rate, although this effect is more prominent at lower temperatures. As shown in **Table 6.7**, the activation energy for reducing the pre-oxidised pellets at temperatures > 1143 K is only marginally than that of the Ar-sintered pellets. While below 1143 K, the reduction of the pre-oxidised pellets progressed much faster

than the Ar-sintered pellets, but was not dominantly limited by the interfacial chemical reaction rate. This difference resulted from the pre-oxidation is further analysed in **Section 8.1**.

It is interesting that at lower temperatures (<1143 K), the reduction of the Ar-sintered pellets remains dominantly controlled by the interfacial chemical reaction, while the reduction of pre-oxidised pellets shows mixed control at these temperatures (with diffusion through the product layer also playing a role). Furthermore, though the discussion in this chapter shows that the single interface SCM can be successfully applied to the experimental data up to X=~90%, the rate controlling reaction at the single reaction interface was not identified in this chapter. To achieve this, a clearer understanding of effects of Ti on the phase evolution during the reduction is required. This is discussed in the next chapter.

Chapter 7
Influences of Ti on the reduction process of the Ar-sintered and pre-oxidised pellets in H_2 gas

NZ titanomagnetite ironsand differs from non-titaniferous magnetite ores due to its relatively high Ti concentration. A key question is: *How does this Ti concentration affect the evolution of phases and morphologies during reduction of the pellets in H_2 gas?* In this chapter, the influence of Ti on the reduction process is analysed. This analysis is based on the results obtained from the *in-situ* ND measurements (**Sections 4.2** and **5.2**), as well as the SEM-EDS analysis of the partially reduced pellets in both cases (**Sections 4.3** and **5.3**).

This chapter is divided into the following sections:

- **Section 7.1**: Reactions occurring during H_2 gas reduction process
- **Section 7.2**: Analysis of the distribution of Ti in the phases evolving during reduction
- **Section 7.3**: Influences of experimental conditions on the evolution of FeO at 1223 K
- **Section 7.4**: Summary of the conclusions from this chapter

7.1 Reactions occurring during reduction of the pellets

The reactions occurring during reduction of conventional non-titaniferous ores are well determined [77], [86], [105], [139], [140], and typically follow the reduction path, $Fe_2O_3 \rightarrow Fe_3O_4 \rightarrow (FeO) \rightarrow Fe$ (where the generation of FeO depends on reaction temperature, see **Figure 2.9**). However, the existence of Ti in the pellets investigated here is expected to change this, as there are additional possible reactions [143], [146], [147], [150], [157] (as summarised in the literature review in **Subsection 2.4.3**). Based on this previous literature knowledge, as well as the results presented in **Chapters 4** and **5**, the possible reactions which may occur during H_2 gas reduction of both types of pellets are listed in **Table 7.1**. This table also notes evidence for or against each reaction occurring during the reduction experiments studied here, based on observations from the results in **Chapters 4** and **5**. Note that for reactions **7.1**, **7.2**, **7.3**, and **7.5**, a functional reaction **(a)** is also given as a simplified illustration of the balanced chemical reaction **(b)**.

***Table 7.1** – Summary table of the possible reactions occurring during reduction of the pellets, and the corresponding evidence for/against the occurrence of each reaction*

No.	Reduction reactions	Comments	Evidence for/against
		Formation of TTM	
7.1a	$TTH + H_2 \rightarrow TTM + H_2O$	Reduction of TTH to TTM: Note that $3y_0 = 2x_0$. (where y_0 and x_0 are the initial values in the TTH and TTM respectively). This happens at the earliest stage of reduction	For: 1. ND results show that TTH rapidly decreases to zero at beginning of reduction, with no other products generated except TTM (**Figures 4.7, 4.13**, **5.7** and **5.13**). 2. Optical microscopy and SEM results show the conversion of TTH to TTM in the particles (**Figure 5.15** and **Appendices C.5** to **C.7**). 3. Same reaction has been reported in previous literature: Pre-oxidised TTM ore (7.4 wt% TiO_2) non-isothermally reduced in CO-Ar to 1373 K [143]; Pre-oxidised TTM pellets (4.5 wt% TiO_2) non-isothermally reduced in H_2-CO-CO_2 to 1500 K [128]; and Pre-oxidised TTM briquette (11.4 wt% TiO_2) in carbothermic reduction at 1523 K [125].
7.1b	$3Fe_{2-y}Ti_yO_3 + H_2 \rightarrow 2Fe_{3-x}Ti_xO_4 + H_2O$		
		Formation of FeO	
7.2a	$TTM + H_2 \rightarrow TTM_{-Ti\ enriched} + FeO + H_2O$	Reduction of TTM to FeO leading to Ti enrichment (in the remaining TTM): Note that δ>0 indicates the enrichment of Ti in TTM. When x+δ=x'=1, this produces Fe_2TiO_4 - the end-point of this series.	For: 1. ND and SEM-EDS results suggest Ti enrichment in TTM must occur (see **Subsections 7.2.1** and **7.2.2**). This is consistent with a low solubility of Ti in FeO [35], [124], [156]. 2. Similar effect has recently also been observed in literature on fluidised bed reduction at 1223 K of NZ ironsand (7.9wt% TiO_2) [156].
7.2b	$(x+\delta)\cdot Fe_{3-x}Ti_xO_4 + \delta\cdot H_2 \rightarrow x\cdot Fe_{3-(x+\delta)}Ti_{(x+\delta)}O_4 + 3\delta\cdot FeO + \delta\cdot H_2O$		
7.3a	$TTM + H_2 \rightarrow FeTiO_3 + FeO + H_2O$	Reduction of TTM to FeO + $FeTiO_3$: No clear evidence in this thesis to show the occurrence of this reaction	Against: 1. SEM results show no clear evidence of $FeTiO_3$ produced in regions where FeO is present. 2. At no time period in the ND results are the concentrations of both FeO and $FeTiO_3$ going up together (**Figures 4.7, 4.13**, **5.7** and **5.13**). 3. However, this reaction has been proposed in previous literature: TTM powers (9.0 wt% TiO_2) reduced in H_2-Ar gas non-isothermally to 1290 K [119], and isothermally at 1123 K [118];
7.3b	$Fe_{3-x}Ti_xO_4 + (1-x)\cdot H_2 \rightarrow x\cdot FeTiO_3 + (3-2x)\cdot FeO + (1-x)\cdot H_2O$		

***Table 7.1** – Summary table of the possible reactions occurring during reduction of the pellets, and the corresponding evidence for/against the occurrence of each reaction (continued)*

No.	Reduction reactions	Comments	Evidence for/against
		Formation of Fe	
7.4	$FeO + H_2 \rightarrow Fe + H_2O$	Reduction of FeO to Fe: This must happen in order to remove FeO from the system	For: 1. ND results show the concentration of FeO goes down while that of Fe goes up (**Figures 4.7, 4.13**, **5.7** and **5.13**). 2. SEM results show the generation of Fe from FeO, by following FeO structure (**Appendix B.7** and **Appendices C.6** to **C.7**). 3. Same reaction is reported in previous literature for the reduction of titanomagnetite ores [118], [119], [125], [128], [143], [156].
		Formation of $FeTiO_3$	
7.5a	$TTM + H_2 \rightarrow Fe + FeTiO_3 + H_2O$	Reduction of TTM to Fe + $FeTiO_3$: This may happen, but depends on the experimental conditions (as these can decrease the thermodynamic driving force for the competing reaction **7.2** [156]).	For: 1. ND results show that the concentrations of both $FeTiO_3$ and Fe grow while that of TTM goes down (**Figures 4.7, 4.13**, **5.7** and **5.13**). 2. It is consistent with SEM results observed at X=~80% - TTM being converted directly to Fe and Ti-bearing oxides (**Appendix B.7** and **Appendices C.6** to **C.7**). 3. This direct reduction path has also been proposed in previous literature for the reduction of titanomagnetite ores [143], [156].
7.5b	$Fe_{3-x}Ti_xO_4 + (4-3x)\cdot H_2 \rightarrow x\cdot FeTiO_3 + (3-2x)\cdot Fe + (4-3x)\cdot H_2O$		

***Table 7.1** – Summary table of the possible reactions occurring during reduction of the pellets, and the corresponding evidence for/against the occurrence of each reaction (continued)*

No.	Reduction reactions	Comments	Evidence for/against
Formation of other Ti-bearing oxides			
7.6	$FeTiO_3 + H_2 \rightarrow Fe + TiO_2 + H_2O$	Reduction of $FeTiO_3$ to Fe + TiO_2 (either amorphous or crystalline): Potentially happens at latest stages of reaction (X>~90%)	For: 1. XRD shows that crystalline TiO_2 was observed in some fully reduced pellets from TGA experiments (**Figures 4.3** and **5.3**). 2. ND results show at latest stages (when FeO and TTM was no longer detected at X>~90%), the concentration of $FeTiO_3$ goes down while that of Fe goes up slightly (**Figures 4.7, 4.13**, **5.7** and **5.13**). 3. This direct reduction path has also been reported in previous literature for the reduction of titanomagnetite ores [125], [143]. Against: 1. No clear evidence from ND results as TiO_2 was not detected (either amorphous/nano-crystalline, or below detection threshold). However, the phases present in ND cannot account for all Ti (**Subsection 4.2.4**).
7.7	$Fe + TiO_2 + FeTiO_3 \rightarrow Fe_2TiO_5$	Formation of PSB: Might happen at latest stages of reduction (X>~90%). The PSB detected may have the stoichiometry of ferro-PSB ($FeTi_2O_5$)	For: 1. XRD shows that crystalline PSB/ferro-PSB is observed in some fully reduced pellets from TGA experiments (**Figures 4.3** and **5.3**). 2. This reaction has also been suggested in literature on Fluidised bed reduction of NZ ironsand [156]. Against: 1. No clear evidence from ND results as PSB/ferro-PSB was not observed (either amorphous/nano-crystalline, or below detection threshold). However, the phases present in ND cannot account for all Ti (**Subsection 4.2.4**).

Note that reaction **7.7** only shows an indication of PSB (ferro-PSB) formation, as it was only observed in the fully reduced pellets at temperatures >1243 K (**Figures 4.3** and **5.3**). This temperature is slightly higher than the highest temperature achieved in *in-situ* ND measurement.

In **Table 7.1**, reaction **7.1** describes the reduction of TTH to TTM, which is confirmed to occur from the listed evidence. ND results show that for the pre-oxidised pellets, 100wt% TTH was rapidly reduced within a few minutes of the reduction starting. Similarly for the Ar-sintered pellets, the initial ~5wt% of TTH was rapidly reduced before any other reactions were observed to occur. Once the TTH was consumed, the remaining reaction progress appears similar for both types of pellets. It should be noted that due to the spatial variation in reactions taking place during pellet reduction, it is not generally possible to determine whether these remaining reaction steps occur sequentially or simultaneously. This is because multiple different reactions take place simultaneously at different locations within the pellet.

Reaction **7.2** describes the generation of FeO from TTM, and the resulting enrichment of Ti within the remaining TTM matrix. This is also consistent with a low solubility of Ti in FeO [35], [124], [156]. The following subsection (**Subsection 7.2)** discusses evidence for this Ti enrichment from both ND results and SEM-EDS analysis. Note that here stoichiometric FeO has been assumed. This reaction is substantially different from that occurring within non-titaniferous magnetite ores, as the continuing enrichment of Ti in the residual TTM phase changes its chemistry and properties (see **Subsection 7.2.3**). Reaction **7.3** shows the generation of $FeTiO_3$ and FeO from TTM, but there is no clear evidence for this reaction occurring in the pellets studied in this thesis. Reaction **7.4** shows the reduction of FeO to Fe, which must happen as FeO is not found within the fully reduced pellets. This reaction is the same as the final step in the reduction of non-titaniferous magnetite ores. Reaction **7.5** shows the direct generation of Fe and $FeTiO_3$ from TTM, without the generation of the intermediate product FeO. This reaction may occur if the TTM reaches the end point of the solubility series (compositionally close to Fe_2TiO_4), which could possibly be caused by the enrichment of Ti (see **Subsection 7.2.3**). Reactions **7.6** and **7.7** show the generation of other Ti-containing phases (TiO_2 and PSB/ferro-PSB). These minor phases were detected in XRD patterns from final reduced pellets (**Sections 4.1** and **5.1**), but were not observed in the ND measurements, probably due to the limited sensitivity of that technique (**Subsection 4.2.4**). The formation of these minor phases is expected to occur at the latest stages of the reduction process (X>~90%), and may in point be responsible for the poor agreement with the SCM at those times, as observed in **Chapter 6**.

The reactions listed in **Table 7.1** provide a framework to consider the reduction process for both types of pellets. A key difference from the reduction of conventional magnetite and hematite ores is the Ti enrichment in residual TTM which occurs through reaction **7.2**. The following section (**Section 7.2**) provides further discussion and evidence for this phenomenon.

7.2 Analysis of the distribution of Ti in the phases evolved during reduction

In this section, the distribution of Ti between the various phases present during reduction of both types of pellets is examined. This analysis is helpful to establish evidence for the determination of reaction **7.2** (in **Table 7.1**), and to highlight the unique features observed during reduction of the titanomagnetite ores.

In **Subsection 7.2.1,** EDS-maps of the particles are examined to illustrate the changing distribution of Ti in the particles during reduction at a microscopic scale.
In **Subsection 7.2.2**, the *in-situ* ND data is used to calculate a stoichiometric estimate of the average Ti mole fraction (*x*) in the remaining TTM ($Fe_{3-x}Ti_xO_4$) throughout the reaction.
Finally, in **Subsection 7.2.3** other effects of Ti on the reduction process are also discussed.

7.2.1 Microstructural evidence for the enrichment of Ti in TTM during reduction

1. EDS evidence for Ti-enrichment with formation of FeO

The enrichment of Ti in TTM during reduction can be observed in the EDS-maps performed on pellets obtained from the quenching reduction experiments. Example results are shown in **Figure 7.1**. EDS-maps are shown from particles at the centre of Ar-sintered and pre-oxidised pellets, both of which had been partially reduced to *X*=~50% at 1223 K in 100vol% H_2 gas above the critical flow rate (see **Figures 4.15** and **5.15**). Comparison of the ND and TGA results shows that *X*=~50% approximately corresponds to the maximum peak in FeO concentration. (see later in **Figure 7.6(c)** and **(d)**).

In **Figure 7.1**, a back-scattered SEM image of a central particle of the *X*=~50% reduced Ar-sintered pellet is shown in **(a)**, while that of the pre-oxidised pellet is shown in **(b)**. In both images, the light grey areas indicate FeO, while the darker grey areas represent TTM (as identified previously from **Figures 4.21** and **5.21**). The pre-oxidised pellet also shows small sub-micron voids (black) which are not observed in the Ar-sintered pellets. These are believed to be caused by the significant volume change accompanying the removal of oxygen from the pre-oxidised TTH. As can be seen, in the Ar-sintered pellets, FeO formed a channelled structure in the particles. However, in the pre-oxidised pellets, the channelled structure of FeO is less well developed. This may be a result of the micro-cracks (voids) observed in the pre-oxidised

particles. The effects of these micro-cracks on the reduction are further discussed in **Section 7.3**.

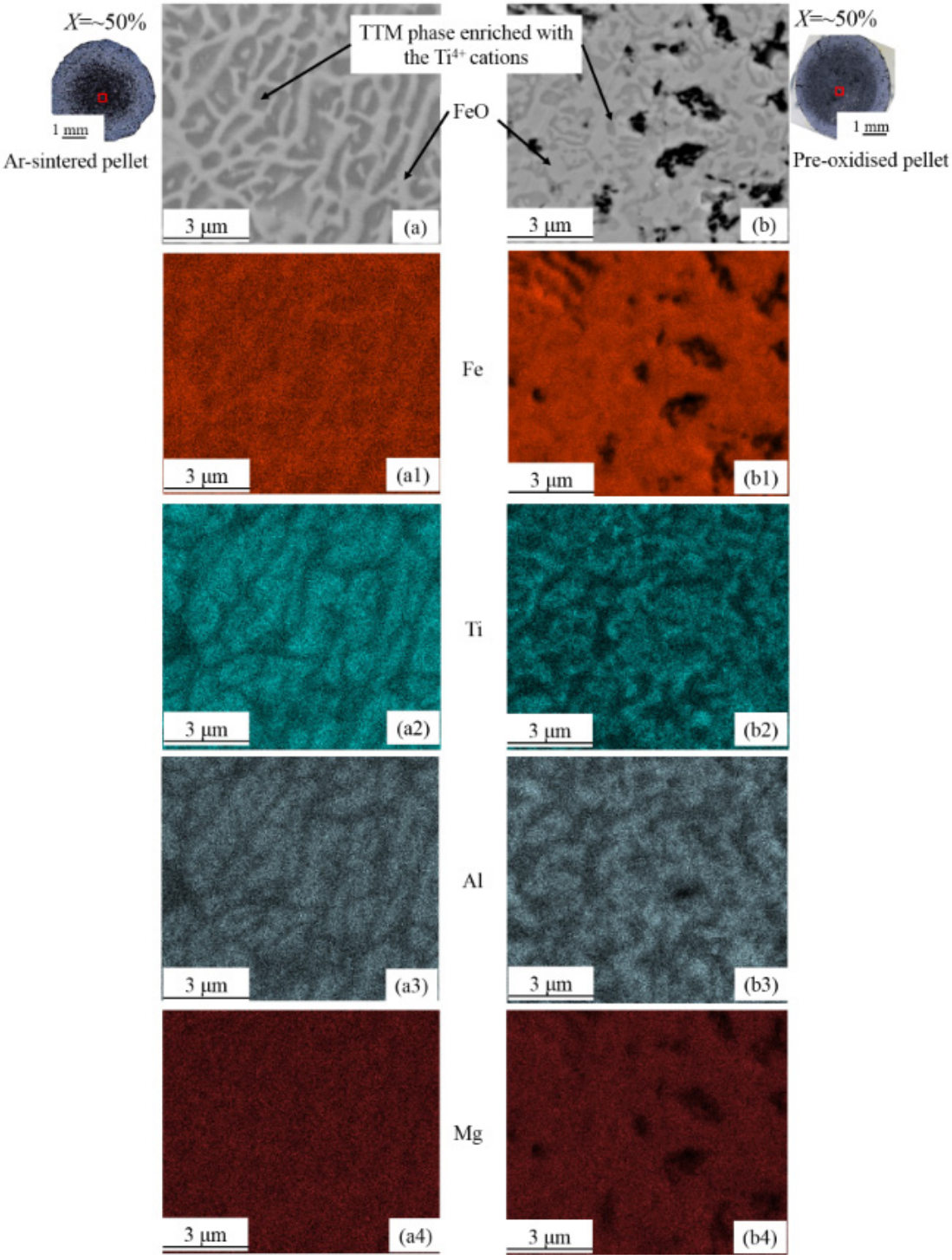

Figure 7.1 *– Back-scattered SEM images and EDS element maps of the central particle of pellets partially reduced to X=~50% at 1223 K by 100vol% H_2 gas. (a) Back-scattered SEM image of Ar-sintered pellet. (b) Back-scattered SEM image of pre-oxidised pellet. Underneath each SEM image, EDS-maps show the respective elemental distributions of Fe ((a1) and (b1)), Ti ((a2) and (b2)), Al ((a3) and (b3)) and Mg (((a4) and (b4))*

EDS-maps for the corresponding areas are illustrated underneath each back-scattered SEM image, showing the distribution of the corresponding elements. For both pellets, the light grey FeO regions show slightly higher Fe concentration than the surrounding areas of grey TTM. This is consistent with the expected relative Fe content in each of these phases. It is also clear that the element Ti is almost completely excluded from the light grey FeO channels. Instead it appears to have been expelled into the surrounding regions of unreduced grey TTM. This is consistent with expectation that Ti has a low solubility in FeO [35], [124], [156].

The direct observation of Ti-enriched TTM around the FeO channels is consistent with the occurrence of reaction **7.2** ($TTM \rightarrow FeO + TTM_{\text{-Ti enriched}}$).

In **Figure 7.1(a3)** and **(b3)**, a similar phenomenon of exclusion (from FeO) and enrichment (in TTM) is also observed for Al, which is also present as a minor contaminant in the original titanomagnetite ironsand. This can similarly be explained by the low solubility of Al^{3+} in FeO [10], [166], [167]. By contrast, the element Mg is observed to be homogeneously distributed between the FeO and TTM areas examined in these maps (**(a4)** and **(b4)**). This is consistent with the higher solubility of Mg^{2+} in FeO [168], [169].

2. Why FeO forms channelled structure in the Ar-sintered pellets

As observed in **Figure 7.1(a)**, FeO forms channelled structures within the TTM matrix during the reduction of the Ar-sintered pellets at 1223 K. This is a distinctly different morphology to that typically observed for non-titaniferous magnetite ores, where FeO normally develops into a dense layer in the particles during reduction [170]–[172]. Below, we discuss how this difference in morphology can be attributed to the influence of localised Ti enrichment in the TTM matrix, as the reduction proceeds.

Kapelyushi *et al.* [167] have studied the reduction of Fe_3O_4 doped with Al_2O_3. During reduction they concluded that, Al^{3+} cations also needed to diffuse away from FeO into the surrounding Fe_3O_4-$FeAl_2O_4$ solid solution. It was suggested that FeO is preferably formed from the {220} plane of Fe_3O_4, and the growth of FeO was through the expansion of this plane [167]. However, the expulsion of Al^{3+} cations resulted in a particle-scale network structure of FeO [167], similar to the channelled structure that observed here.

In the case of NZ ironsand, it is Ti which is the majority substituent and so likely to be mainly responsible for the formation of the channel-structured FeO. Similar to Al, Ti also has a very low solubility in FeO [35], [124], [156]. With the nucleation and growth of FeO, Ti is rejected and enriched in the surrounding unreduced TTM (as confirmed in **Subsections 7.2.1** and **7.2.2**). These regions of Ti-enriched TTM will then become more difficult to reduce to FeO, as increasing quantities of Ti would need to be exsolved in order to allow this to occur. The local Ti concentration in the TTM will be highest at the 'side-walls' of the FeO channel, meaning that this restricts the growth rate of FeO in that direction and prevents merging of individual FeO channels. Instead, growth will prefer to occur at the tip of each channel where the Ti content of the surrounding TTM is lower. This makes the channel longer (but not wider), and eventually forms a network of channels in the particle. This growth mechanism will continue until all of the surrounding unreduced TTM has been sufficiently enriched with Ti that further formation of FeO is not possible. At that point, islands of Ti-enriched TTM will be left between the FeO channels.

A schematic illustrating this mechanism for development of the FeO channels during reduction is shown in **Figure 7.2**. For comparison, this figure also shows the formation of FeO during reduction of a non-titaniferous magnetite ore. In that case there are no surrounding regions of Ti-enriched TTM to restrict the lateral growth of FeO. This means that the initially formed nuclei are able to merge with each other and finally form into a single extended region of FeO (**Figure 7.2(a)**), which is consistent with observations that have been widely described in previous literature [170]–[172].

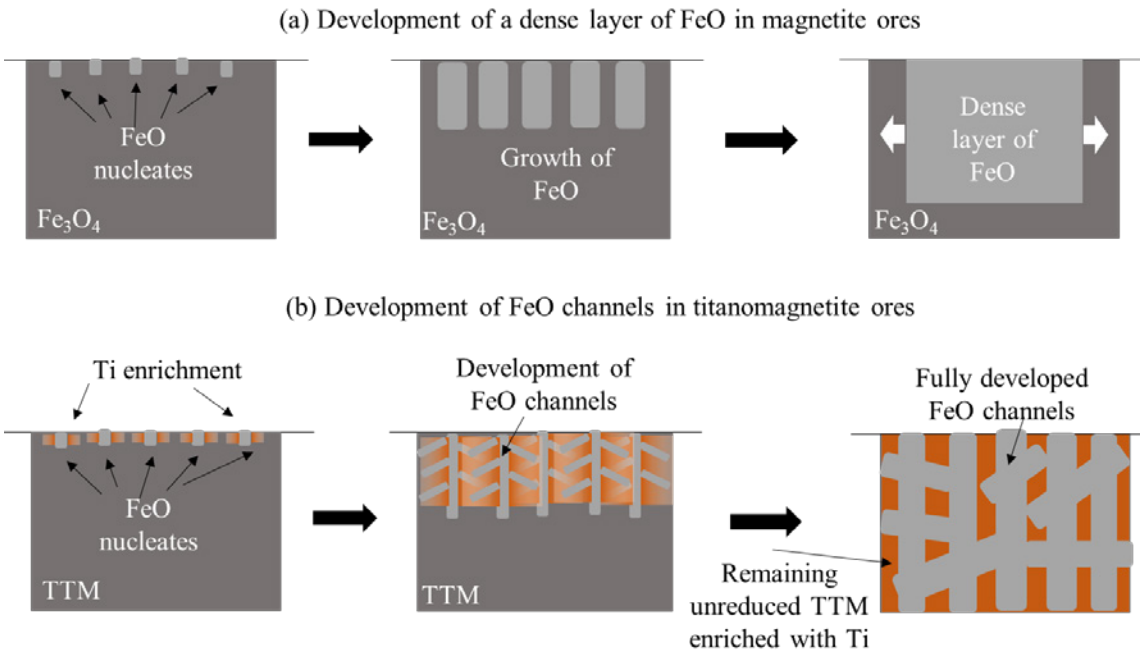

***Figure 7.2** – Schematic showing the development of FeO into: (a) a dense structure during reduction of non-titaniferous magnetite ores; and (b) a channel-like structure during reduction of titanomagnetite ores. Note that the orange colour gradient corresponds to a gradient in Ti concentration. The more Ti enriched in TTM, the darker the orange colour. Note that this schematic is derived from [167]*

As noted above, some Al (3.7wt% Al_2O_3) is also present in the unreduced ironsand TTM, and this is also not soluble in FeO (see **Figure 7.1**). Although present at lower concentrations than Ti, it is likely the Al also plays a similar role in the growth mechanism described above, consistent with [167]. In contrast, Mg is not likely to have this effect on the morphology, as Mg is soluble in FeO [168], [169], and is not observed to be segregated between the FeO and TTM regions in the partially reduced pellets.

7.2.2 Tracking the distribution of Ti between the phases observed during reduction

The SEM-EDS evidence presented in **Subsection 7.2.1** confirms that reduction at 1223 K via reaction **7.2** drives enrichment of Ti in the remaining TTM. To examine this, a calculation of the expected Ti mole fraction within TTM during reduction was conducted using the ND data. This approach assumes that the amount of total Ti present in the ND measured crystalline phases is constant throughout the reaction. It is also assumed that $FeTiO_3$ contains a stoichiometric quantity of Ti at all times. Under these assumptions, the Ti molar fraction within TTM can be quantitatively calculated according to equation **7.8**. This equation is obtained by converting the concentration of each phase to a molar ratio. There is a constant molar ratio of

Fe and Ti in the pellets at all times during reduction, as O is the only element which is lost to the gas phase.

$$\frac{2-y_0}{y_0} = \frac{(3-x')\, n_{TTM}+n_{FeO}+n_{Fe}+n_{FeTiO_3}}{x'\, n_{TTM}+n_{FeTiO_3}} = \frac{(3-x_0)}{x_0} \quad \textbf{(7.8)}$$

with $$n_i = {wt\%_i}/{M_i} \quad \textbf{(7.9)}$$

and $$M_{TTM} = 232 - 8x' \quad \textbf{(7.10)}$$

Here n_i indicates the molar fraction of each phase present in the pellets during reduction. $wt\%_i$ is the phase concentration obtained from the ND expressed as a %, and M_i represents the molar mass of each phase. x_0 and y_0 represent the solubility of Ti in TTM ($Fe_{3-x}Ti_xO_4$) and TTH ($Fe_{2-y}Ti_yO_3$) prior to the start of the reduction respectively. x'(equals $(x+\delta)$ as listed in **Table 7.1**) is the Ti mole fraction in $Fe_{3-(x+\delta)}Ti_{(x+\delta)}O_4$ which changes over time during reduction. Note that M_i is a constant for each phase (assuming FeO is stoichiometric), except for TTM. The molar mass of TTM, M_{TTM}, decreases slightly with the enrichment of Ti as given in equation **7.10**.

The initial values, $x_0 = 0.26$ (calculated from **Table 3.2**) and accordingly, $y_0 = 0.17$, are closely match those previously reported for NZ ironsand by Park *et al*. [143].

TTM is a solid solution along the binary phase from Fe_3O_4 (x=0) to Fe_2TiO_4 (x=1) by the replacement of Fe^{3+} by Ti^{4+}, as indicated in reaction **7.11** [164], [173]. It should be noted that the Ti mole fraction in TTM must lie within the range of ($0 \leq x \leq 1$) as these represent the end points of the Fe_3O_4-Fe_2TiO_4 solubility series. A value of x=0 indicates no Ti content in the TTM phase, which is simply Fe_3O_4. A value of x=1 gives Fe_2TiO_4, which is ulvospinel. If the assumptions above are valid, it should not be possible to obtain a calculated value of x'>1 from equation **7.8**.

$$Fe^{3+} + Fe^{3+} \rightarrow Fe^{2+} + Ti^{4+} \quad \textbf{(7.11)}$$

Reaction **7.2** is expected to be most relevant during the period of each reduction when the concentration of FeO is growing rapidly. The largest maximum concentration of FeO was observed during the reduction experiments at 1223 K in 5vol% H_2 – 95vol% Ar gas mixture

(shown in **Figure 4.11(a)** and **Figure 5.11(a)**). These reduction experiments also provide the most available data points for the calculation at 1223 K (as the reduction rate at these conditions was also the slowest). Therefore, these two data sets are shown as examples of the calculated value of x' throughout the reduction using equation **7.8**. Plots of the evolving value of x' versus reaction time are shown in **Figure 7.3** for both types of pellet. Further plots showing the values of x' calculated in a similar manner for the other experimental conditions studied are given in **Appendix D**. It should be noted that this analysis approach is only achievable as a result of the large continuous data series obtained from the *in-situ* ND measurements, which further emphasises the advantages of this experimental technique.

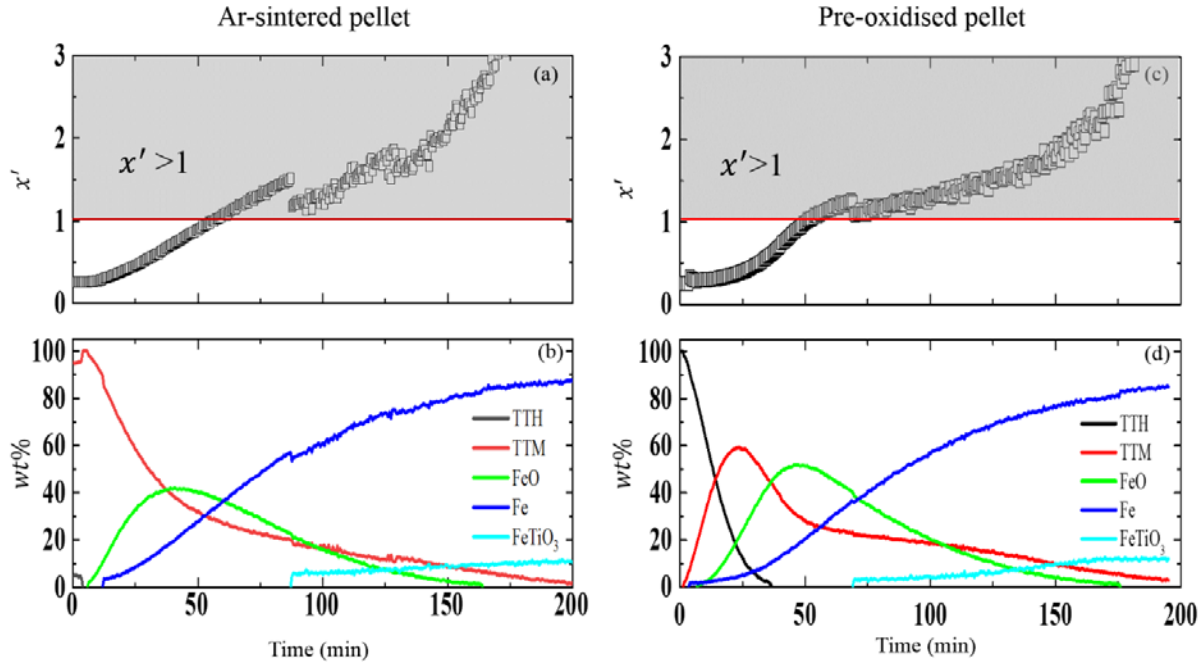

***Figure 7.3**– Plots showing examples of the apparent Ti enrichment in TTM calculated from equation **7.8**, for reductions of the Ar-sintered and pre-oxidised pellets in 5vol% H_2 at 1223 K. Experiments were performed at a flow of 250 ml/min gas mixture. (a) and (c) show the calculated Ti mole fraction (x') in TTM against reduction time. The grey highlighted areas indicate when the calculated value of $x' > 1$. (b) and (d) show the concentration curves of each phase during reduction measured by in-situ ND*

Figure 7.3(a) and **(c)** show the calculated Ti mole fraction in TTM versus the reduction time, while **(b)** and **(d)** show the evolving concentration of each crystalline phase in the pellet on the same time axis. During the early stages of the reduction, a similar pattern in the change of Ti mole fraction (x') is observed for both types of pellets. The relatively quick reduction of TTH means that x' is ~0.26 for both pellets at the start of the reduction. Once FeO is detected, x' starts to increase (as this corresponds to the reduction of TTM → FeO). At all times before

FeO reaches its peak, x' is calculated to fall in the range $0 < x' < 1$, as required by the assumptions made above.

However, a significant issue with this analysis approach is illustrated by the highlighted areas in **(a)** and **(c),** which show that during the later stages of the reaction, the values of x' calculated from equation **7.8** are > 1. This issue is also observed in the other experimental data sets (**Appendix D)**, although in every reaction studied, calculated values of $x'>1$ only occur later in the reaction after the peak of the FeO has been reached. A possible explanation of this result is that some of the Ti, present at the start of the reaction, 'goes missing' from the calculation at later reaction times. This might be attributed to the limitation of the ND measurements that not all the Ti-containing phases are accounted for (as discussed in **Subsection 4.2.4)**.

Despite this concern, it can be seen that during the early stages of the reaction (while the concentration of FeO is still increasing) the calculated value of x' is always <<1. This is consistent with the enrichment of Ti in TTM observed in the SEM-EDS images (**Figure 7.2**).

In principle, a complementary approach to confirm the Ti-enrichment during this period could be to trace the peak position of TTM from the ND pattern in order to determine whether a systematic shift in lattice constant also occurred. However, unfortunately the peak width obtained in the ND experiment is too broad to enable this analysis to be performed effectively.

7.2.3 The effect of Ti enrichment on the reduction of TTM

The enrichment of Ti in the remaining TTM changes its chemical composition, affecting its subsequent reduction rate.

The ND results show that as the FeO concentration reaches a peak, a clear slowdown in the consumption of TTM is then observed during the reduction of both types of pellets at 1223 K at a flow of 250 ml/min. This feature is particularly clear in the pre-oxidised pellets at lower H_2 gas concentrations (where more data points were able to be obtained). **Figure 7.4** displays example plots showing this slowdown for both types of pellets at 5 vol% H_2 gas concentration. The slowdown in TTM consumption occurs shortly after the peak in FeO is observed, and is

believed to be due to the stabilising effect of Ti in TTM. This is expected to occur as the Ti-enriched TTM approaches the end-point of the TTM series (Fe_2TiO_4).

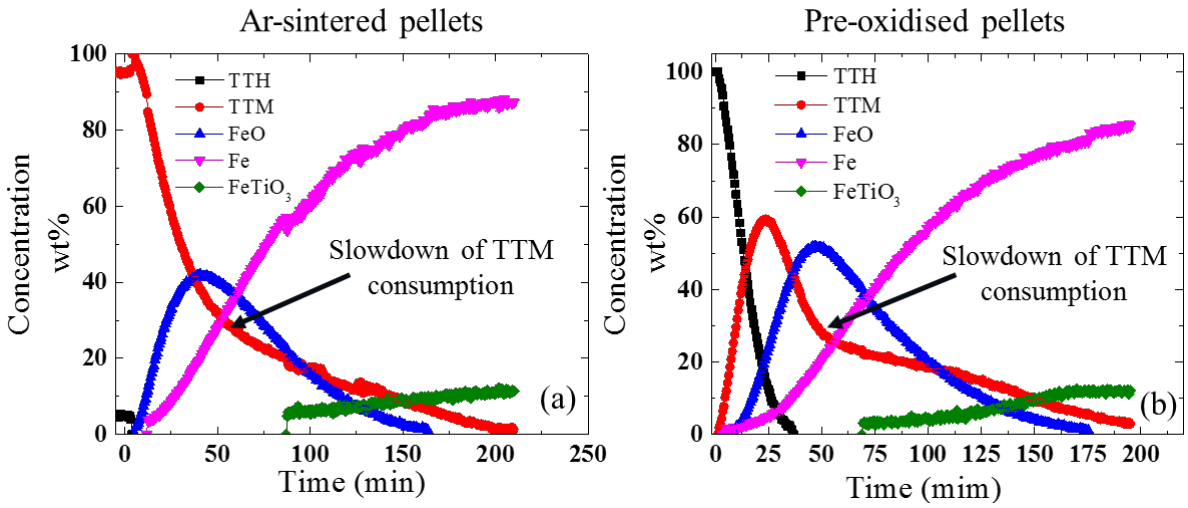

***Figure 7.4** – Plots showing the slowdown in TTM consumption which occurs after the FeO concentration peak. The reduction experiments were conducted at 1223 K in a flow of 250 ml/min by 5vol% H_2 gas concentration using: (a) Ar-sintered pellets; and (b) pre-oxidised pellets. Data obtained from the in-situ ND measurement at Wombat beamline*

The slowing in reduction rate of TTM could be caused by the switching of the reaction from reaction **7.2** ($TTM \rightarrow FeO + TTM_{\text{-Ti enriched}}$) to reaction **7.5** ($TTM \rightarrow Fe + FeTiO_3$). This must occur once $TTM_{\text{-Ti enriched}}$ reaches Fe_2TiO_4 (i.e. $x = 1$), although it may occur at a lower value of x if the thermodynamic driving force for reaction **7.2** decreases significantly with Ti-enrichment [156].

Supporting evidence for the hypothesised switch in reaction pathway is that the TTM slowdown occurs shortly after the peak in FeO, and shortly before measurable levels of $FeTiO_3$ start to be detected (**Figures 4.11** and **5.11**). Both these features are consistent with the TTM reaction switching to proceed via reaction **7.5**. However, some care must be taken with this last observation, as $FeTiO_3$ could only be detected when its concentration was above the detection threshold for the ND analysis. This means that the first moment at which $FeTiO_3$ was generated at low levels cannot be accurately determined from these plots.

To examine this hypothesis further, a simple calculation was made to understand the expected TTM concentration if reaction **7.2** is assumed to continue to the end point of the TTM solution series, Fe_2TiO_4 (ulvospinel). In that case reaction **7.2** may be rewritten as:

$$Fe_{3-x_0}Ti_{x_0}O_4 + (1-x_0)\cdot H_2 \rightarrow x_0 \cdot Fe_2TiO_4 + 3(1-x_0)\cdot FeO + (1-x_0)\cdot H_2O \quad \textbf{(7.12)}$$

Based on reaction **7.12**, 1 mol TTM phase would generate x_0 mol Fe_2TiO_4 and $3(1-x_0)$ mol FeO. It should be noted that FeO is likely to be further reduced to Fe via reaction **7.4**, in which case 1 mole FeO produces 1 mole Fe. Therefore, a mole ratio among the solid products can be obtained by equations **7.13** and **7.14** (assuming other potential simultaneous reactions can be neglected):

$$\frac{x_0}{3(1-x_0)} = \frac{n_{Fe_2TiO_4}}{n_{FeO}+n_{Fe}} \quad \textbf{(7.13)}$$

$$\frac{n_{Fe_2TiO_4}}{n_{FeO}+n_{Fe}} = \frac{\frac{wt\%_{Fe_2TiO_4}}{M_{Fe_2TiO_4}}}{\frac{wt\%_{FeO}}{M_{FeO}}+\frac{wt\%_{Fe}}{M_{Fe}}} \left(\approx \frac{\frac{wt\%_{TTM}}{M_{Fe_2TiO_4}}}{\frac{wt\%_{FeO}}{M_{FeO}}+\frac{wt\%_{Fe}}{M_{Fe}}}\right) \quad \textbf{(7.14)}$$

where $n_i = {wt\%_i}/{M_i}$ stands for the molar fraction of each phase. Equation **7.13** gives a constant value as x_0= 0.26. In equation **7.14**, the ratio can be calculated from the concentration of each phase measured from ND at each condition. However, it should be noted that $wt\%_{Fe_2TiO_4}$ is not directly obtained from ND (as Fe_2TiO_4 is not detected). Instead, to make this calculation applicable, it is assumed that the remaining TTM at the maximum concentration of FeO is compositionally close to Fe_2TiO_4. In this case, the value of $wt\%_{Fe_2TiO_4}$ is replaced by the $wt\%_{TTM}$which was directly obtained from the ND results. If the values from both equations are comparable with each other, then it implies that reaction **7.2** continues with the remaining TTM reaching the end-points of its solution series (Fe_2TiO_4). The comparison is plotted in **Figure 7.5**, and a close agreement is observed for the reduction of both types of pellets at the lowest H_2 gas concentration, suggesting that reaction **7.2** almost runs to the end point of the TTM solution series, and the remaining TTM is compositionally close to Fe_2TiO_4.

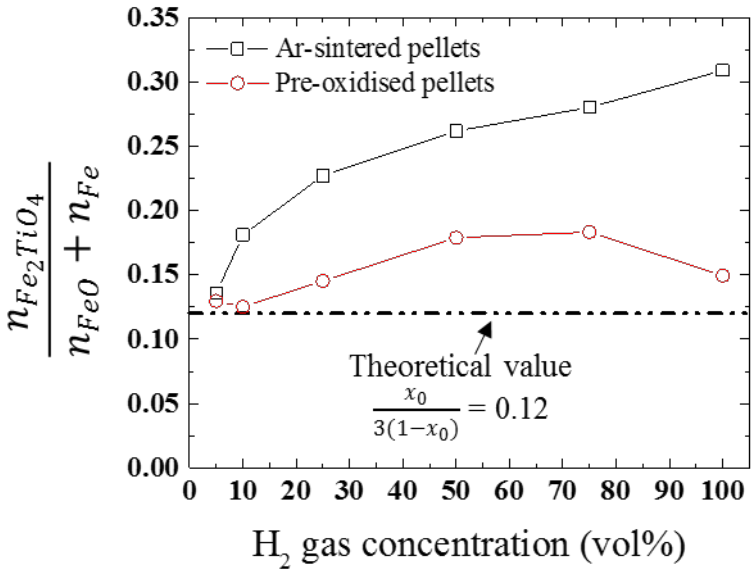

***Figure 7.5** – Plots showing the comparison of the values between equations **7.13** and **7.14**. Data obtained from the Wombat beamline for both types of pellets reduced at 1223 K at a flow of 250 ml/min*

As shown in **Figure 7.5** for the Ar-sintered pellets, the calculated ratio is much higher than the theoretical one at higher H_2 gas concentrations. This indicates that in these conditions, not all the remaining TTM present at the peak concentration of FeO is compositionally close to Fe_2TiO_4. This is supported by the observations in **Figure 7.4**, the slowing in the reduction rate of TTM at higher H_2 gas concentration at 1223 K (especially for Ar-sintered ones) was not as marked, but nonetheless can still be observed to occur. This discrepancy in behaviour may be due to a slower generation rate of FeO from TTM in the Ar-sintered pellets than in the pre-oxidised ones (discussed further in **Section 7.3**), and the spatial variations across the pellets for the overlapping of the reactions. This could lead to a period in the reduction when both reactions **7.2** and **7.5** were occurring simultaneously (after FeO reaches the maximum concentration).

7.3 Analysis of the effects of experimental conditions on FeO evolution at 1223 K

As discussed in the previous sections, the evolution of FeO from TTM significantly affects the overall reduction process and the particle morphologies at 1223 K. In this section, the influence of varying the experimental conditions (types of pellet and H_2 gas concentration) at 1223 K on the evolution of FeO is analysed. The effects of temperature on the FeO evolution is discussed in **Section 8.1**. The analysis here is aimed at improved understanding of the following observations from the *in-situ* ND measurements (**Sections 4.2** and **5.2**):

- **Subsection 7.3.1**: *Why is the maximum concentration of FeO always higher for pre-oxidised pellets than for Ar-sintered pellets reduced at each H_2 gas concentration at 1223 K?*

- **Subsection 7.3.2**: *Why does the maximum concentration of FeO vary with H_2 gas concentration at 1223K for the Ar-sintered pellets, but not the pre-oxidised ones*?

7.3.1 Why the maximum concentration of FeO is larger for pre-oxidised pellets than for Ar-sintered ones reduced at each H_2 gas concentration at 1223 K?

Observation:

In **Figure 7.6**, the evolution of FeO is shown for both types of pellets reduced at each H_2 gas concentration at 1223 K. **Figure 7.6(a)** and **(b)** show FeO concentration plotted against reaction time, while plots **(c)** and **(d)** show the same data now plotted against calculated reduction degree, *X*. Here the overall reduction degree has been calculated according to equations **3.3** and **3.4**. Note the discontinuity in the data observable in **Figure 7.6(c)** is a result from the introduction of additional phases into the calculation of reduction degree once their concentration becomes higher than the detection threshold of the ND measurement (e.g. metallic Fe emerges at X=~8% which causes an increase of X, whilst $FeTiO_3$ emerges at X=~65% with a corresponding of decrease in Fe concentration, which causes X to go backwards).

It is clear from **Figure 7.6(a)-(d)** that the maximum concentration of FeO achieved in the pre-oxidised pellets is always higher than that of the Ar-sintered ones at each H_2 gas concentration. **Figure 7.6(e)** shows the maximum (peak) value of FeO attained in each pellet at each gas concentration studied.

Figures 7.6 (c) and **(d)** also clearly show that in every case FeO is present up to a reduction degree of X=~90%. This shows that FeO is present during the majority of the reduction process for both types of pellets at 1223 K. Interestingly, X=~90% is the same value that was identified as the maximum limit for the single interface SCM presented in **Chapter 6**. This implies that the SCM likely breaks down once all of the FeO has been consumed.

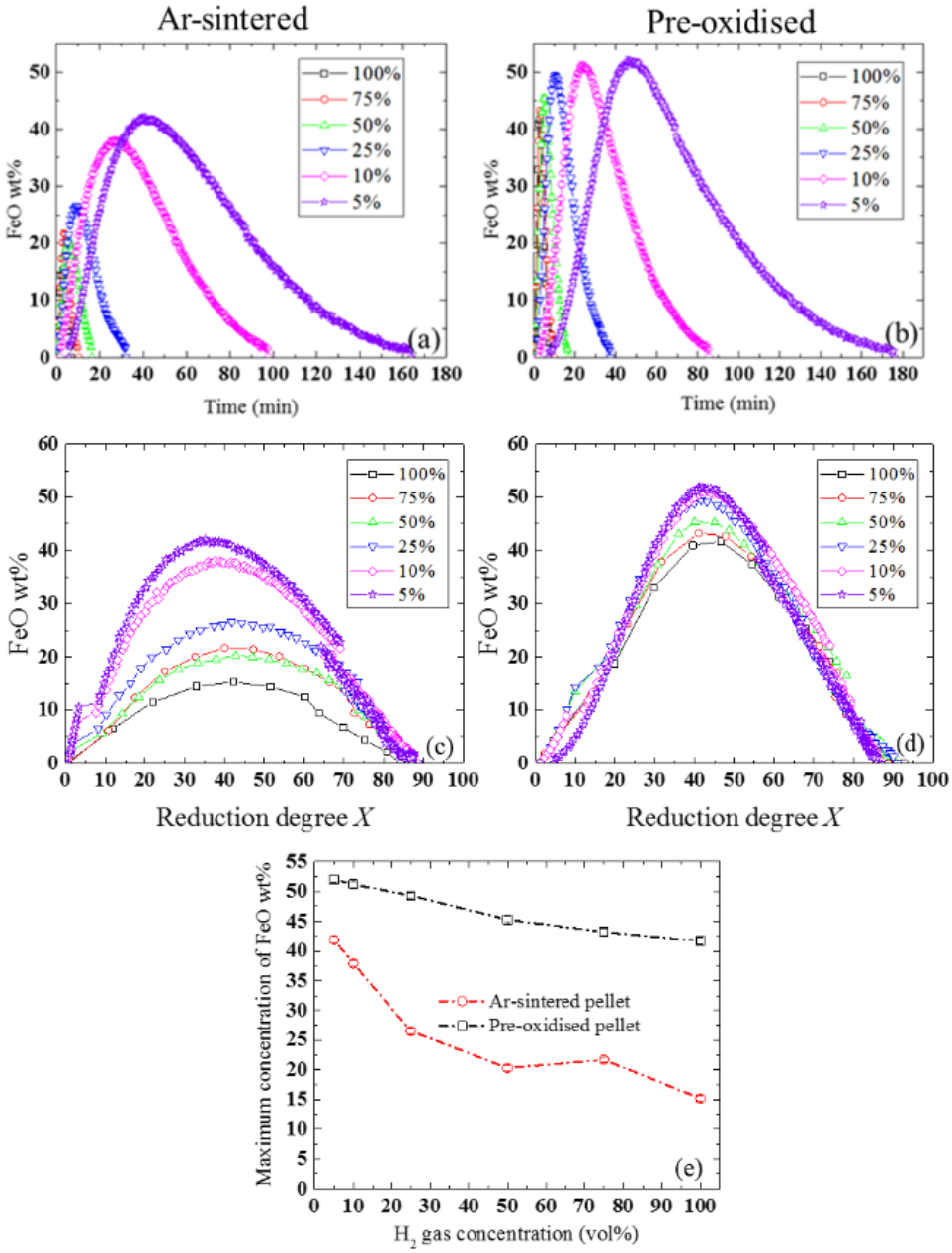

Figure 7.6 *– Plots showing the evolution of FeO during reduction of both types of pellets under various H_2 gas concentrations at 1223 K at a flow rate of 250 ml/min (above the critical flow rate). Concentration of FeO is plotted against reduction time for: (a) Ar-sintered pellets; and (b) Pre-oxidised pellets. Concentration of FeO is plotted against calculated reduction degree X for: (c) Ar-sintered pellets and (d) pre-oxidised pellets. Plot (e) shows a summary plot of the maximum (peak) concentration of FeO for both types of pellets and each H_2 gas concentration at 1223 K. Based on data obtained from the in-situ ND measurement*

Approach and analysis:

The evolution of FeO concentration is dependent on both its generation and consumption rate. This can be accordingly expressed as a mass-based rate equation:

$$d[\mathrm{FeO}]/_{dt} = Generation\ rate\ of\ FeO - Consumption\ rate\ of\ FeO \qquad (\mathbf{7.15})$$

where $\{FeO\}$ stands for the concentration of FeO measured from the *in-situ* ND. As listed in **Table 7.1**, the only reaction path for the consumption of FeO is reduction to metallic Fe via reaction **7.4**. Until all of the FeO has been consumed (i.e. for X<~90%), it is reasonable to assume that the consumption rate of FeO can be determined by an approximation of the generation rate of metallic Fe (the change in the concentration of metallic Fe), such that:

$$\frac{Consumption\ rate\ of\ FeO}{M_{FeO}} = \frac{Consumption\ rate\ of\ FeO}{M_{Fe}} = \frac{d[Fe]/_{dt}}{M_{Fe}} \qquad (\mathbf{7.16})$$

Here M stands for the molar mass of each corresponding phase. This equation correlates that 1 mol of FeO generates 1 mol of metallic Fe. The concentration of metallic Fe for both types of pellets is plotted in **Figure 7.7**. The generation rates of metallic Fe are similar for both types of pellets at each H_2 gas concentration at 1223 K, implying similar consumption rates for FeO in each case. As the concentration of FeO does vary significantly between the two types of pellets (from **Figure 7.6**), this further implies that it must be the FeO generation rate which differs between the two types of pellets.

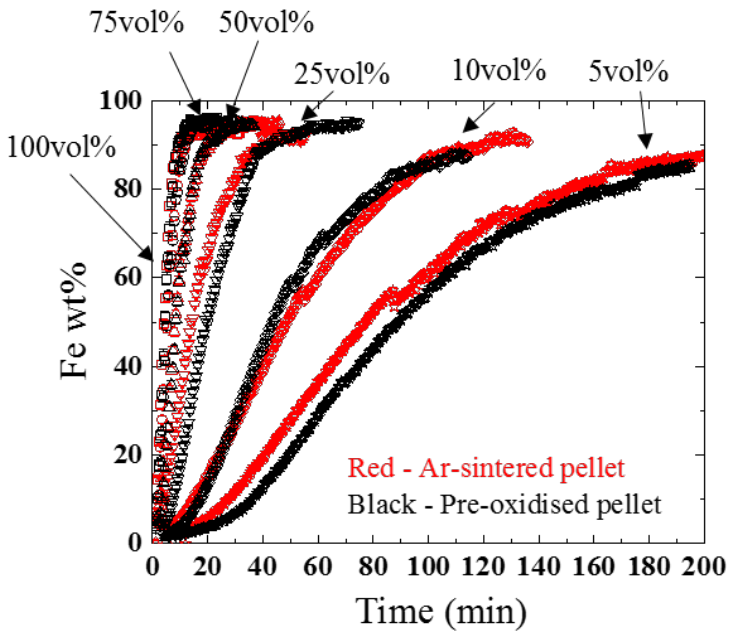

***Figure 7.7** – Plots showing the concentration of metallic Fe for both types of pellets at each H_2 gas concentration at 1223 K at an equivalent flow (250 ml/min) above the critical flow rate. Data obtained from the in-situ ND measurement at the Wombat beamline*

To visualise the generation rate of FeO for both types of pellets, equation **7.15** can be combined with equation **7.16** to yield:

$$Generation\ rate\ of\ FeO = {}^{d[FeO]}/_{dt} + Consumption\ rate\ of\ FeO$$
$$\approx {}^{d[FeO]}/_{dt} + ({}^{d[Fe]}/_{dt}) \cdot ({}^{M_{FeO}}/_{M_{Fe}}) \qquad \textbf{(7.17)}$$

In **Figure 7.8**, the generation rates of FeO calculated from equation **7.17** for both types of pellets are compared at each H_2 gas concentration at 1223 K. Note that data are only shown up to the point at which the concentration of FeO reaches its maximum. (As it is assumed that during these early stages of the reduction alternative Fe-generating reactions can be neglected). From the plots it can be seen that in both pellets, the generation rate of FeO rises to a peak before decreases. This decrease is likely caused by the content change from Fe^{3+} to Fe^{2+} as TTM reduced to FeO, which lower the tendency of FeO formation. However, at each H_2 gas concentration, the generation rate of FeO in the pre-oxidised pellets is consistently faster than that of the Ar-sintered pellets. Furthermore, the lower the H_2 gas concentration, the smaller the difference between the generation rate in each type of pellets. This is consistent with **Figure 7.6(e)** which showed that similar maximum concentrations of FeO are observed in both types of pellet at the lowest H_2 gas concentration.

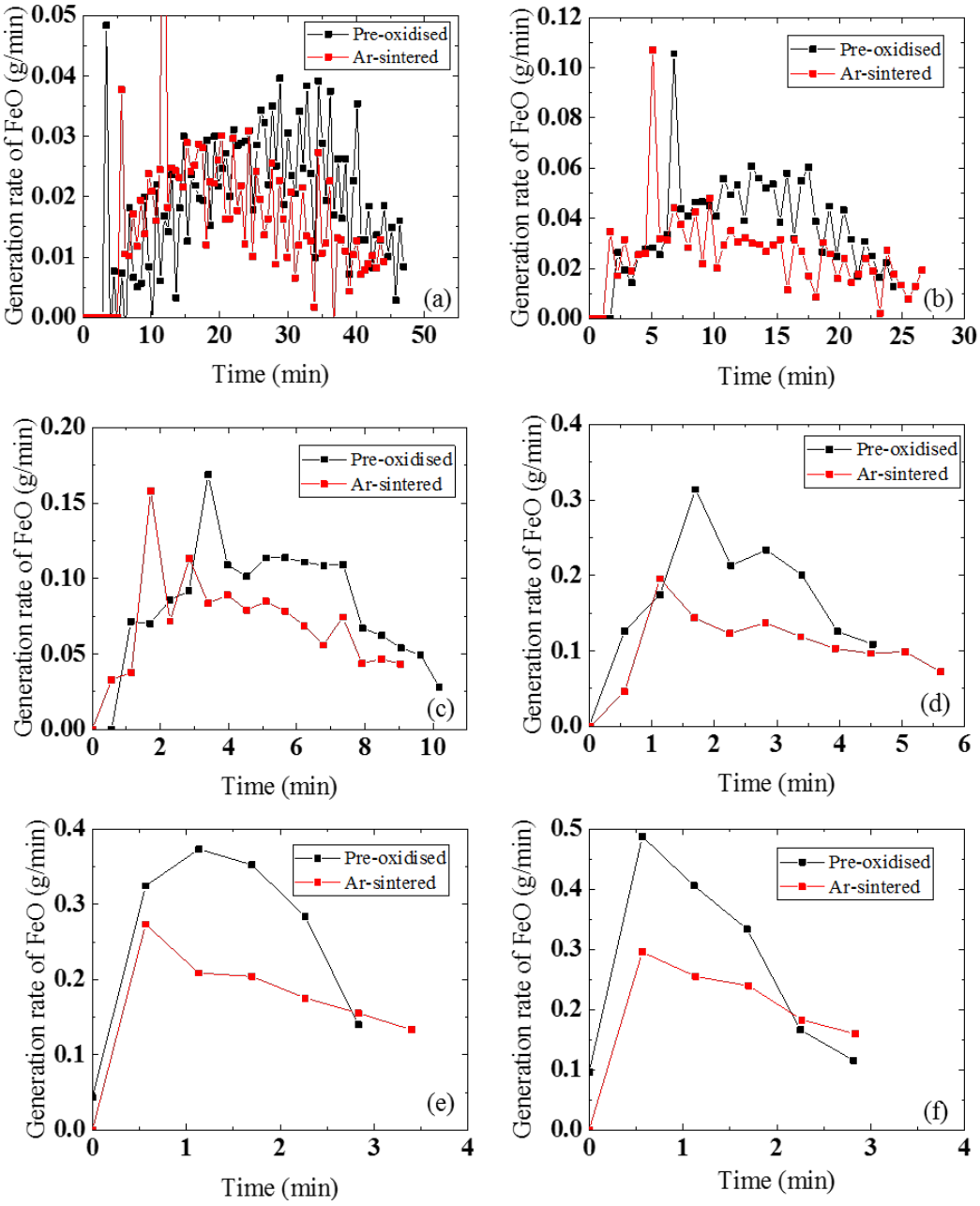

Figure 7.8 *– Plots showing the calculated generation rate of FeO during reduction of Ar-sintered (red) and pre-oxidised (black) pellets at each H_2 gas concentration at an equivalent flow (250 ml/min) above the critical flow rate. (a) 5vol% H_2, (b) 10vol% H_2, (c) 25vol% H_2, (d) 50vol% H_2, (e) 75vol% H_2, and (f) 100vol% H_2. Note that data only shown to the maximum concentration of FeO obtained from in-situ ND measurement at Wombat beamline*

In summary, **Figures 7.7** and **7.8** indicate that at high H_2 gas concentration, FeO is generated faster in the pre-oxidised pellets than in the Ar-sintered pellets, but a similar FeO consumption rate is observed in both types of pellets. This results in higher maximum observed concentrations of FeO in the pre-oxidised pellets during reduction at 1223 K.

Interpretation:

The increased generation rate of FeO in the pre-oxidised pellets may be attributed to the particle-scale cracks formed in these pellets as a result of the volume expansion associated with the transition from rhombohedral TTH to cubic TTM. (Some examples of the particle-scale cracks observed in these pellets are shown in **Figures 5.24** and **5.26)**. These cracks increase the contact area and improve gas mobility which allows the gases to access throughout the whole particles, and may lead to an increase in the number of nucleation sites of FeO. In contrast, the Ar-sintered pellets do not contain particle-scale cracks, and so the generation and growth of FeO may be limited by the diffusion of species through the solid matrix. This would then lead to a slower generation rate of FeO in the Ar-sintered pellets than in the pre-oxidised pellets at each condition. This is supported by the morphology of the particles in the pellets shown in **Figure 7.1**, where more structured morphology of FeO is observed in the Ar-sintered pellets than in the pre-oxidised pellets.

In addition to the diffusion of reactant (H_2) and product (H_2O) species, Ti atoms must also diffuse away from the 'side walls' of the FeO channels (**Figure 7.2**) as these channels 'thicken'. This diffusion of Ti within the solid matrix is further discussed below in **Subsection 7.3.2**.

7.3.2 Why does the maximum concentration of FeO vary with H_2 gas concentration at 1223 K for the Ar-sintered pellets, but not for the pre-oxidised ones?

Observation:

The observed results which motivate this question are also displayed in **Figure 7.6**. For the Ar-sintered pellets reduced at 1223 K at 250 ml/min, the maximum observed concentration of FeO increases with decreasing H_2 gas concentration. However, this effect is much less pronounced for the pre-oxidised pellets.

Approach and analysis:

The morphology of FeO formed in the particles is different between the two types of pellets. Back-scattered SEM images showing the morphology of FeO in the Ar-sintered pellets are illustrated in **Figure 7.9**. At the centre of the X=~20% pellet (**Figure 7.9(a)**), FeO channels are present but are sparser than for particles closer to the pellet surface (**Figure 7.9(b)**), where FeO channels are developed throughout each whole particle. Once reduction has progressed to

X=~50% (**Figure 7.9(c)** and **(d)**), FeO channels were found to be much denser in the particles at both positions. This implies that the generation of FeO in the Ar-sintered pellets starts from channels, which gradually become denser and thicker as the reduction progresses. This is consistent with the schematic in **Figure 7.2**.

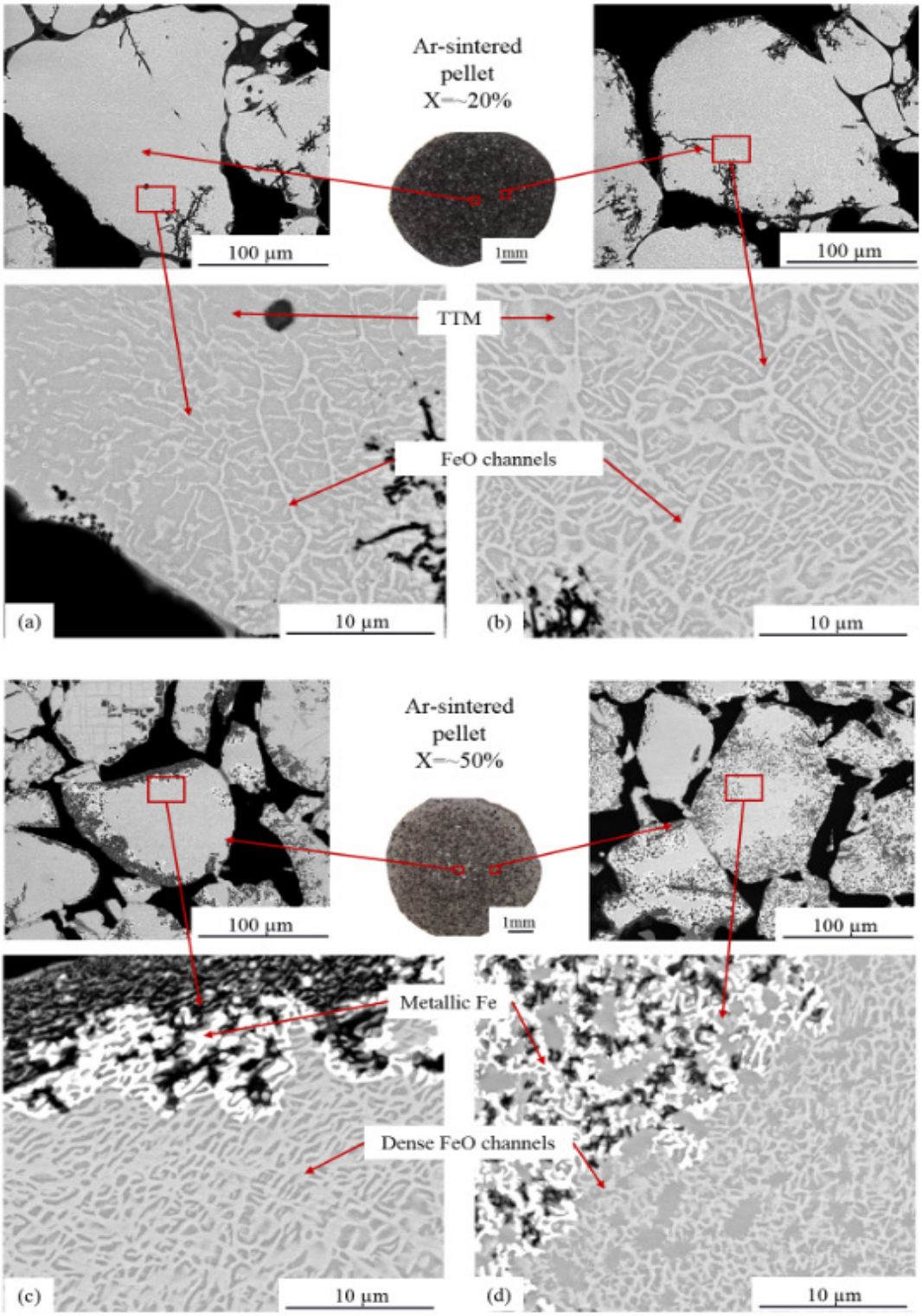

***Figure 7.9** – Back-scattered SEM images showing the morphology of FeO in the Ar-sintered pellets reduced at 1223 K with 100vol% H_2 gas (above the critical flow rate) at: (a) X=~20% and, (b) X=~50%*

On the other hand, in the pre-oxidised pellets at *X*=~20%, very small (sub-micron) FeO nucleates were observed throughout each whole particle (see **Figure 7.10(a)**). Through a combination of nucleate-growth and the generation of more nucleate sites, FeO eventually occupies the majority of the particles by the time reduction has progressed to *X*=~50% (**Figure 7.10(b)**).

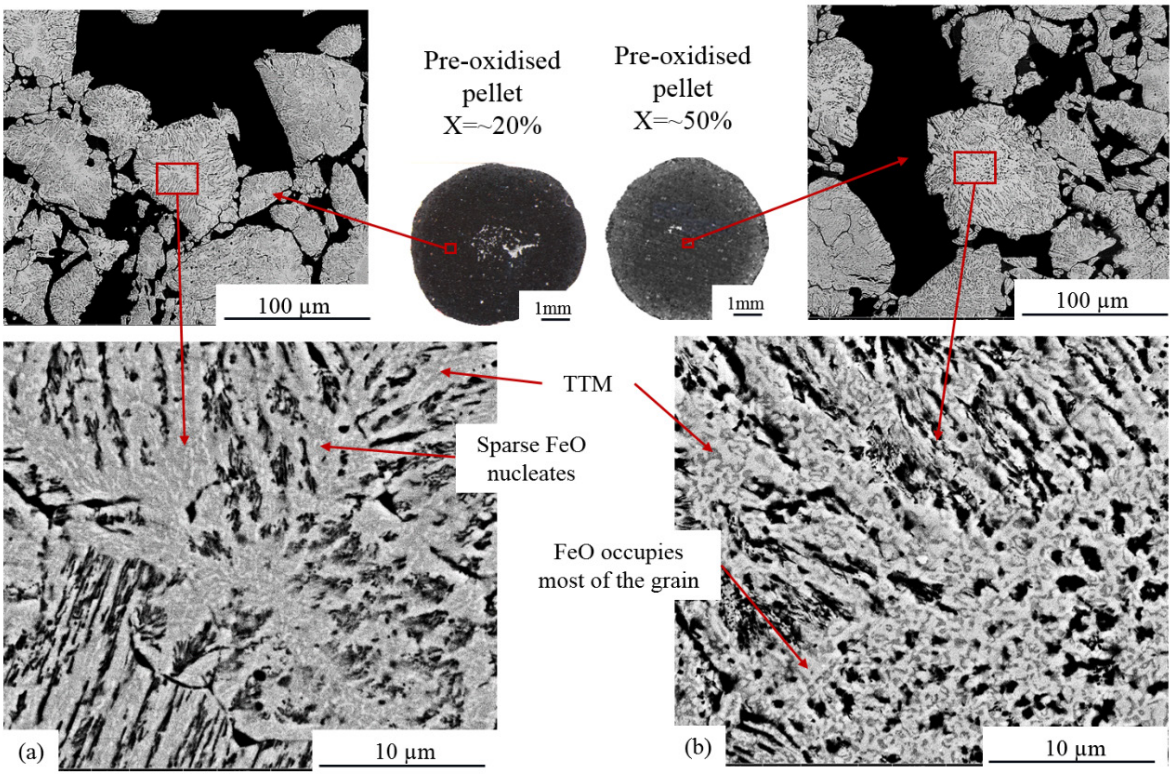

Figure 7.10 *- Back-scattered SEM images showing the morphology of FeO in the pre-oxidised pellets reduced at 1223 K with 100vol% H_2 gas above the critical flow rate at (a) X=~20% and (b) X=~50%*

Interpretation:

Back-scattered SEM images were not obtained for reduction at lower H_2 concentrations, and this makes it challenging to directly identify the cause of the increasing FeO concentration with decreasing H_2 concentration in the Ar-sintered pellets. However, a proposed hypothesis might be constructed from the different FeO morphologies observed in each type of pellets (**Figures 7.9** and **7.10**), as follows:

During the reduction of TTM to FeO in the Ar-sintered pellets, FeO channels are formed with Ti exsolved from the FeO channels and built up in the 'side wall' of TTM regions on either side of the channel **(**see **Subsection 7.2.1**). In order for the initially-formed channels to become broaden/thicken with further reduction, some Ti atoms must then diffuse away from the 'side

walls' through the TTM matrix. Importantly, the diffusion rate of Ti in the solid matrix should not be affected by the H_2 gas concentration.

However, H_2 gas concentration will affect the generation rate of FeO (i.e. the reduction rate of TTM → FeO) - as shown in **Figure 7.8**. The generation rate of FeO increases with increasing H_2 gas concentration. As a result, in the Ar-sintered pellets at higher H_2 gas concentrations, the diffusion rate of Ti in the solid matrix may become comparable to the generation rate of FeO. The slow diffusion rate of Ti might then limit the rate at which FeO channels can thicken, which would slow the relative rate of FeO generation.

By contrast, this mechanism should not occur in the pre-oxidised pellets, as particle-scale voids and micro-cracks enable FeO to nucleate throughout each whole particle. With new nucleation sites forming throughout the reduction process, the diffusion of Ti within the solid matrix will have a less significant effect on FeO growth rate (as it should not be expected to limit the nucleation of new FeO sites). Alternatively, Ti may diffuse into the micro-cracks, which again presents a less influence on the generation of FeO. This would imply that the generation rate of FeO is dominantly determined by the H_2 gas concentration, and this is also expected to be the case for the FeO consumption rate. Assuming the generation and consumption rates vary similarly with H_2 gas concentration, then similar values for the maximum observed concentration of FeO should also be expected for each different H_2 gas concentration. This is consistent with the results observed for the pre-oxidised pellets reduced at 1223 K (**Figure 7.6(b)** and **(d)**).

7.4 Summary

In this chapter, the generation of FeO in both types of pellets at 1223 K has been analysed and discussed, with an emphasis on understanding the influence of Ti on the observed phase transitions, particle morphology, and consumption rate of TTM.

A set of reactions occurring during reduction of both types of pellets are proposed. Evidence for each reaction draws on results obtained from TGA, *in-situ* ND and SEM-EDS analysis. It is concluded that the reduction of both types of pellets follows a similar reduction path at the reduction conditions studied: $TTH \rightarrow TTM \rightarrow TTM_{\text{-Ti enriched}} + FeO \rightarrow Fe + FeTiO_3 \rightarrow Fe +$ *'Ti-containing phases (TiO_2 or PSB/ferro-PSB)'*. Specifically, any TTH present is rapidly reduced to TTM (reaction **7.1**). After this point, TTM is reduced to FeO, with Ti becoming increasingly enriched in the remaining TTM (reaction **7.2**). FeO is then further reduced to metallic Fe (reaction **7.4**). Later in the reduction process, the reduction of the remaining Ti-enriched TTM appears to switch to instead form metallic Fe and $FeTiO_3$ (reaction **7.5**). Other reactions, such as the generation of TiO_2 (reactions **7.6**) and PSB/ferro-PSB (reaction **7.7**) are also expected to occur during the latest stage of the reduction process.

The enrichment of Ti in TTM from reaction **7.2** is a key feature in the reduction of the titanomagnetite ironsand studied in this work, and differentiates this material from non-titaniferous iron ores. This enrichment is confirmed by EDS-maps of partially reduced particles (X=~50% pellet) which show that Ti is rejected by FeO and enriched in the surrounding TTM. A key morphological feature of this Ti enrichment is the formation of channel-like FeO structures within individual particles. Moreover, the enrichment of Ti in TTM is likely the reason that reaction pathway switches so that TTM is directly reduced to metallic Fe and $FeTiO_3$ during the later stages of the reduction process. This change of reaction pathway results can be observed as a slowing in the consumption rate of the remaining Ti-enriched TTM. It should be noted that FeO is completely consumed at X=~90%, which corresponds to the point at which the application of the single interface SCM breaks down (from **Chapter 6**).

The effects of experimental conditions on the evolution of FeO in both types of pellets at 1223 K has also been discussed. Pre-oxidation is found to increase the generation rate of FeO under all conditions. This is attributed to the micro-cracks and voids formed during the early

reduction stages of the pre-oxidised pellets. These cracks provide improved gas access to reaction sites, leading to the nucleation of FeO throughout each whole particle.

In contrast, in the Ar-sintered pellets the maximum observed concentration of FeO is found to decrease with increasing H_2 gas concentration. One possible explanation for this puzzling effect is that, at high H_2 gas concentrations, the growth rate of FeO channels in the Ar-sintered pellets might be limited by the diffusion rate of Ti atoms away from the channel walls (i.e. within the Ti-enriched TTM matrix). This would lead to slower FeO generation rates in these conditions.

Chapter 8
The effect of temperature on the evolution of phase morphologies at the particle- and pellet-scale, and their relationship to the SCM

In the previous chapter (**Chapter 7**), the progress of the reaction at a single temperature (1223 K) has been discussed. In this Chapter, the influence of varying the reaction temperature is now considered, with particular respect to the morphological evolution of phases, at both the pellet- and particle-scale. This data is then used to identify the different rate-limiting reactions which appear to occur at different temperatures. A transition from pellet-scale to particle-scale effects is also observed with decreasing temperature. This challenges some of the underlying assumptions of the SCM presented in **Chapter 6**, and this chapter concludes with a short discussion of how the SCM results and morphological observations can be connected.

This chapter is divided into the following sections:

- **Section 8.1**: The effect of temperature on the observed levels of FeO present during reduction
- **Section 8.2**: Comparing pellet- and particle-scale morphological evolution at different temperatures, and relating this to the SCM
- **Section 8.3**: Limitations of the SCM at higher reduction degrees
- **Section 8.4**: Summary of the discussion

8.1 The effects of temperature on the evolution of FeO

8.1.1 The evolution of FeO in both types of pellets at each temperature

As noted previously, the generation of FeO from TTM plays an important role in determining the overall reaction progress. It is therefore useful to consider the effect of temperature on this reaction step.

In **Figure 8.1**, plots are shown of the FeO concentration against both reduction time and calculated reduction degree, *X*, for reductions in 100vol% H_2 gas at each of the three temperatures studied in the *in-situ* ND measurements (1023 K, 1123 K and 1223 K). As can be seen, the observed maximum concentration of FeO increases with increasing reduction temperature for both types of pellets. In all cases, the level of FeO detected in the Ar-sintered

pellets was significantly lower than in the pre-oxidised pellets. In fact, at 1023 K, FeO was not detected at all in the Ar-sintered pellets, but a small amount was still clearly seen during the reduction of the pre-oxidised pellet. Moreover, it should be noted that FeO is present up to a reduction degree of X=~90% during both the reduction of Ar-sintered pellets at 1223 K, and for pre-oxidised pellets above 1123 K. This is again consistent with the range of reduction degree over which the SCM model was found to be valid (in **Chapter 6**), providing further evidence that this model primarily describes the progress of the reduction path via FeO.

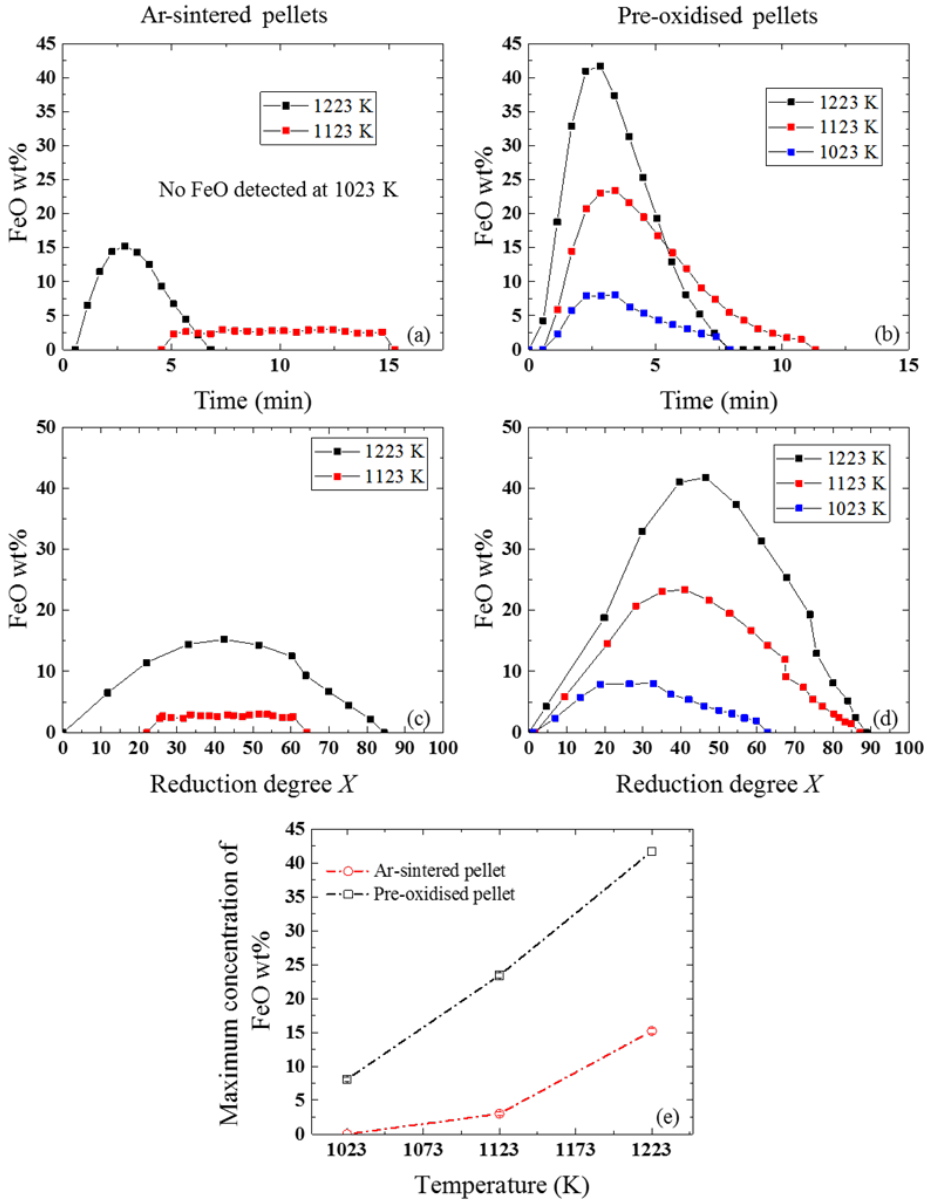

Figure 8.1 *- Plots showing the evolution of FeO during reduction of both types of pellets at each temperature in 100vol% H_2 gas at 250 ml/min (above the critical flow rate). Concentration of FeO is plotted against reduction time for: (a) Ar-sintered pellets; and (b) Pre-oxidised pellets. Concentration of FeO is plotted against reduction degree, X, for: (c) Ar-sintered pellet; and (d) pre-oxidised pellets. Plot (e) shows the maximum concentration of FeO observed in both types of pellets at each temperature. Data obtained from the in-situ ND measurements*

In **Tables 8.1** and **8.2**, back-scattered SEM images of the particles at X=~50% of both types of pellets are shown for each reduction temperature, along with summaries of key features from analysis of the SCM and *in-situ* ND data. It is shown in **Figure 8.1(c)** and **(d)** that X=~50% represents the reduction degree where the concentration of FeO is at maximum for most of the pellets. (Only for the reduction of pre-oxidised pellets at 1023 K, does the maximum concentration of FeO appear at a lower value of X=~30%).

*Ar-sintered pellets (**Figure 8.2**)*

For the Ar-sintered pellets reduced at 1023 K, FeO is barely observed in any particles throughout the whole pellet. At 1123 K, FeO is observed in a sparse fine structure close to the outer layer of metallic Fe forming in each particle. At 1223 K, FeO has fully developed into channelled structures throughout all of the particles (as noted in **Chapter 7**). These observations are consistent with the ND results (**Figure 8.1**) which show that the maximum FeO concentration decreases with decreasing temperature and is approximately zero at 1023 K.

The back-scattered SEM images also suggest that with decreasing temperature, the reduction process tends to shift from the pellet-scale towards the particle-scale. At 1223 K, a pellet-scale reaction interface is clearly distinguished for the reaction step of FeO → metallic Fe (EDS-line scan results in **Figure 4.19**). In the region of this pellet-scale interface, particles containing both metallic Fe and FeO are observed, with the generation of metallic Fe following the pre-existing FeO channels. Particles lying outside the pellet-scale interface contain metallic Fe and no visible FeO, while particles inside the interface contain FeO channels and negligible metallic Fe.

In contrast, at the lower temperature of 1023 K, particle-scale shrinking core morphologies are observed in particles throughout the pellet, with a particle-scale interface appearing to separate regions of metallic Fe and TTM (FeO barely is observed in these particles). In addition to this particle-scale effect, the reduction progress also appears to exhibit a pellet-scale gradient – with particles near the pellet surface forming metallic Fe more quickly than those particles at the pellet centre. This phenomenon is further discussed in **Section 8.2**.

Despite the apparent shift from the pellet-scale to particle-scale phenomena, the analysis in **Chapter 6** showed data obtained over the entire temperature range is well fitted by a single interface SCM (up to X=~90%). This SCM analysis indicated interfacial chemical reaction control at all temperatures.

*Pre-oxidised pellets (**Figure 8.3**)*

In the pre-oxidised pellets, decreasing temperature also leads to decreasing observed levels of FeO. The *in-situ* ND showed that at 1023 K, FeO was still present with a concentration of ~6wt% at X=~50%. However, this is difficult to clearly observe in the back-scattered SEM images. It is assumed that the small intersperse dendritic features with bright contrast (**Figure 8.3**, 1023 K, back-scattered SEM image (b)) are a combination of metallic Fe and FeO.

In addition, the pre-oxidised pellets appear to show a less pronounced shift from pellet-scale to particle-scale behaviour with temperature. Results from **Chapter 6** showed that for the pre-oxidised pellets, a single interface SCM could again be applied at all temperatures. This implied that interfacial chemical reaction control dominated at 1223 K, but mixed control (diffusion through the product layer and interfacial chemical reaction) occurred at lower temperatures.

Back-scattered SEM images of Ar-sintered pellets reduced at X=~50%		
1023 K	1123 K	1223 K
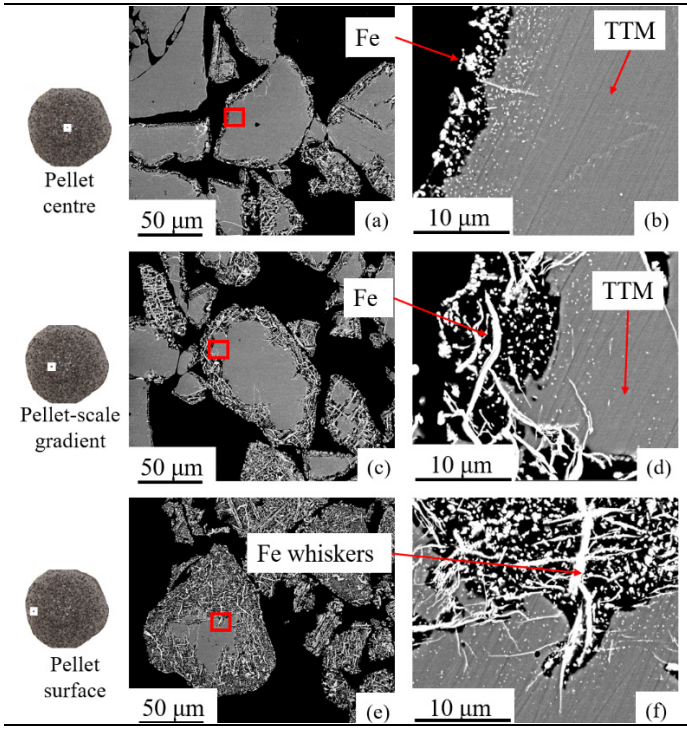	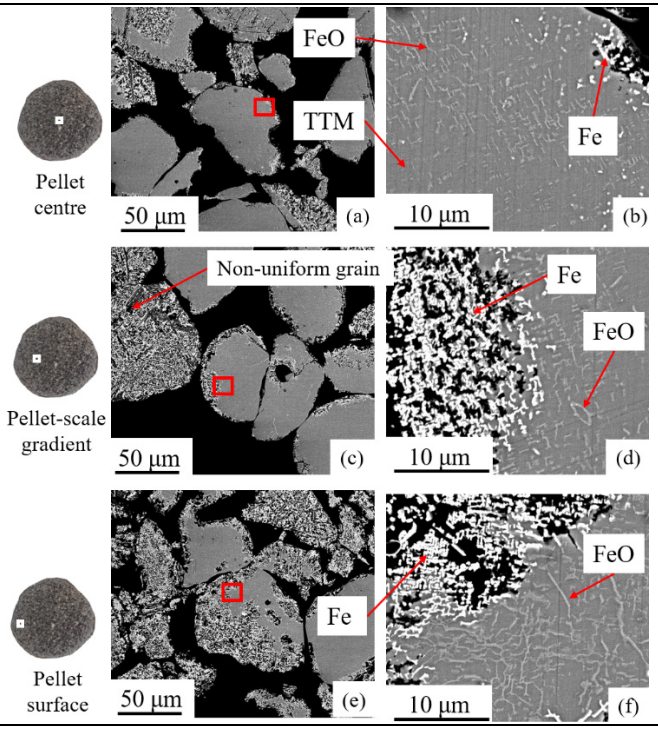	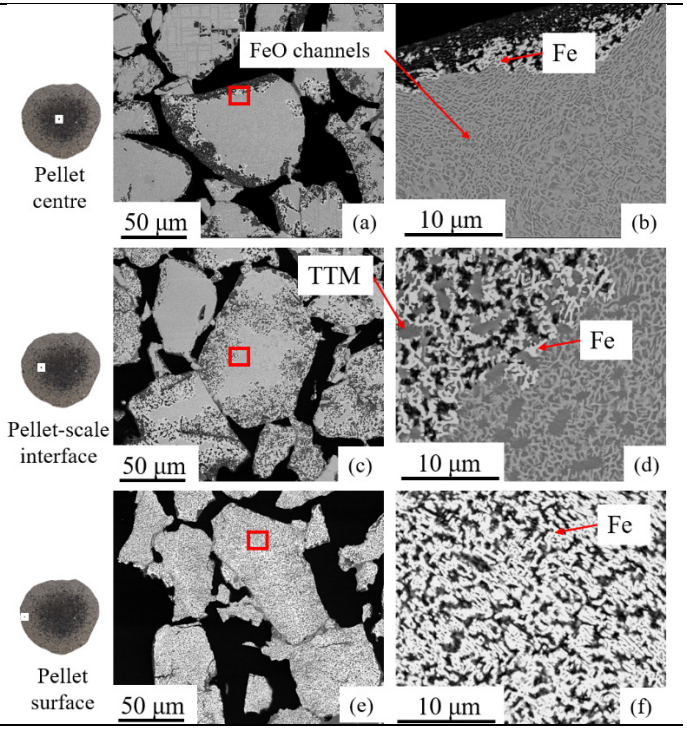
No FeO detected from *in-situ* ND	~3wt% FeO measured from *in-situ* ND	~15wt% FeO measured from *in-situ* ND
Pellet-scale single interface SCM – Interfacial chemical reaction control over the temperature		
E_A= 89 ± 5 kJ/mol		E_A= 41 ± 1 kJ/mol

Figure 8.2 *- Summary of in-situ ND results, rate-limiting step from SCM, and the back-scattered SEM images of particles in the Ar-sintered pellets reduced at X=~50% at each temperature. All the reduction experiments using 100vol% H_2 gas at the flow rate above the critical flow rate*

Back-scattered SEM images of Pre-oxidised pellets reduced at X=~50%		
1023 K	1123 K	1223 K
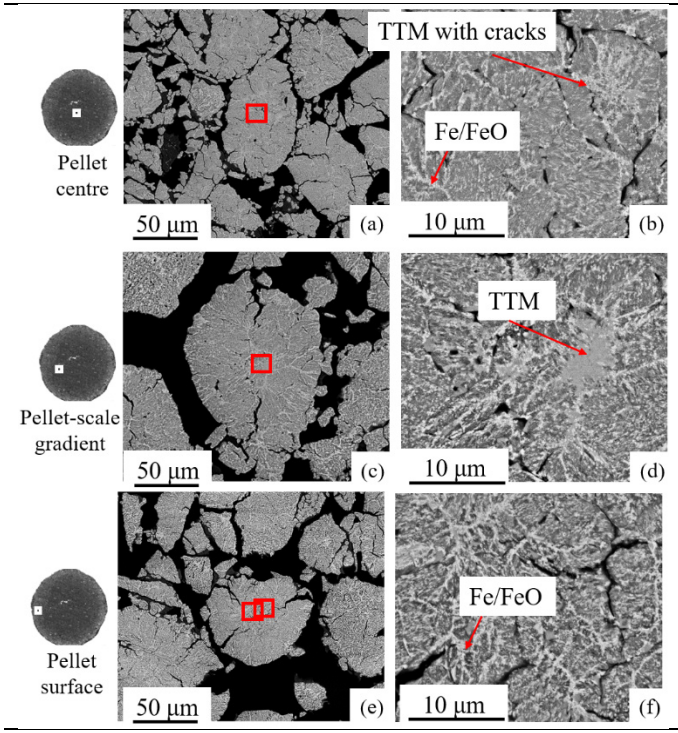	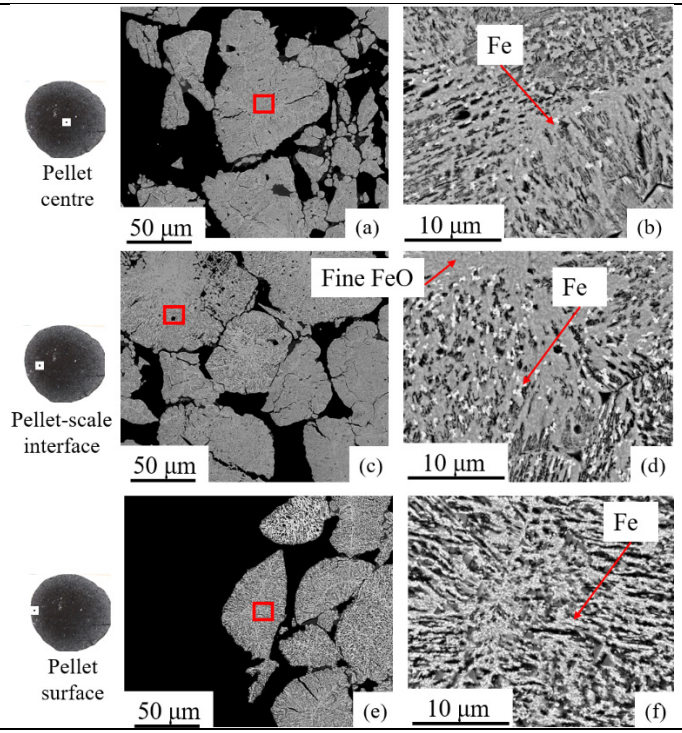	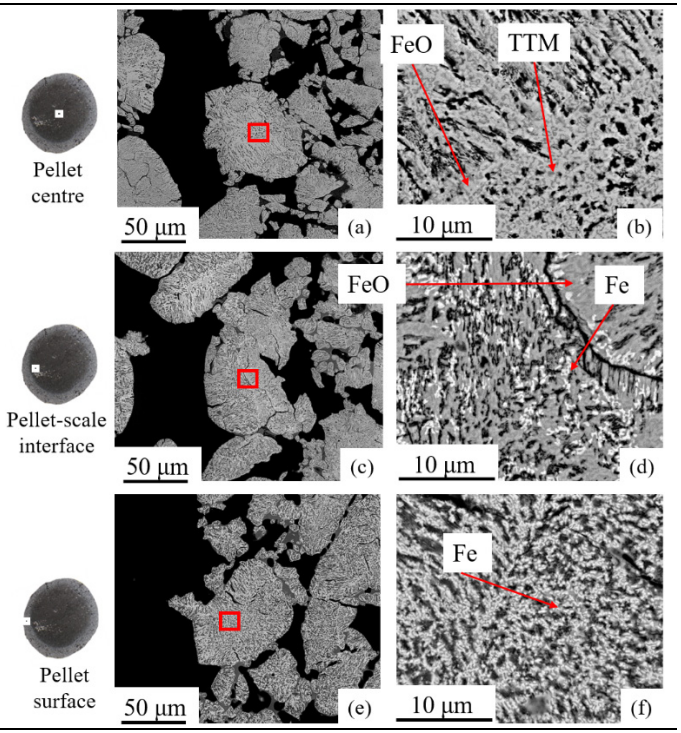
~6wt% FeO from *in-situ* ND	~23wt% FeO measured from *in-situ* ND	~42wt% FeO measured from *in-situ* ND
Pellet-scale single interface SCM		
Mixed control		Interfacial chemical reaction control, E_A= 31 ± 1 kJ/mol

Figure 8.3 *- Summary of in-situ ND results, rate-limiting step from SCM, and the back-scattered SEM images of particles in the pre-oxidised pellets reduced at X=~50% at each temperature. All the reduction experiments using 100vol% H_2 gas at the flow rate above the critical flow rate*

8.1.2 Why does the maximum observed FeO level decrease with decreasing temperature

The quantity of FeO observed in the pellets throughout the reaction is controlled by the integral of the net generation rate of FeO (= *generation rate – consumption rate*), as presented in equation **7.15**. **Figure 8.1** indicates that the net generation rate decreases as temperature decreases for both types of pellets. In fact, the net generation rate of FeO appears to be zero throughout the whole reduction at 1023 K for the Ar-sintered pellets, as FeO is barely observed in the particles. It could be argued that FeO might not be formed due to the thermodynamic limitation (temperature or gas composition in **Figure 2.9**). However, this seems unlikely to be the case here, as non-zero levels of FeO are still produced within the pre-oxidised pellets under the same reaction conditions. This implies that the initial production of FeO should also still be thermodynamically possible in the Ar-sintered pellets.

It should also be noted that the minimum temperature at which FeO can be produced during reduction of conventional non-titaniferous magnetite ores is ~840 K (**Figure 2.9**), which is well below the lowest temperature studied here.

If it is accepted that the production of FeO at lower temperatures is not thermodynamically prohibited, then an alternative explanation is that this effect is instead due to kinetic limitations, such that the reaction rate for the consumption of FeO exceeds its generation rate at these temperatures. This would mean that very little FeO will be observed during reaction, because FeO will only exist as a short-lived intermediate state during the conversion of TTM to metallic Fe.

From the single interface SCM discussed in **Section 6.1**, it was found that the interfacial chemical reaction rate plays a role in the reduction rate of both types of pellets in the temperature range of 1023 K to 1223 K. The temperature dependence of a chemical reaction rate is determined by its activation energy. In conventional non-titaniferous magnetite ores, the reduction of $Fe_3O_4 \rightarrow FeO$ (50 kJ/mol to 77 kJ/mol [93], [174]) generally exhibits a higher activation energy than the reduction of FeO → metallic Fe (23 kJ/mol to 42 kJ/mol [93], [175]). This implies that the chemical reaction rate of $Fe_3O_4 \rightarrow FeO$ will decrease more rapidly with decreasing temperature than for FeO → metallic Fe.

It is likely that for titanomagnetite ores, it will also be the case that the activation energy of TTM → FeO is larger than that of FeO → metallic Fe. This is because the reaction for FeO → metallic Fe should be same as in the non-titaniferous ore reduction, while TTM → FeO is either similar or more thermodynamically stable than the reaction of Fe_3O_4 → FeO [124], [144], [147]. As a result, in an interfacial chemical reaction-controlled system, one would expect to find that with decreasing temperature, the reaction rate of TTM → FeO decreases more rapidly than that of FeO → metallic Fe. This will result in a lower net generation rate of FeO with decreasing temperature, and hence less FeO present in the pellets.

Following the same logic, at a sufficiently low temperature the generation rate of FeO (TTM → FeO) will become slower than its consumption rate (FeO → metallic Fe). At this temperature the net generation rate of FeO would then be zero at all times. This seems to agree with the results shown for the Ar-sintered pellets at 1023 K in **Figures 8.1** and **8.2**.

It is also notable that for the Ar-sintered pellets, two different activation energies in different temperature regimes were established from the SCM analysis (**Subsection 6.2.1)**. For temperatures above 1193 K, an activation energy of E_A= 41 ± 1 kJ/mol was obtained, but for temperatures below 1143 K, a significantly higher value of E_A= 89 ± 5 kJ/mol was determined. This implies a change in the rate-limiting reaction step between these two temperature regimes, with the reaction with the higher E_A becoming the rate-limiting step at lower temperatures. This is also consistent with the observations in **Figures 8.1** and **8.2**, where TTM → FeO appears to be the rate-limiting reaction at temperatures <1143K, whilst FeO → metallic Fe appears to be the rate-limiting reaction at temperatures >1193K.

In the pre-oxidised pellets, an activation energy of E_A= 31 ± 1 kJ/mol could only be identified for temperatures > 1143 K where interfacial chemical reaction control dominated. This value is similar in magnitude to the Ar-sintered pellets at high temperature, and hence broadly consistent with the reduction of FeO → metallic Fe [93], [175]. At temperatures below 1143 K, mixed control was observed, indicating diffusion through the product layer occurs at similar rates to the chemical reaction rate. As discussed in **Section 7.3**, the presence of micro-cracks leads to a higher initial generation rate of FeO in the pre-oxidised pellets, this means that at 1023 K FeO is still initially generated and hence able to be observed. Nonetheless, the *in-situ* ND results and back-scattered SEM images (**Figure 8.3**) still show a clear decreasing trend in the maximum concentration of FeO with decreasing temperatures.

8.2 Comparing pellet- and particle-scale morphological evolution at different temperatures, and relating this to the SCM

In the previous section, it is highlighted that a transition from pellet-scale to particle-scale reduction interface is observed as the temperature decreases. This is more complicated than the assumptions considered in the development of the SCM in **Chapter 6**, where a pellet-scale dependence was observed at 1343 K, and assumed to hold throughout.

To help understand how the SCM is able to describe the pellet reduction progress even at low temperatures where particle-scale processes are occurring, schematics of the partially reduced pellet morphologies (both Ar-sintered and pre-oxidised) have been constructed. These are shown in **Figures 8.4** and **8.5**. These schematics show the detailed particle-scale reduction features at high and low temperatures, which are adopted from the graphics developed to describe the particle-scale SEM results (**Figures 4.25** to **4.27,** and **Figures 5.24** to **5.26**). The corresponding right-hand schematics.

*Ar-sintered pellets (**Figure 8.4**)*

For the Ar-sintered pellets reduced at high temperature (**Figure 8.4 top**), a pellet-scale reaction interface occurs for the reaction FeO → metallic Fe (since the reaction rate of TTM → FeO is faster at high temperatures (**Section 8.1**). This pellet-scale interface can be observed as a thin boundary-layer of particles which exhibit particle-scale shrinking core phenomenon. For particles located at the pellet-scale interface, metallic Fe is generated from the particle surface to the particle centre by following the pre-existing FeO channels. By contrast, at the pellet surface, the initial FeO channels in each particle seem to have been completely reduced to metallic Fe. Conversely, at the pellet centre, the FeO channels in each particle remain unaffected without any observable metallic Fe yet found. It is important to note that this particle morphological evolution is observed in the homogeneous TTM particles which accounts for 90% of the particles in the pellets.

However, at lower temperatures (**Figure 8.4 bottom**), the generation of metallic Fe is observed to occur via a particle-scale shrinking core over a wider region of the pellet, suggesting that the pellet-scale reaction interface has ‘broadened’. This broadening means that there is now a pellet-scale gradient in the reduction progress of individual particles, with the reduction of

particles near the pellet surface being further advanced than those nearer the pellet centre. It is noted that the onset of this pellet-scale 'broadening' occurs at a similar temperature for which the change in the activation energy of the reduction process was observed (i.e. < 1143 K). This suggests that the shift to the particle-scale shrinking core morphology is likely to be related to the change in the rate-limiting reaction from FeO → metallic Fe to TTM → FeO. (This is consistent with FeO being barely observed in the particle-scale shrinking cores at 1023 K).

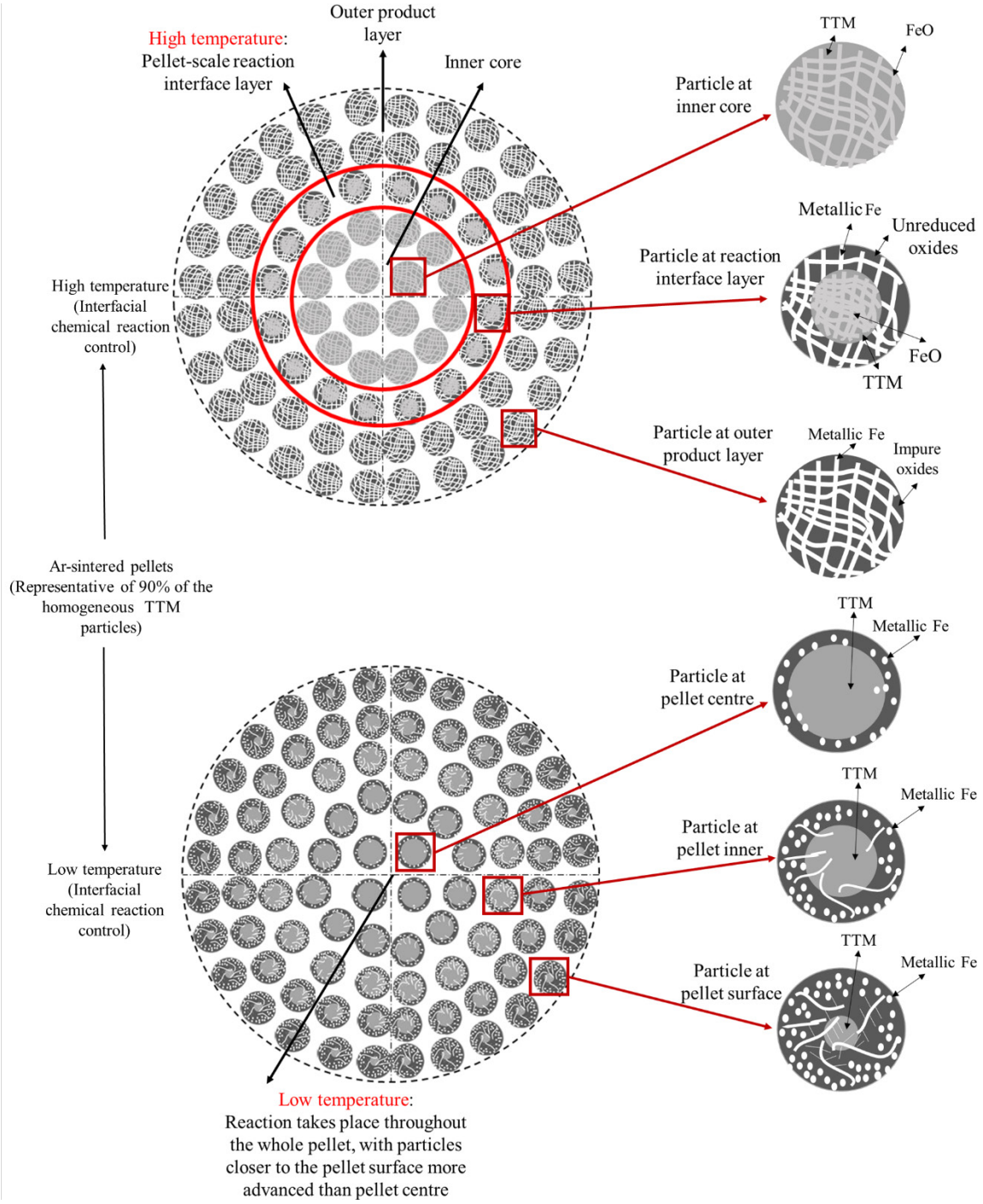

Figure 8.4 *– Illustrative schematics of particle-scale and pellet-scale morphologies within a partially reduced Ar-sintered pellet at high (top) and low (bottom) temperatures. The specific particle-scale features are adopted from* ***Figures 4.25*** *to* ***4.27***

A change from a pellet-scale shrinking core mechanism to a particle-scale shrinking core mechanism might be expected if the limiting chemical reaction rate becomes sufficiently slow. This is because in this case the interfacial reaction rate would be much slower than the rate at which gas can diffuse though the pores between particles throughout the entire pellet. This is consistent with the interpretation from the previous section that at low temperature TTM → FeO becomes the rate-limiting reaction. The high E_A of this reaction means that, at low enough temperatures, this might be expected to become much slower than any other potential rate-limiting reactions within the pellet.

It is important to note that the SCM fitting performed in **Section 6.4** provided a good description of reaction progress (up to 90%) even at the lowest temperatures studied. This is because the parameters fitted to the model ($ln\left(\frac{A}{B}\right)$ and E_A in **Figures 6.4** and **6.6**) were assigned different values for the high temperature and low temperature regimes. This means that in fact two entirely different models were fitted for the separate regimes in which pellet-scale shrinking cores (high temperature) and particle-scale shrinking cores (low temperature) are observed. Whilst **Section 6.3** showed that the SCM had a pellet-scale dependence at high temperature (1343 K), a similar investigation was not performed at lower temperatures. From the SEM data discussed above it seems possible that the fitted SCM obtained at lower temperatures might describe a particle-scale mechanism.

*Pre-oxidised pellets (**Figure 8.5**)*

Figure 8.5(a) and **(b)** shows similar schematics for the pre-oxidised pellets reduced at higher temperatures. Here, the pellet-scale reaction interface is a clear boundary between an outer region in which all particles contain metallic Fe, and an inner core in which no particles contain metallic Fe. At the reaction interface, reduction of each particle proceeds via nucleation of FeO and metallic Fe at multiple sites within the particle. By contrast, at lower temperatures (**Figure 8.5(c)** and **(d)**), metallic Fe nucleates are present in particles throughout the whole pellet. In fact at X=~50%, metallic Fe can be observed all the way to the pellet centre which again suggests that the reaction interface has 'broadened' with decreasing temperature. Despite this, a pellet-scale gradient is again still observed, as the reduction progress of particles nearer to the pellet surface is substantially ahead of those nearer to the centre. The broadening of the pellet-scale reaction interface occurs at a similar temperature to the change in the SCM from interfacial chemical reaction control to a mixed control (as determined in **Chapter 6**). This

might suggest that the change to mixed control at lower temperature is associated with the increased importance of the particle-scale effects.

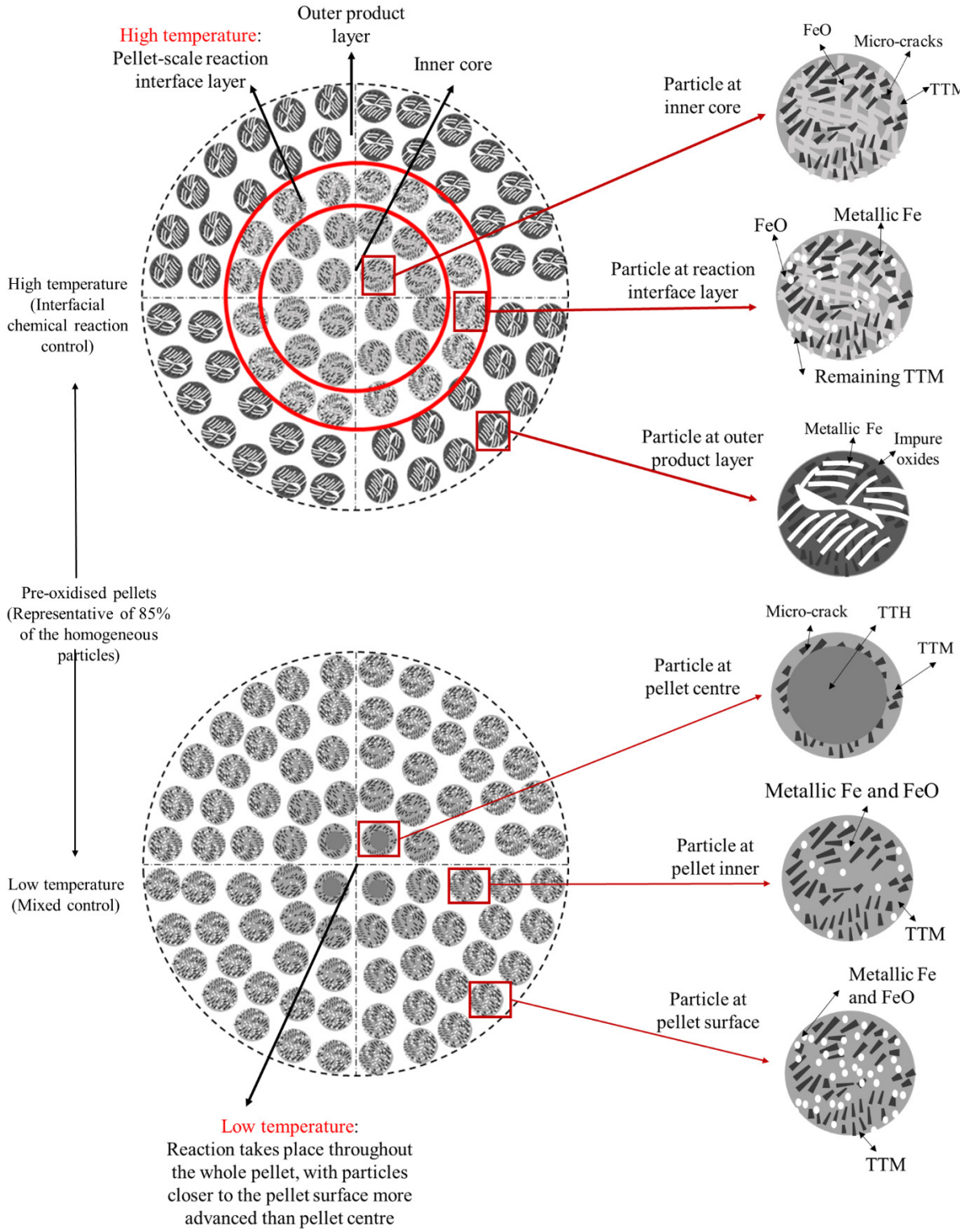

Figure 8.5 *- Illustrative schematics of particle-scale and pellet-scale morphologies within a partially reduced Ar-sintered pellet at high (top) and low (bottom) temperatures. The specific particle-scale features are adopted from* ***Figure 5.24*** *to* ***5.26***

At higher temperatures (>1143 K) the SEM data shows a pellet-scale interface for the rate-limiting reaction step (FeO → metallic Fe) which is consistent with the SCM considered in **Chapter 6**. But, in contrast to the Ar-sintered pellets, particle-scale shrinking core morphologies are not observed at lower temperatures. Instead the reduction of each particle appears to occur at multiple nucleation sites spread throughout each particle. This means that a particle-scale shrinking core model cannot be relevant for the pre-oxidised pellets at any temperature.

Despite this, the pellet-scale interface is still observed to broaden at the lowest temperature. This suggests that at these temperatures, the reaction rates within each particle at the 'interface' become slower than the diffusion of gas between the particle pores. As a result, H_2 (and/or H_2O) is able to diffuse beyond the outermost reacting particles and hence also enable reactions in particles located closer to the centre of the pellet.

However, whilst this interpretation can explain the broadening of the pellet-scale interface, it is not in agreement with the conclusion from the SCM model that the reduction of pre-oxidised pellets experiences mixed control at the lowest temperature. (i.e. rate of diffusion through a product layer and interfacial reaction rates are of similar magnitude)

In order to reconcile this, it is important to note that in **Chapter 6**, only one dataset at the lowest temperature (1043 K) was fitted using the mixed-control SCM. Whilst a reasonable fit was obtained, this is not strong evidence that a similar function would hold at even lower temperatures. Furthermore, the broadening of the pellet-scale interface means that this situation does not really meet the underlying assumptions of the shrinking core model. In particular, the SCM model is derived from an assumption that there is single thin reaction interface experiencing a constant gas composition, which is not likely to be true for a broadened interface through which gas diffusion is occurring between particle pores. As a result, whilst the reduction progress at 1043 K can be described using a linear combination of $I(X_a)$ and $D(X_a)$ (as in equation **6.1**), the SEM data indicates that we cannot be confident that this truly represents 'mixed control' from fully independent 'diffusion rate through the product layer' and 'interfacial chemical reaction rate' mechanisms.

8.3 Limitation of the SCM at higher reduction degrees

As discussed previously, the applied single interface SCM presents a reasonable mathematical description of the majority of the reduction data (**Chapter 6**), which is consistent with the evolution of phase morphologies at most conditions (**Chapter 8**). (The exception being the reduction of pre-oxidised pellets at 1043 K, where the SEM results do not appear to show a clear shrinking core mechanism).

Another important point is that at X>~90%, the SCM no longer exhibits good linear fits to the reduction progress for either type of pellet (**Section 6.1**). This implies that the shrinking-core model breaks down at the latest stage of reduction. This may be attributed to the fact that FeO is completely consumed at X=~90% at most conditions measured from ND results (**Figure 7.6**). This 90% reduction degree appears to be in a close agreement with the theoretical value when the FeO is completely consumed during reduction of TTM/TTH. These values, based on the theoretical weight loss ratio between the solid reactants and products, are illustrated in **Figure 8.6**. It is assumed that X=100% if TTM/TTH are completely reduced to metallic Fe and TiO_2, then the theoretical reduction degree can be calculated at different end points. Note that X has already exceeded 90% at the end point of metallic Fe + $FeTiO_3$, which confirms that only the evolution of Fe-Ti-O phases contributes to the reduction process at the latest stage. This is also consistent with the ND data that the maximum reduction degree achieved is above 90% with $FeTiO_3$ existing as the product (**Figures 4.11** and **5.11**).

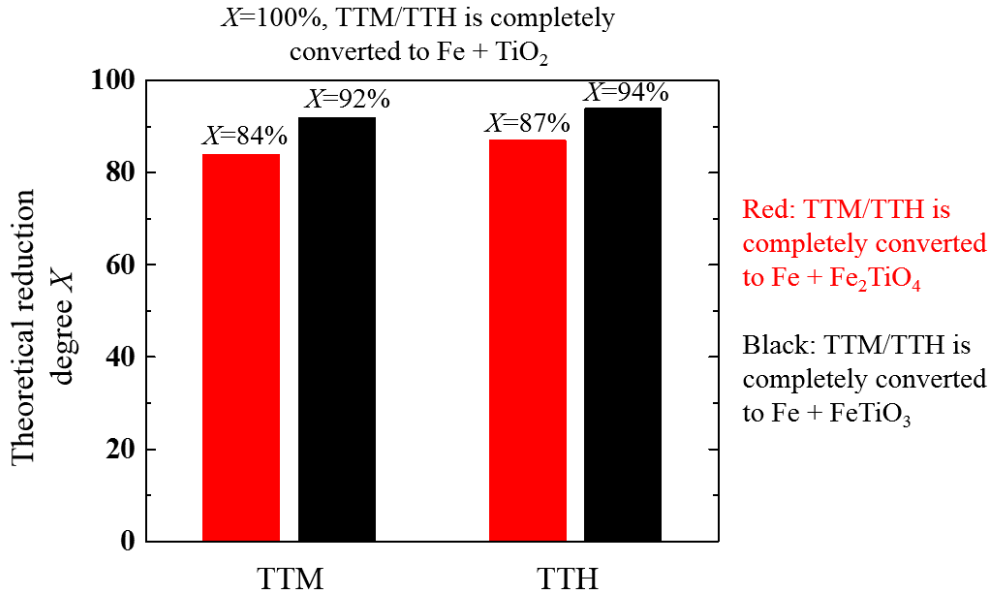

Figure 8.6 *– Theoretical calculation of the reduction degree X at different end points during reduction of TTM/TTH*

As a result, it is expected that at the latest stages of the reduction process, reactions are only taking place with the residual Fe-Ti-O phases which are dispersed throughout the whole pellet. Supporting evidence for this interpretation includes:

- In the fully reduced pellets (at maximum reduction degree), crystalline TiO_2, $FeTiO_3$, and PSB (ferro-PSB) are found to coexist with metallic Fe (**Figures 4.3** and **5.3**). This implies that the associated reduction of Fe-Ti-O phases must occur (as suggested in **Table 7.1**), even though only one of these phases ($FeTiO_3$) was observed in the *in-situ* ND data.
- SEM images of particle morphologies at the highest reduction degrees (**Appendices B.5** to **B.7**, and **C.5** to **C.7**) show that the residual Fe-Ti-O phases are established throughout each particle within the whole pellet. The Fe-Ti-O phases form many small islands (of sub-micron size), which are interspersed within the fine structure of metallic Fe. This means that a 'shrinking core' of reacting material is no longer present.

As a consequence, it is not surprising that the reduction of residual Fe-Ti-O phases at X>~90% is not well represented by a single interface SCM. If a model is required for this late stage of the reduction process, then it is likely that a non-shrinking core kinetic model would be required to be incorporated. However, in spite of this it is expected that the analytical expression obtained in **Chapter 6** will be sufficient for most practical purposes. Indeed, many industrial DRI processes terminate at a reduction degree of <~ 90% (~80% metallisation degree at NZ steel [176] and ~85% metallisation in most Midrex DRI plants [177]) .

8.4 Summary

In this chapter, the effects of temperature on the evolution of FeO in both types of pellets are discussed. As temperature decreases, less FeO was detected. This phenomenon can be explained by different activation energies for the reduction of TTM → FeO versus FeO → metallic Fe. If $E_{A(TTM \rightarrow FeO)}$ is greater than $E_{A(FeO \rightarrow Fe)}$ then with decreasing temperature, the chemical reaction rate of TTM → FeO will slow more rapidly than that of FeO → Metallic Fe. This will then lead to less FeO generated at lower temperatures. This explanation is consistent with the observation of two different activation energies in separate temperature regimes for the Ar-sintered pellets. (In the pre-oxidised pellets, no activation energy could be determined for the low temperature regime as only one data set is fitted using the SCM.)

In addition, as temperature decreases for both types of pellets, a tendency is observed for the broadening of the pellet-scale reaction interface. The broadening may occur if the reaction rate at the 'interface' becomes slower than the gas diffusion between the particle pores. This enables H_2 (and/or H_2O) to diffuse beyond the outermost reacting particles, activating the reactions in the particles in the inner of the pellets. Despite this broadening, the reduction data obtained at lower temperatures can still be fitted by a single interface SCM. However, caution is needed to reconcile the model to the SEM results at lower temperatures. For the Ar-sintered pellets, it seems that the SCM might describe a particle-scale mechanism. While for the pre-oxidised pellets, the SCM appears not to be connected with the SEM results, where the 'shrinking core' phenomenon was not observed. By contrast, for both types of pellets reduced at high temperature, the SCM describes well a pellet-scale shrinking core mechanism.

The breakdown of the model at X=~90% is likely to be caused by the completion of FeO. Afterwards, the reduction of the residual Fe-Ti-O phases occurs dispersing at each particle throughout the whole pellet. This no longer presents a 'shrinking core' mechanism. Therefore, a non-shrinking core model may be needed to be incorporated to describe the whole reduction process. Despite this, it is expected that the SCM will be satisfactory to describe the reduction process for practical purposes.

Chapter 9
Conclusions and industrial implications

In this thesis, a comprehensive analysis is presented of the DR characteristics and mechanisms for reduction in H_2 gas of Ar-sintered and pre-oxidised pellets made from NZ titanomagnetite ironsand. A series of reduction experiments have been performed, analysed and discussed. In general, the results obtained from these reduction experiments are consistent with each other, and the research aims set for this work (**Section 1.2**) have been accomplished. In summary:

- Ar-sintered and pre-oxidised pellets were successfully generated from a disc-pelletiser with the addition of bentonite and water, and reasonable values for the RSI and compressive strength have been measured (**Section 3.2**);
- The overall reduction progress of the pellets in H_2 gas at high temperatures has been measured in a TGA system (**Sections 4.1** and **5.1**), and interpreted using a single interface SCM (**Chapter 6**);
- The evolution of crystalline phases formed during the reduction has been determined from *in-situ* ND reduction experiments at temperatures up to 1223 K (results in **Sections 4.2** and **5.2**, analysis in **Chapter 7** and **8**);
- The evolution of pellet- and particle-scale morphologies has been established through SEM microscopy upon samples obtained from a series of quenching reduction experiments (results in **Sections 4.3** and **5.3**, analysis in **Chapter 8**); and
- The morphological evolution during reduction has been compared with results from the single interface SCM analysis (**Chapter 8**), and related to apparent changes in the rate-limiting behaviour at different temperatures.

This final chapter summarises the findings form this work, and is divided into the following sections:

- **Section 9.1**: Conclusions of this thesis
- **Section 9.2**: Industrial implications
- **Section 9.3**: Recommendations for future work

9.1 Conclusions

9.1.1 Key findings:

This research investigated the H_2-based direct reduction kinetics of the NZ TTM pellets, and the following knowledge gap has been filled. The activation energies are established using rate constants obtained from application of the SCM. The activation energies for NZ TTM ironsand pellets in H_2 gas have not been reported in the literature. The reduction pathway has also been studied through an *in-situ* analysis, with an emphasis on the effects of Ti existence on the initial reduction stages. Furthermore, the establishment of the morphological evolution of the pellet during reduction is used to inform understanding of the kinetic model.

In general, the following key findings can be concluded:

- *What is the DR behaviour in H_2 gas of NZ ironsand pellets?*

  The reduction of both Ar-sintered and pre-oxidised pellets presents a faster reduction rate with increasing temperature, H_2 flow rates and H_2 gas concentrations. At 1343 K it is also observed that decreasing the pellet diameter increases the reduction rate. The maximum reduction degree (~97%) of each type of pellet is achieved at 1443 K and gas flows above the critical flow rate. Pellets of ~7 mm diameter are fully reduced at this temperature within 10 minutes. While for the reduction at gas flows below the critical flow rate, it was found that the generation rate of metallic Fe is linearly dependent on the rate of H_2 gas delivery.

- *How does the morphology of key phases evolve during reduction of the pellets?*

  1. For the reduction of both types of pellets at high temperatures (> 1223 K), a pellet-scale shrinking core phenomenon is observed. Metallic Fe is initially generated at the pellet surface with a reaction interface then moving inwards towards the pellet centre. However, at lower temperatures, this pellet-scale reaction interface is less obvious. Instead, it seems that there is a trend which shifts from a pellet-scale process to a particle-scale one. Despite this, the particle-scale reactions at lower temperatures (down to 1023 K) are still

observed to follow a pellet-scale gradient, with the reduction of particles closer to the pellet surface going more quickly than those closer to the pellet centre.

2. For the reduction of Ar-sintered pellets at 1223 K, the morphology of FeO is observed to form a network of intersecting channels. This is caused by the enrichment of Ti in TTM during reduction. These channels are then further reduced to form metallic Fe from the particle surface to the particle centre, which follows the same morphology. By contrast, in the pre-oxidised pellets, FeO and metallic Fe form many small nucleates throughout the whole particles.

3. At temperatures much lower than 1223 K, metallic Fe shows either a whiskered structure (for Ar-sintered pellets) or a structure with disordered branches coming off larger central spines (for pre-oxidised pellets). At temperatures much higher than 1223 K, the final morphology of metallic Fe in the fully reduced particles coarsens, and forms into bulbous clusters in both types of pellets.

4. Over the whole temperature range, the unreduced oxides present in the fully reduced particles are interspersed as fine islands within the metallic Fe structure.

- *What is the reaction path during reduction of the pellets?*

1. The phase evolution for both types of pellets is interpreted from the data measured by the *in-situ* ND method. A similar reduction path is observed for both types of pellets, and is summarised as $TTH \rightarrow TTM \rightarrow TTM_{\text{-Ti enriched}} + FeO \rightarrow Fe + FeTiO_3 \rightarrow Fe +$ *'Ti-containing phases (TiO_2 or PSB/ferro-PSB)'*. TTH is initially rapidly reduced to TTM. Then TTM is reduced to FeO with Ti accumulating in the remaining TTM. Afterwards. FeO is further reduced to metallic Fe, and the remaining Ti-enriched TTM is reduced to metallic Fe and $FeTiO_3$. Although not seen in the *in-situ* ND data, *ex-situ* XRD data shows that other Ti-containing phases (TiO_2 and PSB/ferro-PSB) are also generated at the latest reduction stages.

2. During this reduction path, Ti is enriched within the surrounding TTM when FeO is generated. This is a key feature which is substantially different from non-titaniferous iron ores. The enrichment of Ti in TTM is confirmed by EDS-maps of partially reduced particles containing FeO. The effects of this Ti enrichment on the reduction process is summarised in **Subsection 9.1.2**.

- *What is the rate-limiting mechanism for the reduction of each type of pellet?*

1. A single interface SCM has successfully been applied to describe the reduction process at reduction degrees up to X=~90%. At higher reduction degrees a mismatch between the model and experimental data is observed. This is attributed to the transition which occurs following the complete consumption of FeO such that the remaining reduction occurs mainly through reaction of the residual Fe-Ti-O phases dispersed in the pellets, as outlined in **Subsection 9.1.2**. However, for many practical applications, X>90% is above the industrial limit, hence equations based upon the single interface SCM provide a reasonable description of the reduction progress.

2. For the reduction of the Ar-sintered pellets at the temperature range studied (993 K to 1443 K), the rate-limiting step was found to be interfacial chemical reaction. However, the activation energy for this reaction varied at separate temperature ranges. Above 1193 K, the activation energy was 41 ± 1 kJ/mol, with the rate controlling reaction at the interface reduction being FeO → metallic Fe. Below 1193 K, the activation energy is found to increase to 89 ± 5 kJ/mol, which is attributed to a change in the rate controlling reaction to TTM → FeO. At higher temperatures, it seems that the SCM for the Ar-sintered pellets describes a pellet-scale shrinking core mechanism. But at lower temperatures the SEM results suggest it is more consistent with a particle-scale shrinking core mechanism.

3. For the reduction of the pre-oxidised pellets, interfacial chemical reaction was found to be the rate-limiting step at temperatures above 1043 K. The activation energy established for this reaction was 31 ± 1 kJ/mol, which also appears to be consistent with the rate-controlling reaction being FeO → metallic Fe at higher temperatures. However, when the temperature dropped to 1043 K, the SCM analysis implied a mixed control mechanism with the rate of reduction being affected by both interfacial chemical reaction rates and diffusion rates through a product layer. However, it is difficult to reconcile this interpretation with the SEM results which showed only a broad pellet-scale gradient, and no clear shrinking core morphology at the particle-scale.

9.1.2 Key differences in the reduction of titanomagnetite ironsand pellets compared to non-titaniferous magnetite ores

It is generally accepted that the reduction of the titanomagnetite ores is slower than that of the non-titaniferous magnetite [124], [144], [147]. The work presented in this thesis highlights several key differences in the reduction of the TTM ironsand pellets studied, compared to the expected behaviour of conventional magnetite. These are mainly caused by the presence of Ti in the initial TTM lattice. Key features observed include:

1. Initially TTM is reduced to FeO, with Ti found to be enriched in the surrounding unreduced TTM. As the overall reduction process progresses, this Ti-enrichment causes the stoichiometry of the remaining TTM to be shifted towards the end-point of its solubility series, which is Fe_2TiO_4. Eventually, this changing stoichiometry leads to a change in the preferred reaction pathway, and the Ti-enriched TTM is instead directly reduced to metallic Fe and $FeTiO_3$. This change of reaction pathway also appears to slow the consumption rate of TTM, although this is most noticeable only at higher temperatures.
2. The existence of Ti in the original TTM lattice also affects the morphology of the FeO formed during reduction. In the Ar-sintered pellets, FeO forms a structure of intersecting channels throughout the particles, rather than a dense continuous structure as is typically observed for non-titaniferous magnetite ores [170]–[172]. This is caused by the Ti enrichment in the surrounding TTM matrix, which directs initial FeO growth to occur along channels, and then prevents these channels from merging. Eventually FeO forms a channelled network structure, which surrounds small isolated ‘islands’ of Ti-enriched TTM. In the pre-oxidised pellets, though FeO does not show well-structured channels, the ‘islands’ of Ti-enriched TTM is still observed in the particles.
3. The redistribution of Ti during reduction results in the formation of several minor Ti-containing phases ($FeTiO_3$, TiO_2 and PSB/ferro-PSB) during the latest stage of the reduction process. These residual Fe-Ti-O phases are dispersed throughout each particle within the whole pellets, meaning that at the latest stage of reduction (X>~90%), a shrinking core morphology is no longer observed. Accordingly, the single interface SCM is not applicable to the latest stage of reduction, which is consistent with the poor fits to the SCM of experimental data at X>~90%.

9.1.3 The effect of a pre-oxidation on reduction of the ironsand pellets

At low temperatures pre-oxidised pellets are observed to be reduced faster than Ar-sintered pellets. However, at temperatures ≥ 1243 K there is little apparent difference between the overall reduction rate of each type of pellet. This similar reduction rate agrees with the temperature above which the rate-limiting reaction step for both types of pellet is likely to be FeO → metallic Fe. The difference in behaviour at lower temperatures suggest that pre-oxidation primarily affects the reduction rate of TTM → FeO, as this appears to be the rate-limiting step for Ar-sintered pellets at 1023 K and 1123 K, but not for pre-oxidised pellets.

The beneficial effects resulting from pre-oxidation are mainly attributed to the formation of micro-cracks during early stages of transforming TTH to TTM. These micro-cracks facilitate and assist the transport and exchange of gas to the reaction sites, and this also increases the number of nucleation sites for FeO.

As a result, for the pre-oxidised pellets, the generation rate of FeO is faster than the Ar-sintered pellets at each condition studied. This is also in line with the FeO morphology developed in each type of pellets. For the Ar-sintered pellets, the generation of FeO occurs topochemically with channels developing. By contrast, in the pre-oxidised pellets, the cracks provide improved gas access to reaction sites, leading to the nucleation of FeO throughout each whole particle.

9.2 Industrial implications

The knowledge obtained from this research has potentially useful industrial implications. This study has shown that the reduction of pellets at high temperature in H_2 gas can be well described by a single interface SCM. Moreover, at high temperatures (>1193 K) the reduction is dominantly controlled by the interfacial chemical reaction rate (with rate limiting reaction step being FeO → metallic Fe). As a result, parameters which will affect the reaction rate, such as temperature, initial pellet diameter, may be optimised to achieve a faster reduction process. It is recommended from this study that reduction of smaller pellets at 1443 K could achieve a faster reduction rate. However, in a practical vertical fixed-bed reactor, the permeability of the reactor should also be taken into consideration. The smallest pellet size may ultimately be dictated by the reactor permeability. This represents a possible topic for future research.

Comparing the reduction characteristics of the Ar-sintered and pre-oxidised pellets, there appear to be some advantages in sintering the 'green' pellets in air rather than in Ar gas. Sintering in air is relatively easier to be conducted than sintering in Ar gas, and pre-oxidation increases the overall reduction rate of the pellets at temperatures below 1243 K.

However, it should be noted that additional oxygen is also introduced to the pellets during pre-oxidation. Removing this extra O_2 gas during reduction will increase the consumption of H_2 gas by ~11% for the generation of the same amount of metallic Fe.

The successful application of the SCM can also assist in the future design of an ironsand-pellet shaft reactor for H_2 direct reduction. However, in order to make the full use, a reaction model that incorporates the effect of H_2/H_2O on the reaction rate is also required. This should be a key aspect of future work (see **Section 9.3**).

9.3 Recommendations for future work

The scope of the research in this thesis has been aimed at understanding the DR characteristics of the NZ ironsand pellets in H_2 gas and determining the rate-limiting reduction mechanisms. While these have been thoroughly investigated in this research, further studies are recommended in the following aspects:

- This study has investigated the reduction behaviour of small numbers of pellets (either 1 or 4) in H_2 gas. However, a future industrial process would need to reduce large quantities of pellets at the same time. Therefore, the performance of reducing a large number of pellets in a fixed bed reactor is worth further examining. This might include the investigation of binder combination to optimise pellets properties (such as strength and porosity), the reactor permeability, and measurements to determine whether sticking or degradation of the pellets happens during reduction. In addition, the design of future reactors will require more knowledge of the effect of the H_2/H_2O ratio on the pellet reaction rate, so this also needs to be measured.

- Although the SCM successfully described the majority of the reduction process, it fails to interpret the data above 90% reduction degree. Further, at lower reduction temperatures, particle-scale mechanisms appear to be significant. Further work is required to develop a universal reduction model that incorporates both pellet-scale and particle-scale phenomena.

- There is limited existing experimental data on the thermodynamic phase diagram for the Fe-Ti-O system. Further experimental measurements of this system would help fully understand the phase evolution during reduction of ironsand, and in particular the driving force for the apparent switch in reduction pathway from TTM → FeO to TTM → $FeTiO_3$ + metallic Fe.

- It is also recommended to apply the knowledge obtained from this research to optimise the subsequent smelting process. This work has shown that many small 'islands' of Ti-containing slag are formed within the metallic Fe structure during reduction. It is possible that during the subsequent smelting process, these Ti-containing particles could become entrapped within the metal and hence not properly separated. A method will be needed to

ensure that these small particles can be melted and separated from the molten metallic Fe. This may include the mixing of slag-fluxing agents into the pellet at an earlier stage of the process.

Reference

[1] L. Carter, “Ironsand in continental shelf sediments off western New Zealand—a synopsis,” *New Zeal. J. Geol. Geophys.*, vol. 23, no. 4, pp. 455–468, 1980.

[2] A. B. Christie and R. G. Barker, “Mineral, coal and petroleum resources: production, exploration and potential,” *Ecosyst. Serv. New Zeal. Cond. trends*, vol. 2, 2013.

[3] D. C. Lawton and M. P. Hochstein, “Geophysical study of the taharoa ironsand deposit, west coast, North Island, New Zealand,” *New Zeal. J. Geol. Geophys.*, vol. 36, no. 2, pp. 141–160, 1993.

[4] J. B. Wright, “Iron-titanium oxides in Some New Zealand ironsands,” *New Zeal. J. Geol. Geophys.*, vol. 7, no. 3, pp. 424–444, 1964.

[5] T. Christie and B. Brathwaite, “Mineral Commodity Report 15 — Iron,” 1987.

[6] Y. Zhao, T. Sun, H. Zhao, C. Xu, and S. Wu, “Effect of MgO and $CaCO_3$ as additives on the reduction roasting and magnetic separation of beach titanomagnetite concentrate,” *ISIJ Int.*, vol. 59, no. 6, pp. 981–987, 2019.

[7] “Waikato North Head Mine Site | New Zealand Steel.” [Online]. Available: https://www.nzsteel.co.nz/new-zealand-steel/the-story-of-steel/the-mining-operations/waikato-north-head-mine-site/. [Accessed: 30-Jan-2020].

[8] Y. Zhao, T. Sun, and Z. Wang, “Extraction of Iron from Refractory Titanomagnetite by Reduction Roasting and Magnetic Separation,” pp. 1–7, 2020.

[9] “New Zealand Steel Production | 1992-2019 Data | 2020-2022 Forecast | Calendar.” [Online]. Available: https://tradingeconomics.com/new-zealand/steel-production. [Accessed: 12-Feb-2020].

[10] “Taharoa ironsand mining and ship loading | Engineering New Zealand.” https://www.engineeringnz.org/our-work/heritage/heritage-records/taharoa-ironsand-mining-and-ship-loading/ (accessed Jan. 30, 2020).

[11] J. Meyers *et al.*, “Onshore ironsand exploration on the North Island of New Zealand: regional prospecting to resource definition in a short time frame by utilising geophysical methods and data integration,” *Conf. Proc. 2010 AusIMM New Zeal. Branch Annu. Conf.*, pp. 421–432, 2011.

[12] South Taranaki Bight | Trans-Tasman Resources.” [Online]. Available: https://www.ttrl.co.nz/projects/south-Taranaki-bight.

[13] Z. Gao, S. Yang, X. Xue, H. Yang, and G. Cheng, “Extraction method for valuable elements of low-grade vanadia–titania magnetite,” *J. Clean. Prod.*, vol. 250, p. 119451, 2020.

[14] P. R. Taylor, S. A. Shuey, E. E. Vidal, and J. C. Gomez, “Extractive metallurgy of vanadium-containing titaniferous magnetite ores: A review,” *Miner. Metall. Process.*, vol. 23, no. 2, pp. 80–86, 2006.

[15] “The Ironmaking Process | New Zealand Steel.” [Online]. Available: https://www.nzsteel.co.nz/new-zealand-steel/the-story-of-steel/the-science-of-steel/the-ironmaking-process/. [Accessed: 12-Feb-2020].

[16] “Emissions tracker | Ministry for the Environment.” [Online]. Available: https://www.mfe.govt.nz/climate-change/state-of-our-atmosphere-and-climate/emissions-tracker. [Accessed: 30-Jan-2020].

[17] “About New Zealand’s emissions reduction targets | Ministry for the Environment.” [Online]. Available: https://www.mfe.govt.nz/climate-change/climate-change-and-government/emissions-reduction-targets/about-our-emissions. [Accessed: 30-Jan-2020].

[18] N. A. El-Hussiny, A. El-Amir, S. T. Abdel-Rahim, K. El hossiny, and M. E.-M. H. Shalabi, “Kinetics of Direct Reduction Titanomagnetite Briquette Produced from Rossetta-Ilmenite via Hydrogen,” *OALib*, vol. 01, no. 05, pp. 1–11, 2014.

[19] P. Halli, P. Taskinen, and R. H. Eriç, “Mechanisms and Kinetics of Solid State Reduction of Titano Magnetite Ore with Methane,” *J. Sustain. Metall.*, vol. 3, no. 2, pp. 191–206, 2017.

[20] G. H. Han, T. Jiang, Y. B. Zhang, Y. F. Huang, and G. H. Li, “High-temperature oxidation behavior of vanadium, titanium-bearing magnetite pellet,” *J. Iron Steel Res. Int.*, vol. 18, no. 8, pp. 14–19, 2011.

[21] T. P. Battle, “Sustainability in ironmaking: The rise of direct reduction,” *TMS Annu. Meet.*, pp. 277–288, 2014.

[22] M. Cojić and S. Kožuh, “Development of direct reduction processes and smelting reduction processes for the steel production,” *Kem. u Ind. Chem. Chem. Eng.*, vol. 55, no. 1, pp. 1–10, 2006.

[23] K. Endo and Y. Matsushita, “Technological Developments in the Direct Reduction of Iron Ore in Japan,” *Tetsu-to-Hagane*, vol. 48, no. 6, pp. 796–802, 1962.

[24] N. Saleh and S. Rochani, “Study on reduction of iron ore concentrate in rotary kiln to produce direct reduced iron,” *Indones. Min. J.*, vol. 22, no. 2, pp. 87–98, 2019.

[25] K. Tacke and R. Steffen, “Hydrogen as a reductant for iron ores and the effects on CO_2 formation,” In Proc. Int. Symp on Global Environment and Steel Industry (ISES'03), 06, 2013.

[26] A. Ranzani da Costa, D. Wagner, and F. Patisson, “Modelling a new , low CO_2 emissions , hydrogen steelmaking process,” *J. Clean. Prod.*, vol. 46(May), pp. 27–35, 2013.

[27] “Global Trends and Outlook for Hydrogen,” IEA Hydrogen, December, 2017.

[28] Ministry of Business, Innovation and Employment, “A Vision for Hydrogen in New Zealand Green Paper,” no. September, 2019, [Online]. Available: www.mbie.govt.nz.

[29] W. Li, N. Wang, G. Fu, M. Chu, and M. Zhu, “Effects of preheating temperature and time of hongge vanadium titanomagnetite pellet on its gas-based direct reduction behavior with simulated shaft furnace gases,” *ISIJ Int.*, vol. 58, no. 4, pp. 594–603, 2018.

[30] R. Briggs, J. Laurent, T. Hume, and A. Swales, “Provenance of black sands on the west coast , North Island , New Zealand Black sand placer deposits,” In Proc. the 42nd AusIMM New Zealand Branch Annual Conference, pp. 41-50, 2009.

[31] R. L. Brathwaite, M. F. Gazley, M. Exploration, and A. B. Christie, “Stratigraphy , mineralogy and provenance of the sand sequence at Waikato North Head , south Auckland,” Presented at NZ Branch AusIMM conference, 2018.

[32] R. L. Brathwaite, M. F. Gazley, and A. B. Christie, “Provenance of titanomagnetite in ironsands on the west coast of the North Island, New Zealand,” *J. Geochemical Explor.*, vol. 178, pp. 23–34, 2017.

[33] “The History of Ironsand | New Zealand Steel.” [Online]. Available: https://www.nzsteel.co.nz/new-zealand-steel/the-story-of-steel/the-history-of-ironsand/. [Accessed: 30-Jan-2020].

[34] G. D McAdam at. el., “Direct gas reduction of NZ Ironsands,” *NEW Zeal. J. Sci.*, vol. 12, no. 4, pp. 649–668, 1969.

[35] G. D McAdam, "Instability of ironsands in reducing gases,” *Ironmaking and Steelmaking*, No.3, pp 138-149, 1974.

[36] W. Shannon, W. Kitt, T. Marshall, “Spouted bed reduction of NZ ironsands,” *NEW Zeal. J. Sci.*, no. 3, pp. 74-92, 1960.

[37] R. J. Longbottom, B. J. Monaghan, S. A. Nightingale, and J. G. Mathieson, “Strength and bonding in reduced ironsand-coal compacts,” *Ironmak. Steelmak.*, vol. 40, no. 5, pp. 381–389, 2013.

[38] R. J. Longbottom, B. J. Monaghan, and J. G. Mathieson, “Development of a bonding phase within titanomagnetite-coal compacts,” *ISIJ Int.*, vol. 53, no. 7, pp. 1152–1160, 2013.

[39] N. J. Bristow and C. E. Loo, “Sintering Properties of Iron Ore Mixes Containing Titanium.,” *ISIJ Int.*, vol. 32, no. 7, pp. 819–828, 1992.

[40] C. Geng, T. Sun, H. Yang, Y. Ma, E. Gao, and C. Xu, “Effect of Na_2SO_4 on the embedding direct reduction of beach titanomagnetite and the separation of titanium and iron by magnetic separation,” *ISIJ Int.*, vol. 55, no. 12, pp. 2543–2549, 2015.

[41] D. S. Pogudin, A. A. Morozov, G. B. Sadykhov, T. V. Olyunina, T. V. Goncharenko, and L. I. Leont’ev, “Phase formation during the reduction of the titanomagnetite from the Gremyakha-Vyrmes deposit,” *Russ. Metall.*, vol. 2010, no. 9, pp. 759–762, 2010.

[42] A. A. Adetoro, H. Sun, S. He, Q. Zhu, and H. Li, “Effects of Low-temperature Pre-oxidation on the Titanomagnetite Ore Structure and Reduction Behaviors in a Fluidized Bed,” *Metall. Mater. Trans. B Process Metall. Mater. Process. Sci.*, vol. 49B, no. 2, pp. 846–857, 2018.

[43] D. S. Chen, B. Song, L. N. Wang, T. Qi, Y. Wang, and W. J. Wang, “Solid state reduction of Panzhihua titanomagnetite concentrates with pulverized coal,” *Miner. Eng.*, vol. 24, no. 8, pp. 864–869, 2011.

[44] Z. Wang *et al.*, “Behavior of New Zealand Ironsand During Iron Ore Sintering,” *Metall. Mater. Trans. B Process Metall. Mater. Process. Sci.*, vol. 47, no. 1, pp. 330–343, 2016.

[45] J. B. Wright and J. F. Lovering, “Electron-probe micro-analysis of the iron–titanium oxides in some New Zealand ironsands,” *Mineral. Mag. J. Mineral. Soc.*, vol. 35, no. 272, pp. 604–621, 1965.

[46] Midrex, “The MIDREX ® Process,” *Midrex Technol. Inc.*, 2013.

[47] D. Fernández-González, J. Piñuela-Noval, and L. F. Verdeja, “Iron Ore Agglomeration Technologies,” *Iron Ores Iron Oxide Mater.*, 2018.

[48] D. Zhu, J. Pan, L. Lu, and R. J. Holmes, Iron ore: Mineralogy, Processing, and Enviromental Issues, Woodhead Publishing, pp 435-473, 2015.

[49] T. Nomura, N. Yamamoto, T. Fujii, and Y. Takiguchi, “Beneficiation plants and pelletizing plants for utilization of low grade iron ore,” *R D Res. Dev. Kobe Steel Eng. Reports*, vol. 64, no. 1, pp. 8–13, 2014.

[50] “Iron Ore Pelletizing Essential in Meeting Future Steel Needs.” [Online]. Available: https://feeco.com/iron-ore-pelletizing-essential-in-meeting-future-steel-needs/. [Accessed: 29-Jan-2020].

[51] J. Fu, T. Jiang, and D. Zhu, Sintering and pelletizing. Press of Central South University of Technology, Changsha, pp. 282, 1995.

[52] J. Fu, and D. Zhu, Fundamental Principles, Technologies and Equipments, 1st edition, Chang Sha, China: Central South University Industry Press, 2005.

[53] V. Shatokha, *Iron Ores and Iron Oxide Materials*. InTech, 2018. Note: @2018 De Moraes SL, Baptista de Lima JR, Ramos Ribeiro T. Published in [short citation] under CC BY 3.0 license. Available from: htpp://dx.doi.org/10.5772/intechopen.73164.

[54] K. Meyer. “Pelletizing of iron ores.” Springer-Verlag, 1980.

[55] W. Pietsch, *Agglomeration processes : phenomena, technologies, equipment*. Wiley-VCH, 2002.

[56] A. Z. M. Abouzeid and A. A. Seddik, “Effect of iron ore properties on its balling behaviour,” *Powder Technol.*, vol. 29, no. 2, pp. 233–241, 1981.

[57] N. Tugrul, M. E. Derun, and M. Piskin, “Effects of calcium hydroxide and calcium chloride addition to bentonite in iron ore pelletization,” *Waste Manag. Res.*, vol. 24, no. 5, pp. 446–455, 2006.

[58] J. A. Halt, S. C. Roache, and S. K. Kawatra, “Cold Bonding of Iron Ore Concentrate Pellets,” *Miner. Process. Extr. Metall. Rev.*, vol. 36, no. 3, pp. 192–197, 2015.

[59] M. Iljana, "Iron ore pellet properties under simulated blast furnace conditions : investigation on reducibility, swelling and softening," Doctoral thesis, University of Oulu, Oulu, 2017.

[60] A. K. Mandal, A. Sarkar, and O. P. Sinha, “Utilization of Lime Fines as an Effective Binder as well as Fluxing Agent for Making Fluxed Iron Ore Pellets,” *J. Inst. Eng. Ser. D*, vol. 97, no. 1, pp. 69–75, 2016.

[61] O. Sivrikaya and A. I. Arol, “Alternative Binders To Bentonite for Iron Ore Pelletizing: Part I: Effects on Physical and Mechanical Properties,” *Holos*, vol. 3, p. 94-103, 2014.

[62] S. L. De Moraes, J. R. B. De Lima, and J. B. F. Neto, “Influence of dispersants on the rheological and colloidal properties of iron ore ultrafine particles and their effect on the pelletizing process - A review,” *Journal of Materials Research and Technology*, vol. 2, no. 4, pp. 386–391, 2013.

[63] J. Pal, C. Arunkumar, Y. Rajshekhar, G. Das, M. C. Goswami, and T. Venugopalan, “Development on iron ore pelletization using calcined lime and MgO combined flux replacing limestone and bentonite,” *ISIJ Int.*, vol. 54, no. 10, pp. 2169–2178, 2014.

[64] T. C. Eisele and S. K. Kawatra, “A review of binders in iron ore pelletization,” *Miner. Process. Extr. Metall. Rev.*, vol. 24, pp. 1-90, 2003.

[65] R. Béchara, H. Hamadeh, O. Mirgaux, and F. Patisson, “Optimization of the iron ore direct reduction process through multiscale process modeling,” *Materials (Basel).*, vol. 11, no. 7, pp. 1–18, 2018.

[66] S. K. Kuila, R. Chatterjee, and D. Ghosh, “Kinetics of hydrogen reduction of magnetite ore fines,” *Int. J. Hydrogen Energy*, vol. 41, no. 22, pp. 9256–9266, 2016.

[67] Y. Nasiri, M. Panjepour, and M. Ahmadian, “The kinetics of hematite reduction and cementite formation with CH_4-H_2-Ar gas mixture,” *Int. J. Miner. Process.*, vol. 153, pp. 17–28, 2016.

[68] S. M. Jung and S. H. Yi, “Kinetic study on reduction in carbon composite magnetite pellet employing thermogravimetry and quadruple mass spectrometry,” *Ironmak. Steelmak.*, vol. 41, no. 1, pp. 38–46, 2014.

[69] C. Lu *et al.*, “Chemical looping reforming of methane using magnetite as oxygen carrier: Structure evolution and reduction kinetics,” *Appl. Energy*, vol. 211, pp. 1–14, 2018.

[70] Y. Wang, X. Wang, X. Hua, C. Zhao, and W. Wang, “The reduction mechanism and kinetics of Fe_2O_3 by hydrogen for chemical-looping hydrogen generation,” *J. Therm. Anal. Calorim.*, vol. 129, no. 3, pp. 1831–1838, 2017.

[71] O. J. Wimmers, P. Arnoldy, and J. A. Moulijn, “Determination of the reduction mechanism by temperature-programmed reduction: application to small iron oxide (Fe_2O_3) particles,” *J. Phys. Chem.*, vol. 90, no. 7, pp. 1331–1337, 2005.

[72] Y. D. Wang, X. N. Hua, C. C. Zhao, T. T. Fu, W. Li, and W. Wang, “Step-wise reduction kinetics of Fe_2O_3 by CO/CO_2 mixtures for chemical looping hydrogen generation,” *Int. J. Hydrogen Energy*, vol. 42, no. 9, pp. 5667–5675, 2017.

[73] E. Turkdogan and J. Vinters, “Gaseous reduction of iron oxides: Part III. Reduction-oxidation of porous and dense iron oxides and iron,” *Metall. Trans.*, vol. 3, no. 6, pp. 1561–1574, 1972.

[74] H. Wang, “Reduction Kinetics of Iron Ore Concentrate Particles Relevant To a Novel Green Ironmaking Process,” Doctoral thesis, University of Utah. Utah, 2011.

[75] E. R. Monazam, R. W. Breault, R. Siriwardane, G. Richards, and S. Carpenter, “Kinetics of the reduction of hematite (Fe_2O_3) by methane (CH_4) during chemical looping combustion: A global mechanism,” *Chem. Eng. J.*, vol. 232, pp. 478–487, 2013.

[76] J. Chen *et al.*, “Direct reduction of oxidized iron ore pellets using biomass syngas as the reducer,” *Fuel Process. Technol.*, vol. 148, pp. 276–281, 2016.

[77] R. Longbottom and L. Kolbeinsen, “Iron ore Reduction with CO and H_2 Gas Mixtures – Thermodynamic and Kinetic Modelling,” *Ulcos Semin. - New Direct Reduct.*, pp. 1–13, 2008.

[78] W. Zhang, J. H. Zhang, Z. S. Zou, Q. Li, and Y. H. Qi, “Influences of non-stoichiometry on thermodynamics and kinetics of iron oxides reduction processes,” *Ironmak. Steelmak.*, vol. 41, no. 9, pp. 715–720, 2014.

[79] D. Guo *et al.*, “Kinetics and mechanisms of direct reduction of iron ore-biomass composite pellets with hydrogen gas,” *Int. J. Hydrogen Energy*, vol. 40, no. 14, pp. 4733–4740, 2015.

[80] Y. Qu, Y. Yang, Z. Zou, C. Zeilstra, H. K. A. Meijer, and R. Boom, “Reduction Kinetics of Fine Hematite Ore Particles with a High Temperature Drop Tube Furnace,” *ISIJ Int.*, vol. 55, no. 5, pp. 952–960, 2015.

[81] A. Amiri, G. D. Ingram, A. V. Bekker, I. Livk, and N. E. Maynard, “A multi-stage, multi-reaction shrinking core model for self-inhibiting gas-solid reactions,” in *Advanced Powder Technology*, vol. 24, no. 4, pp. 728–736, 2013.

[82] B. Hou, H. Zhang, H. Li, and Q. Zhu, “Study on Kinetics of Iron Oxide Reduction by Hydrogen,” *Chinese J. Chem. Eng.*, vol. 20, no. 1, pp. 10–17, 2012.

[83] B. Hou, H. Zhang, H. Li, and Q. Zhu, “Determination of the intrinsic kinetics of iron oxide reduced by carbon monoxide in an isothermal differential micro-packed bed,” *Chinese J. Chem. Eng.*, vol. 23, no. 6, pp. 974–980, 2015.

[84] L. Guo, J. Gao, Y. Zhong, and Z. Guo, “Flash Suspension Reduction of Ultra-fine Fe_2O_3 Powders and the Kinetic Analyzing,” vol. 55, no. 9, pp. 1797–1805, 2015.

[85] J. Dang, K. C. Chou, X. J. Hu, and G. H. Zhang, “Reduction kinetics of metal oxides by hydrogen,” *Steel Res. Int.*, vol. 84, no. 6, pp. 526–533, 2013.

[86] H. Zuo, C. Wang, J. Dong, K. Jiao, and R. Xu, “Reduction kinetics of iron oxide pellets with H_2 and CO mixtures,” *Int. J. Miner. Metall. Mater.*, vol. 22, no. 7, pp. 688–696, 2015.

[87] J. Yu, Y. Li, W. Li, P. Gao, and Y. Han, “Mechanism and Kinetics of the Reduction of Hematite to Magnetite with CO–CO_2 in a Micro-Fluidized Bed,” *Minerals*, vol. 7, no. 11, 2017.

[88] M. S. Valipour, M. Y. Motamed Hashemi, and Y. Saboohi, “Mathematical modeling of the reaction in an iron ore pellet using a mixture of hydrogen, water vapor, carbon monoxide and carbon dioxide: An isothermal study,” *Adv. Powder Technol.*, vol. 17, no. 3, pp. 277–295, 2006.

[89] T. Usui, M. Ohmi, and E. Yamamura, “Analysis of rate of hydrogen reduction of porous wustite pellets basing on zone-reaction models.,” *ISIJ Int.*, vol. 30, no. 5, pp. 347–355, 1990.

[90] S. Natsui, T. Kikuchi, and R. O. Suzuki, “Numerical Analysis of Carbon Monoxide–Hydrogen Gas Reduction of Iron Ore in a Packed Bed by an Euler–Lagrange Approach,” *Metall. Mater. Trans. B Process Metall. Mater. Process. Sci.*, vol. 45, no. 6, pp. 2395–2413, 2014.

[91] F. Chen, Y. Mohassab, S. Zhang, and H. Y. Sohn, “Hydrogen Reduction Kinetics of Hematite Concentrate Particles Relevant to a Novel Flash Ironmaking Process,” *Metall. Mater. Trans. B Process Metall. Mater. Process. Sci.*, vol. 46, no. 4, pp. 1716–1728, 2015.

[92] B. Weiss, J. Sturn, F. Winter, and J. L. Schenk, " Empirical reduction diagrams for reduction of iron ores with H_2 and CO gas mixtures considering non-stoichiometries of oxide phases ," *Ironmak. Steelmak.*, vol. 36, no. 3, pp. 212–216, 2009.

[93] A. A. Barde, J. F. Klausner, and R. Mei, "Solid state reaction kinetics of iron oxide reduction using hydrogen as a reducing agent," *Int. J. Hydrogen Energy*, vol. 41, no. 24, pp. 10103–10119, 2016.

[94] A. Bonalde, A. Henriquez, and M. Manrique, "Kinetic Analysis of the Iron Oxide Reduction Using Hydrogen-Carbon Monoxide Mixtures as Reducing Agent," *ISIJ Int.*, vol. 45, no. 9, pp. 1255–1260, 2005.

[95] H. Chen, Z. Zheng, Z. Chen, and X. T. Bi, "Reduction of hematite (Fe_2O_3) to metallic iron (Fe) by CO in a micro fluidized bed reaction analyzer: A multistep kinetics study," *Powder Technol.*, vol. 316, pp. 410–420, 2017.

[96] H. Y. Lin and Y. W. Chen, "The mechanism of reduction of iron oxide by hydrogen," *Thermochim. Acta*, vol. 400, pp. 61–67, 2003.

[97] M. A. Hararah, M. Al-Harahsheh, and A. H. Tobgy, "A preliminary study on the hydrogen reduction of jordanian iron ore," *Miner. Process. Extr. Metall.*, vol. 118, no. 2, pp. 105–108, 2012.

[98] E. R. Monazam, R. W. Breault, and R. Siriwardane, "Reduction of hematite (Fe_2O_3) to wüstite (FeO) by carbon monoxide (CO) for chemical looping combustion," *Chem. Eng. J.*, vol. 242, pp. 204–210, 2014.

[99] L. Stonawski, T. Wiltowski, H. Lorethova, K. Piotrowski, K. Mondal, and T. SzymanskiI, "Effect of gas composition on the kinetics of iron oxide reduction in a hydrogen production process," *Int. J. Hydrogen Energy*, vol. 30, no. 15, pp. 1543–1554, 2004.

[100] E. Nyankson and L. Kolbeinsen, "Kinetics of Direct Iron Ore Reduction with CO-H_2 Gas Mixtures," *Int. J. Eng. Res.*, vol. V4, no. 04, pp. 934–940, 2015.

[101] G. Y. Lee, J. ll Song, and J. S. Lee, "Reaction kinetics and phase transformation during hydrogen reduction of spherical Fe_2O_3 nanopowder agglomerates," *Powder Technol.*, vol. 302, pp. 215–221, 2016.

[102] W. Liu, J. Y. Lim, M. A. Saucedo, A. N. Hayhurst, S. A. Scott, and J. S. Dennis, "Kinetics of the reduction of wüstite by hydrogen and carbon monoxide for the chemical looping production of hydrogen," *Chem. Eng. Sci.*, vol. 120, pp. 149–166, 2014.

[103] J. Feinman, N. D. Smith, and D. A. Muskat, "Effect of gas flow rate on the kinetics of reduction of iron oxide pellets with hydrogen," I&*EC Process Design and Development*, vol.4, no.3, pp. 270-274, 1965.

[104] R. Beheshti, J. Moosberg-Bustnes, M. W. Kennedy, and R. E. Aune, "Reduction kinetics of commercial haematite pellet in a fixed bed at 1123-1273 K," *Ironmak. Steelmak.*, vol. 43, no. 5, pp. 394–402, 2016.

[105] W. K. Jozwiak, E. Kaczmarek, T. P. Maniecki, W. Ignaczak, and W. Maniukiewicz, "Reduction behavior of iron oxides in hydrogen and carbon monoxide atmospheres," *Appl. Catal. A Gen.*, vol. 326, no. 1, pp. 17–27, 2007.

[106] M. Kazemi, B. Glaser, and D. Sichen, “Study on direct reduction of hematite pellets using a new TG setup,” *Steel Res. Int.*, vol. 85, no. 4, pp. 718–728, 2014.

[107] M. H. Jeong, D. H. Lee, and J. W. Bae, “Reduction and oxidation kinetics of different phases of iron oxides,” *Int. J. Hydrogen Energy*, vol. 40, no. 6, pp. 2613–2620, 2015.

[108] Z. Wang, J. Zhang, K. Jiao, Z. Liu, and M. Barati, “Effect of pre-oxidation on the kinetics of reduction of ironsand,” *J. Alloys Compd.*, vol. 729, pp. 874–883, 2017.

[109] H. Chen, Z. Zheng, and W. Shi, “Investigation on the kinetics of iron ore fines reduction by CO in a micro-fluidized bed,” *Procedia Eng.*, vol. 102, pp. 1726–1735, 2015.

[110] D. R. Parisi and M. A. Laborde, “Modeling of counter current moving bed gas-solid reactor used in direct reduction of iron ore,” *Chem. Eng. J.*, vol. 104, no. 1–3, pp. 35–43, 2004.

[111] Z. Chen, J. Dang, X. Hu, and H. Yan, “Reduction kinetics of hematite powder in hydrogen atmosphere at moderate temperatures,” *Metals (Basel).*, vol. 8, no. 10, 2018.

[112] H. Y. Sohn and J. Szekely, “A structural model for gas—solid reactions with a moving boundary—IV. Langmuir—Hinshelwood kinetics,” *Chem. Eng. Sci.*, vol. 28, no. 5, pp. 1169–1177, 1973.

[113] N. Takeuchi, Y. Nomura, K. Ohno, T. Maeda, K. Nishioka, and M. Shimizu, “Kinetic Analysis of Spherical Wustite Reduction Transported with CH_4 Gas,” *ISTJ Int.*, vol. 94, no. 3, pp. 115–120, 2009.

[114] D. Yu, M. Zhu, T. A. Utigard, and M. Barati, “TGA kinetic study on the hydrogen reduction of an iron nickel oxide,” *Miner. Eng.*, vol. 54, pp. 32–38, 2013.

[115] F. Chen, Y. Mohassab, S. Zhang, and H. Y. Sohn, “Kinetics of the Reduction of Hematite Concentrate Particles by Carbon Monoxide Relevant to a Novel Flash Ironmaking Process,” *Metall. Mater. Trans. B Process Metall. Mater. Process. Sci.*, vol. 46, no. 4, pp. 1716–1728, 2015.

[116] H. Wang and H. Y. Sohn, “Hydrogen reduction kinetics of magnetite concentrate particles relevant to a novel flash ironmaking process,” *Metall. Mater. Trans. B Process Metall. Mater. Process. Sci.*, vol. 44, no. 1, pp. 133–145, 2013.

[117] M. Kazemi, M. S. Pour, and D. Sichen, “Experimental and Modeling Study on Reduction of Hematite Pellets by Hydrogen Gas,” *Metall. Mater. Trans. B*, vol 48, pp.1114-1122, 2017.

[118] J. Dang, X. Hu, G. Zhang, X. Hou, X. Yang, and K. Chou, “Kinetics of reduction of titano-magnetite powder by H_2,” *High Temp. Mater. Process.*, vol. 32, no. 3, pp. 229–236, 2013.

[119] J. Dang, G. H. Zhang, X. J. Hu, and K. C. Chou, “Non-isothermal reduction kinetics of titanomagnetite by hydrogen,” *Int. J. Miner. Metall. Mater.*, vol. 20, no. 12, pp. 1134–1140, 2013.

[120] X. F. She, H. Y. Sun, X. J. Dong, Q. G. Xue, and J. S. Wang, “Reduction mechanism of titanomagnetite concentrate by carbon monoxide,” *J. Min. Metall. Sect. B Metall.*, vol. 49, no. 3, pp. 263–270, 2013.

[121] H. Sun, J. Wang, Y. Han, X. She, and Q. Xue, “Reduction mechanism of titanomagnetite concentrate by hydrogen,” *Int. J. Miner. Process.*, vol. 125, pp. 122–128, 2013.

[122] Y. Li, H. Guo, and L. Li, “Hydrogen reduction mechanism of Indonesia ironsand oxidized pellets,” *Chinese J. Eng.*, vol. 40, no. 2, pp. 154–157, 2011.

[123] Y. Sui, Y. Guo, T. Jiang, X. Xie, S. Wang, and F. Zheng, “Gas-based reduction of vanadium titano-magnetite concentrate: behavior and mechanisms,” *Int. J. Miner. Metall. Mater.*, vol. 24, no. 1, pp. 10–17, 2017.

[124] R. J. Longbottom, B. Ingham, M. H. Reid, A. J. Studer, C. W. Bumby, and B. J. Monaghan, “*In-situ* neutron diffraction study of the reduction of New Zealand ironsands in dilute hydrogen mixtures,” *Miner. Process. Extr. Metall.*, pp. 1–10, 2018.

[125] Y. Liu, J. Zhang, Z. Liu, and X. Xing, “Phase transformation behavior of titanium during carbothermic reduction of titanomagnetite ironsand,” *Int. J. Miner. Metall. Mater.*, vol. 23, no. 7, pp. 760–768, 2016.

[126] J. Tang and M. S. Chu, “Non-Isothermal Gas-Based Direct Reduction Behavior of High Chromium Vanadium-Titanium Magnetite Pellets and the Melting Separation of Metallized Pellets,” *Metals (Basel).*, vol. 7, no. 5, p. 153, 2017.

[127] J. Chen, W. Chen, L. Mi, Y. Jiao, and X. Wang, “Kinetic Studies on Gas-Based Reduction of Vanadium Titano-Magnetite Pellet,” *Metals (Basel).*, vol. 9, no. 1, 2019.

[128] J. Tang, M. sheng Chu, F. Li, Y. ting Tang, Z. gen Liu, and X. xin Xue, “Reduction mechanism of high-chromium vanadium–titanium magnetite pellets by H_2–CO–CO_2 gas mixtures,” *Int. J. Miner. Metall. Mater.*, vol. 22, no. 6, pp. 562–572, 2015.

[129] J. Chen, Y. Jiao, and X. Wang, “Thermodynamic studies on gas-based reduction of vanadium titano-magnetite pellets,” *Int. J. Miner. Metall. Mater.*, vol. 26, no. 7, pp. 822–830, 2019.

[130] Y. Sui, Y. Guo, T. Jiang, and G. Qiu, “Reduction kinetics of oxidized vanadium titano-magnetite pellets using carbon monoxide and hydrogen,” *J. Alloys Compd.*, vol. 706, pp. 546–553, 2017.

[131] D. Guo *et al.*, “Direct reduction of oxidized iron ore pellets using biomass syngas as the reducer,” *Fuel Process. Technol.*, vol. 148, pp. 276–281, 2016.

[132] M. H. Jeong *et al.*, “Reduction-oxidation kinetics of three different iron oxide phases for CO_2 activation to CO,” *Fuel*, vol. 202, pp. 547–555, 2017.

[133] D. Spreitzer and J. Schenk, “Reduction of Iron Oxides with Hydrogen—A Review,” *Steel Res. Int.*, vol. 90, no. 10, 2019.

[134] M. V. C. Sastri, R. P. Viswanath, and B. Viswanathan, “Studies on the reduction of iron oxide with hydrogen,” vol. 7, no. 12, pp. 951–955, 1982.

[135] M. J. Tiernan, P. A. Barnes, and G. M. B. Parkes, “Reduction of iron oxide catalysts: The investigation of kinetic parameters using rate perturbation and linear heating thermoanalytical techniques,” *J. Phys. Chem. B*, vol. 105, no. 1, pp. 220–228, 2001.

[136] I. J. Moon, C. Rhee, and D. Min, “Reduction of hematite compacts by H_2-CO gas mixtures,” *Steel Res. Int.*, vol. 69, no. 8, pp. 302–306, 1998.

[137] B. Moghtaderi and H. Song, “Reduction properties of physically mixed metallic oxide oxygen carriers in chemical looping combustion,” *Energy and Fuels*, vol. 24, no. 10, pp. 5359–5368, 2010.

[138] O. Levenspiel, Chemical reaction engineering, John Wiley and Sons. 1999.

[139] J. Zieliński, I. Zglinicka, L. Znak, and Z. Kaszkur, “Reduction of Fe_2O_3 with hydrogen,” *Appl. Catal. A Gen.*, vol. 381, no. 1–2, pp. 191–196, 2010.

[140] W. Du *et al.*, “Hydrogen Reduction of Hematite Ore Fines to Magnetite Ore Fines at Low Temperatures,” *J. Chem.*, vol. 2017, 2017.

[141] H. I. Ünal, E. Turgut, S. H. Atapek, and A. Alkan, “Direct Reduction of Ferrous Oxides to form an Iron-Rich Alternative Charge Material,” *High Temp. Mater. Process.*, vol. 34, no. 8, pp. 751–756, 2015.

[142] J. O. Edstrom: “The mechanism of reduction of iron oxides”, *Journal of the iron and steel institute*, pp.289-304, 1953.

[143] E. Park and O. Ostrovski, “Effects of preoxidation of titania-ferrous ore on the ore structure and reduction behavior,” *Isij Int.*, vol. 44, no. 1, pp. 74–81, 2004.

[144] R. J. Longbottom, O. Ostrovski, and E. Park, “Formation of Cementite from Titanomagnetite Ore,” *ISIJ Int.*, vol. 46, no. 5, pp. 641–646, 2006.

[145] Z. Y. Wang *et al.*, “Phase Transitions and Atomic-Scale Migration During the Preoxidation of a Titania/Ferrous Oxide Solution,” *Jom*, vol. 68, no. 2, pp. 656–667, 2016.

[146] E. Park and O. Ostrovski, “Reduction of Titania – Ferrous Ore by Hydrogen,” *ISIJ Int.*, vol. 44, no. 6, pp. 999–1005, 2004.

[147] E. Park and O. Ostrovski, “Reduction of titania-ferrous ore by Carbon Monoxide,” *ISIJ Int.*, vol. 43, no. 9, pp. 1316–1325, 2003.

[148] W. Li, G. Q. Fu, M. S. Chu, and M. Y. Zhu, “Gas-Based Direct Reduction of Hongge Vanadium Titanomagnetite-Oxidized Pellet and Melting Separation of the Reduced Pellet,” *Steel Res. Int.*, vol. 88, no. 1, pp. 1–11, 2017.

[149] B. Kennedy, N. H. Daneils, T. Marshall, “Gaseous reduction of sintered titanomagnetite pellets,” *NEW Zeal. J. Sci.*, vol. 12, no. 4, pp. 701–720, 1969.

[150] H. Sun, A. A. Adetoro, Z. Wang, F. Pan, and L. Li, “Direct Reduction Behaviors of Titanomagnetite Ore by Carbon Monoxide in Fluidized Bed,” *ISIJ Int.*, vol. 56, no. 6, pp. 936–943, 2016.

[151] W. Li, N. Wang, G. Fu, M. Chu, and M. Zhu, “Influence of TiO_2 addition on the oxidation induration and reduction behavior of Hongge vanadium titanomagnetite pellets with simulated shaft furnace gases,” *Powder Technol.*, vol. 326, pp. 137–145, 2018.

[152] A. Mommadov and A. M. Gasimova, “Reduction of the Adzhinaur Titanomagnetite Concentrates of Azerbaijan by Natural Gas for the Production of Iron Powder and Titanium Dioxide,” *AZƏRBAYCAN KİMYA JURNALI*, no.1, pp.37-43 2018.

[153] R. J. Longbottom, O. Ostrovski, J. Zhang, and D. Young, “Stability of cementite formed from hematite and titanomagnetite ore,” *Metall. Mater. Trans. B Process*

Metall. Mater. Process. Sci., vol. 38, no. 2, pp. 175–184, 2007.

[154] Y. Yang, K. Raipala, and L. Holappa, "Ironmaking," in *Treatise on Process Metallurgy*, vol. 3, Elsevier Books Limieted, pp. 2–88, 2014.

[155] Y. L. Sui, Y. F. Guo, T. Jiang, and G. Z. Qiu, "Sticking behaviour of vanadium titano-magnetite oxidised pellets during gas-based reduction and its prevention," *Ironmak. Steelmak.*, vol. 44, no. 3, pp. 185–192, 2017.

[156] S. W. Prabowo, R. J. Longbottom, B. J. Monaghan, D. del Puerto, M. J. Ryan, and C. W. Bumby, "Sticking-Free Reduction of Titanomagnetite Ironsand in a Fluidized Bed Reactor," *Metall. Mater. Trans. B*, vol 50, pp. 1729-1744 2019.

[157] O. Inoue, S. Itoh, and T. Azakami, "Phase relations and equilibrium oxygen partial pressures in the iron- titanium-oxygen system at 1373 k," *J. Japan Institute Metals*, vol. 60. pp. 834–840, 1996.

[158] A. F. Buddington and D. H. Lindsley, "Iron-titanium oxide minerals and synthetic equivalents," *J. Petrol.*, vol. 5, no. 2, pp. 310–357, 1964.

[159] Z. Wang, J. Zhang, J. Ma, and K. Jiao, "Gaseous reduction of titania-ferrous solution ore by H_2-Ar mixture," *ISIJ Int.*, vol. 57, no. 3, pp. 443–452, 2017.

[160] P. Satyananda, A. Kumar, and V. Rayasam, "The effect of particle size on green pellet properties of iron ore fines," *J. Min. Metall. A Min.*, vol. 53, no. 1, pp. 31–41, 2017.

[161] N. Y. Harun and M. T. Afzal, "Effect of Particle Size on Mechanical Properties of Pellets Made from Biomass Blends," in *Procedia Engineering*, vol. 148, pp. 93–99, 2016.

[162] A. Zhang, B. J. Monaghan, R. J. Longbottom, M. Nusheh, and C. W. Bumby, "Reduction Kinetics of Oxidized New Zealand Ironsand Pellets in H_2 at Temperatures up to 1443 K," *Metall. Mater. Trans. B Process Metall. Mater. Process. Sci.*, vol. 51, no. 2, pp. 492–504, 2020.

[163] R. Welberry and R. Whitfield, "Single Crystal Diffuse Neutron Scattering," *Quantum Beam Sci.*, vol. 2, no. 1, p. 2, 2018.

[164] B. A. Wechsler, D. H. Lindsley, and C. T. Prewitt, "Crystal structure and cation distribution in titanomagnetites ($Fe_{3-x}Ti_xO_4$).," *Am. Mineral.*, vol. 69, no. 7–8, pp. 754–770, 1984.

[165] "Properties of the Neutron." http://pd.chem.ucl.ac.uk/pdnn/inst3/neutrons.htm (accessed Apr. 08, 2021).

[166] N. Shigematsu and H. Iwai, "Effect of SiO_2 and/or Al_2O_3 addition on reduction of dense wustite by hydrogen.," *Trans. Iron Steel Inst. Japan*, vol. 28, no. 3, pp. 206–213, 1988.

[167] Y. Kapelyushin, Y. Sasaki, J. Zhang, S. Jeong, and O. Ostrovski, "Formation of a Network Structure in the Gaseous Reduction of Magnetite Doped with Alumina," *Metall. Mater. Trans. B Process Metall. Mater. Process. Sci.*, vol. 48, no. 2, pp. 889–899, 2017.

[168] E. Prestes, A. S. A. Chinelatto, and W. S. Resende, "Post mortem analysis of burned magnesia-chromite brick used in short rotary furnace of secondary lead smelting,"

Cerâmica, vol. 55, no. 333, pp. 61–66, 2009.

[169] J. Lin *et al.*, "Stability of magnesiowustite in Earth's lower mantle," *PNAS*, vol. 100, no. 8, pp. 4405-4408, 2003.

[170] M. Bahgat and M. H. Khedr, "Reduction kinetics, magnetic behavior and morphological changes during reduction of magnetite single crystal," *Mater. Sci. Eng. B Solid-State Mater. Adv. Technol.*, vol. 138, no. 3, pp. 251–258, 2007.

[171] S. Geva, M. Farren, D. H. S. John, and P. C. Hayes, "The effects of impurity elements on the reduction of wustite and magnetite to iron in CO/CO_2 and H_2/H_2O gas mixtures," *Metall. Trans. B*, vol. 21, no. 4, pp. 743–751, 1990.

[172] Y. Kapelyushin, "The Use of Magnetite Ore in Advanced Ironmaking," Doctoral thesis, The University of New South Wales, Sydney, 2017.

[173] F. Bosi, U. Hålenius, and H. Skogby, "Crystal chemistry of the magnetite-ulvöspinel series," *Am. Mineral.*, vol. 94, no. 1, pp. 181–189, 2009.

[174] G. Munteanu, L. Ilieva, and D. Andreeva, "Kinetic parameters obtained from TPR data for α-Fe_2O_3 and Au/α-Fe_2O_3 systems," *Thermochim. Acta*, vol. 291, no. 1–2, pp. 171–177, 1997.

[175] D. Spreitzer and J. Schenk, "Iron Ore Reduction by Hydrogen Using a Laboratory Scale Fluidized Bed Reactor: Kinetic Investigation—Experimental Setup and Method for Determination," *Metall. Mater. Trans. B Process Metall. Mater. Process. Sci.*, vol. 50, no. 5, pp. 2471–2484, 2019.

[176] "Iron Making | New Zealand Steel." [Online]. Available: https://www.nzsteel.co.nz/new-zealand-steel/the-story-of-steel/the-steel-making-process/iron-making/. [Accessed: 23-Oct-2020].

[177] "World Direct Reduction Statistics 2018 Contents," Midrex Technologies, Inc., pp. 12-15, 2019.

Appendix A
Additional information for Chapter 3

A.1 Reduction swelling index (RSI) and compressive strength of sintered pellets

1. RSI and compressive strength of Ar-sintered pellets

The RSI of the pellets was obtained from measurements of the pellet volume before and after reduction in H_2 gas based on equation **A.1**:

$$RSI = \frac{V_{reduced} - V_0}{V_0} \quad \textbf{(A.1)}$$

where $V_{reduced}$ represents the volume of the pellet after reduction in H_2 gas, while V_0 is the volume of the pellet before reduction. Pellet volume was measured using the water immersion method. Several sintered pellets (diameter ~7 mm) were reduced at 1343 K for 25 minutes. After measuring the volumes of the pellets before and after reduction, it was found that the volume of the pellets had expanded on average by ~5% during the course of reduction.

The determination of the compressive strength of the pellets was conducted using a parallel-plate compression fixture in a Tinius Olsen Testing Machine, H10KT (UK). The pre-load was set to be 10 N with a travel speed of 0.5 mm/min. During the test, the load at which the first crack in the pellet appeared was regarded as the compressive strength. The results from compression tests of seven pellets are shown in **Figure A.1**. It was determined that the Ar-sintered pellets (diameter ~7 mm) had an average compressive strength of 800 N ± 100 N per pellet.

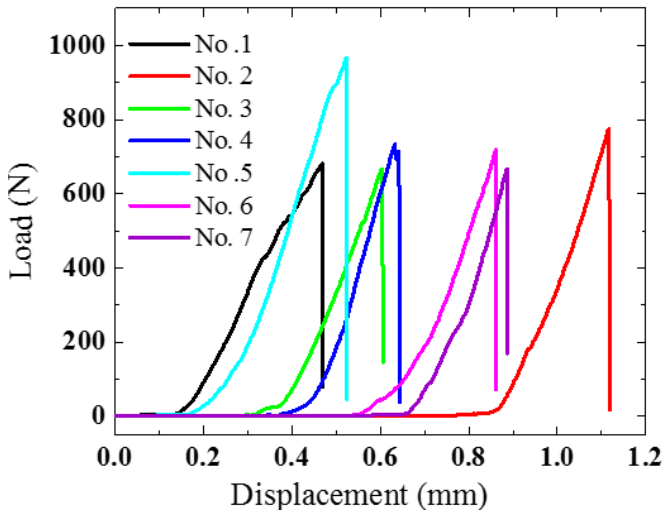

Figure A.1*– A plot showing the compressive strength of the seven sintered titanomagnetite pellets with an average diameter of 7 mm. The average compressive strength is found to be 800 N per pellet*

2. RSI and compressive strength of pre-oxidised pellets

Similar to before, the RSI and compression strength of the pre-oxidised pellets was also characterised. After reduction in H_2 gas at 1343 K for 25 minutes, the pre-oxidised pellets (diameter ~7 mm) also exhibited ~5% volume expansion. The results for the compressive tests of the pre-oxidised pellets (diameter ~7 mm) are shown in **Figure 3.9**. These pellets showed an average compressive strength of ~1100 ± 200 N per pellet. This is slightly higher than the Ar-sintered pellets, indicating that oxidative sintering improved the pellet strength.

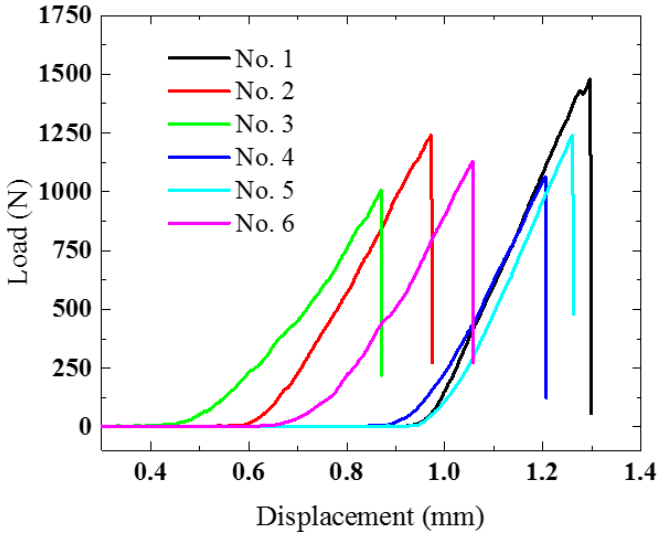

Figure A.2 *– A plot showing the compressive strength of six pre-oxidised pellets with an average diameter of 7 mm. The average compressive strength is found to be 1100 N per pellet*

A.2 Calculation of the reduction degree *X* from TGA experiments

1. Reduction of the Ar-sintered pellets

In equation **3.1**, the factor 0.23 presents the total weight fraction of removable (reducible) oxygen in the Ar-sintered pellets. Its determination is based on the balance of electrons during reduction as follows:

In the as-received ironsand, there are 21.9wt% Fe^{2+} (from titration) and 60wt% total Fe (from XRF). This then gives 38.1wt% Fe^{3+}. To reduce one atom Fe^{2+} into metallic Fe, two electrons are needed as shown below. Similarly, three electrons are needed to reduce one atom of Fe^{3+} into metallic Fe.

$$Fe^{2+} + 2e^{-} \rightarrow Fe \qquad \textbf{(A.2)}$$

$$Fe^{3+} + 3e^{-} \rightarrow Fe \qquad \textbf{(A.3)}$$

Therefore, the average amount of electrons needed to reduce the ironsand into metallic Fe is

$$avergae\ amount\ of\ electrons = \frac{0.219\times2+0.381\times3}{0.219+0.381} = 2.64 \qquad \textbf{(A.4)}$$

These needed electrons are obtained by the removal of oxygen: two electrons are released from removing one atom of oxygen ($O^{2-} \rightarrow O + 2e^{-}$). Hence, the total weight fraction of removable oxygen in the ironsand which contains 60wt% total Fe is:

$$Total\ weight\ fraction\ of\ reducible\ oxygen = \frac{2.64}{2} \times \frac{16.00}{55.85} \times 0.60 = 0.23 \qquad \textbf{(A.5)}$$

Therefore, for w_0 grams Ar-sintered pellets, the total weight of the removable oxygen is $0.23 \times w_0$ grams.

2. Reduction of the pre-oxidised pellets

In equation **3.2**, the factor 0.26 presents the total weight fraction of removable (reducible) oxygen in the pre-oxidised pellets. Its determination is as follows:

On oxidative sintering, TTM in the pellets were completely converted to TTH (see **Figure 3.7**). Based on the XRF analysis of the roasted ironsand shown in **Table 3.2**, 84.5wt% Fe_2O_3 presented. Similarly, it can assume that the pre-oxidised pellets also contain 84.5wt% Fe_2O_3. In addition, by completely reducing Fe_2O_3 to metallic Fe, 30% weight loss is expected from mass of oxygen in Fe_2O_3. As a result, the maximum weight loss of reducing the pre-oxidised pellets to metallic Fe is 0.3×0.85 (=0.26).

Therefore, for w_0 grams pre-oxidised pellets, the total weight of the removable oxygen is $0.26 \times w_0$ grams.

A.3 Calibration of the high temperature furnaces for the reduction experiments

During this study, several different furnaces were used to conduct reduction experiments. To enable effective comparison, the temperature at the sample position in the hot zone of each furnace was calibrated. Temperature calibration plots for each furnace are shown in **Figure A.3, Figure A.4**, and **Figure A.5** respectively, where the set temperature of the furnace is plotted against the measured temperature by a thermocouple inserted at the sample (pellet) position.

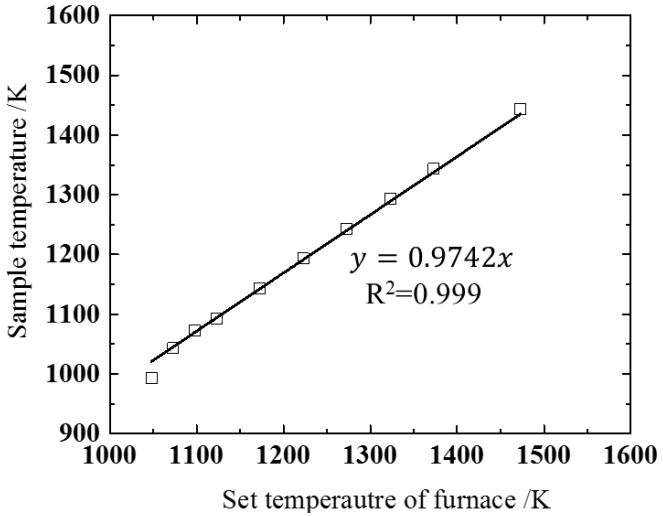

***Figure A.3** – Temperature calibration of the TGA furnace at Callaghan Innovation for the H_2 gas reduction of the pellets at high temperatures (furnace set up shown in **Figure 3.8**)*

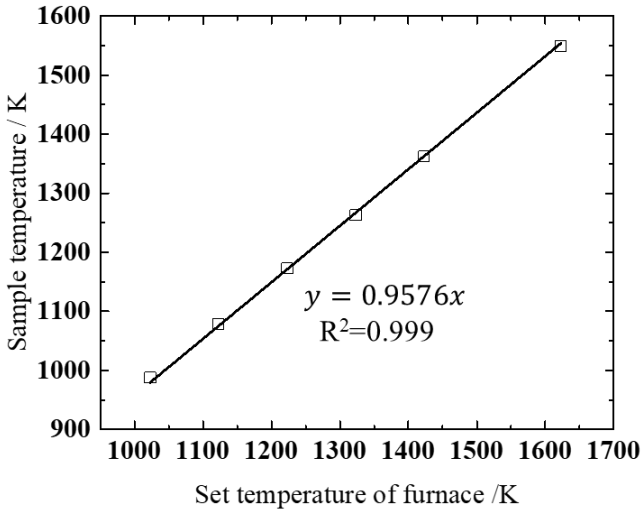

***Figure A.4** – Temperature calibration of the TGA furnace at UOW for the H_2 reduction and quenching of the pellets (furnace set up shown in **Figure 3.11**)*

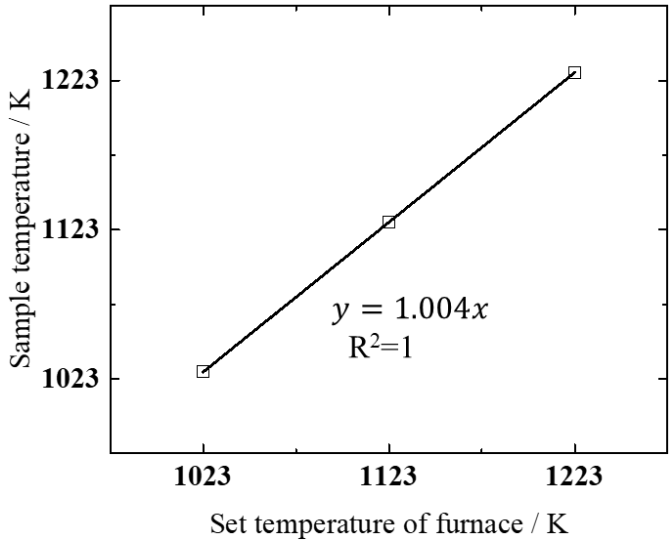

***Figure A.5** – Temperature calibration of the high-temperature vacuum furnace in the ND reduction experiment*

The gases used for the reduction experiments were N_2, Ar and H_2, with the purities listed in **Table A.1**.

***Table A.1** – Purities of the gases used in the reduction experiment*

H_2	N_2	Ar
> 99.98%	> 99.99%	> 99.99%

Appendix B
Additional information of reducing Ar-sintered pellets for Chapter 4

B.1 The full XRD pattern obtained from the fully reduced pellets following reduction at each temperature from 1043 K to 1443 K

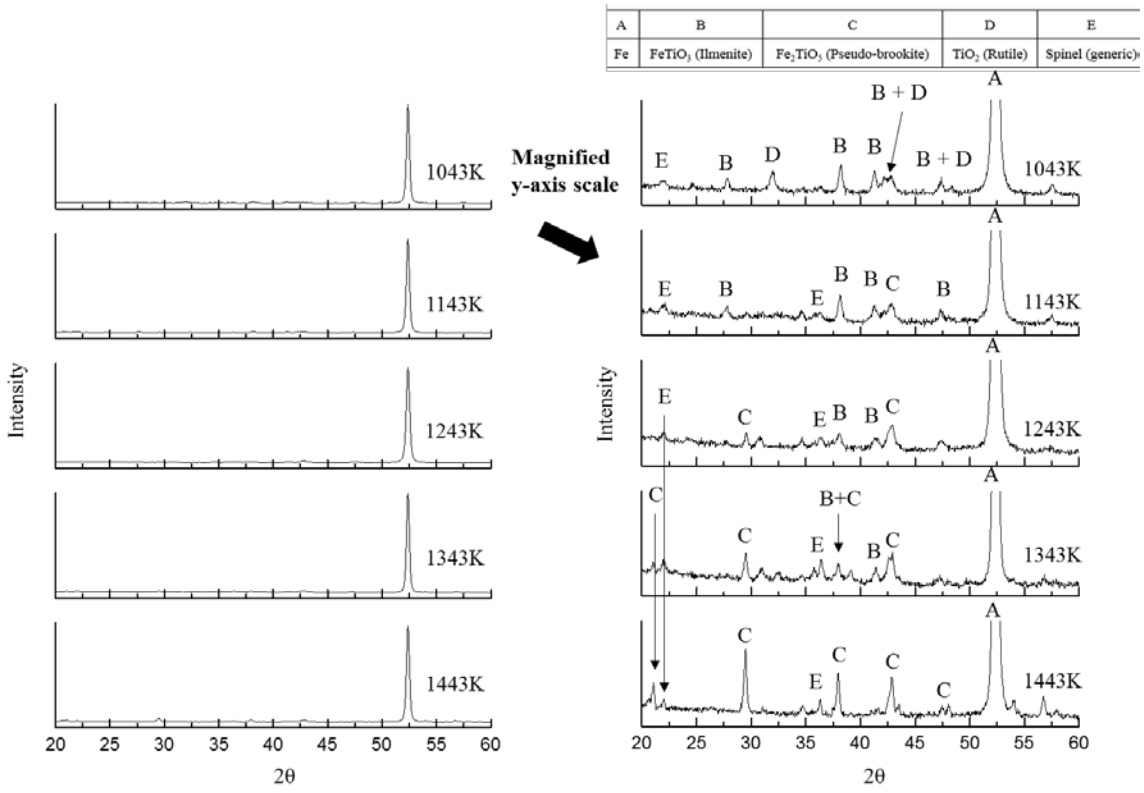

***Figure B.1**- (Left) Unmagnified XRD diffractograms obtained from fully reduced pellets (Ar-sintered) at each reduction temperature. Note that only the Fe peak (Peak A) can be readily distinguished in each spectrum, such that all spectra appear broadly identical. (Right) The same XRD diffractograms shown on a magnified y-axis scale which allows peaks from minor oxide phases to be determine*

B.2 Concentration curves of each crystalline phase during reduction of Ar-sintered pellets at each H_2 gas concentration in H_2-Ar gas mixtures at a flow of 250 ml/min at 1023 K

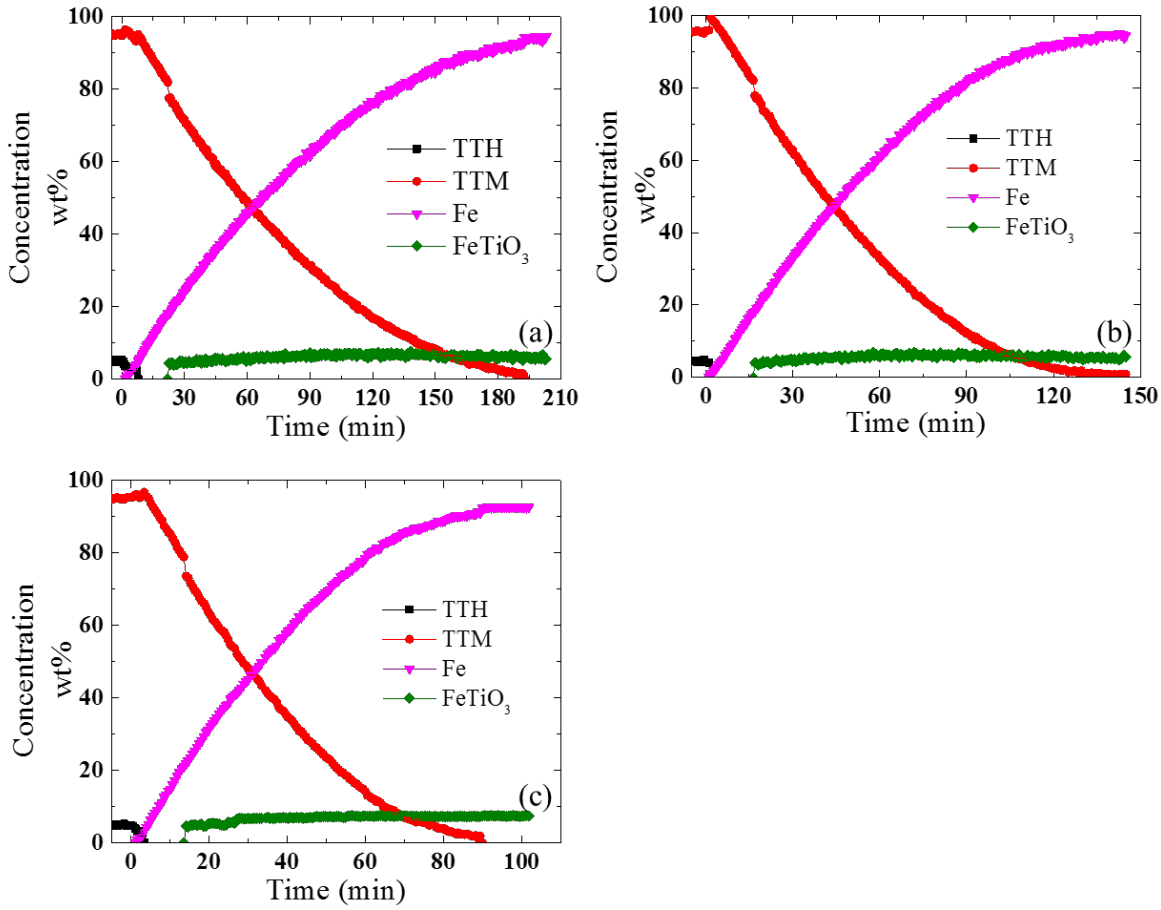

Figure B.2*- The concentration (wt%) curves of each crystalline phase during reduction of Ar-sintered pellets at a flow of 250 ml/min at 1023 K by H_2-Ar gas mixtures with (a) 50vol% H_2, (b) 75vol% H_2, and (c) 100vol% H_2*

B.3 Concentration curves of each crystalline phase during reduction of Ar-sintered pellets at each H_2 gas concentration in H_2-Ar gas mixtures at a flow of 250 ml/min at 1123 K

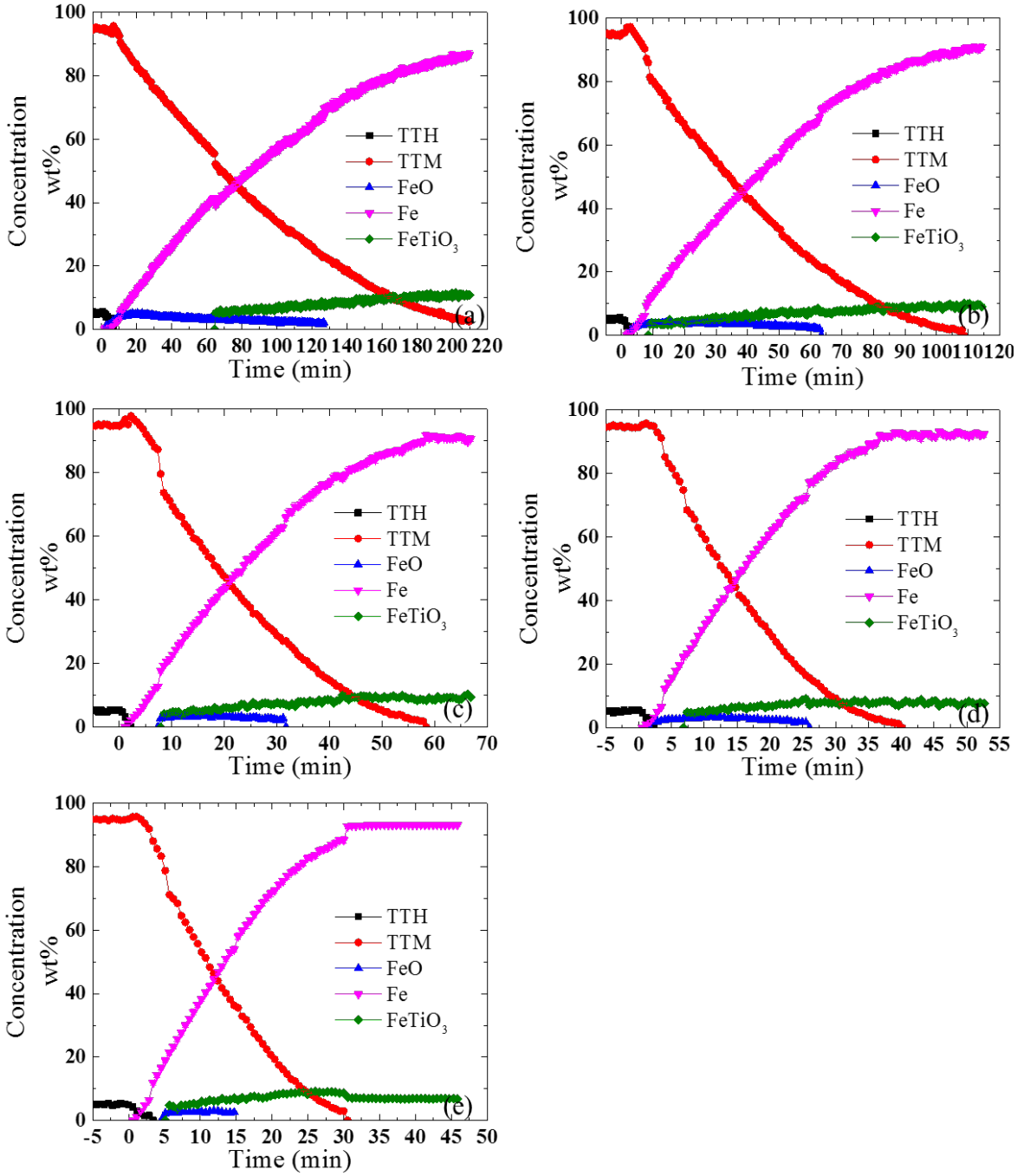

***Figure B.3**- The concentration (wt%) curves of each crystalline phase during reduction of Ar-sintered pellets at a flow of 250 ml/min at 1123 K by H_2-Ar gas mixtures with (a) 10vol% H_2, (b) 25vol% H_2, (c) 50vol% H_2, (d) 75vol% H_2, and (e) 100vol% H_2*

B.4 The characterisation of the representative particles in the Ar-sintered pellet prior to reduction

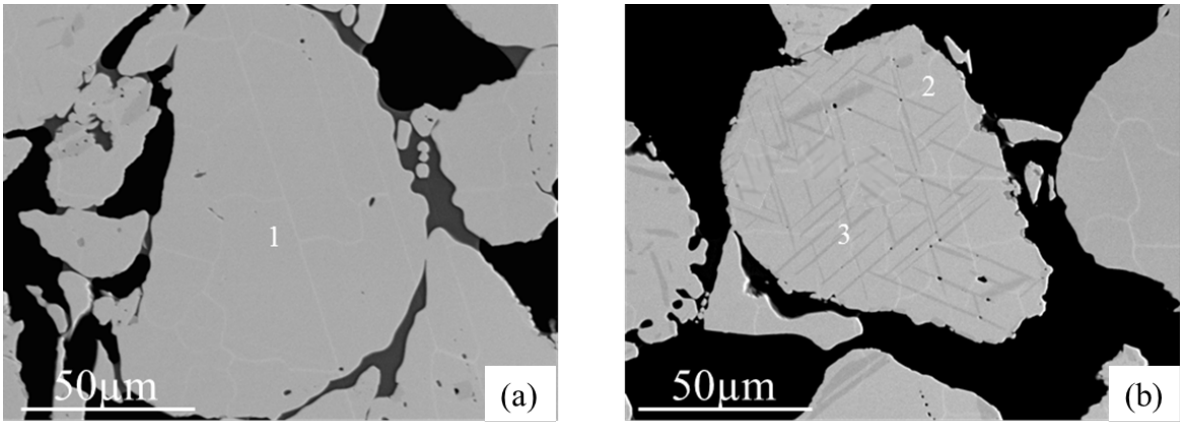

Figure B.4*– Back-scattered SEM images showing the particles in the Ar-sintered pellets before reduction. (a) uniform particles and (b) non-uniform particles*

Table B.1*– EDS point analysis (wt%) of specified spots in the particles of Ar-sintered pellets (in* ***Figure B.4****, the point analysis in the dark areas were averaged)*

	Points	O	Fe	Ti	V	Al	Mg	Mn	O/(Fe+Ti)
Ar-sintered pellets	1	24.3	65.8	4.3	0.3	2.4	2.0	0.6	0.3
	2	24.0	66.6	4.3	0.3	2.0	2.0	0.7	0.3
	3	27.6	54.4	16.0	0.4	0.7	1.4	0.4	0.4

B.5 Back-scattered SEM images of the representative partially reduced Ar-sintered pellets at 1023 K

1. *X*=21% reduced pellet

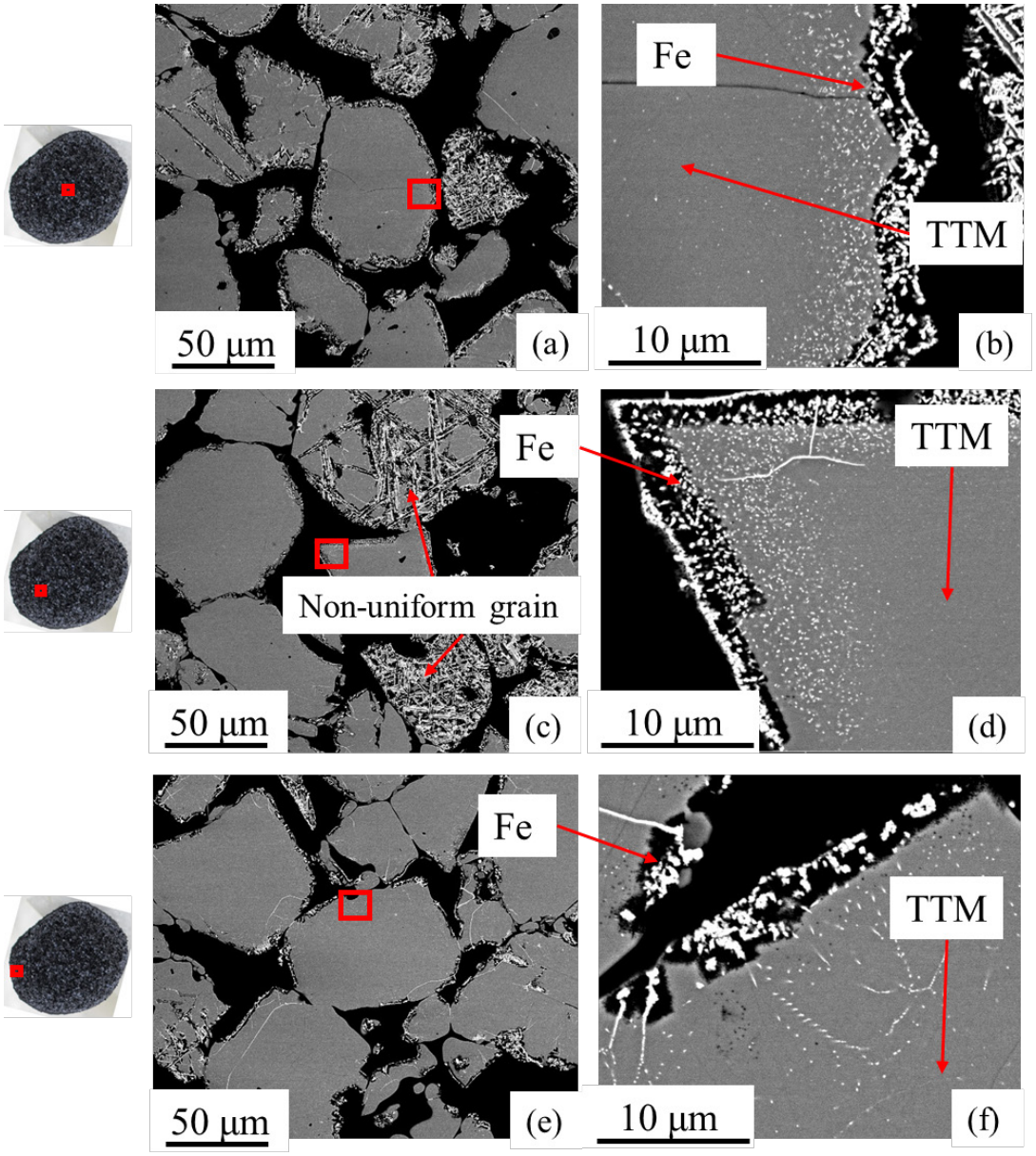

Figure B.5*- Particle morphologies at different areas of the 21% pellet reduced at 1023 K: (a), (c), and (e) are lower magnification photos of particles at each location, while (b), (d), and (f) are corresponding areas at higher magnification.*

2. *X*=50% reduced pellet

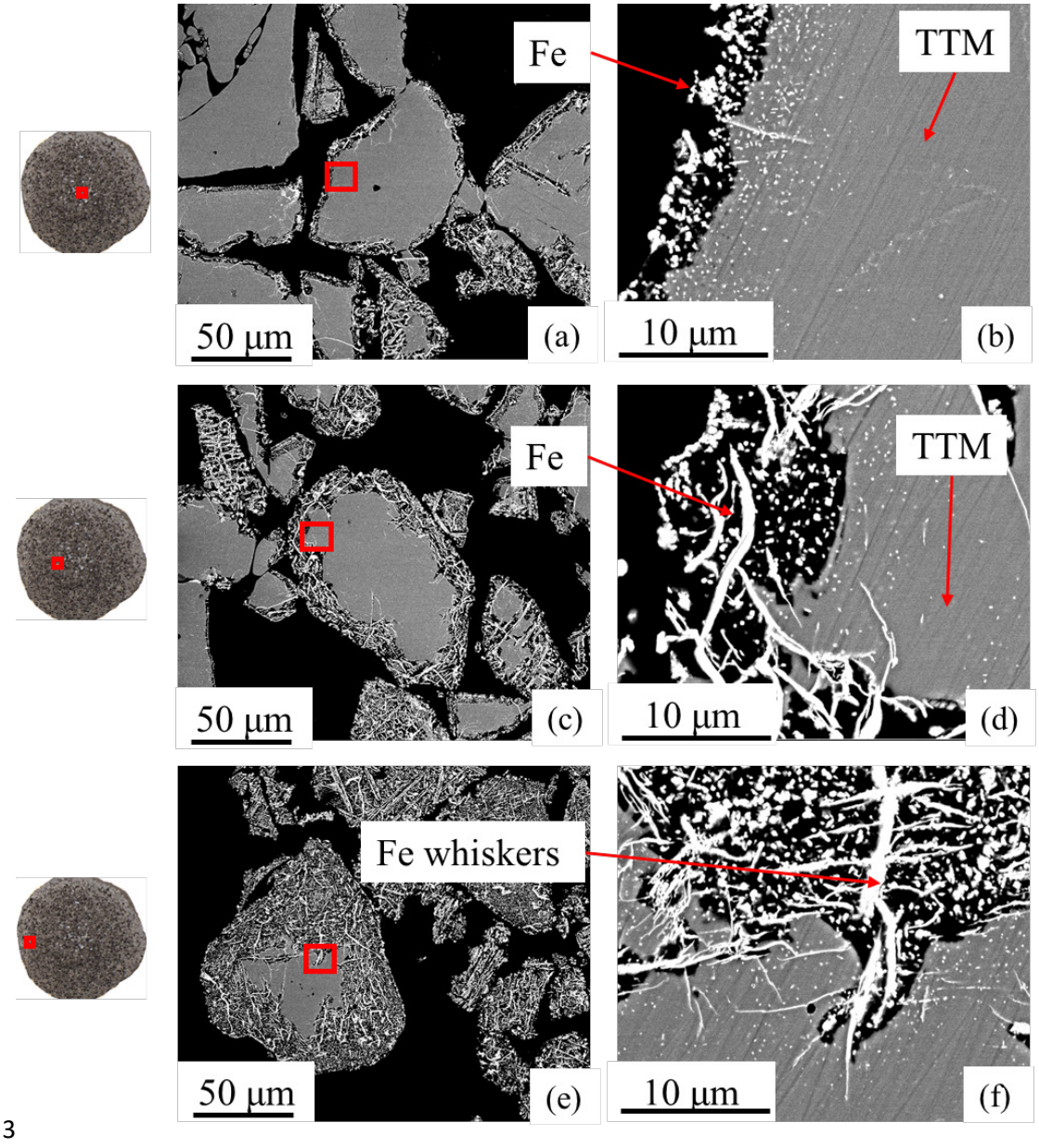

3

Figure B.6*- Particle morphologies at different areas of the 50% pellet reduced at 1023 K: (a), (c), and (e) are lower magnification photos of particles at each location, while (b), (d), and (f) are corresponding areas at higher magnification.*

3. *X*=81% reduced pellet

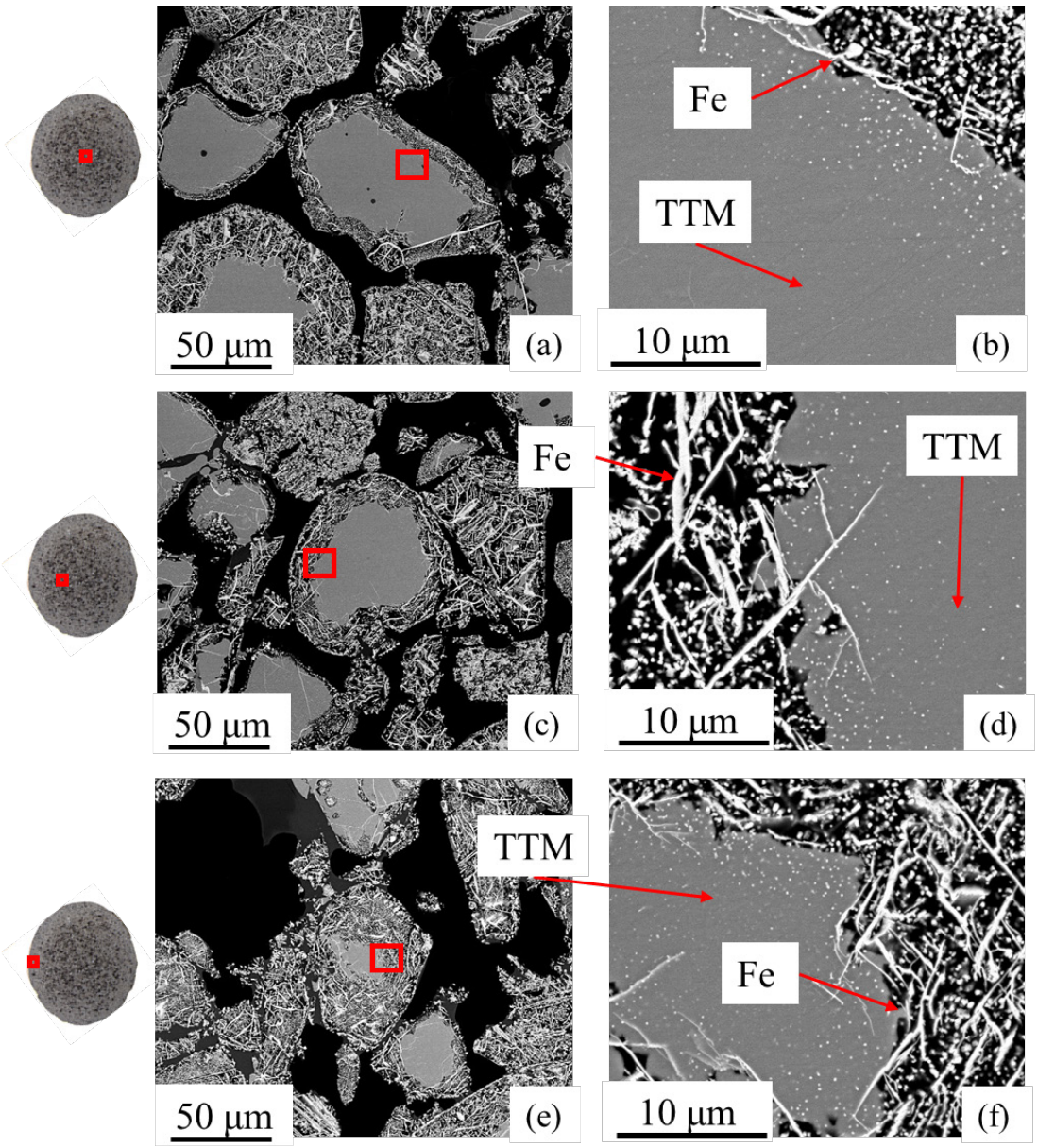

Figure B.7*- Particle morphologies at different areas of the 81% pellet reduced at 1023 K: (a), (c), (e) and (g) are lower magnification photos of particles at each location, while (b), (d), (f) and (h) are corresponding areas at higher magnification.*

4. Fully reduced pellet

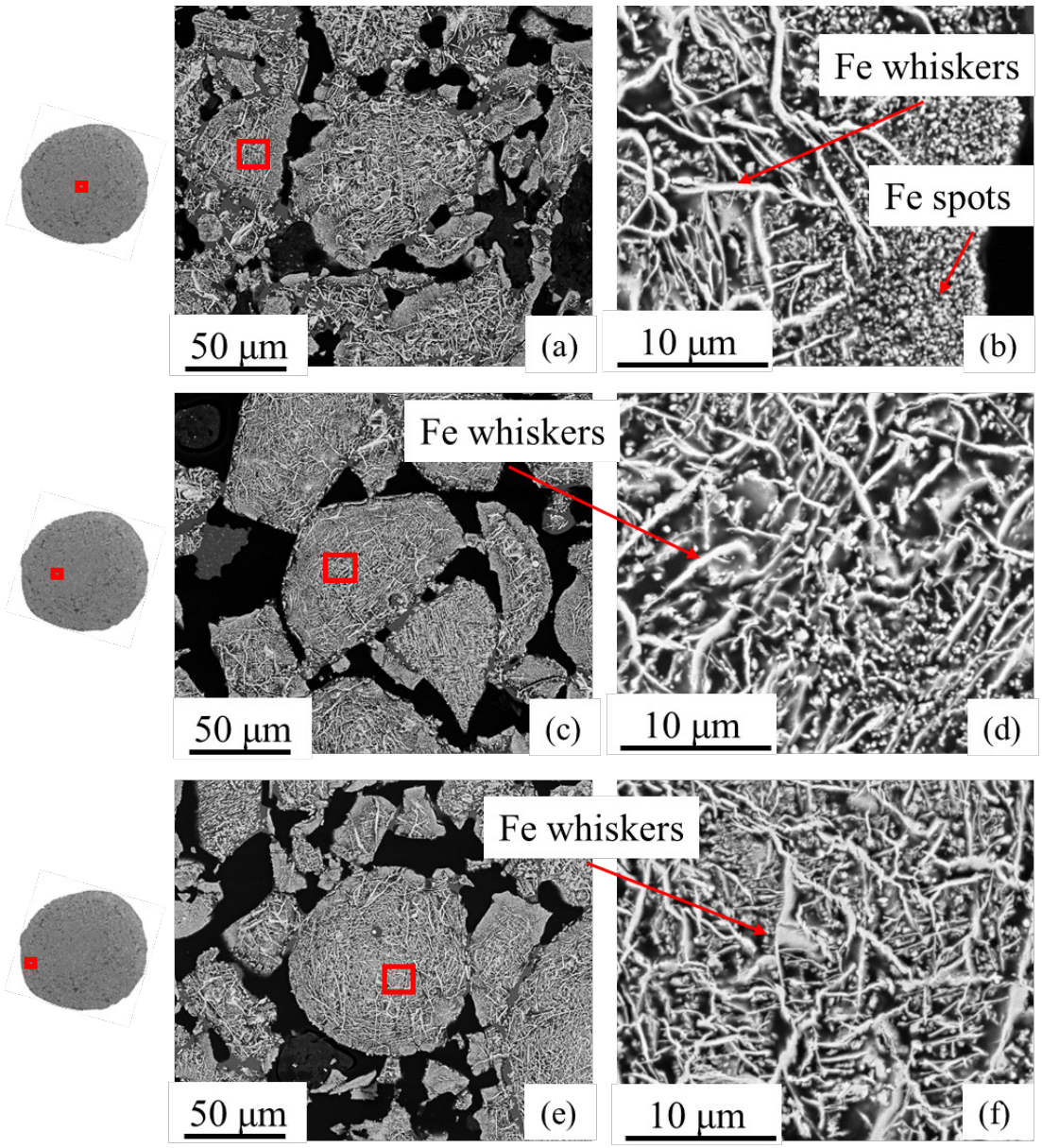

Figure B.8*- Particle morphologies at different areas of the fully reduced pellet at 1023 K: (a), (c), and (e) are lower magnification photos of particles at each location, while (b), (d), and (f) are corresponding areas at higher magnification.*

B.6 Back-scattered SEM images of the representative partially reduced Ar-sintered pellets at 1123 K

1. *X*=21% reduced pellet

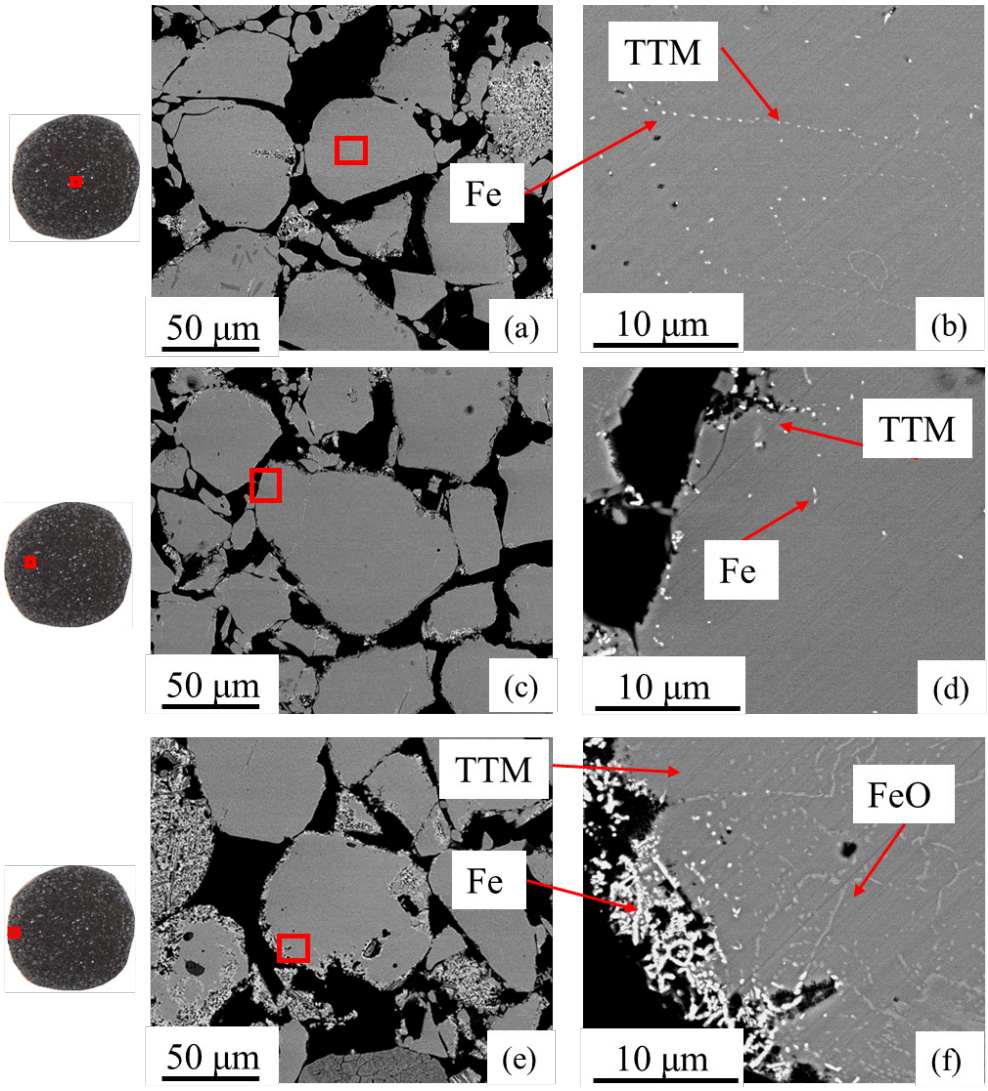

Figure B.9 *- Particle morphologies at different areas of the X=21% pellet reduced at 1123 K: (a), (c), and (e) are lower magnification photos of particles at each location, while (b), (d), and (f) are corresponding areas at higher magnification*

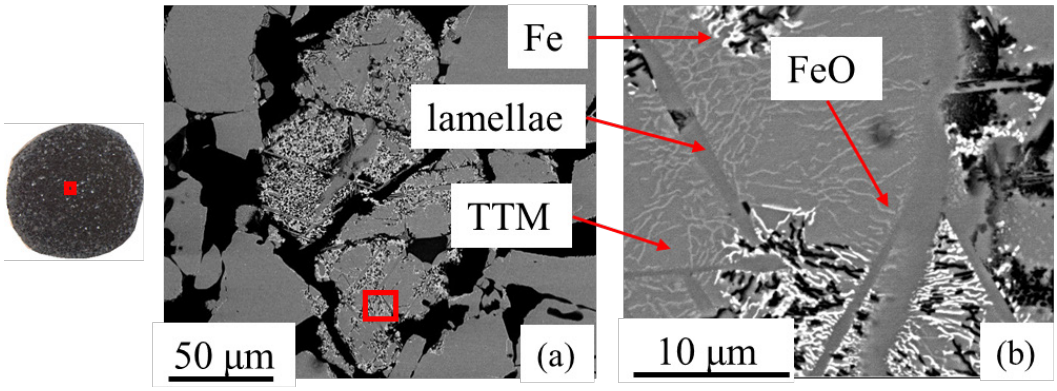

Figure B.10 *– Non-uniform particle morphologies at pellet centre of the X=21% pellet reduced at 1123 K at (a) lower magnification and (b) higher magnification*

2. *X*=50% reduced pellet

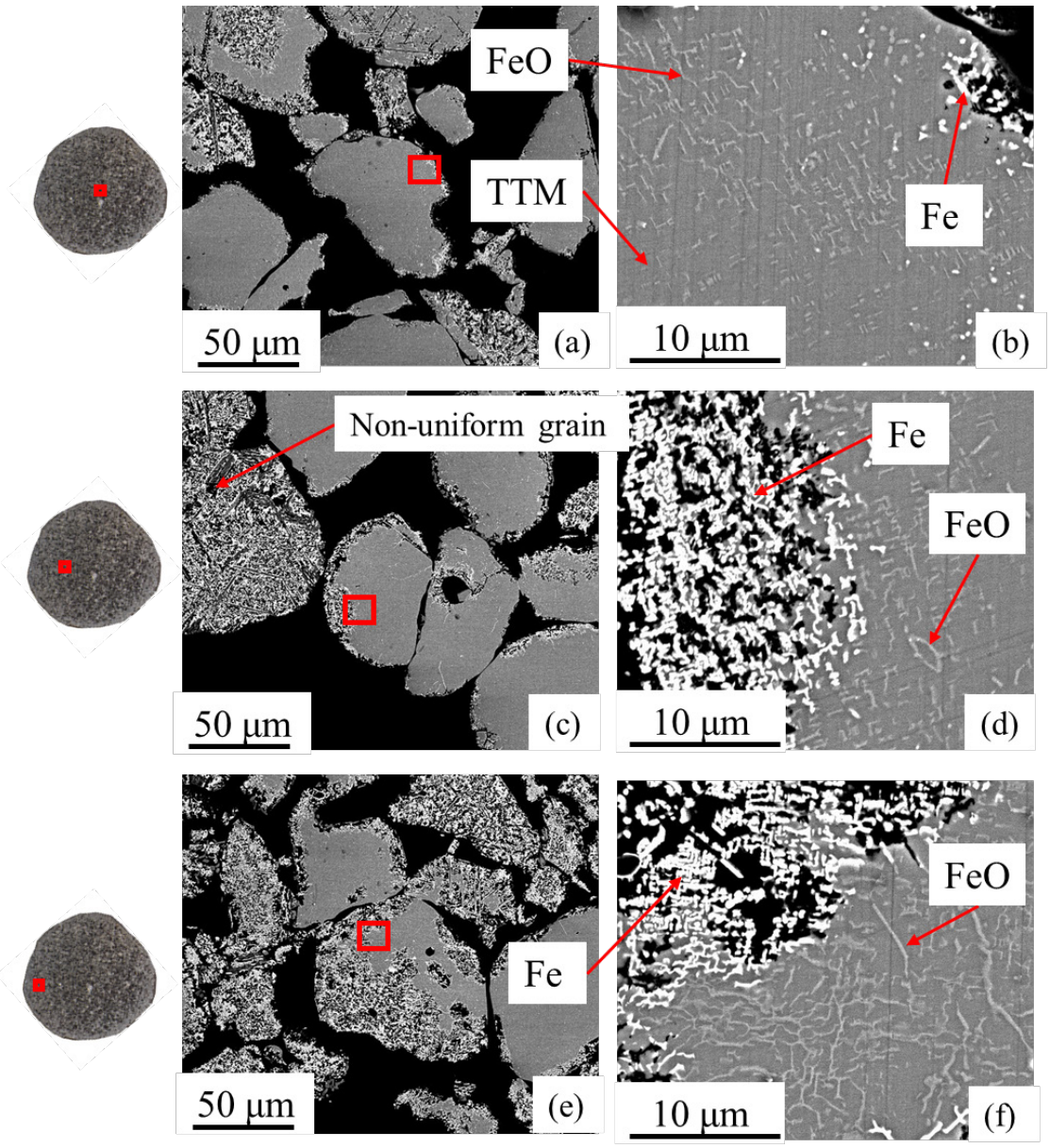

***Figure B.11**- Particle morphologies at different areas of the X=50% pellet reduced at 1123 K: (a), (c), and (e) are lower magnification photos of particles at each location, while (b), (d), and (f) are corresponding areas at higher magnification.*

3. *X*=78% reduced pellet

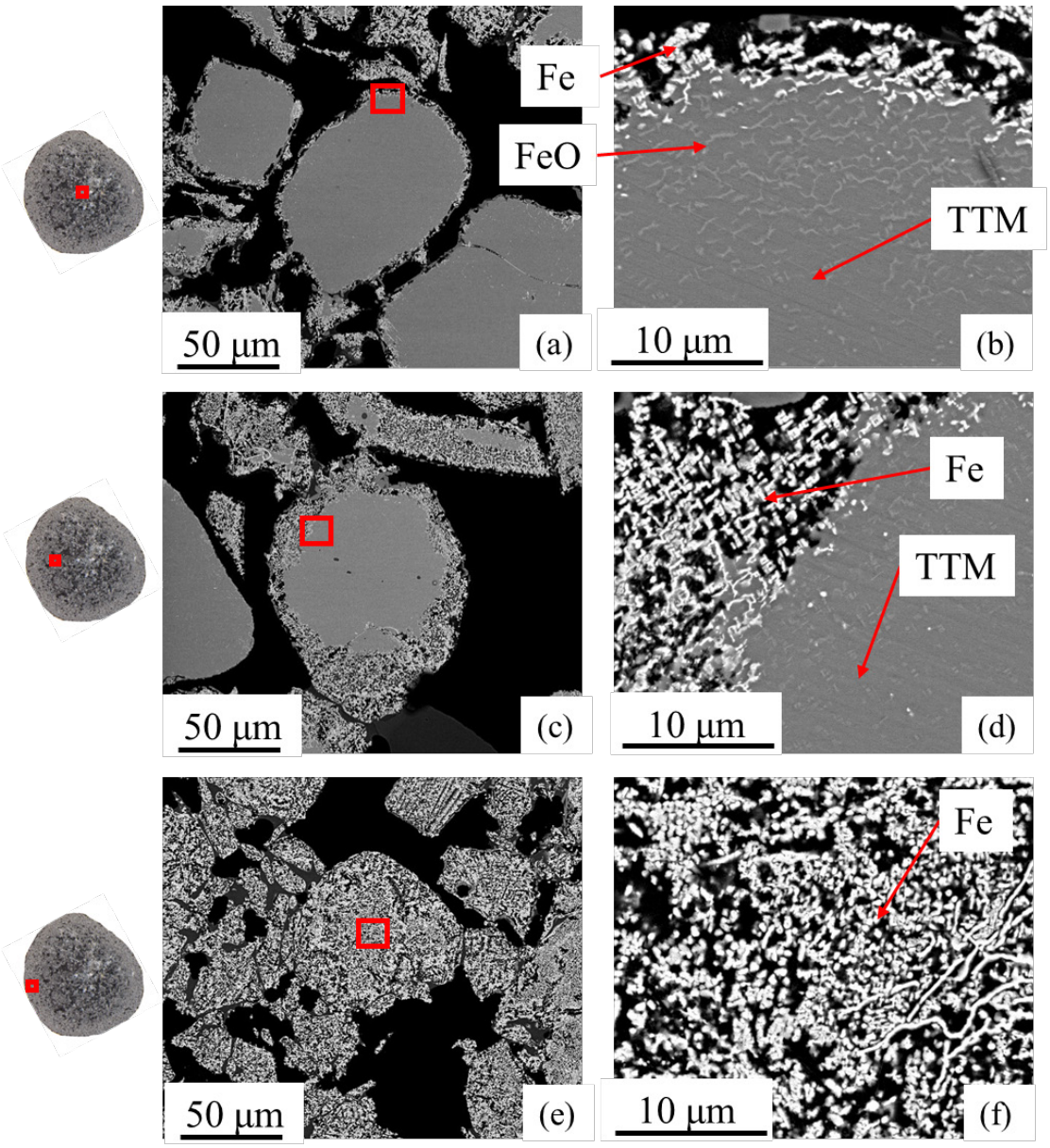

Figure B.12- *Particle morphologies at different areas of the X=78% pellet reduced at 1123 K: (a), (c), and (e) are lower magnification photos of particles at each location, while (b), (d), and (f) are corresponding areas at higher magnification.*

4. Fully reduced pellet

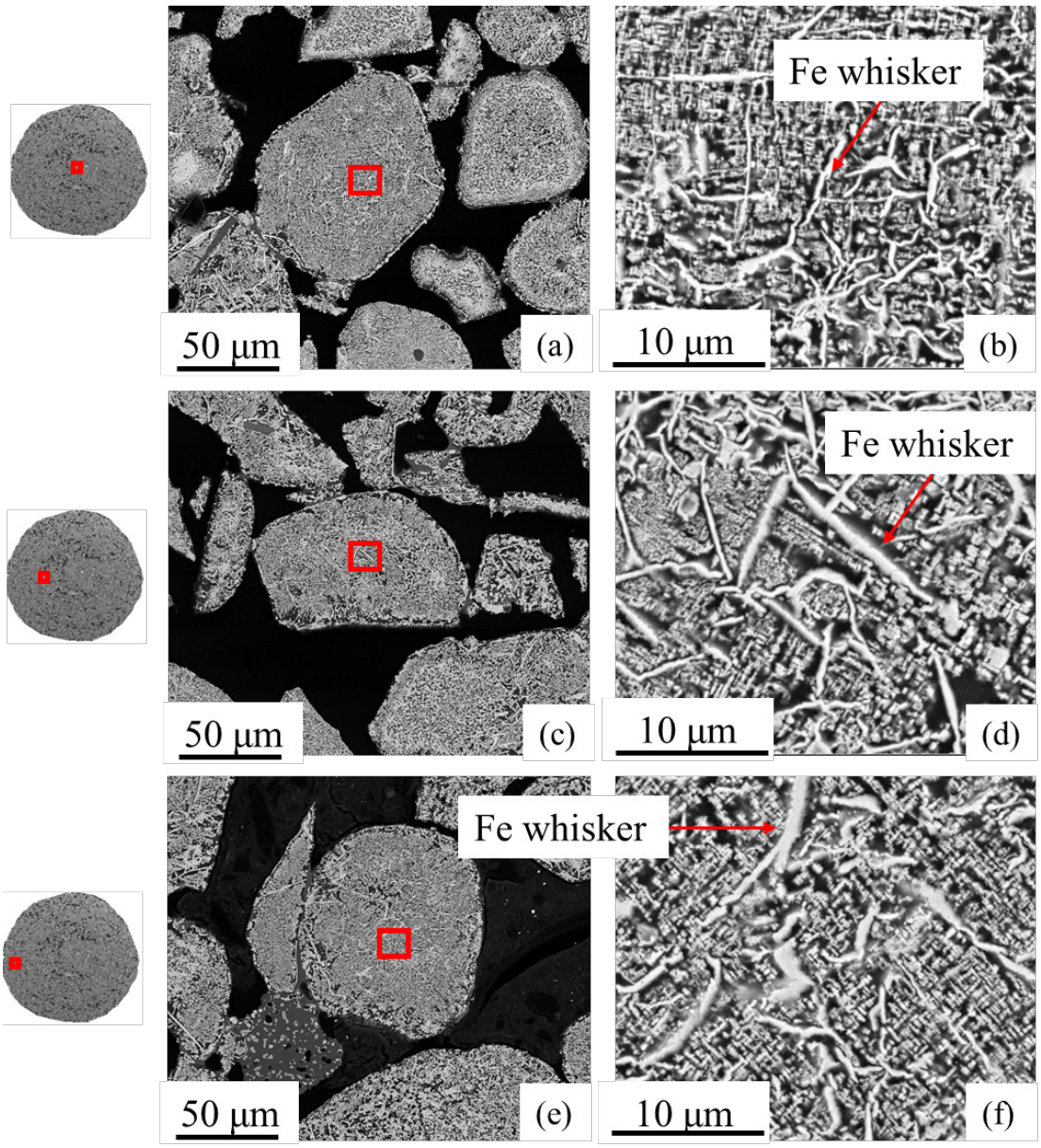

Figure B.13*- Particle morphologies at different areas of the fully reduced pellet at 1123 K: (a), (c), and (e) are lower magnification photos of particles at each location, while (b), (d), and (f) are corresponding areas at higher magnification.*

B.7 Back-scattered SEM images of the representative partially reduced Ar-sintered pellets at 1223 K

1. *X*=25% reduced pellet

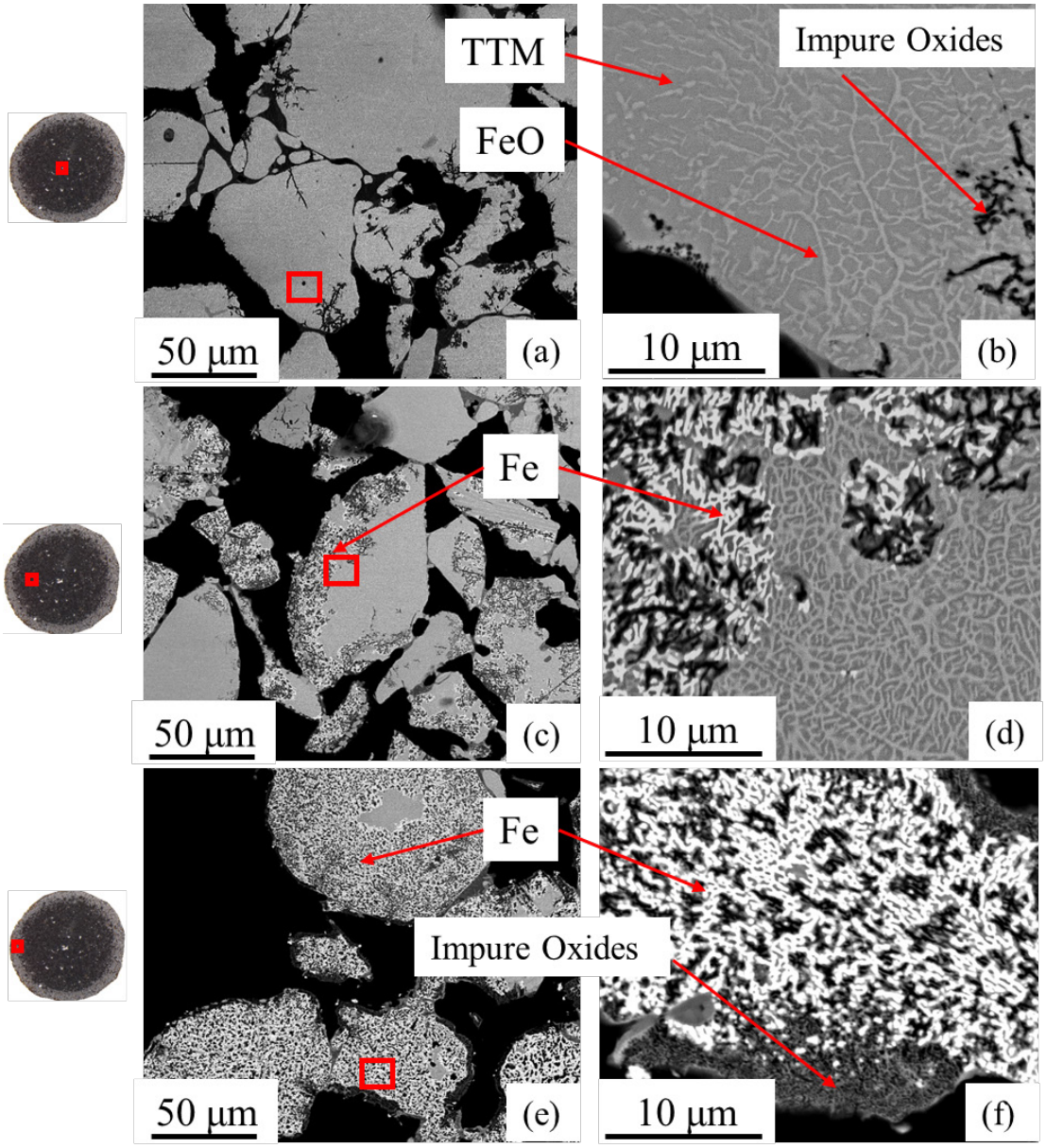

***Figure B.14**- Particle morphologies at different areas of the X=25% pellet reduced at 1223 K: (a), (c), and (e) are lower magnification photos of particles at each location, while (b), (d), and (f) are corresponding areas at higher magnification.*

2. *X*=54% reduced pellet

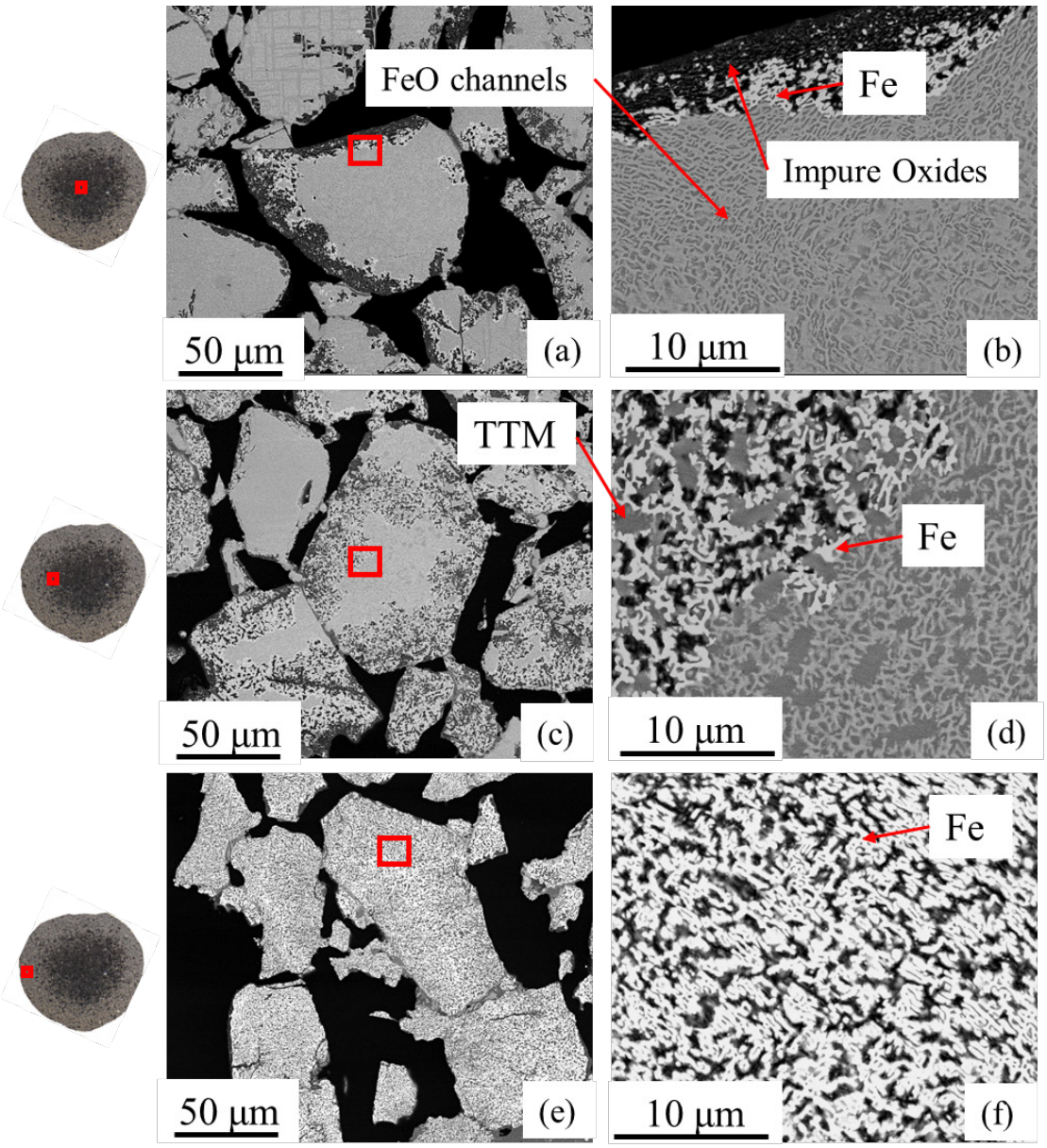

Figure B.15- *Particle morphologies at different areas of the X=54% reduced pellet at 1223 K: (a), (c), and (e) are lower magnification photos of particles at each location, while (b), (d), and (f) are corresponding areas at higher magnification.*

3. *X*=82% reduced pellet

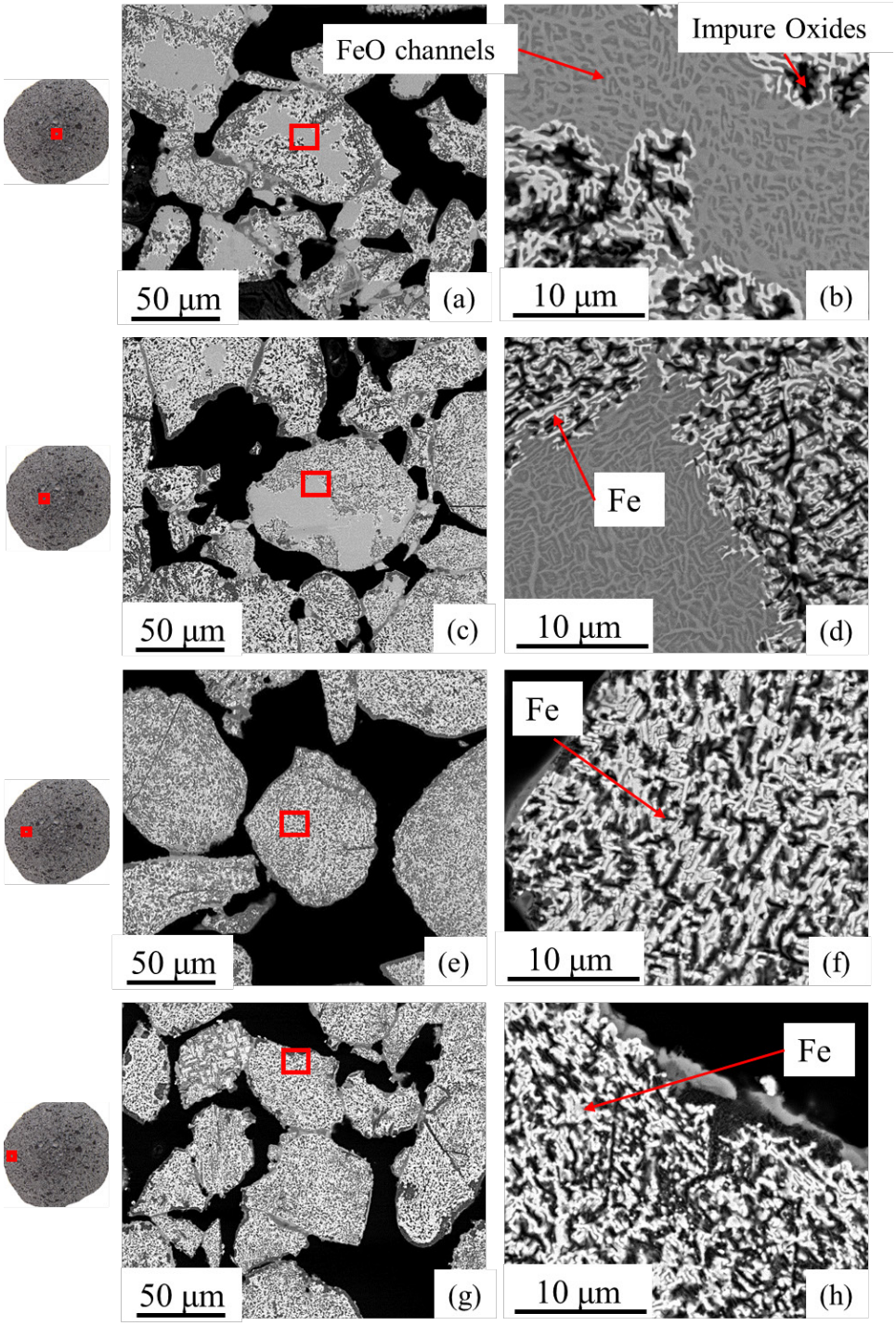

Figure B.16*- Particle morphologies at different areas of the X=82% pellet reduced at 1223 K: (a), (c), and (e) are lower magnification photos of particles at each location, while (b), (d), and (f) are corresponding areas at higher magnification.*

4. Fully reduced pellet

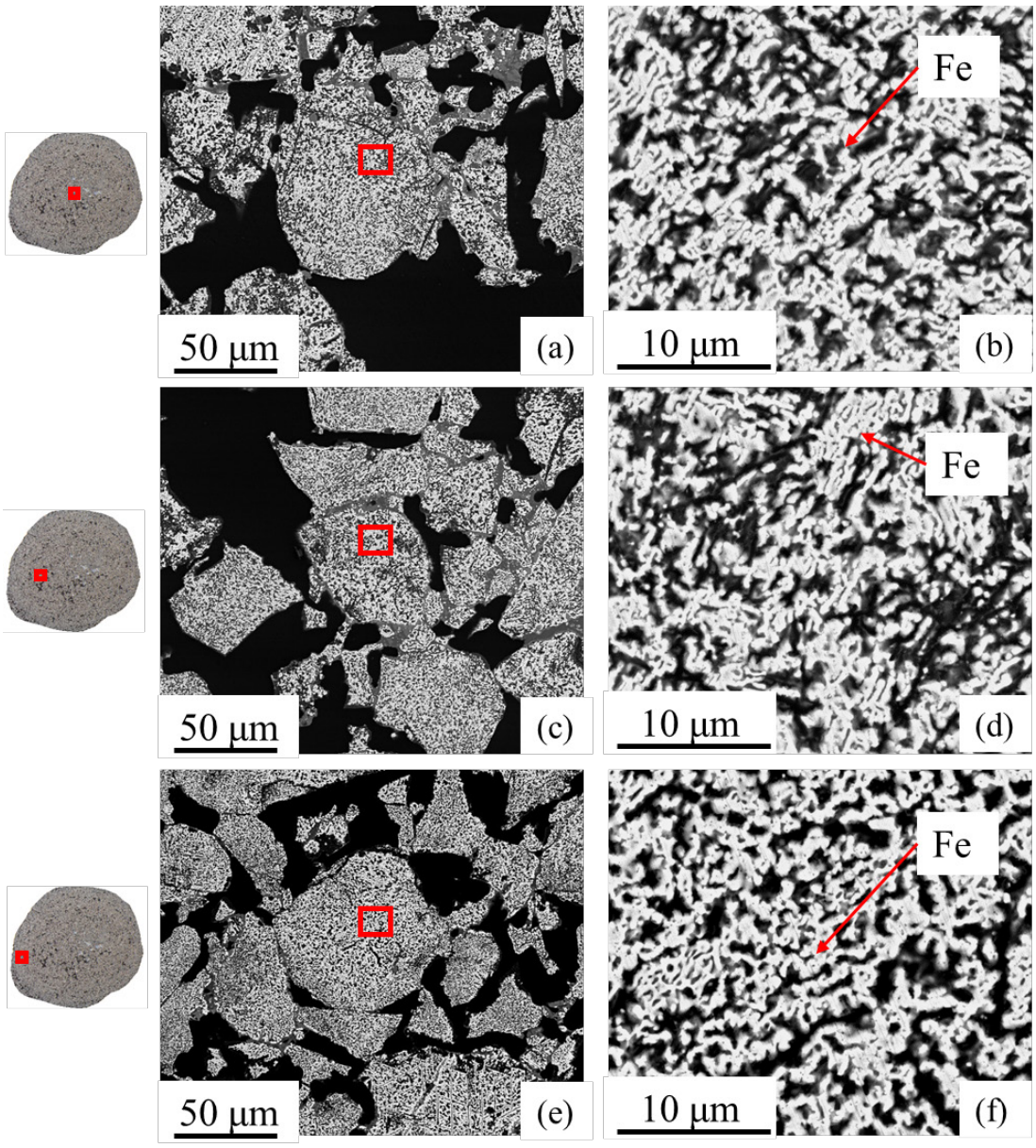

Figure B.17*- Particle morphologies at different areas of the fully reduced pellet at 1223 K: (a), (c), and (e) are lower magnification photos of particles at each location, while (b), (d), and (f) are corresponding areas at higher magnification.*

Appendix C
Additional information of reducing pre-oxidised pellets for Chapter 5

C.1 The full XRD pattern obtained from the fully reduced pellets following reduction at each temperature from 1043 K to 1443 K

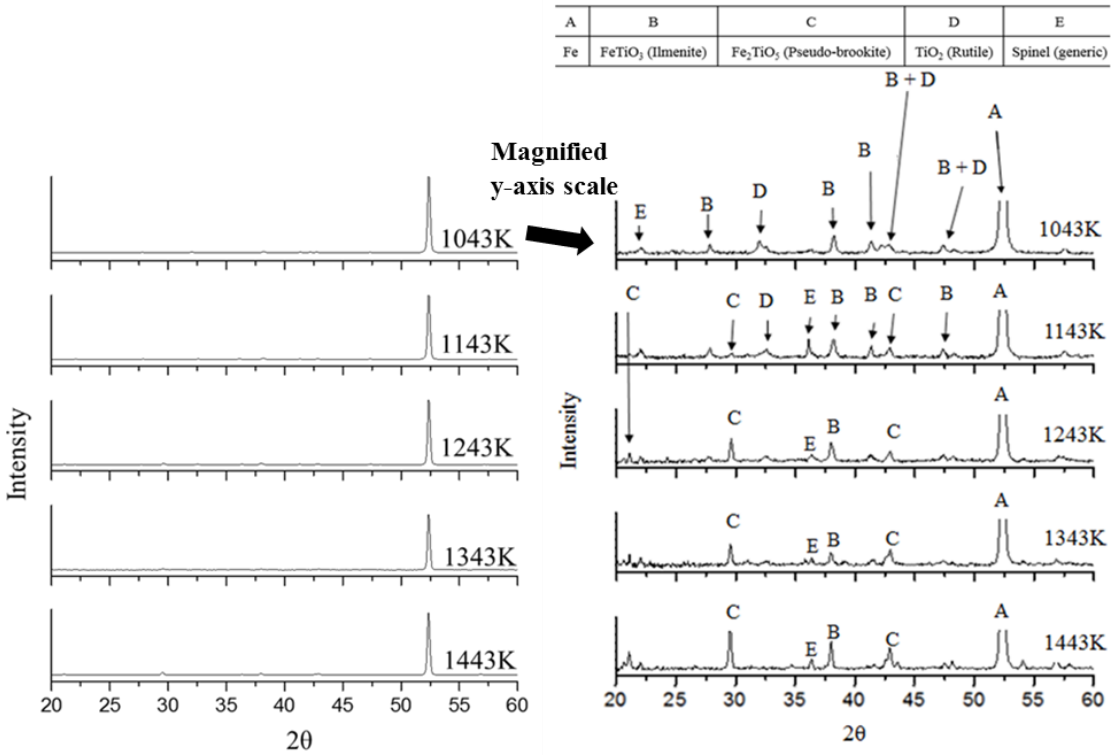

Figure C.1*- (Left) Unmagnified XRD diffractograms obtained from fully reduced pellets (pre-oxidised) at each reduction temperature. Note that only the Fe peak (Peak A) can be readily distinguished in each spectrum, such that all spectra appear broadly identical. (Right) The same XRD diffractograms shown on a magnified y-axis scale which allows peaks from minor oxide phases to be determined.*

C.2 Concentration curves of each crystalline phase during reduction of pre-oxidised pellets at each H_2 gas concentration in H_2-Ar gas mixtures at a flow of 250 ml/min at 1023 K

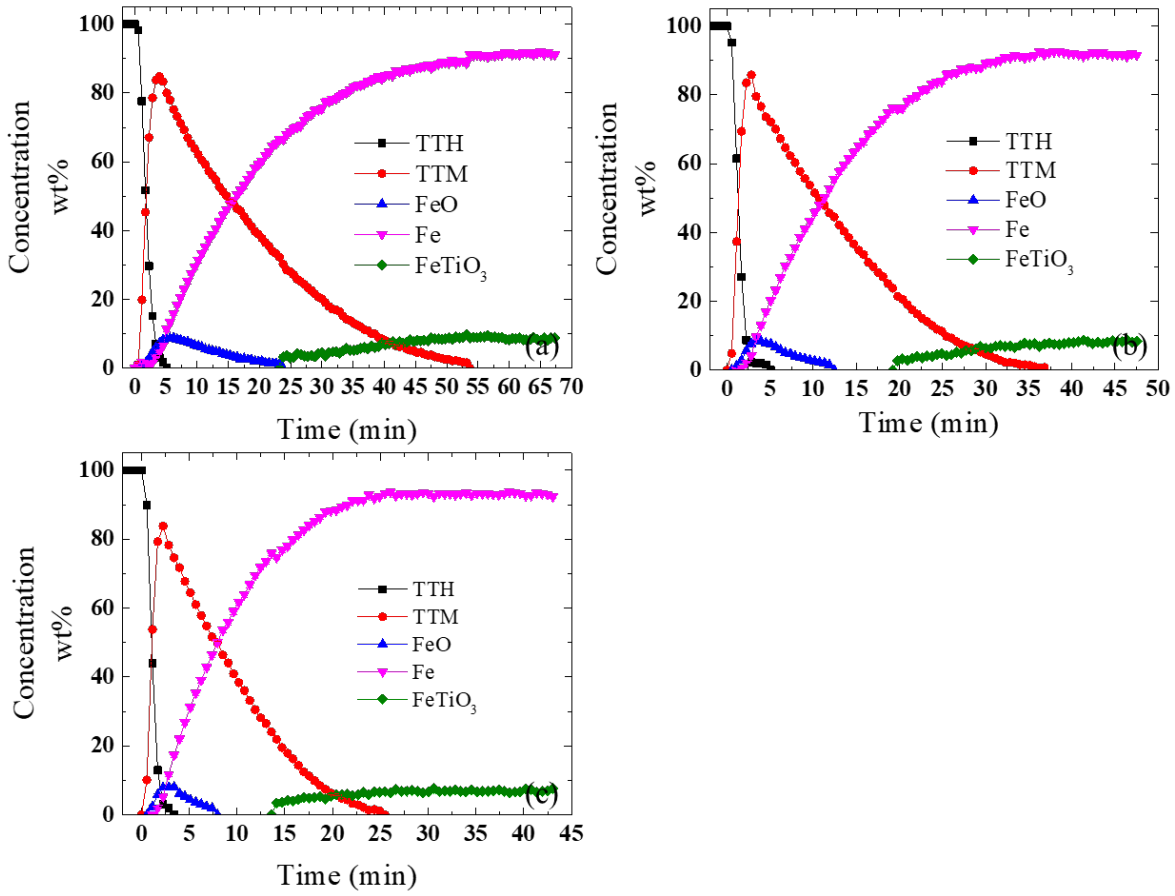

Figure C.2*- The concentration (wt%) curves of each crystalline phase during reduction of pre-oxidised pellets at a flow of 250 ml/min at 1023 K by H_2-Ar gas mixtures with (a) 50vol% H_2, (b) 75vol% H_2, and (c) 100vol% H_2*

C.3 Concentration curves of each crystalline phase during reduction of pre-oxidised pellets at each H_2 gas concentration in H_2-Ar gas mixtures at a flow of 250 ml/min at 1123 K

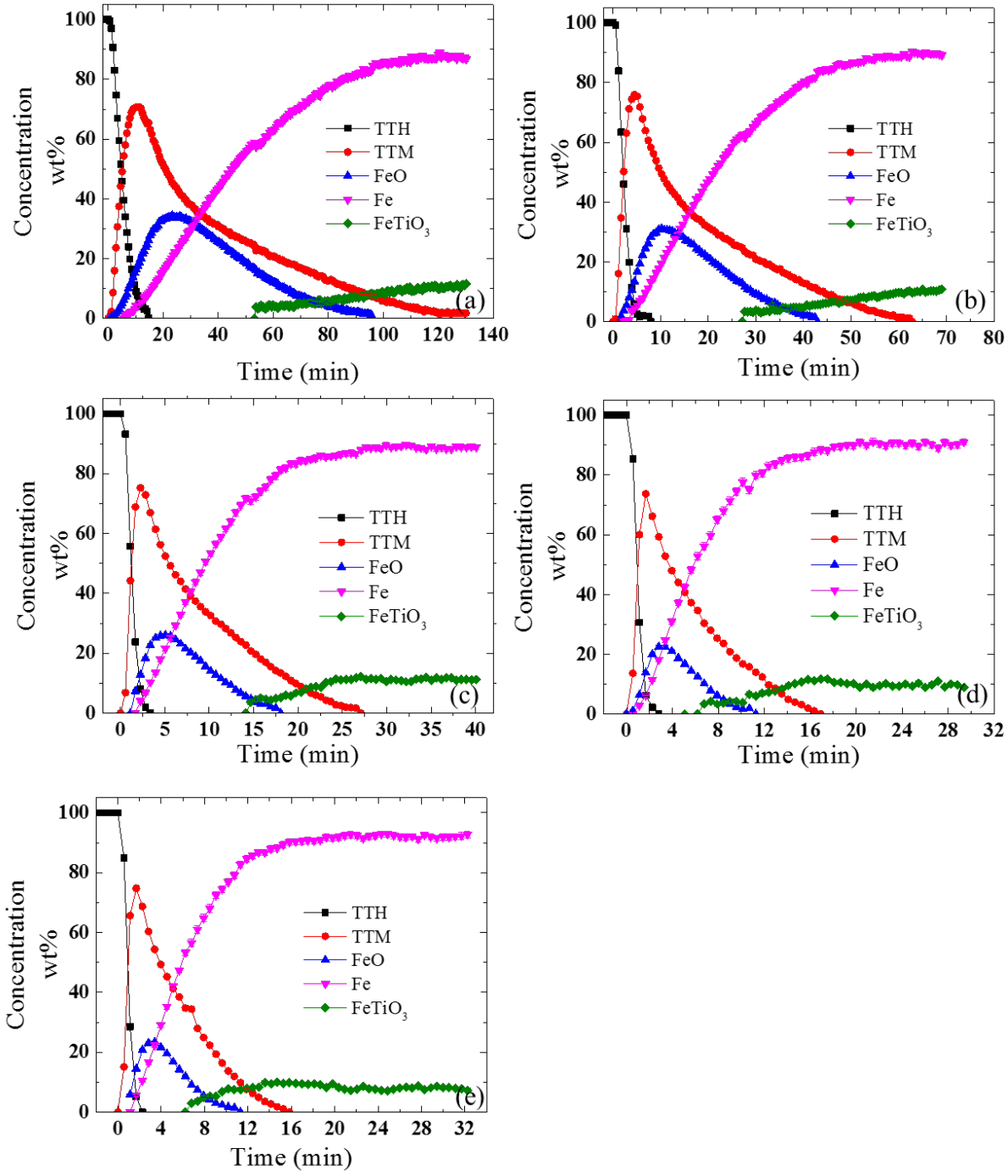

Figure C.3 *- The concentration (wt%) curves of each crystalline phase during reduction of pre-oxidised pellets at a flow of 250 ml/min at 1123 K by H_2-Ar gas mixtures with (a) 10vol% H_2, (b) 25vol% H_2, (c) 50vol% H_2, (d) 75vol% H_2, and (e) 100vol% H_2*

C.4 The characterisation of the representative particles in the pre-oxidised pellet prior to reduction

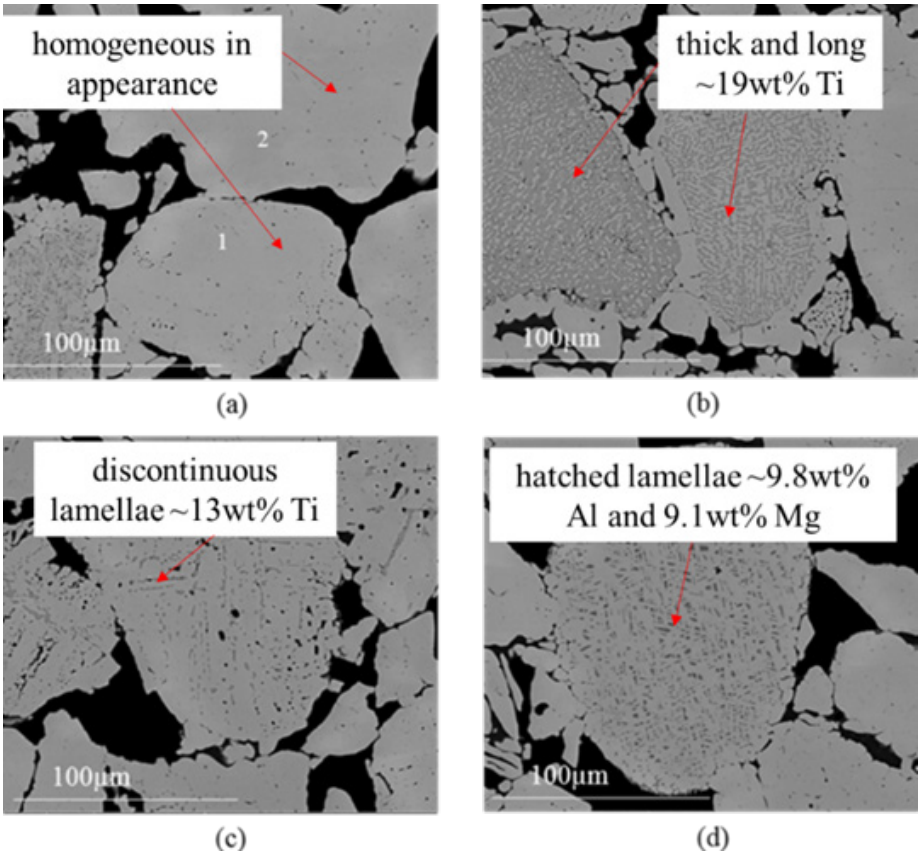

Figure C.4 *- Back-scattered SEM images showing the particles in the pre-oxidised pellets before reduction. (a) uniform particles. (b), (c) and (d) non-uniform particles Note this figure has already been published in a paper from the author [162]*

Table C.1*- EDS point analysis (wt%) of specified spots in the particles of pre-oxidised pellets (in* ***Figure C.4****, the point analysis in the dark areas were averaged) Note this table has already been published in a paper from the author [162]*

Areas	O	Fe	Ti	Al	Mg	Mn	O/(Fe+Ti)
Particle 1	28.3	63.2	4.2	1.5	1.8	1	0.4
Particle 2	28.5	62.6	4.3	2.0	1.9	0.8	0.4
Dark phase in (b)	31.9	46.2	19.2	1.1	1.3	-	0.5
Light phase in (b)	28.6	61.0	6.0	1.0	2.6	0.8	0.4
Dark phase in (c)	29.7	53.5	13.7	1.8	1.4	-	0.4
Light phase in (c)	28.5	62.3	5.0	1.7	1.8	0.7	0.4
Dark phase in (d)	29.9	48.6	1.9	9.8	9.1	0.8	0.6
Light phase in (d)	28.3	63.1	3.6	3	2.1	-	0.4

C.5 Back-scattered SEM images of the representative partially reduced pre-oxidised pellets at 1023 K

1. *X*=21% pellet

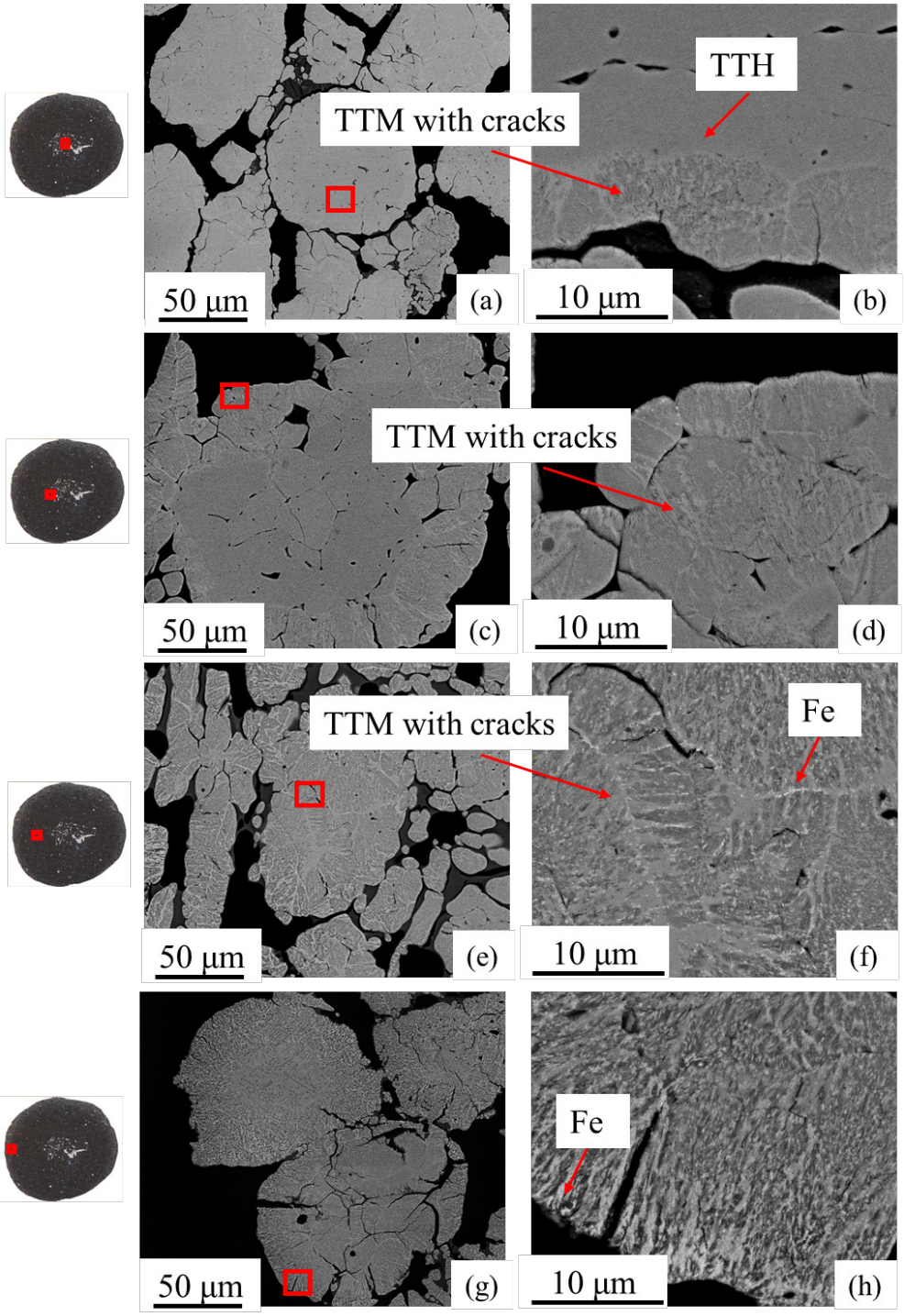

Figure C.5 *- Particle morphologies at different areas of the X=21% pellet reduced at 1023 K: (a), (c), (e) and (g) are lower magnification photos of particles at each location, while (b), (d), (f) and (h) are corresponding areas at higher magnification.*

2. *X*=55% pellet

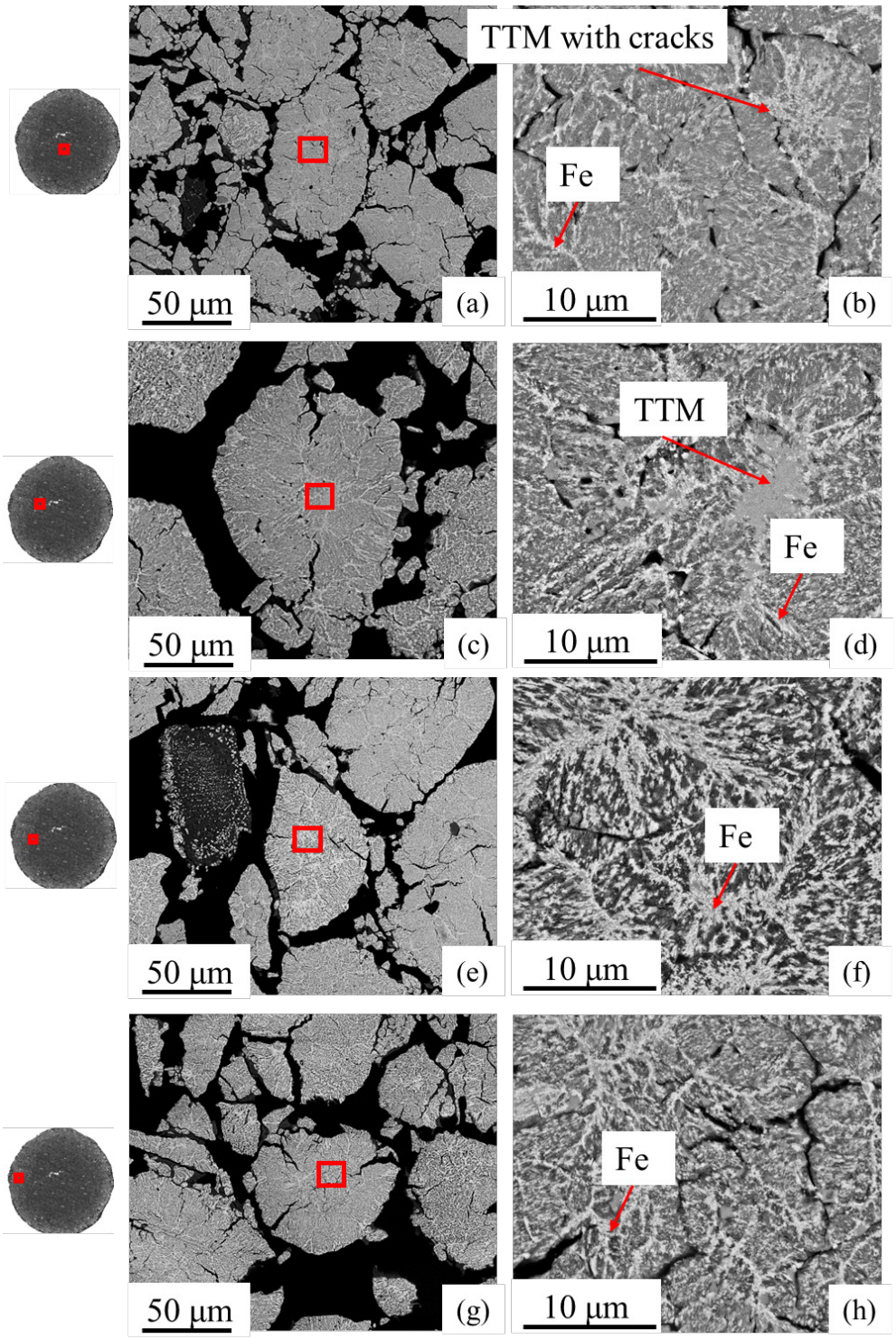

Figure C.6 *- Particle morphologies at different areas of the X=55% pellet reduced at 1023 K: (a), (c), and (e) are lower magnification photos of particles at each location, while (b), (d), (f) and (h) are corresponding areas at higher magnification.*

3. *X*=79% pellet

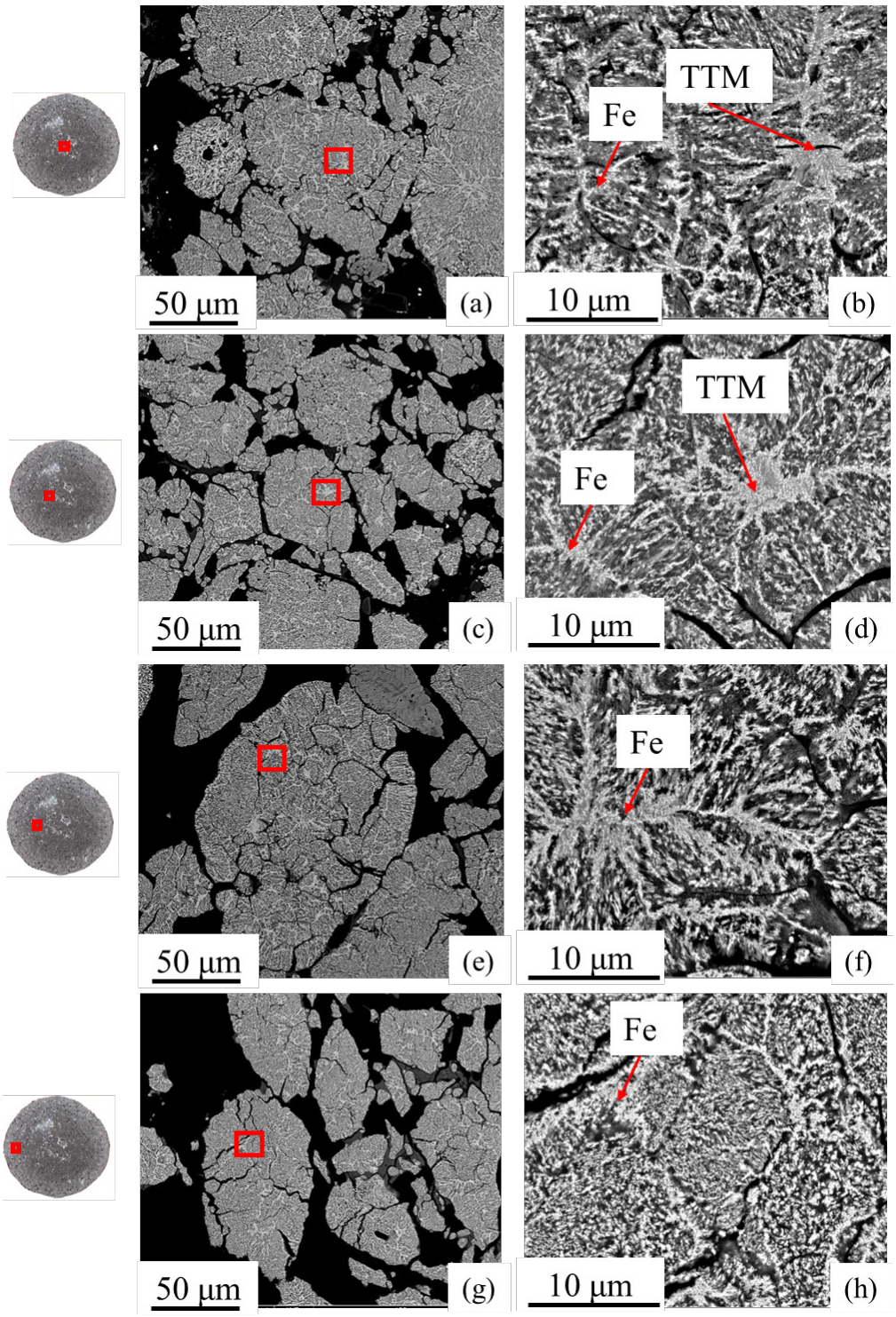

Figure C.7*- Particle morphologies at different areas of the X=79% pellet reduced at 1023 K: (a), (c), and (e) are lower magnification photos of particles at each location, while (b), (d), (f) and (h) are corresponding areas at higher magnification.*

4. Fully reduced pellet

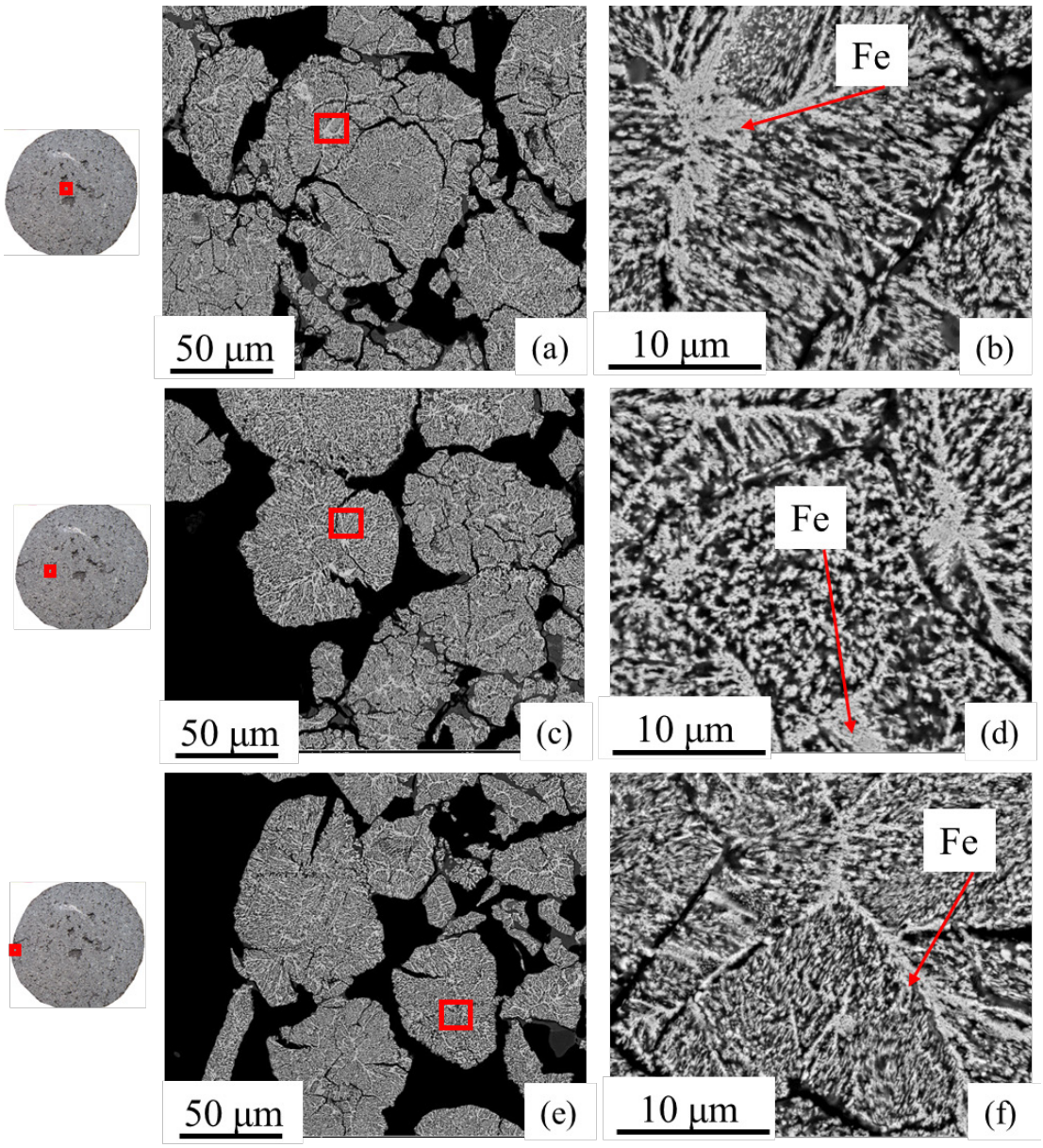

Figure C.8 *- Particle morphologies at different areas of the fully reduced pellet at 1023 K: (a), (c), and (e) are lower magnification photos of particles at each location, while (b), (d), and (f) are corresponding areas at higher magnification.*

C.6 Back-scattered SEM images of the representative partially reduced pre-oxidised pellets at 1123 K

1. *X*=18% pellet

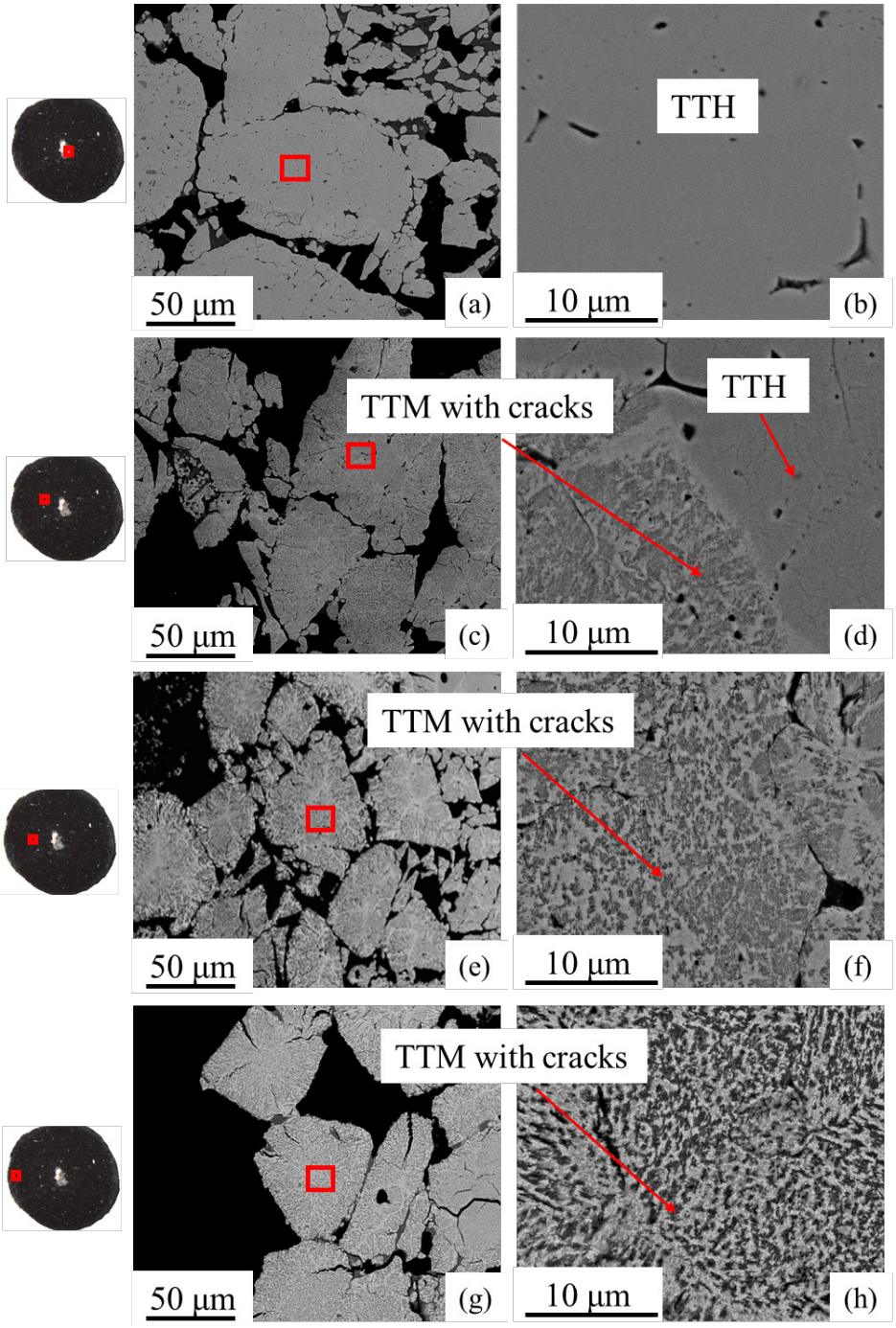

Figure C.9*- Particle morphologies at different areas of the 18% pellet reduced at 1123 K: (a), (c), (e) and (g) are lower magnification photos of particles at each location, while (b), (d), (f) and (h) are corresponding areas at higher magnification*

2. *X*=56% pellet

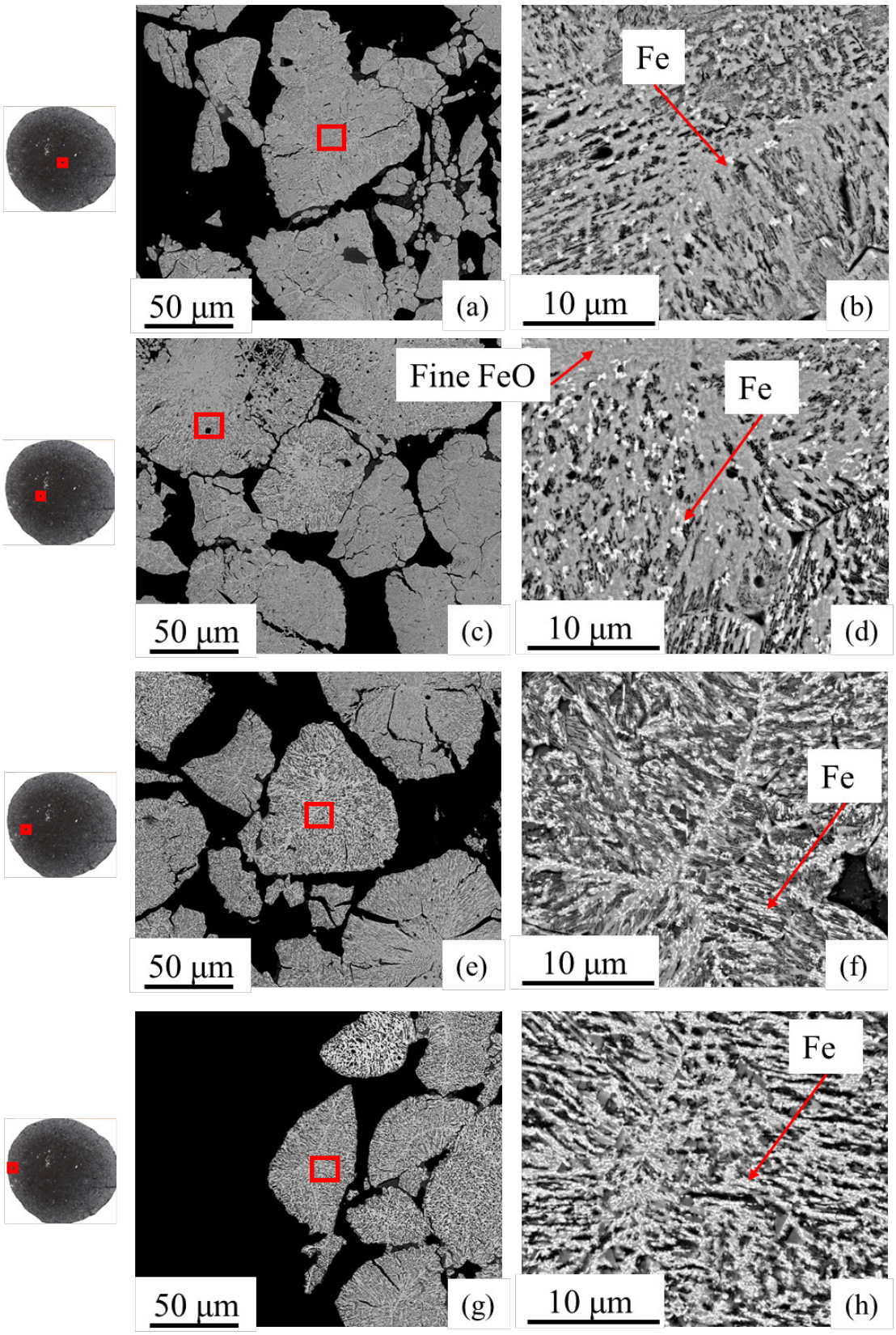

Figure C.10*- Particle morphologies at different areas of the 56% pellet reduced at 1123 K: (a), (c), (e) and (g) are lower magnification photos of particles at each location, while (b), (d), (f) and (h) are corresponding areas at higher magnification.*

3. *X*=80% pellet

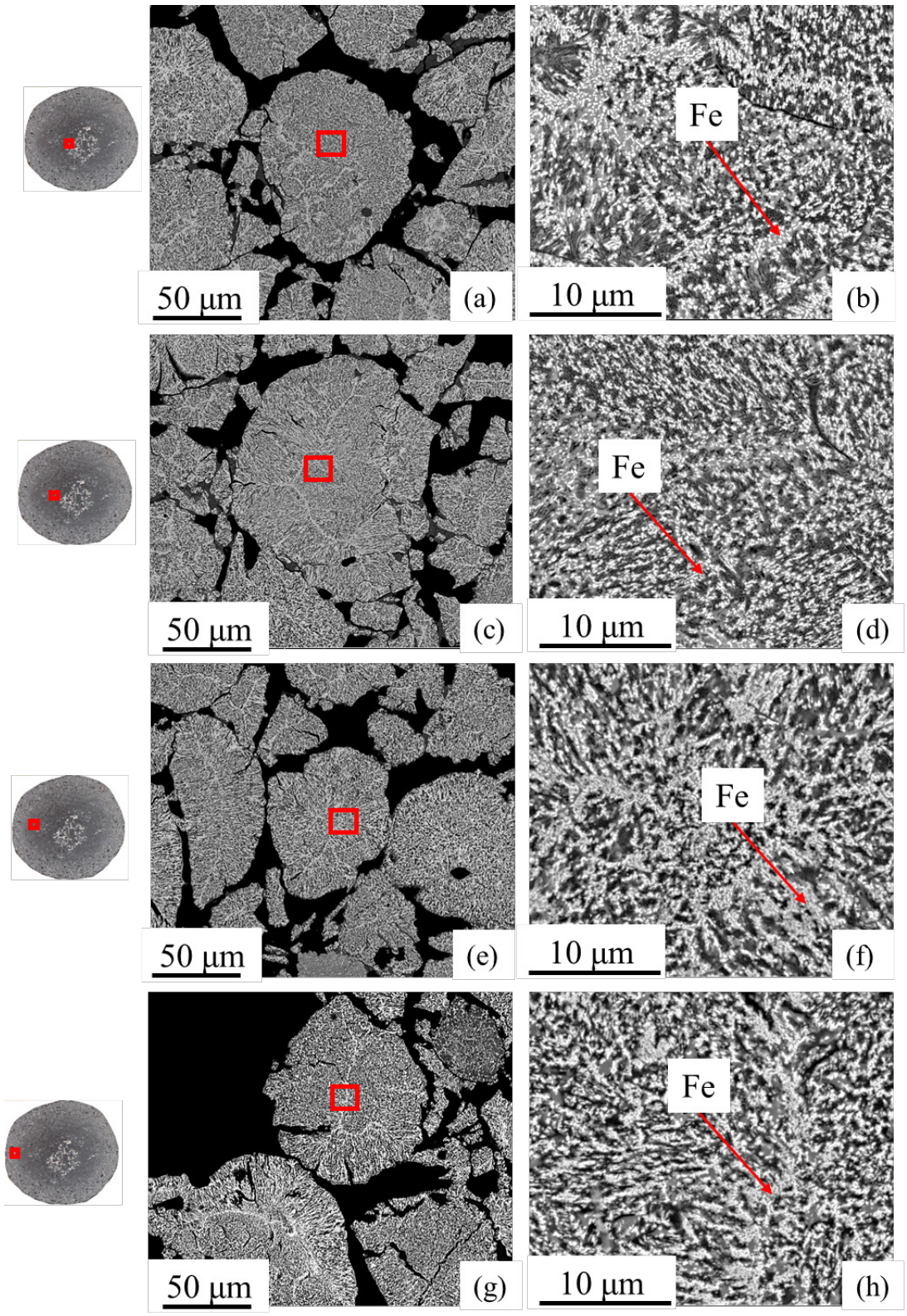

Figure C.11- *Particle morphologies at different areas of the 80% pellet reduced at 1123 K: (a), (c), (e) and (g) are lower magnification photos of particles at each location, while (b), (d), (f) and (h) are corresponding areas at higher magnification.*

4. Fully reduced pellet

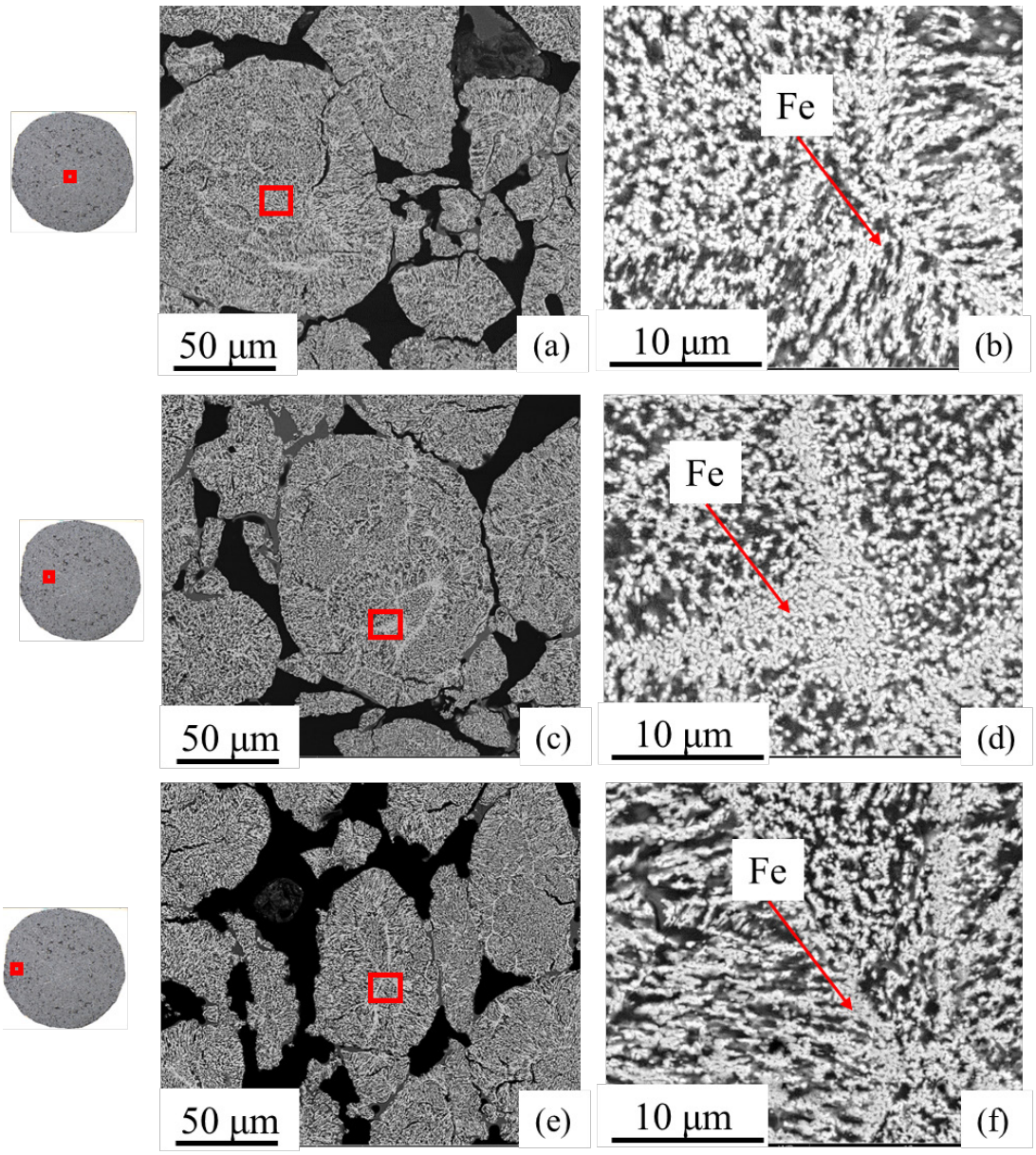

Figure C.12*- Particle morphologies at different areas of the fully reduced pellet at 1123 K: (a), (c), and (e) are lower magnification photos of particles at each location, while (b), (d), and (f) are corresponding areas at higher magnification.*

C.7 Back-scattered SEM images of the representative partially reduced pre-oxidised pellets at 1223 K

1. *X*=23% pellet

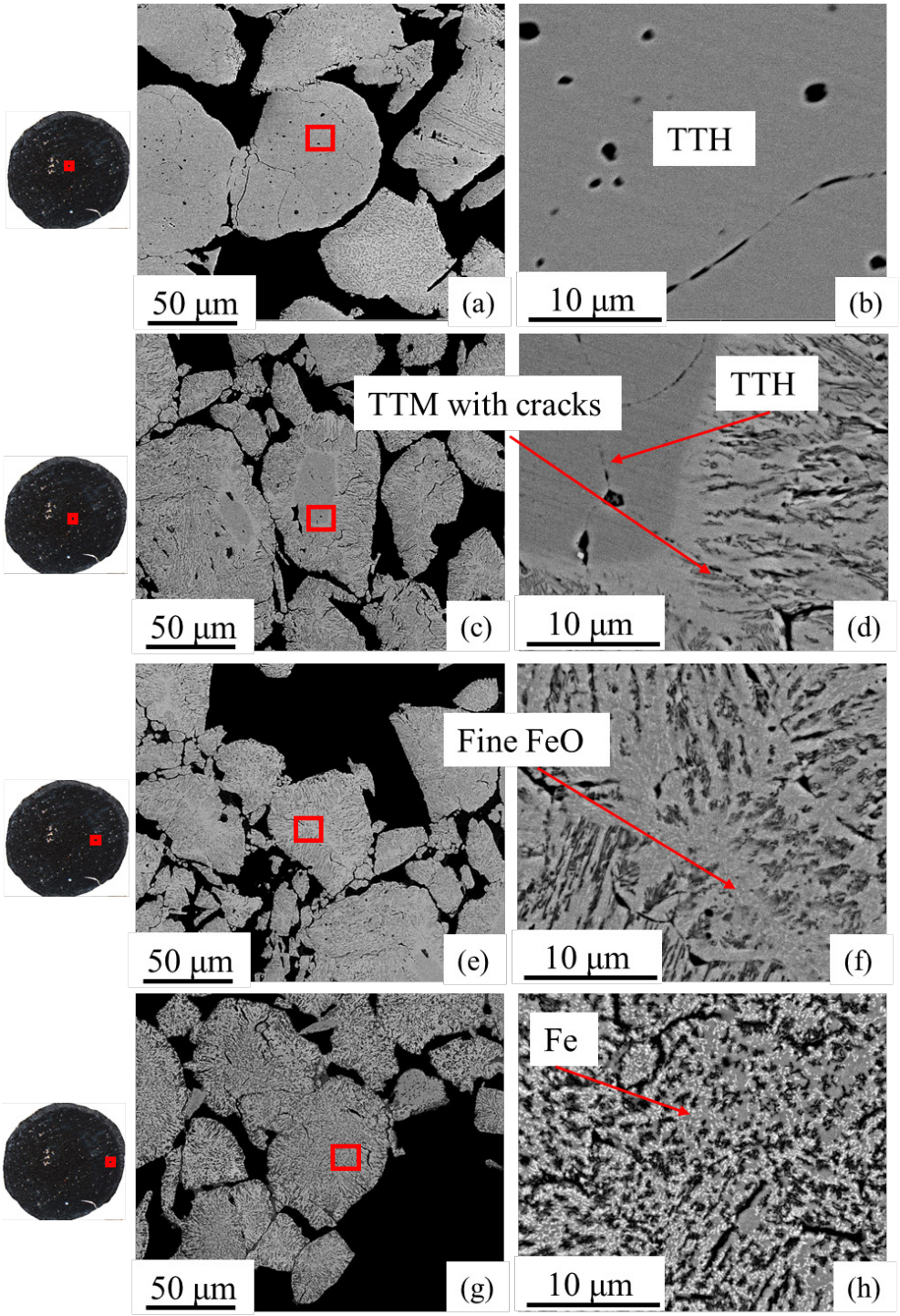

Figure C.13*- Particle morphologies at different areas of the 23% pellet reduced at 1223 K: (a), (c), (e) and (g) are lower magnification photos of particles at each location, while (b), (d), (f) and (h) are corresponding areas at higher magnification.*

2. *X*=53% pellet

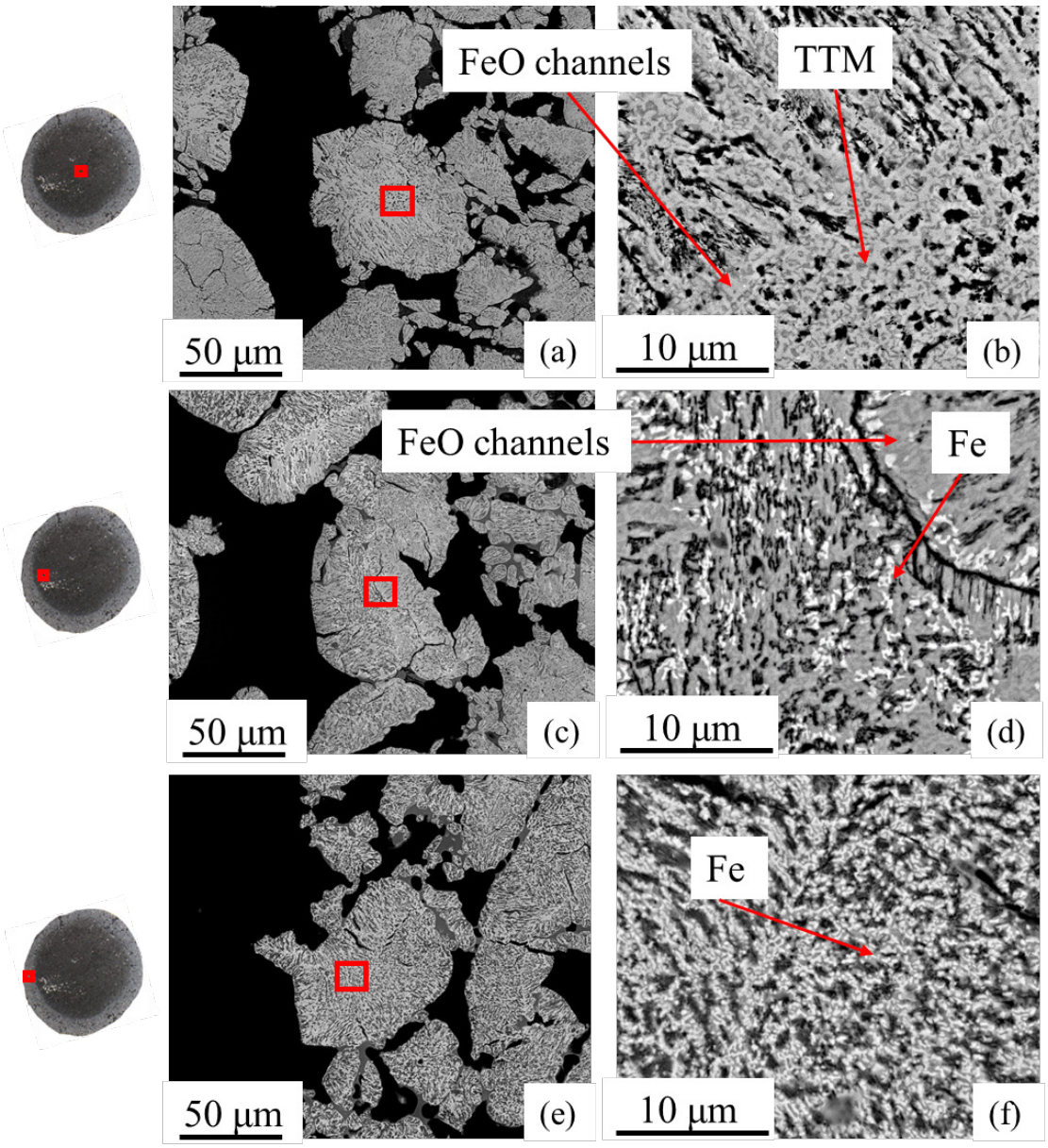

Figure C.14*- Particle morphologies at different areas of the 53% pellet reduced at 1223 K: (a), (c), and (e) are lower magnification photos of particles at each location, while (b), (d), and (f) are corresponding areas at higher magnification.*

3. *X*=81% pellet

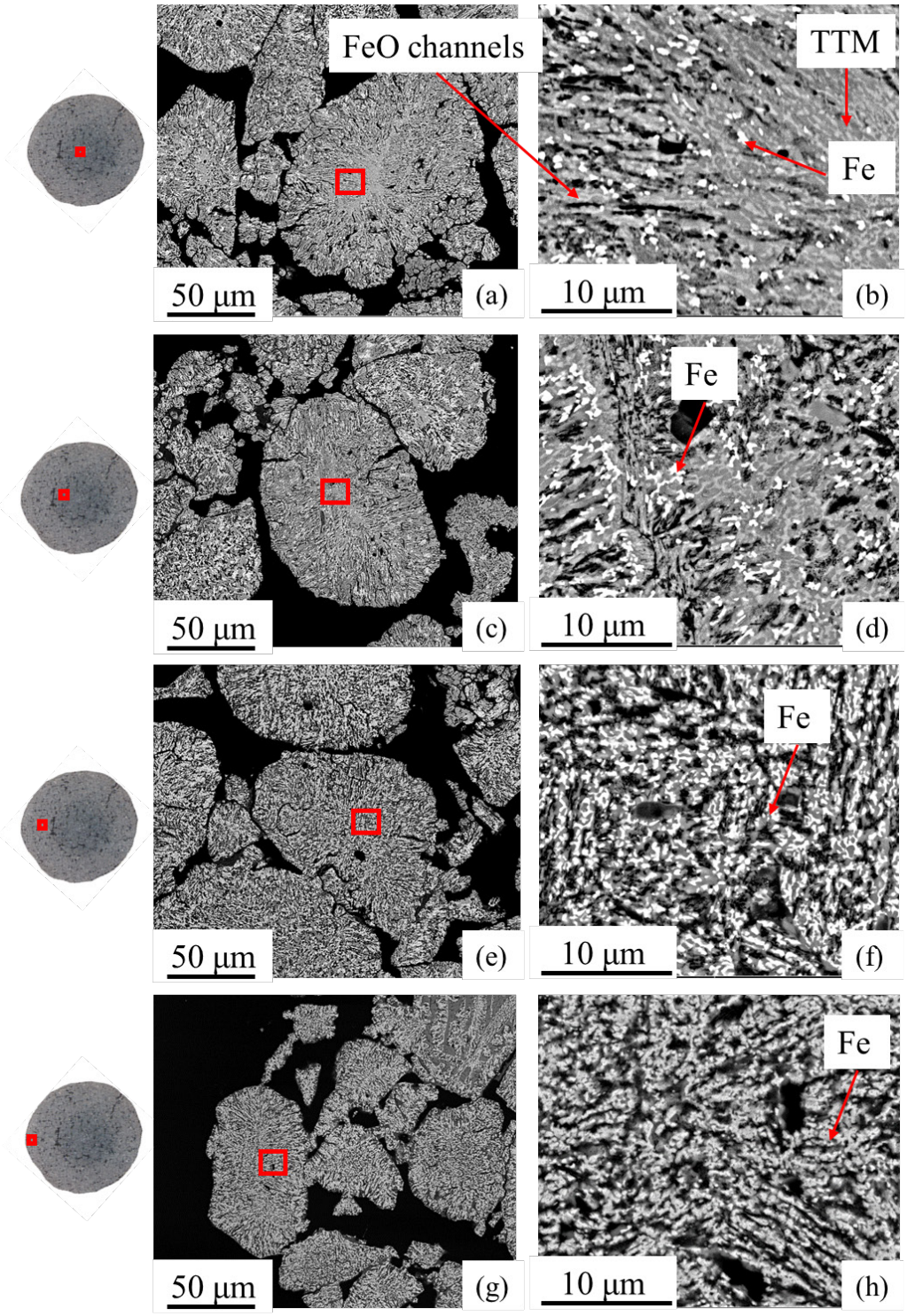

Figure C.15*- Particle morphologies at different areas of the 81% pellet reduced at 1223 K: (a), (c), (e) and (g) are lower magnification photos of particles at each location, while (b), (d), (f) and (h) are corresponding areas at higher magnification.*

4. Fully reduced pellet

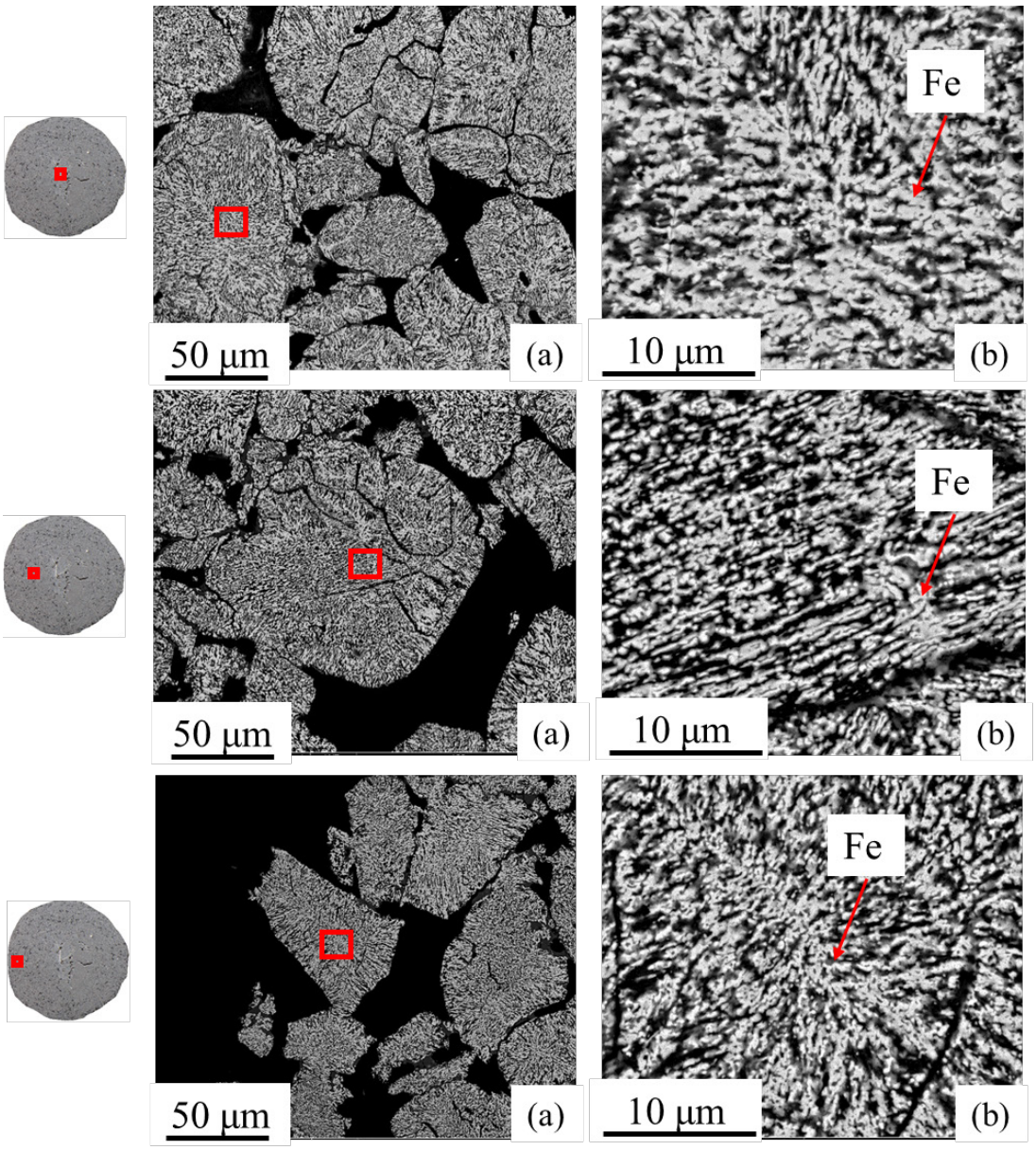

Figure C.16 *- Particle morphologies at different areas of the fully reduced pellet at 1223 K: (a), (c), and (e) are lower magnification photos of particles at each location, while (b), (d), and (f) are corresponding areas at higher magnification.*

Appendix D
Additional information for Chapter 7 – Calculation of Ti stoichiometry in TTM during reduction

D.1 Ar-sintered pellets at 1023 K

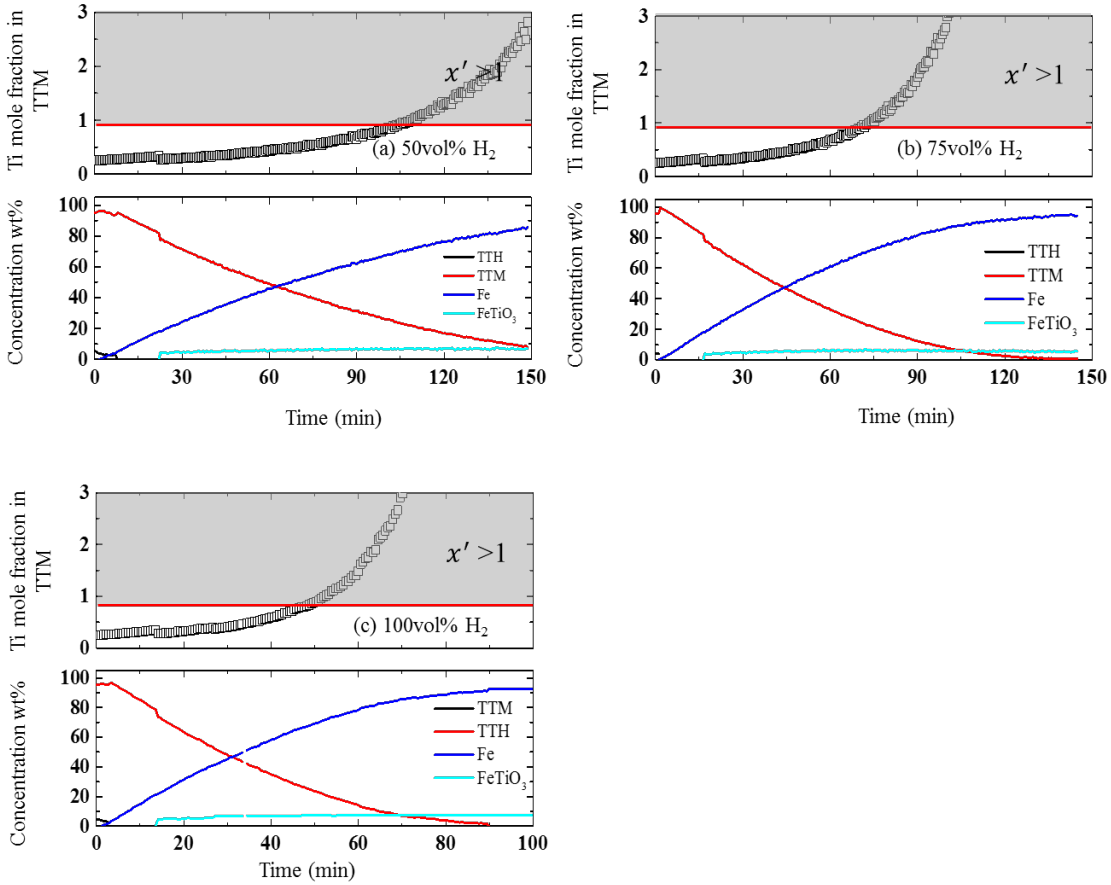

Figure D.1*– The change of Ti mole fraction during reduction of Ar-sintered pellets at each H_2 gas content at 1023 K. (a) 50vol%, (b) 75vol%, and (c) 100vol%*

D.2 Ar-sintered pellets at 1123 K

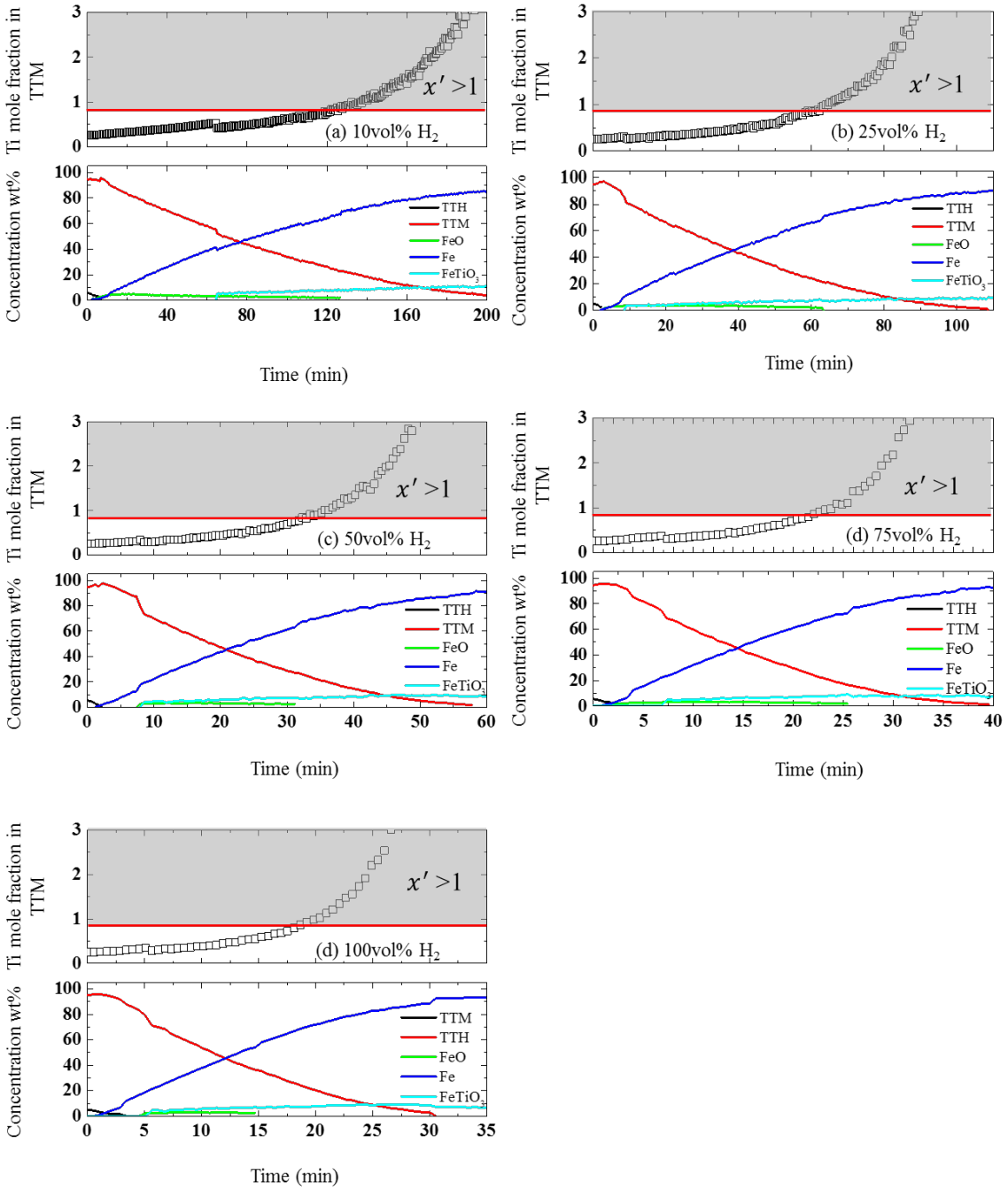

Figure D.2– *The change of Ti mole fraction during reduction of Ar-sintered pellets at each H_2 gas content at 1123 K. (a) 10vol%, (b) 25vol%, (c) 50vol%, (d) 75vol%, and (e) 100vol%*

D.3 Ar-sintered pellets at 1223 K

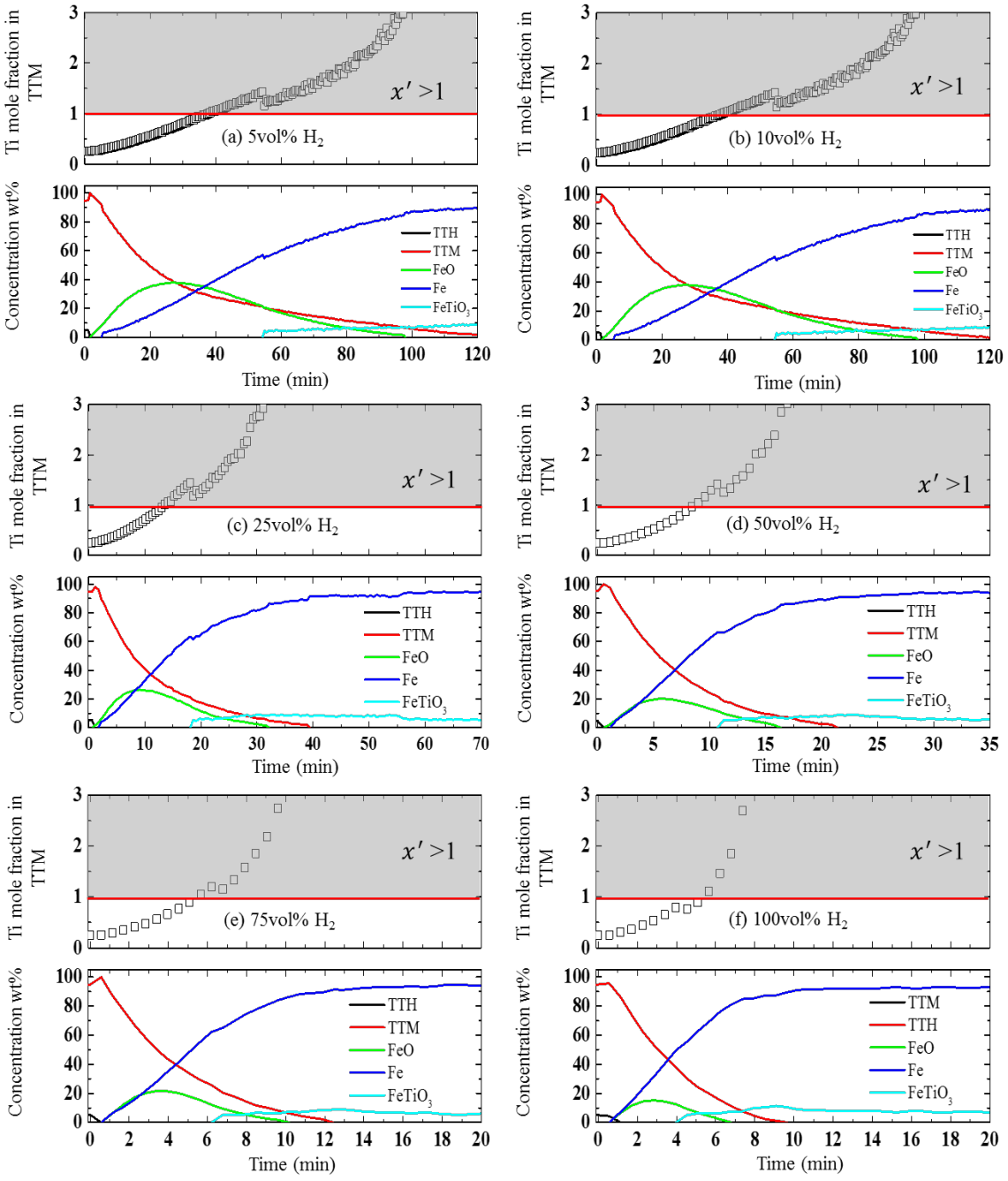

Figure D.3*– The change of Ti mole fraction during reduction of Ar-sintered pellets at each H_2 gas content at 1223 K. (a) 5vol%, (b) 10vol%, (c) 25vol%, (d) 50vol%, (e) 75vol%, and (f) 100vol%*

D.4 Pre-oxidised pellets at 1023 K

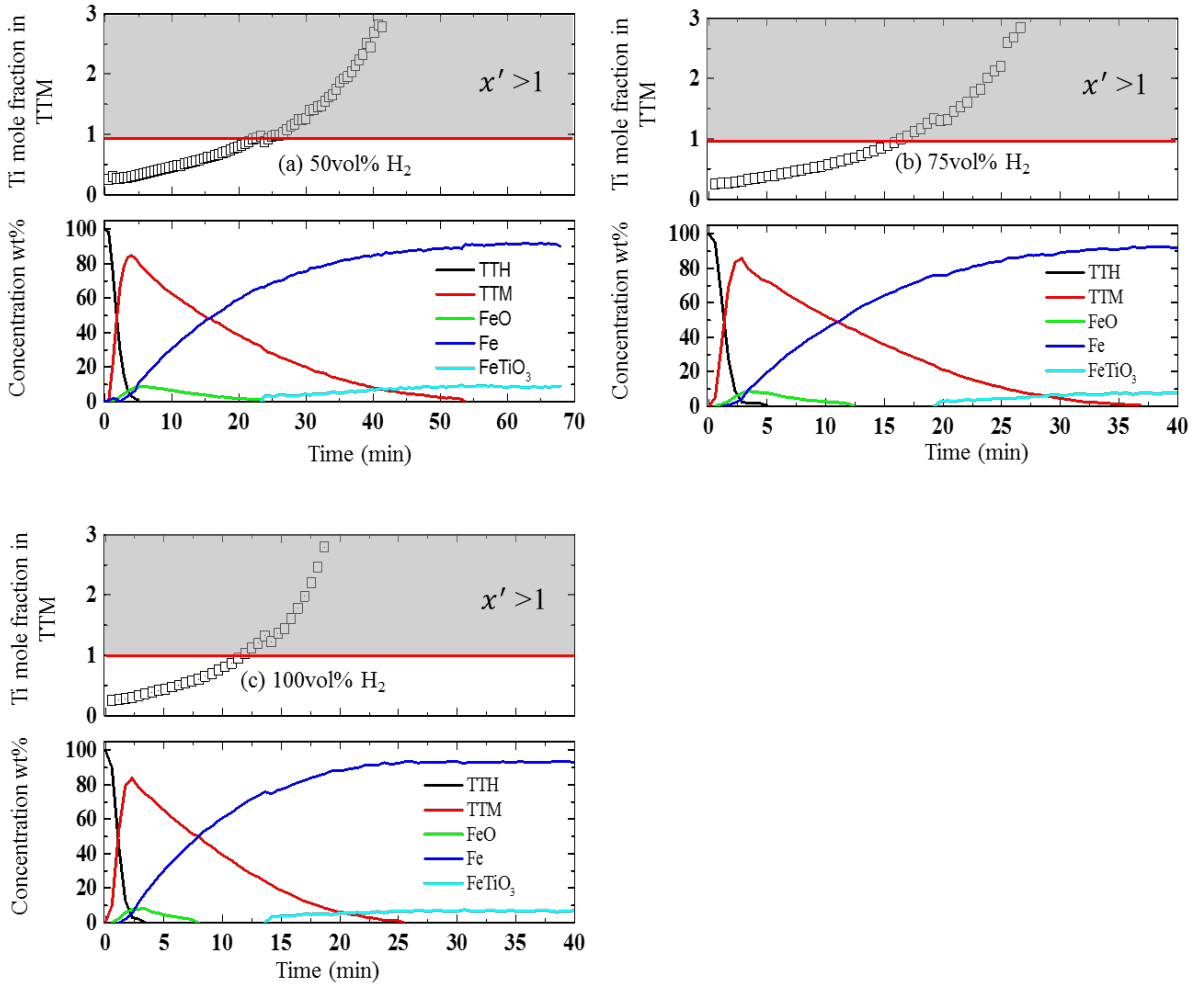

Figure D.4*– The change of Ti mole fraction during reduction of pre-oxidised pellets at each H_2 gas content at 1023 K. (a) 50vol%, (b) 75vol%, and (c) 100vol%*

D.5 Pre-oxidised pellets at 1123 K

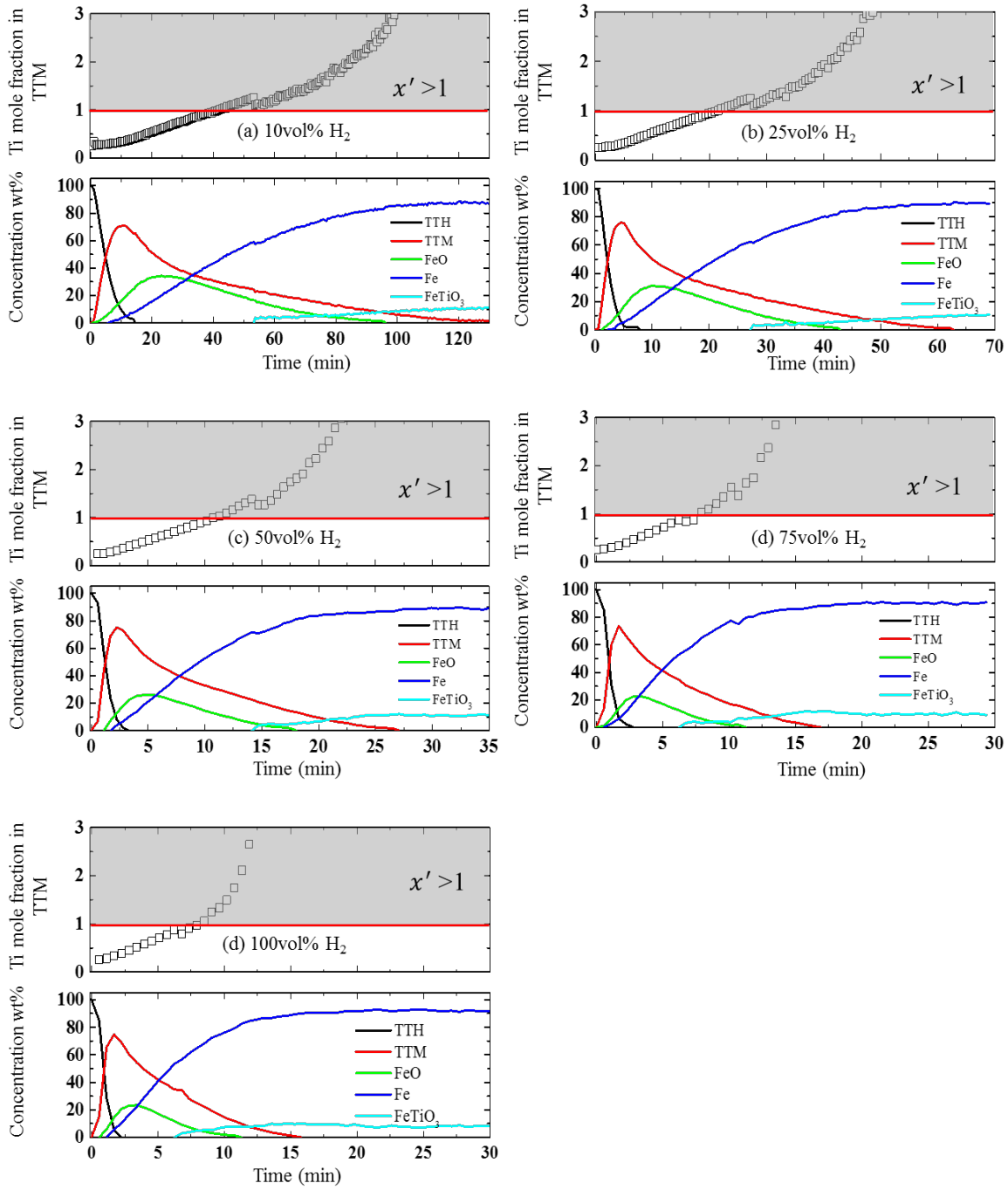

***Figure D.5**– The change of Ti mole fraction during reduction of pre-oxidised pellets at each H_2 gas content at 1123 K. (a) 10vol%, (b) 25vol%, (c) 50vol%, (d) 75vol% and (e) 100vol%*

D.6 Pre-oxidised pellets at 1223 K

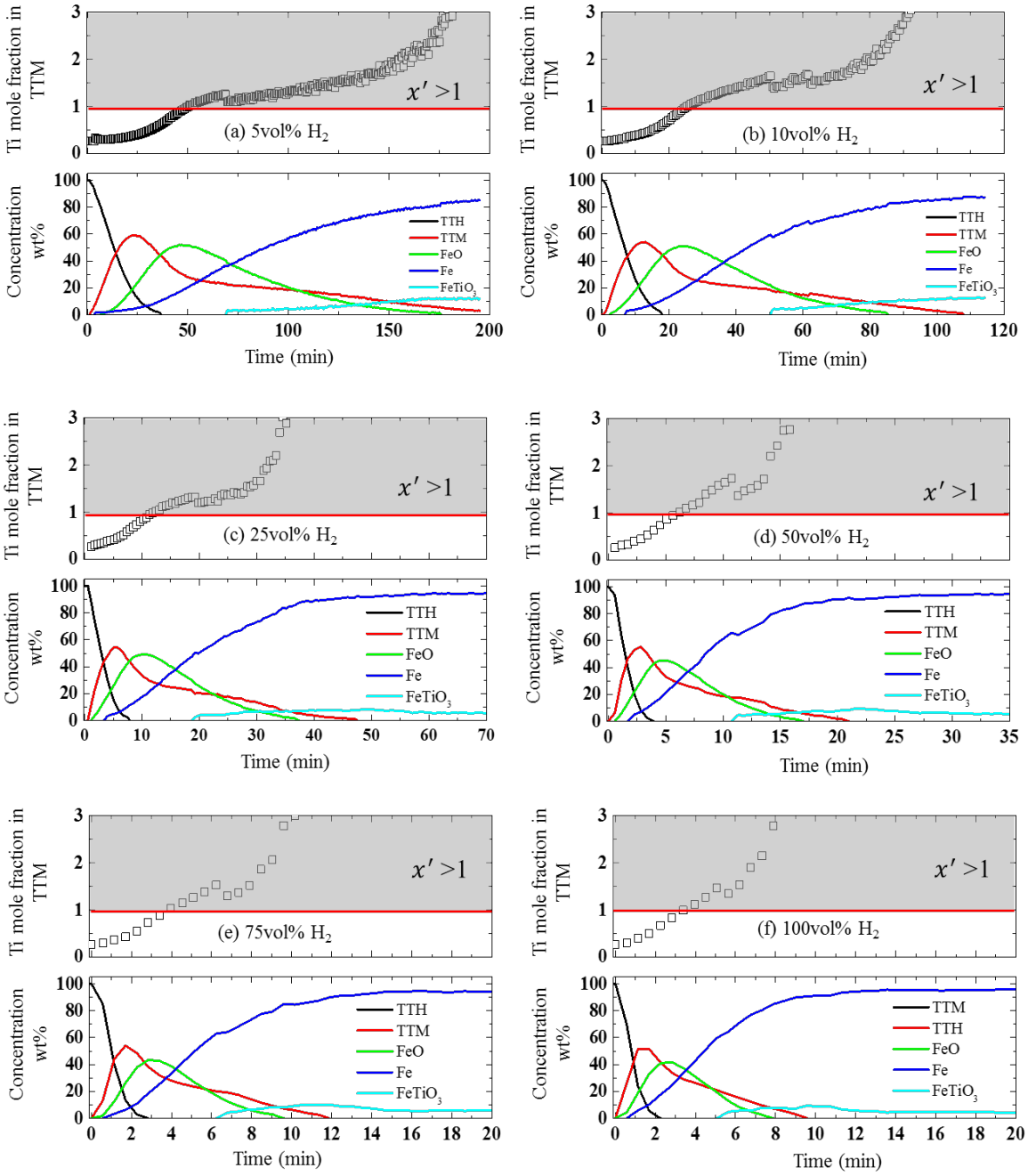

***Figure D.6**– The change of Ti mole fraction during reduction of pre-oxidised pellets at each H_2 gas content at 1223 K. (a) 5vol%, (b) 10vol%, (c) 25vol%, (d) 50vol%, (e) 75vol%, and (f) 100vol%*